Direct Simulation Studies of Suspended Particles and Fibre-filled Suspensions

A thesis submitted in fulfillment
of the requirements for the degree of
Doctor of Philosophy

School of
Aerospace, Mechanical and Mechatronic Engineering
The University of Sydney
August, 2003

Clint G. Joung©

Dedication

> Of the second-rate rulers, people speak respectfully, saying, *'He has done this, he has done that'*. Of the first-rate rulers they do not say this. They say: *'We have done it all ourselves'*.
>
> Lao Tze 604 – 531 BC, *Tao Te Ching Ch.* 17

This work is dedicated to a mentor of my earlier years, John Van Opstal.

Declaration

I declare that this thesis does not incorporate without acknowledgement any material previously submitted for a degree or diploma in any university; and that to the best of my knowledge and belief it does not contain any material previously published or written by another person where due reference is not made in the text.

Acknowledgements

I wish to thank Professors Nhan Phan-Thien and Xijun Fan for their effective and wise supervision in the early years of my candidature. I also wish to thank Professor Roger Tanner who supervised me for the remainder. Roger has always shown good humour and great understanding towards me. I appreciated his allowing me the indulgence to dictate my own pace and set my own course. This gave me the freedom to breath and explore which I value enormously. For the people and places I have met and seen, and the abilities and opportunities I have gained under their guidance, I am greatly in debt to my three supervisors.

I acknowledge and thank the financial support of the Australian Research Council (ARC), and Moldflow Inc. who arranged for the provision of the APA(I) scholarship awarded to me during my candidature.

I thank current and former members of the Rheology group who also acted in times as unofficial co-supervisors. In particular I acknowledge and thank Drs Yurun Fan, Hua Shu Dou and Shicheng Xue, who each helped substantially when I needed further technical guidance. I thank Dr Xiaolin Luo from CMIS CSIRO for his help with aspects in programming with *Fastflo*. I am grateful to Mark Waring and Optimus Pty Ltd, who have continued to support me while I finish my candidature, and have shown great interest in my career development.

The friendship of the Rheology group members were invaluable to me during my candidature. I appreciated the welcoming hand extended to me by Simin Nasseri, Surjani Uthayakumaran, Ping Jiang, Jane Liu, Marcus Newberry, Howard See, Damien Marik and Babatunde Fasheun. The many extracurricular activites enjoyed with 'the group' are the most memorable of my stay. Outside of the group, I am grateful for the great and loyal friends I have in Morteza Nateghi - the eternal student and Linux installer extraordinaire, and 'the captain', Darren Lysenko, my first choice on any away team. My friends kept me together during my candidature and so I thank them all once again for getting me over the line.

Finally my family took the burden of my years as a student with unending patience, understanding and good humour. To Wendy, Grace, Neal and my mum, I am eternally grateful.

Abstract

A new Direct Simulation fibre model was developed which allowed flexibility in the fibre during the simulation of fibre suspension flow. This new model was called the 'Chain-of-Spheres' model. It was hypothesised that particle shape and deformation could significantly affect particle dynamics, and also suspension bulk properties such as viscosity. Data collected from the simulation showed that *flexible* fibres in shear flow resulted in an order of $7-10\%$ bulk relative viscosity increase over the 'rigid' fibre result. Results also established the existence of a relationship between bulk viscosity and particle stiffness. In comparison with experimental results, other more conventional rigid fibre based methods appeared to underpredict relative viscosity. The flexible fibre method thus markedly improved the ability to estimate relative viscosity. The *curved* rigid fibre suspension also exhibited increased viscosity of the order twice that of the equivalent straight rigid fibre suspension. With such sensitivity to fibre shape, this result has some important implications for the quality of fibre inclusions used. For consistent viscosity, the shape quality of the fibres was shown to be important.

The 'Chain of Spheres' simulation was substantially extended to create a new simulation method with the ability to model the dynamics of arbitrarily shaped particles in the Newtonian flow field. This new '3D Particle' simulation method accounted for the inertial force on the particles, and also allowed particles to be embedded in complex flow fields. This method was used to reproduce known dynamics for common particle shapes, and then to predict the unknown dynamics of various other particle shapes in shear flow. In later sections, the simulation demonstrated inertia-induced particle migration in

the non-linear shear gradient Couette cylinder flow, and was used to predict the fibre orientation within a diverging channel flow. The performance of the method was verified against known experimental measurements, observations and theoretical and numerical results where available. The comparisons revealed that the current method reproduced single particle dynamics with great fidelity.

The broad aim of this research was to better understand the microstructural dynamics within the fibre-filled suspension and from it, derive useful engineering information on the bulk flow of these fluids. This thesis represents a move forward to meet this broad aim. It is hoped that future researchers may benefit from the new approaches and algorithms developed here.

Contents

List of Figures

List of Tables

Chapter 1

Introduction

1.1 Motivation

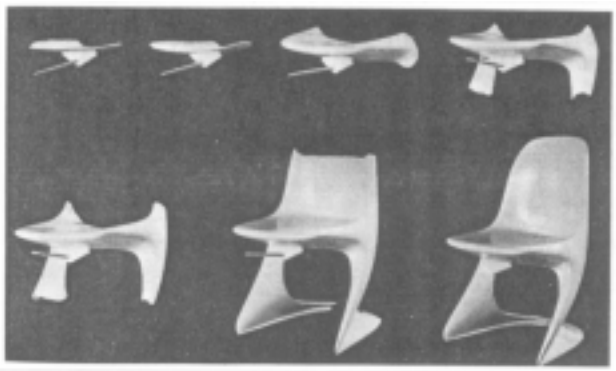

Figure 1.1: Various stages during the injection moulding of a plastic chair. From *Injection Molding - An Introduction*, G. Potsch and W. Michaeli, Hanser Pub. (1995).

Injection moulding is the dominant process in industry for forming plastics. A wide and diverse range of products are manufactured using this process. These may range from simple domestic items which may simply benefit aesthetically from the use of molded plastic (e.g. Fig. 1.1), through to completely mechanically functional plastic parts used for example in load bearing, light-weight, high performance equipment (e.g. Fig 1.2). It is in the latter situation where the fibre-filling method is of most interest to engi-

neers. The inclusion of short fibres in the melt during the injection moulding process can significantly improve the mechanical performance of the finished moulded product [1]. This method has the added benefit that little or no modification of equipment or procedure is required to convert to fibre-filled

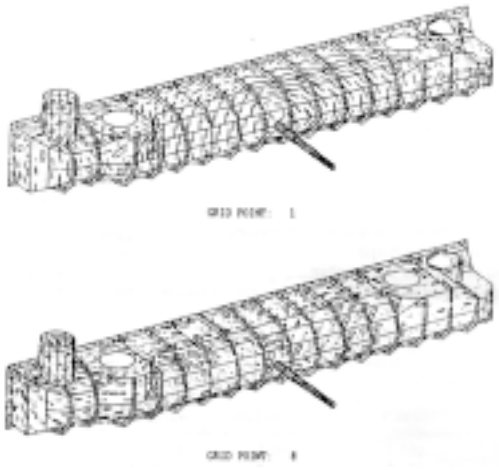

Figure 1.2: Fibre reinforced automotive radiator top: Fibre filled plastics are increasingly used in parts requiring mechanical strength, heat or chemical resistance. This was the domain of the metals, but performance plastics are now increasingly being used instead. From *Macroscopic Modelling of the Evolution of Fibre Orientation During Flow*, N. Phan-Thien and R. Zheng, pp $77-111$, Ch. 3 from *Flow-Induced Alignment in Composite Materials*, Woodhead Pub. (1997).

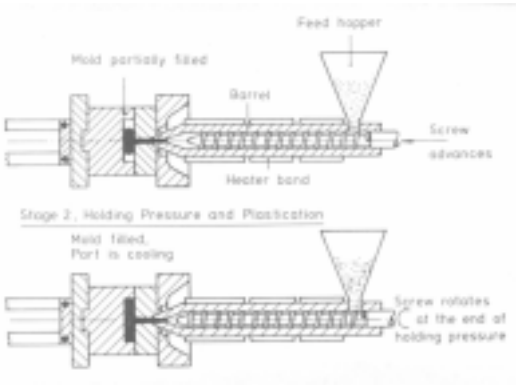

Figure 1.3: The Injection Moulding machine; Short fibre inclusions may be added with the plastic. From *Flow Analysis of Injection Molds*, P. Kennedy, Hanser Pub. (1995).

plastic production. Therefore this type of injection moulding is a popular method for the enhancement of moulded plastics (see Fig 1.3). Upon subsequent cooling and solidification it is found that the moulded part usually displays an increase in tensile strength and rigidity [1]. Specifically, the part is stiffer in the direction to which most fibres are aligned, and more compliant relatively in directions where fibres are not aligned [2]. It has also been observed that the presence of fibres dominates the warpage behaviour during cooling [3] and its inclusion will significantly affect the final shape and residual stresses in the part. These phenomena are directly related to the position and orientation of the embedded fibre population (Fig. 1.4). In turn the fibre positions and orientations are directly related to the influence of flow field on the suspension, in the mould during the filling stage [4][5].

To take best advantage of the benefits of fibre inclusions we must first understand the dynamics of the fibres during the filling stage and their effect on the bulk flow characteristics of the suspension. This understanding would eventually allow engineers to refine mould design and control the moulding process to enhance the desired mechanical properties. Controlling the orientation of the fibres induced by the suspension flow is crucial in maintaining quality control [6]. Similar concerns of suspension characterization (and manipulation) are shared amongst other diverse areas such as in plasma and blood products for the biological sciences [4][7], and other various industrial processes involving for example, paints, slurries and long distance piping [8]. The demand for predictive capabilities in suspensions warrants the current efforts of researchers in this field and it is on this basis that the current work is justified.

1.2 Goals

Theories which provide solutions for particle translation and rotation in a flow field have existed for some time now (e.g., Jeffrey [4] and Advani and Tucker [5]). A theoretical framework exists which allows the calculation of

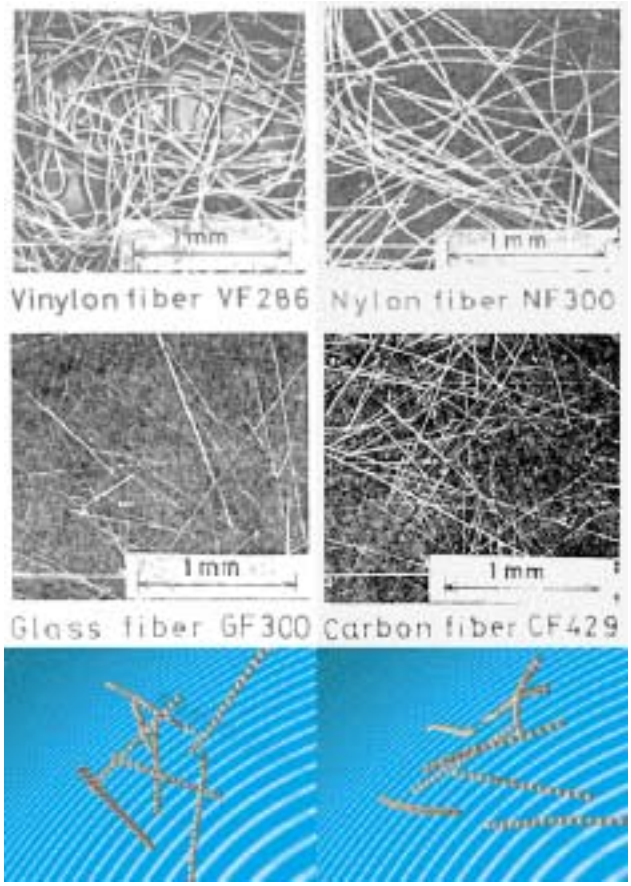

Figure 1.4: (*top*) Micrographs of various fibre types embedded within fluids. From *The Flow Behavior of Fiber Suspensions in Newtonian Fluids and Polymer Solutions.* 1. *Mechanical Properties*, S. Goto, H. Nagazono and H. Kato, Vol.25, pp 119 – 129, Rheologica Acta, (1986). (*bottom*) Snapshots of a representative population of flexible fibres in numerical direct simulation.

stresses and viscosities of suspensions from the flow kinematics (e.g., Ericksen [9], Hand [10] and Batchelor [11]). Using these, commercial software[1] is now able to predict to varying degrees of accuracy the fibre orientations and other material properties of finished moulded parts. The predictive capabilities of these software simulations are impressive [12][13][3]. They are however limited by the shortcomings of the theory. With the increasing use of short fibre-filled plastics in industry, the accuracy of performance predictions should be improved, and anomalous behaviour understood to meet the improving quality control standards. Evaluation of current theories by Bay [14] suggest that our capabilities are *adequate* but there is still much that can be improved.

The level of understanding of a physical system is improved in direct proportion to how fundamental an approach we take in modelling it. For the fibre suspension, the important dynamics occur on the microscopic level, and so it is argued that our attention should be directed there. By modelling on a highly fundamental and microscopic level we may benefit in several ways. The mathematical form of the models tend to be simpler. Theories, laws and equations tend to be based on simpler, and more reliable mechanisms. This leads to a reduced propensity to bias results, and unwittingly embed assumptions and preconceptions into the design of experiments. Reflecting this philosophy, the approach taken throughout this thesis is to focus attention on the microstructural detail of the suspension, i.e. to focus the modelling effort towards the constituent particles within the suspension. From a sound basis for modelling the micro-structure, the second step relating microscopic detail to bulk properties is merely an elaborate extrapolation.

Instead of using one of the common engineering numerical methods e.g. Finite Difference, Finite Element, Boundary Element, or Finite Volume methods, a newer and less commonly known numerical method known as Direct Simulation is used. This method, though highly computationally intensive,

[1] eg. mouldflow, C-Flow, Cadmould, Timon, Simuflow, CAE-mould, Caplas, McKam etc [8]

is well suited to the microscopic approach. Using this method, the goal is to achieve the capability of knowing at any instant the state of the suspension and determining the orientation of fibres in suspension. From this, an accurate estimation of bulk viscosity, stress and normal stress differences is possible.

It is a priority in this work to improve the quantitative predictive capabilities for these variables. One area which is shown to be beneficial is in developing an improved account for fibre shape, and fibre flexbility. A great deal of the work in part II focuses on the effect of fibre shape on the bulk properties. It is shown that accounting for shape considerations has an enormous effect on the related key bulk parameters, stress and viscosity.

It is a secondary goal to generate, via this work, new approaches, innovations and refinements in the Direct Simulation method which may be of benefit to future researchers who may choose to explore this approach. The Direct Simulation method to date is not well developed but with demonstrations of the results which can be achieved, it is hoped that researchers may consider this a viable option in their own work. In this thesis, modifications and extensions are presented which allow the modelling of more than merely spheres or cylindrical rod-like fibres. Complex particle shapes, with adjustable stiffness and mass can be simulated within complex flow fields. There is potential with this method which is not yet fully exploited.

1.3 Thesis Layout

This thesis is divided into four parts:

In **Part I**, previous works by other researchers in the field of suspensions are introduced and discussed. The history of the direct simulation method as applied in suspension rheology is discussed, as well as other notable approaches that have been taken. From Part I, it is hoped the reader will obtain a basic understanding of the historical background, and motivation behind the subsequent work of Parts II and III.

In **Part II**, a new direct simulation method is presented. The fibre simulation presented is based on a new 'Chain-of-Spheres' fibre model. This model is directly useful in predictive work for fibre-filled suspensions, as seen in injection moulding. From this model, a substantial new algorithm and method is developed for the prediction of useful fibre suspension bulk properties, such as bulk viscosity, and first and second normal stress differences. The bulk viscosity response to fibre shape, fibre stiffness and fibre flexibility is a major focus of this section.

In **Part III**, a second direct simulation method is presented. This method further develops the novel approach established in Part II. The use of hard spheres or rod-like particle shapes, and simple linearly varying flow fields, are basic requirements of a typical direct simulation method. With the approach described in this section however, simulation of particles with complicated shape embedded in complex flows are nevertheless made viable. Results in this section demonstrate that the direct simulation method may be extended substantially beyond expectations. The method and simulation described in Part III is capable of reproducing the motion of arbitrarily shaped particles, in a wide range of flow fields. The motion of several common particle shape primitives are studied, and the particle response to various selected flows is explored.

Finally in **Part IV**, the salient findings of the previous sections are revisited in summary form, and the thesis is concluded with a discussion on future directions.

Part I

Background and Review

Chapter 2

Review

2.1 Suspensions

Some fluids are called 'complex' because they exhibit non-Newtonian responses to stress. That is, they do not deform in response to stress in the simple linear way, as described by the equation attributed to Newton, Eq. 2.1, where η is a constant (η is generally not constant for non-Newtonian fluids). Very few fluids in fact behave exactly according to Eq. 2.1, however two important fluids water and air, are close. The 'non-Newtonian' classification is an exclusive one, given by default to fluids which do not fit into the Newtonian description. While it is not particularly informative as to the nature of the fluid (beyond the obvious), it has become convention to make the distinction according to whether a fluid is 'Newtonian' or not. While the term 'complex' can also imply complexity in structure as well as rheological properties, in this context, the terms 'complex' and 'non-Newtonian' may be taken to mean roughly the same thing.

$$\eta = \frac{\sigma}{\dot{\gamma}} \tag{2.1}$$

The particular materials on which we are concerned in this thesis are fluids embedded with short elongated fibre inclusions. This type of fluid is referred to as a fibre-filled suspension. The fibre-filled suspension belongs to

the family of particulate suspensions, which itself is one of several types of complex fluids. (see Fig. 2.1).

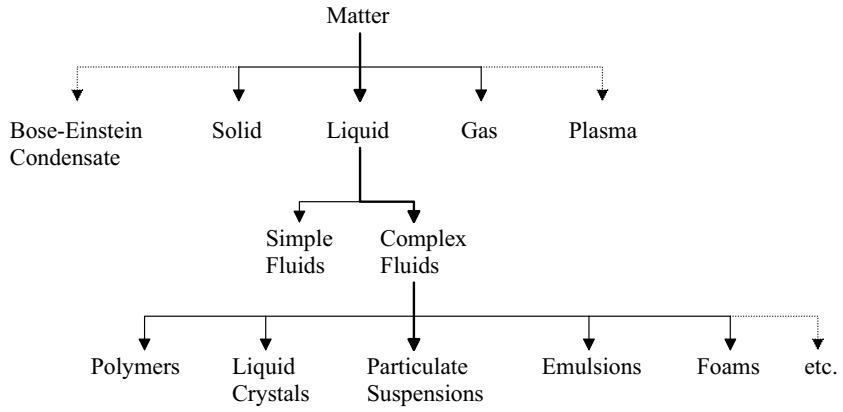

Figure 2.1: The heirarchy of material classifications

Of these complex fluids one can take two approaches to their modelling. The most common approach, supported by a large volume of published works, assume these fluids are homogeneous continua and design constitutive models to exhibit a fibre suspension-*like* response to stress. One approaches this theory with a macroscopic perspective, accounting for and modelling only for the bulk quantities one can see and measure. There are merits to this approach, particularly since it is most practical and bypasses much irrelevant detail for the working engineer. More is said on this topic in Section §2.2.

From a fundamentalist point of view however, the fluid behaviour undoubtedly arises from the evolution of internal microstructures. These mechanisms are not being explored with that approach. The molecular approach attempts to characterise the same fluid from the opposite perspective - to gain a thorough understanding of the microstructure and micromechanics of these fluids, and then attempt to extrapolate this knowledge to the macroscopic scale. This approach was the slower of the two to evolve since it was far more tedious and apparently unrewarding. It is only with the recent improvement in computer speeds that the sheer volume of computations required is no longer such a serious obstacle.

2.1.1 The Molecular Approach

Werner Kuhn [15] is credited with first representing macromolecules as idealized elastically linked dumbbells. The significance of this approach is twofold. Firstly, the elastic dumbbell is simple, and represents the microstructure in a highly literal way. Due to its simplicity, one may develop the required theory and equations with relative ease. Theories required at the microscopic scale are often simpler and visualized easier than those for the macroscale. The elastic dumbbell is no exception. The core theories are far easier to implement as a molecular simulation, than an equivalent discretized continuum algorithm. Secondly, its basic theories in e.g. linear elasticity, hydrodynamics and Brownian motion are imposed at the microscale. The bulk properties of the dumbbell filled fluid are a result of the evolution of the dumbbell microstructure. One may go on to produce broad reaching macroscopic constitutive equations but these are merely extrapolations from fundamentally microscopic modelling. This approach provides an alternative to the traditional macroscale continuum approach. While the continuum modeller must speculate on the micromechanics, the molecular modeller is a direct observer, and thus has a clearer insight into the root causes of experimentally observed phenomena.

Subsequent to Kuhn, Kramers [16] provided an expression for the polymer contributed stress derived from kinetic theory, as did Giesekus [17][18] with his alternative expression. Kirkwood and Riseman [19][20] contributed to the modification for hydrodynamic interactions between monomer units of a macromolecule - shown to be an important consideration particularly for larger macromolecules where the subunits are more numerous. Zimm [21] and Rouse [22] each produced their models of chain-like molecules where spheres are linked with Hookean springs, with and without the hydrodynamic interactions respectively. These early works are well described in Bird *et al.* [23].

2.1.2 The Rod-like Particle

The modelling for suspensions began in the same era as Kuhn, but has since borrowed heavily from the molecular work. Jeffrey's work [4] on the ellipsoid is the basis of many subsequent contributions to suspension rheology. In this work the orientation of a lone, neutrally buoyant, non-Brownian, inertialess ellipsoid in a sheared Newtonian fluid was shown to move in a cyclic and unchanging orbit (see Fig. 2.3). Jeffrey provided formulae for the orientation of the ellipsoid in time. It has since been observed experimentally that the more industrially useful, cylindrical elongated fibre suspended in a sheared Newtonian fluid exhibits a similar orientation motion [24][25], as do other common axi-symmetrical particle shapes such as oblate disks [26]. If the fibre's main axis is represented by the unit orientation vector $\mathbf{P}$ (Fig. 2.2) then the orientation in time is described by the evolution Eq. (2.2),

$$\dot{\mathbf{P}} = \omega \cdot \mathbf{P} + \lambda \left(\mathbf{D} \cdot \mathbf{P} - \mathbf{D} : \mathbf{PPP} \right) \tag{2.2}$$

where, $\omega = \frac{1}{2}\left(\nabla \mathbf{v} - \nabla \mathbf{v}^T\right)$ and $\mathbf{D} = \frac{1}{2}\left(\nabla \mathbf{v} + \nabla \mathbf{v}^T\right)$ describe the flow gradients, $\mathbf{v}$ is the vectorial flow field, $\lambda = \frac{a_r^2 - 1}{a_r^2 + 1}$ and a_r is the fibre aspect ratio. The period of a Jeffrey orbit may be predicted with Eq. (2.3),

$$T_{orbit} = \frac{2\pi}{\dot{\gamma}} \left(a_r + \frac{1}{a_r} \right) \tag{2.3}$$

Meanwhile the eccentricity of the orbit is defined by a single parameter C, sometimes referred to as the 'Orbital Constant'. Yamane *et al.* provide Eq. (2.4) to calculate C from the orientation vector $\mathbf{P}$.

$$\frac{1}{a_r^2} \mathbf{P}_x{}^2 + \mathbf{P}_y{}^2 = C^2 \mathbf{P}_z{}^2 \tag{2.4}$$

In a Cartesian frame with flow towards the (x) axis and shear gradient in the (xy) plane, $C = 0$ represents axial rotation of the vector $\mathbf{P}$ purely in the vorticity axis (z), $C = \infty$ represents a 'head-over-heel' tumble in the (xy) plane, and the range $0 < C < \infty$ represents the infinite closed orbital paths in between. With this, we have a comprehensive, and experimentally verified mathematical model for lone fibre motion.

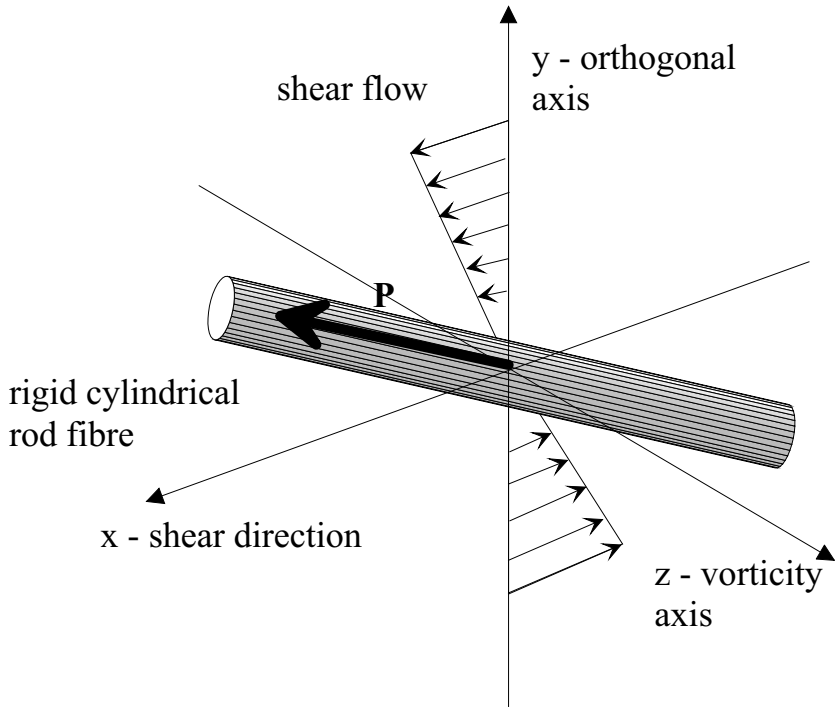

Figure 2.2: Unit orientation vector **P** in shear flow

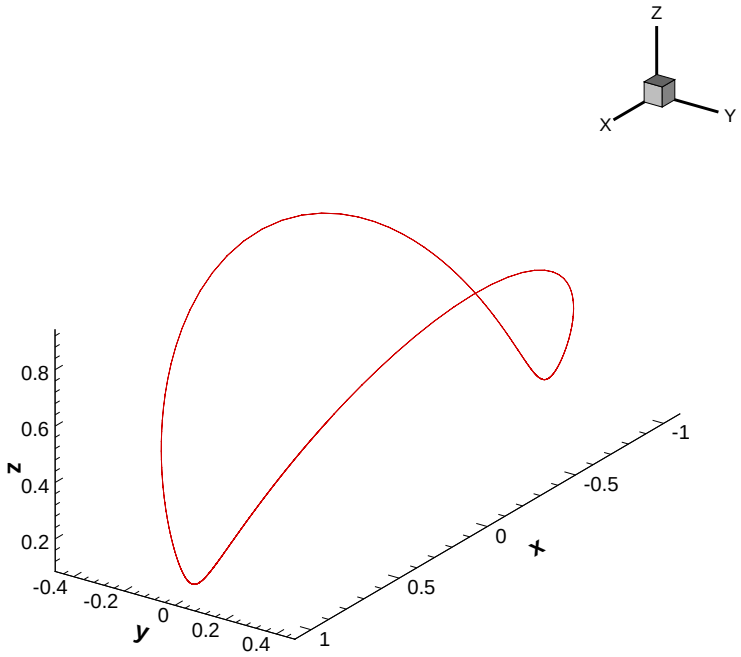

Figure 2.3: The Jeffrey orbit

It was observed in the 1920s by Taylor [27] that a lone undisturbed fibre in fact did not actually follow a closed orbit but drifted slowly through C values until its main axis aligned with the vorticity axis. It was suggested by Saffman [28], and was subsequently verified with further theoretical and numerical studies by Iso *et al.* [29] that this behaviour was due to an extra perturbation from *elastic* stresses in non-Newtonian, *viscoelastic* solvents. The molten plastics used in injection moulding are often viscoelastic in nature however the majority of fibre suspension studies and numerical simulations to this date have been simplified for strictly Newtonian solvents only [5][30][31][32][33][34][35][36][37]. To facilitate comparisons with previous results, the data produced here are also restricted to a Newtonian solvent. For those particularly interested in suspension flows in non-Newtonian solvents, they are referred to works such as, [30][38][39][40][41] and [42], where behaviour qualitatively different from Newtonian suspensions was found and are discussed.

2.1.3 Suspension Modelling

The theoretical study of suspensions continued in earnest from the 1970s with a series of papers by Hinch *et al.* on various aspects of suspensions. In Hinch [43], it was found that including small Brownian motion in a fibre suspension resulted in a stationary distribution of orbits, despite individual fibres (presumably) not having any inherent preference for a particular orbital constant, C. Further works by Hinch *et al.* included constitutive modelling [44][45], characterization of fibre suspensions with Brownian motion [46][47], and time dependent modelling with Brownian motion [48]. Brownian motion is a crucial element in molecular dynamics modelling, however suspension particles are often large enough so that their motion is not noticeably altered by Brownian effects. Throughout this thesis it is assumed that the particles are sufficiently large so that the influence of Brownian effects need not be considered.

Batchelor [11] provided a method of determining bulk stress from the mi-

crostructure of a fibre suspension, with an early use of the *Stokeslet* to represent the local disturbance in the fluid medium due to the particle. Batchelor also specified the conditions for the validity of *ensemble* or *volume averaging*, and its equivalence to statistical pre-averaging - a process used often in subsequent theoretical and numerical works.

At this time, we also saw the beginning of a more focused interest in the individual motion of particles, rather than modelling solely for the purposes of providing preaveraged bulk results. Batchelor used the *Slender Body theory* [49] to model a long thin particle in a flow field. Hinch followed with work on deformable threads [50][51], again applying the Slender Body theory with and without Brownian motion respectively. In these, we see perhaps one of the first more literal interpretations on the modelling of particles in suspension, with a particular emphasis on flow induced particle shape and deformation.

In 1984, Folgar and Tucker [2] produced a mathematical model for fibre suspension orientation distribution with an experimentally obtained term for orientation diffusivity due to fibre interaction. Prior to this, Jeffrey's equation (2.2) was only valid for undisturbed lone fibres and was inappropriate for many interacting fibres. The modification of Jeffrey's equation by Folgar and Tucker (Eq. (2.5)) may be expressed as a combination of Eq. (2.2) with an additional random force term, modelling the fibre-to-fibre interactions which become significant (if not dominant) in non-dilute suspensions.

$$\dot{\mathbf{P}} = \ell \cdot \mathbf{P} - \ell : \mathbf{PPP} + (\delta - \mathbf{PP}) \cdot \mathbf{F}^{(b)}(t) \tag{2.5}$$

$$\begin{gathered} \left\langle \mathbf{F}^{(b)}(t) \right\rangle = \mathbf{0} \\ \left\langle \mathbf{F}^{(b)}(t+s)\, \mathbf{F}^{(b)}(t) \right\rangle = 2D_r \delta(s)\, \delta \end{gathered} \tag{2.6}$$

ℓ is the effective velocity gradient tensor $\ell = \nabla \mathbf{v}^T - \zeta \dot{\gamma}$ with $\dot{\gamma} = \nabla \mathbf{v} + \nabla \mathbf{v}^T$, $\zeta = \frac{1}{a_r^2+1}$, and δ is the unit tensor. The third term in Eq. (2.5) contains the random force $\mathbf{F}^{(b)}(t)$ always directed perpendicularly to $\mathbf{P}$. The random force has the property that the resultant over a sufficiently large timescale is zero, and its magnitude is controlled by the parameter D_r, as expressed in Eq. (2.6). Folgar and Tucker assumed the magnitude of orientation diffusion, D_r is proportional to the flow gradient, hence the equivalence to

an experimentally determined particle *interaction coefficient* multiplied by the shear gradient tensor, $D_r = C_i\dot{\gamma}$. Values of the *interaction coefficient* C_i have been estimated experimentally by Bay [14] ($10^{-3} < C_i < 10^{-2}$) and Folgar and Tucker [2] ($3.2 \times 10^{-3} < C_i < 1.65 \times 10^{-2}$, for varying fibre materials, a_r and volume fraction ϕ), and numerically by Yamane *et al.* [35] ($10^{-5} < C_i < 10^{-4}$) and Fan *et al.* [31] ($C_i \approx 2.56 \times 10^{-3}$ for $\phi = 0.184$ and $a_r = 12.4$, $C_i \approx 3.0 \times 10^{-3}$ for $\phi = 0.168$ and $a_r = 13.5$) (In Chapter §3, a new estimate for C_i is made using the current method). A definitive description of the nature of C_i is yet to be agreed on. The figures above provide a rough estimate, but a quantitative value for C_i is also yet to be established. It has recently been suggested that C_i may be better represented as a tensor instead of a scalar to reflect the anisotropic nature of fibre suspensions [31][8].

Advani and Tucker [5] showed that solving for ensemble averaged tensorial moments of $\mathbf{P}$ (derived from Eq. (2.6)) rather than solving for the unsteady time dependent $\mathbf{P}$ itself, was more convenient in linking the processing conditions to the bulk variables of interest such as stress tensor and average orientation. The second and fourth moments of $\mathbf{P}$ are,

$$\begin{aligned} \mathbf{a}_2 = a_{ij} &= \oint P_i P_j \Psi(\mathbf{P})\, d\mathbf{P} \approx \langle \mathbf{PP} \rangle \\ \mathbf{a}_4 = a_{ijkl} &= \oint P_i P_j P_k P_l \Psi(\mathbf{P})\, d\mathbf{P} \approx \langle \mathbf{PPPP} \rangle \end{aligned} \tag{2.7}$$

where the *orientation distribution* weighting function $\Psi(\mathbf{P})$ is integrated with $\mathbf{P}$ components over all $\mathbf{P}$ in the suspension domain to obtain the orientation tensors $\mathbf{a}_2$ and $\mathbf{a}_4$. The integration is equivalent to the *ensemble average* [11] (as denoted by the angled brackets <>) if taken over a sufficiently large sample of fibres. Advani and Tucker's tensorial orientation evolution may be expressed as Eq. (2.8),

$$\frac{D\mathbf{a}_2}{Dt} = -\frac{1}{2}(\omega \cdot \mathbf{a}_2 - \mathbf{a}_2 \cdot \omega) + \frac{\lambda}{2}(\dot{\gamma} \cdot \mathbf{a}_2 + \mathbf{a}_2 \cdot \dot{\gamma} - 2\dot{\gamma} : \mathbf{a}_4) + 2C_i\dot{\gamma}(\delta - 3\mathbf{a}_2) \tag{2.8}$$

derived from Eq. (2.5) and featuring the fourth order tensor $\mathbf{a}_4$. This equation conveniently links the flow conditions, vorticity ω and $\dot{\gamma}$ to the evolution of the microstructure tensor, $\mathbf{a}_2$ in time. As the higher order $\mathbf{a}_4$ tensor is

required for the solution of $\mathbf{a}_2$, Eq. (2.8) is unfortunately unsolvable. If however $\mathbf{a}_4$ was approximated by a suitable function in $\mathbf{a}_2$, an *approximate* solution to Eq. (2.8) could be found. Tucker and collaborators searched for approximate functions with a review of various *closure approximations* in [5] and [37]. New closure approximations, suitable for various flow types were also developed in [5, *Hybrid Closure*] and [52, *Orthotropic Closure*]. To date, no one closure approximation has been shown to be capable of modelling all flow situations well. Closure approximations are regarded as the single most error prone stage in modelling suspensions in this way [14]. Despite these deficiencies, this approach was computationally efficient and was accessible enough to allow its widespread uptake for industrial purposes such as in injection moulding [12][8][3][13].

2.1.4 Constitutive Model used in this work

Given an *orientation evolution* equation (such as 2.8) and hence the configuration state of the suspension (Eqs. (2.5) and (2.8)) a constitutive equation is required to determine the bulk suspension stress tensor σ. The bulk stress in the fibre suspension comes from two main sources,

$$\sigma_{bulk} = \sigma_{solvent} + \tau_{fibre}, \tag{2.9}$$

where $\sigma_{solvent}$ is the stress contribution from the solvent fluid and τ_{fibre} is the contribution from the fibre inclusion [11][8]. The solvent stress contribution for a Newtonian fluid is expressible as,

$$\sigma_{solvent} = -p\delta + 2\eta_s\mathbf{D} \tag{2.10}$$

where p is the hydrodynamic pressure.

Transversely Isotropic Fluid

It remains then to find the particle contribution to stress. The most appropriate constitutive equation for a dilute elongated fibre suspension is

based on that developed by Ericksen [9] and Hand [10], named the *Transversely Isotropic Fluid* equation, or *TIF*. Originally created to describe non-Newtonian properties in certain polymeric fluids, its use of an orientation vector $\mathbf{P}$ is closely compatible with the orientation evolution models of Folgar and Tucker, and Advani and Tucker (Eq. (2.2) and Eq. (2.8) respectively. Improved for semi-concentrated to concentrated suspensions by Phan-Thien and Graham [53], the *TIF-PTG* equation is,

$$\tau = 2\eta_s \left\{ \mathbf{D} + f(\phi, a_r)\mathbf{D} : \langle \mathbf{PPPP} \rangle \right\} \tag{2.11}$$

where

$$f(\phi, a_r) = \frac{a_r^2 \phi \left(2 - \frac{\phi}{G}\right)}{4\left(\ln(2a_r) - 1.5\right)\left(1 - \frac{\phi}{G}\right)^2}, \qquad G = 0.53 - 0.013a_r, \quad 5 < a_r < 30$$

This equation has been used in a direct simulation by Fan *et al.* [31] for a suspension of rigid fibres, and is also used in Part II of this current work to determine bulk stress of the suspension.

Alternatively, given one can determine the forces and torques acting on the fibres, one may sum the torque, $\mathbf{T}^{(p)}$ and *stresslet*, $\mathbf{S}^{(p)}$ exerted on each fibre $\mathbf{P}$ for all fibres in a representative volume V. V should be large enough so that the variation of the local statistical properties of the suspension are negligible - the required criteria for *ensemble averaging* as discussed in detail by Batchelor [11]). The particle-contributed stress is given by [11].

$$\tau_{ij}^{(p)} = \frac{1}{V} \sum_p \left(S_{ij}^{(p)} + \frac{1}{2} \epsilon_{ijk} T_k^{(p)} \right) \tag{2.12}$$

and the stresslet on particle $\mathbf{P}$ is,

$$S_{ij}^{(p)} = \frac{1}{2} \iint \left(x_i t_j + x_j t_i \right) \psi(\mathbf{r}, \mathbf{P}, t) d\mathbf{P} dS, \tag{2.13}$$

where the surface traction is defined as $t_i = \sigma_{ij} n_j$, and $\mathbf{n}$ is the unit outward normal vector. Here $\mathbf{x}$ is the location on the fibre surface on which the traction $\mathbf{t}$ acts. This method is also widely used. For the work in this thesis however, the *TIF-PTG* equation (2.11) was found to be the most convenient and so was preferred over Eq. (2.12).

Suspension Viscosity

From the bulk stress tensor, the suspension viscosity, η_{bulk} may be determined, as well as first and second normal stress difference coefficients Ψ_1, Ψ_2. η_{bulk} and Ψ_1, Ψ_2 are related to the stress tensor via the relations,

$$\sigma_{yx} = \eta_{bulk}\dot{\gamma}_{yx}, \quad \sigma_{xx} - \sigma_{yy} = \Psi_1 \left(\dot{\gamma}_{yx}\right)^2, \quad \sigma_{yy} - \sigma_{zz} = \Psi_2 \left(\dot{\gamma}_{yx}\right)^2 \quad (2.14)$$

Eq. (2.8) used in combination with the constitutive Eq. (2.11) and Eq. (2.14) combine to quantify the influence of the forming conditions, flow field, and solvent viscosity via temperature and pressure, on the fibre orientation and ultimately determine the material properties of the suspension. The goal is to determine suspension viscosity since it is viscosity that ultimately determines the flow field within the injection mould cavity. It can be said that the main preoccupation in this type of suspension modelling is to accurately determine suspension viscosity since it is from this that all other predictions of the suspension are based.

2.1.5 Decoupled Flow and Particle Dynamics

It should be noted that while the effect of the flow field on the fibre orientation is clear given the modelling description above, the reciprocal influence of fibres on the flow field is not considered in this approach. The effect from coupling particle dynamics to flow field development is known to produce some significant differences, particularly in cases with complex flows featuring both strong elongational as well as sheared components. In such flows the streamlines can be altered due to the presence of fibres [8].

In this thesis however, it is assumed always that dilute particle dynamics apply, and so the de-coupling will not drastically affect the outcome of fibre motion.

2.2 Numerical Method

A fibre suspension may have many thousands or even millions of fibres. It is practically impossible for all but a few uniquely simple scenarios to determine the influence of many individual fibres on bulk properties by analytical means. For other kinds of problems, the complexity of the boundary conditions or domain also discourages analytical solutions of the flow. The only viable alternative is through numerical approximation. One can take two different approaches: (1) Discretized continuum methods, and (2) Molecular methods.

The continuum methods are the most well known and best developed. By continuum method, it is meant the Finite Difference, Finite Volume, Finite Element, Boundary Element methods. They are sometimes greatly different in execution and details, but essentially the approaches are similar in principle. By subdividing a complex flow domain into manageable divisions, regions, or nodes and finding approximate solutions at each individually, a single complex solution is reduced into many small simple problems. The work changes from one of high theoretical complexity, to a large number of repetitive simple problems divided over the domain. After solution, the calculated values at nodes or elements are combined to obtain an approximate flow solution over the entire domain of interest.

When applied to suspensions, these continuum based methods are hampered by a further significant problem. The suspension is in reality made of many discrete particles which are very difficult to represent with discretized meshes. Representing the fibre-fluid interface greatly complicates the process of correctly meshing the domain, as well as the extra physical modelling required for the hydrodynamics on particle surfaces. Furthermore, as the flowing microstructure must evolve with time, the solution typically requires iterative remeshing and resolving with each timestep. To model a suspension in detail in this way becomes exceedingly expensive computationally.

As mentioned earlier in Section §2.1 (pp. 10), the 'simplest' approach to overcoming this problem is to treat the heterogenous fibre-fluid suspen-

sion as an equivalent homogenous continuum[1]; one exhibiting equivalent fibre suspension-like characteristics. This usually involves some form of stochastic diffusing, averaging, or 'smoothing' process within the modelling to account for the contribution of the fibres. That is, the individual discrete fibres per unit volume of actual suspension are replaced with a 'averaged' or 'smoothed' homogenous continuum. The dynamics are governed by an average fibre evolution model such as by Advani and Tucker, Eq. 2.8. (As discussed in earlier sections, the stochastic component of the Advani-Tucker Eq. (2.8) means that explicitly determining the orientation of individual fibres is impossible). An approach similar to this was developed by Fan *et al.* [54] using a fibre evolution equation related to Eq. 2.2, based on the CONNFFESSIT[2] idea of Ottinger [55], in conjunction with a Finite Element method (Sun *et al.* [56][57]) for the viscoelastic flow. The combination of these methods were used to successfully estimate suspension parameters in the non-Newtonian fibre-filled flow past a 2D cylinder.

Others have used the Boundary Element Method (BEM) for the motion of particles in Stokes flows. The main advantage for BEM is that the dimensionality of the problem is reduced by a further order (compared to the other named methods). The BEM problem only requires solutions to be calculated at points on the domain (i.e. particle) surface or other interfaces instead of at all points within the domain volume. Since the numerical solution over a surface is smaller than solutions over a volume, the BEM problem is typically smaller computationally, and more accurate. Some examples of suspension research using BEM include those by Phan-Thien *et al.* [58], Fan *et al.* [59], Qi *et al.* [60][61], and Nasseri *et al.* [62], who use various implementations of BEM to solve for volume-averaged stress tensor, viscosity, velocity and stress fields in the shear flow for periodic, suspended spheroids. Nasseri *et al.* [63] has also used BEM to study the motion and hydrodynamic interactions be-

[1]This approach in fact, is usually *not* as simple as expected in practice. Conceptually however it requires no modification to existing theory. In this way, it is 'simple'.

[2]**C**alculation **O**f **N**on-**N**ewtonian **F**low: **F**inite **E**lement and **S**tochastic **SI**mulation **T**echnique

tween two close swimming micromachines, and Loewenberg *et al.* [64] has studied the collision between two deformable drops in shearing flow.

These methods, and others, are all valid approaches to studying suspensions. There are however other methods based on different approaches. Molecular Dynamics and the direct simulation method is one of these. In the following section, the method used in this thesis will be elaborated further.

2.2.1 Direct Simulation

The method of dynamically simulating suspended particles is known by several names, coined by different researchers. For the purposes of consistency, the name *Dynamic Simulation* will be used here. In *Dynamic Simulation* the speed of the computer is used to rapidly calculate the trajectory and also the orientation of individual particles embedded in a fluid medium at incremental timesteps. The evolution of the entire microstructural state of the suspension is thus calculated in explicit detail, and in reasonable time. The strength of this method as it stands today, is the ability to link the underlying fundamental mechanisms to the macroscopically observable properties of the bulk suspension. It may be possible with increased computational power to simulate entire bulk flows, at microscopic resolution.

Dynamic Simulation is an off-shoot of Kinetic Theory and is similar to its numerical sub-branch, Molecular Dynamics modelling (MD). While the two names, *Dynamic Simulation* and *Molecular Dynamics* modelling would appear to represent the same ideas, the body of publications concerned with these fields suggest that each title has developed separate *de facto* meanings. Molecular Dynamics is typically associated with modelling of atomic (nano) or molecular sized particles, for example, as constituents in a polymer. Dynamic Simulation is commonly associated with larger particles, e.g. spheres or fibres as inclusions in a suspension. While there are certainly commonalities between the two (for example, the aim to calculate bulk fluid stress and viscosity), there are important differences. For example, there is the particular concern in Dynamic Simulation for the accuracy of particle orientation

prediction in flow fields. Dynamic Simulation particles, like *MD*, are usually influenced by viscous (Drag) force and Brownian motion. Dynamic Simulation implementations however have usually been less concerned than *MD* with effects from thermal, electrostatic, magnetic or other nano-scale influences. Dynamic Simulation has a more applied engineering focus, such as in the prediction of microstructures and bulk properties in injection moulding for composites, or slurry and mineral processing.

As the numerical simulation of suspensions is relatively new, there is no specific reference to Dynamic Simulation in reviews (e.g. [23] [65]). For the most part, its core theories are included in their coverage of Kinetic Theory. While Dynamic Simulation and Molecular Dynamic modelling are closely related, they may be separated by their different objectives and levels of theoretical rigor required to meet their objectives. More specifically perhaps, they may be separated by their different physical scales of reference - nano-scale versus micro-scale, or larger. Batchelor [66, pp. 227] is quoted, "*... in some circumstances there exists a structure scale large compared with molecular dimensions and at the same time small compared with the overall dimensions of the given sample of material... the term 'microscopic structure' may then refer to the arrangement and properties on this intermediate scale. In these circumstances ... the problem moves from the domain of the physicist to that of the engineer*". It is suggested that the discerning reader make the distinction between Dynamic Simulation and Molecular Dynamic modelling, and remind oneself of the connotations of each.

The concept of directly tracking the trajectory of multiple particles in suspension is not a new one, but it has only recently become feasible with the increase in computational power since the 1980s. As early as 1957, Alder and Wainwright [67] numerically simulated the motion of discrete particles. The trajectories of 32 hard spheres (a maximum of 500 was attempted) within a periodic repeating rectangular box, were simultaneously calculated over CPU times in the order of several hours. Having imposed initial particle positions and velocities, and defined the mechanism for momentum transfer upon par-

ticle collisions, the numerical simulation was run until a quasi-equilibrium state was achieved, after which the pressure of the system was determined. In its early stages however, it was perhaps viewed mostly as an expensive and impractical, esoteric novelty. In part, this view was due to its extreme demand for computer resources, at a time when computers were expensive and slow. When the computing time was given however, brief but profound glimpses were seen of the fundamental structures and mechanisms behind many observed phenomena and material properties. The potential of this method was clear, but was far from being realized. The research efforts of rheologists gravitated towards other more fruitful endeavors, and rightly so. Now with over 35 years of *Moore's law* growth [68], the availability of computer resources is much less of an issue and the direct simulation method is increasingly being revisited.

The traditional suspension simulation attempted to model an infinite suspension under a field of influence, usually an imposed shear flow. In a practical sense however simulating a truly infinite suspension is impossible and instead requires the concept of a representative simulation domain of finite volume, in combination with periodic boundary conditions. One then uses only a finite number of particles within the *simulation domain*, and stacks copies of the same cubic domain periodically around itself, as if embedded in an infinite three dimensional lattice of bricks. The infinite suspension could thus be *approximated* by a simulation domain with a few representative particles, combined with a method for the summation of an infinite lattice of repeating domains (the Ewald summation technique [69], used by Brady *et al.* [70] and Fan *et al.* [31] amongst others). The so called *simulation domain* is also referred to by different names by different people, e.g. the *unit cell*, *simulation cell* and also *calculation area* by Yamamoto and Matsuoka [71][72][73][74], the *cubic region* by Yamane *et al.* [35], the *reference unit cell* by Fan *et al.* [31], and the implied *periodic boundary condition* by Brady *et al.* [70], Bossis and Brady [75], and Yamane *et al.* [32]. The concept however is the same. The particles being simulated are confined to motion within a

small finite three dimensional volume in space but are taken to represent an entire infinite suspension.

Brady and Bossis [75][76] and later Brady *et al.* [70] demonstrated the feasibility of the *Stokesian dynamics* simulation method. In this method discrete particles (hard spheres) interact through both hydrodynamic, and other interparticle forces in a shearing flow (e.g. lubrication, Brownian, colloidal). In this method the equation of motion for the fluid is the incompressible Navier-Stokes equation, or alternatively the creeping Stokes flow, while the particles are governed by Newton's third law, $\mathbf{M} \cdot \frac{d\mathbf{U}}{dt} = \mathbf{F}_h + \mathbf{F}_p$ where $\mathbf{M}$ is particle mass, $\mathbf{U}$ is particle velocity, $\mathbf{F}_h$ is hydrodynamic force and $\mathbf{F}_p$ are other non-hydrodynamic forces. The hydrodynamic force, $\mathbf{F}_h$ is equal to the force required to maintain the particle's relative position within a moving fluid, plus that required to cause relative velocity through the fluid. Hence, $\mathbf{F}_h = \mathbf{R} \cdot \mathbf{U}^\star + \mathbf{\Phi} : \mathbf{E}$ where $\mathbf{R}$ is the resistance matrix, $\mathbf{U}^\star$ is the particle velocity relative to the fluid, $\mathbf{\Phi}$ is the resistance matrix for bulk flow and $\mathbf{E}$ is bulk flow rate of strain. After substitution, and neglecting particle inertia, the result is expressed by Eq. (2.15),

$$\mathbf{R} \cdot \mathbf{U}^\star + \mathbf{\Phi} : \mathbf{E} + \mathbf{F}_p = 0 \tag{2.15}$$

where all current particle positions and bulk flow velocity are assumed to be known. This leaves particle velocity $\mathbf{U}^\star$ as the remaining unknown to be found. In Stokesian dynamics simulation, a suspension is initialized with particle positions, initial velocities, and a steady flow field. The simulation then proceeds using the newly solved $\mathbf{U}^\star$ to calculate new particle positions, then recalculating the other suspension state variables $(\mathbf{R}, \mathbf{\Phi}, \mathbf{F}_p)$ for the new timestep $t_{n+1} = t_n + \Delta t$ whereafter the entire procedure is repeated. By allowing details such as the precise form of $\mathbf{F}_p$ to be changed on a case by case basis, the method is highly adaptable. The effects of particular forces may be added or removed at will and with little alteration to the simulation algorithm. A variant of the Stokesian Dynamics method is the *Brownian Dynamics method* where a component of $\mathbf{F}_p$ is added to cause random Brownian motion. Larson *et al.* [7] used this method in a numerical simulation

to study the extensional behaviour of DNA molecules in an extensional flow field. While the Stokesian dynamics method (as presented in Brady and Bossis [75]) was strictly for hard spheres in creeping flows, the method was substantially extended in further work by Claeys and Brady [77][78][79]. In this three part work, they simulated ellipsoids instead of spheres and applied their method to study the sedimentation behaviour of ellipsoids, infinite suspensions of ellipsoids with viscosity versus volume fraction prediction, and the role of microstructures in the properties of suspensions.

Yamane *et al.* [35] produced a numerical simulation of rod-like particle suspensions in shear flow in 1994. While their method in principle is similar to that of Brady and Bossis' Stokesian Dynamics, they substituted the hard sphere and associated theories for hydrodynamic drag and interactions with those for a cylindrical rod. The cylindrical rod orientation moved according to Jeffrey's rules for ellipsoids (Eq. (2.2)). For interparticle interactions, Yamane *et al.* considered only close range lubrication forces, assuming that longer range hydrodynamic effects in a suspension are screened by intermediate bodies (Brownian motion was also neglected). Unlike the Folgar-Tucker Eqs. (2.5) and (2.6), where interaction forces were modelled only on average, Yamane *et al.* directly calculated interaction forces between fibre pairs as a function of their relative orientations, velocities and proximity of touching surfaces (see [35, Eqs. $15-21$]). Yamane *et al.* found that the simulated motion of fibres in semi-dilute suspensions were not markedly different to those in the dilute range. Semi-dilute suspension viscosity as found in simulation was found to be closely predicted by existing dilute suspension theory. They concluded that for elongated non-Brownian rods, the dilute theory was valid even in the semi-dilute range. Also, the effect of long range hydrodynamic interaction was very small and the short range lubrication forces alone appeared to be sufficient for an accurate simulation (in apparent contradiction to Claeys and Bradys work with ellipsoids [77][78][79] where the entire range of hydrodynamic interaction was included). In 1995, Yamane *et al.* [32] also added bounded wall considerations to this simulation.

Fan *et al.* [31] extended the method of Yamane *et al.* [35] by including the long range hydrodynamic interactions (using *Slender Body approximation* [49]) which was missing from Yamane *et al.*'s work. In this case qualitative behaviour was similar but divergence from dilute Jeffrey's ellipsoid behaviour occured in the semi-dilute suspension range. This was at a lower concentration than in Yamane *et al.*'s case and more in keeping with experimental observations. Long range hydrodynamic interactions thus had the effect of reducing the concentration range at which the dilute suspension theory failed. Fan *et al.* continued numerical work in fibre suspensions with the *Brownian Configuration Field* method (BCF) [54], combining the CONNFFESSIT scheme of Öttinger [55] for Brownian fibre suspension orientation and stress, with the DAVSS finite element scheme of Sun *et al.* [57] for the momentum equation in viscoelastic flow. In adding the continuum FEA method, the simulation was capable of providing stress component, velocity and pressure contours for highly concentrated fibre suspension flows in actual flow domains. They tested the simulation in the 2D axi-symmetric *falling-ball in a tube* scenario with concentration as high as $\phi = 0.25$ for $a_r = 20$ fibres. Their estimate for the benchmark cylinder drag force in steady flow compared well with established values (maximum error was 1.65% over a range of concentration up to $\phi = 0.25$). Fan *et al.* [80] also considered shear induced fibre migration, adding the migration theory of Phillips *et al.* [81] to their BCF method.

During the 1990s there was a renewed focus on particle shape and motion. While earlier works, (e.g. [49][50][51][77][78][79]) had also considered particle shape, the shapes used in earlier works were invariably near-spherical, ellipsoidal, oblate discs, or cylindrical rods. Apart from Hinch's work with deformable threads, most particles modelled were also rigid. Boundary Element Methods (BEM) did allow accurate modelling of complex shapes with deformable interfaces (e.g. deformation of two interacting drops studied by Loewenberg and Hinch [64]). This method however was prohibitively computationally intensive and current implementations are restricted to only a

few interfaces.

In the early 1990s a simple, more mechanistic method took shape, where complex particle shapes were assembled from interlinked, hard, regular subunits. In this genre, Yamamoto and Matsuoka *et al.* and Klingenberg *et al.* led two notable research efforts. Yamamoto and Matsuoka developed the *Particle Simulation Method* (PSM), equivalent to *Dynamic Simulation* described earlier. PSM is based on the Stokesian Dynamics framework with a few important differences. The rigid spheres in the Stokesian Dynamics method are no longer independent entities, but are linked by internal bonds to construct fibre-*like* bead-chain structures. Linkages between spheres exhibited linear extension, bending and torsional stiffness, allowing the bead-chain structures to be elastically flexible. Eqs. (2.16) and (2.17) are the general linear and rotational equations of motion for each sphere. In Dynamic Simulation and PSM, each sphere is treated as an independent entity regardless of their membership within larger structures.

$$m\frac{d\mathbf{v}}{dt} = \left(\mathbf{F}^h\right)_{viscous} + \left(\sum \mathbf{F}^i\right)_{intraparticle} + \left(\sum \mathbf{F}^p\right)_{interparticle} \tag{2.16}$$

$$\left(\frac{2}{5}ma^2\right)_{sphere}\frac{d\omega}{dt} = \left(\mathbf{T}^h\right)_{viscous} + \left(\sum \mathbf{T}^i\right)_{intraparticle} + \left(\sum \mathbf{T}^p\right)_{interparticle} \tag{2.17}$$

In Eqs. (2.16) and (2.17), m and $\frac{2}{5}ma^2$ are mass and rotational moment of inertia respectively for a sphere. The forces and torques belong to one of three general categories, (1) those arising from hydrodynamic effects including viscous drag, (2) those from intraparticle linkages, and (3) those from interparticle interactions. The PSM was introduced in 1993 by Yamamoto and Matsuoka [82] where they used a linear bead-chain of touching hard spheres to model a cylindrical, flexible rod-like particle. In their paper, the rigid fibre was shown to execute closed Jeffrey orbits, while flexible fibres deviated from Jeffrey orbits. Flexible fibres were observed to assume complex S-shaped configurations during phases of their deviant Jeffrey orbit. Yamamoto and Matsuoka [71] extended the PSM by simulating for multiple bead-chains in suspension, including hydrodynamic intraparticle interactions.

Fibre suspensions were observed to align to shear flow over time as expected. Elasticity in the fibres was found to contribute to an elasticity in the suspension, indicated by the calculated stress tensor components and normal stresses which were characteristic of viscoelastic flow. Yamamoto and Matsuoka [83] and also Nomura, Yamamoto and Matsuoka [74] added the ability to account for fibre breakage in simulation. If a fibre was deflected beyond a critical bending stress, the PSM was capable of simulating breakage by permanently removing the overloaded inter-bead bond within the Sphere-chain. It was hence able to simulate for flow induced fibre fracture, the simulation modelling the interaction of broken fibre fragments alongside the existing unbroken suspension fibres. The PSM model was shown to represent the deflection behaviour well compared to loaded cantilever beam bending theory. In 1996, Yamamoto and Matsuoka [73] added the ability to simulate the motion of bead-chain fibres embedded in a 2D diverging flow field, precalculated using Finite Element Method (FEM). Fibre orientation in 2D divergent flow using the PSM was in good agreement with theoretical predictions. Finally with [34] and [72], Yamamoto and Matsuoka extended PSM once again by allowing the simulation of bead-linked flexible rectangular plates in suspension.

Ross and Klingenberg [84], and Skjetne, Ross and Klingenberg [33] used a similar method to produce their *Particle-level Dynamic Simulation*. Unlike Yamamoto and Matsuoka who constructed structures from linked spheres in direct contact with each other, Ross *et al.* and Skjetne *et al.* respectively attempted linking prolate spheroids, and widely spaced *ball-and-socket* subunits in order to reduce the number of simulated bodies and improve CPU time. They observed similarly complex single flexible fibre dynamics as did Yamamoto and Matsuoka [82]. The results did not seem to change with the nature of the fibre model used. So long as they were flexible multi-bodied fibres and there were enough linkages, the common findings between Yamamoto and Matsuoka *et al.* [82][71], Ross and Klingenberg [84], and Skjetne *et al.* [33], such as vorticity drifting Jeffrey orbits and the various S-

shaped configurations of fibres closely agreed. In another variant by Schmid and Klingenberg [85], small rod segments linked by hinges were used as fibre subunits. Using this model the mechanism of fibre flocculation in flowing suspension was explored in [85] (also by Schmid, Switzer and Klingenberg [86]).

The work of the late 1990s reflects the current state of the Direct Simulation method. The development drive is perhaps motivated now by two separate goals. One remains focused on the accurate modelling of bulk properties. This is the more traditional goal of the numerical rheologist. The other pays a closer attention to the detailed motion of individual particles. There is a particular interest with the microscopic details, for instance in the field of liquid crystal technology, and with electro- or magneto-rheological fluids where the local microstructure arrangements may play a particularly important part in their respective technologies.

In Part II, we see works more in line with the first style of study, where bulk viscosity response is scrutinised. In Part III, the work reflects the second style, focusing on the fidelity of single particle dynamics modelling.

2.3 Summary

In **Part I**, we started with a brief early history of molecular modelling and then followed the various steps which contributed to the current state of suspension rheology, and Direct Simulation method. The issues discussed are directly related to the issues influencing the original work to be presented in Parts II and III.

In **Part II**, the first of two new direct simulation methods is presented. The fibre simulation that will be presented is based on a new 'Chain-of-Spheres' fibre model. This model features linked spheres with semi-rigid joints in a chain configuration. The work in part II will focus on the accurate prediction of bulk properties. In particular, bulk viscosity is predicted, and the effects of influence by particle shape, stiffness, concentration, and flow

field will be explored.

Part II

Chain-of-Spheres Fibre Simulation

Chapter 3

Direct Simulation of Flexible Fibres

3.1 Summary of Results

In this part of the thesis, the first of two major simulation methods is presented. This chapter is based on the paper by Joung *et al.* [87], a copy of which is provided as additional material in the sleeve of this thesis.

It is demonstrated that this simulation can be used to extract basic rheological information about the suspension including fibre orientations and suspension viscosity. The method is based on recent simulation works by Fan *et al.* [31] and Yamane *et al.* [35]. Their method has been modified to allow a small amount of bending and torsion in the fibres. A restoring moment acts to straighten the fibres as they interact in the flow. The viscosity of semi-concentrated to concentrated flexible fibre suspensions are shown to increase by a magnitude of the order $7-10\%$ greater than the equivalent rigid straight fibre suspension tested. This is in qualitative agreement with experimental work by Goto *et al.* [88] and Blakeney [89]. The implication is that any constitutive relation for fibre suspension described by orientation vectors may slightly underestimate suspension viscosity, particularly for fibres of large aspect ratio, or low Young's modulus where the possibility for fibre

flexure is greater [88]. If fibre deformation was accounted for (by whatever means) in the existing constitutive relationship, predictions of bulk suspension parameters such as viscosity would be noticeably improved. A method was developed to modify an existing rigid fibre viscosity to an equivalent flexible fibre viscosity, hence improving viscosity prediction ability.

3.2 Introduction and Background

In most particulate suspension studies it is typical that the embedded particles are assumed to be rigid. This assumption allows one to develop theories about that suspension without the complication of accounting for particle deformation. With this assumption many studies over the past three decades have been performed but almost invariably[1], for either *rigid* spherical or cylindrical rod inclusions. It has however been generally acknowledged that particle *shape* has an important effect on suspension viscosity. For instance, the inclusion of the shape correction factor in Eq. (2.2) is generally accepted, and contributions by researchers such as Anczurowski and Mason [90] and Bretherton [25], clearly suggest qualitative differences in the suspension for different particle shapes.

Early experimental results for 'rigid' (Rayon) rod suspensions by Nawab and Mason [91] were reportedly over-predicting the theoretical relative viscosity predictions of Burgers [92] by a factor of three. They speculated that this may be because some of the fibres used were slightly curved. Forgacs and Mason (1959) [93] showed that slight fibre curvature would drastically change the period of fibre rotation, while Tchen [94] showed that large fibre curvature significantly affects the drag on an ellipsoid translating through viscous fluid. The evidence would suggest that a significant viscosity increase for deformed fibre suspensions may be expected.

Blakeney [89] performing an experimental study, indeed found that *slightly curved* fibre inclusions do significantly increase suspension viscosity over

[1]There have been exceptions such as studies of dilute deformable droplets in suspension.

straight fibres. Relative viscosity η_r can be expressed as a function of volume fraction ϕ (for dilute suspensions) as in Eq. (3.1),

$$\eta_r = 1 + \alpha_0 \phi, \tag{3.1}$$

Blakeney found that for a straight fibre suspension $\alpha_0 = 1.98$, while for fibres with a mild bend of $\theta = 176°$ (Fig. 3.1), $\alpha_0 = 3.57$. That is, for the case where volume fraction $\phi = 0.1$ and $\theta = 176°$, the curved fibre suspension was observed to be at least 13% more viscous than an equivalent straight fibre suspension. Blakeney's work was cited by Ganani and Powell

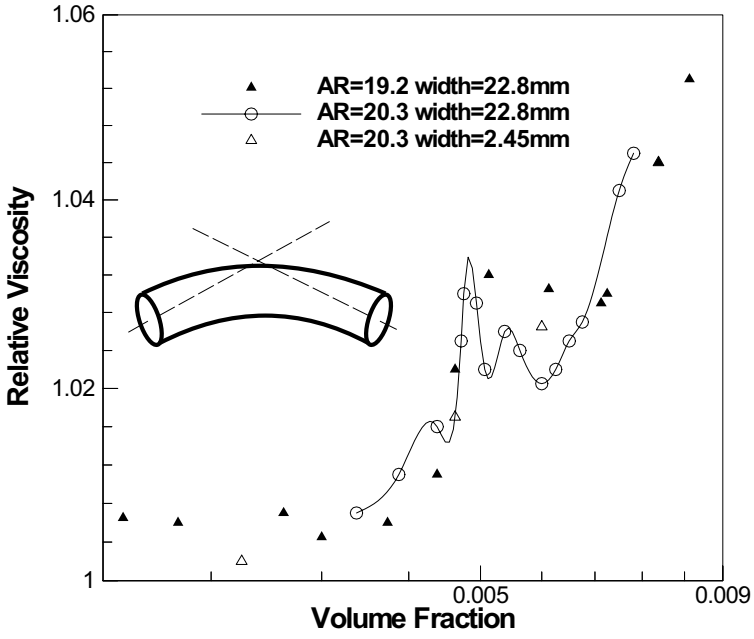

Figure 3.1: Viscosity for curved fibres versus straight fibres. Redrawn from Blakeney's experimental results. The 'bump' region occurs in the volume fraction region centred on $\phi = 0.005$.

[38, pp. 210] in their review on works relating to rod-like suspensions, and concluded that '*relative viscosity depends upon volume fraction, aspect ratio, shear rate and particle flexibility*'. It follows logically that if particle *flexibility*

is significant then particle *shape* is equally important. While the first three items mentioned by Ganani and Powell have each been well studied, there are very few works devoting anything more than a passing interest to the fourth, *fibre flexibility*, and even less to its effects on suspension viscosity.

One of the first theoretical works devoted to flexibility in particles comes from Hinch [50] where, utilizing the slender-body theory of Batchelor [49], he developed the equations of motion for a lone inextensible thread in a Newtonian shear flow. Another work by Doi and Kuzuu [95] studied the stresses generated in flexible fibres. However none has characterized flexible fibre suspensions in the same way that has been done for rigid fibre suspensions.

On the experimental side, Kitano *et al.* [96] presented an empirical relationship between relative viscosity and volume fraction for various fillers such as glass and carbon fibres. While Kitano *et al.* did not set out to study flexibility directly, their results are worth noting since it was implied that different materials (and different material stiffness) produced different suspension viscosities. The last and most directly related experimental work is produced by Goto *et al.* [88][97], where viscosity effects due to flexibility, between different material fibres were directly compared against each other. Goto *et al.* [88] observed firstly that a suspension of highly flexible fibres will have a significantly greater relative viscosity than a stiffer fibre suspension of equivalent fibre shape over a comparable range of volume fractions[2]. They concluded that '*the viscous properties of the fibre suspensions depended ... particularly strongly on* [the fibres] *flexibility*' [88, pp. 129].

[2]In suspension theories, there are three recognized concentration regimes: *dilute*, *semi-concentrated*, and *concentrated*. The classification of a suspension is determined by the ability of a fibre in suspension to freely rotate. A straight fibre has a length l, diameter d, aspect ratio $a_r = l/d$, and the suspension has a volume fraction ϕ. In the *dilute* region, the distance between any two fibres is statistically greater than l and therefore fibres are totally free to rotate unimpeded. In the dilute region, $\phi a_r^2 < 1$. In the *semi-concentrated* region, the fibre spacing is less than l but greater than d on the average. Inter-fibre collisions occur regularly. In this region, $1 < \phi a_r^2 < a_r$. In the concentrated region, fibre spacing is within d and fibre-fibre interactions are most frequent. In this region, $a_r < \phi a_r^2$.

In this chapter, the method for a new flexible fibre simulation is described. The motivation for creating this simulation was to,

- reproduce the flexibility dependent behaviour of suspensions observed by Goto *et al.* [88];
- to illustrate some of the complex behaviour of flexible fibre systems and
- to predict the viscosity of flexible fibre suspensions.

In a similar manner to previous works by Yamane *et al.* [32][35] and Fan *et al.* [31], a direct numerical simulation was produced and from it relevant data such as relative viscosity and fibre configuration state were determined. The flexible fibre was modelled by a modified version of an inextensible '*chain-of-beads*' model as described by Bird *et al.* [23].

The fibres interact with the solvent and with each other through viscous drag, long-range hydrodynamic effects and short-range lubrication forces acting on the beads. The chain of beads featured bending and torsion restoring moments in a manner similar to recent numerical work by Skjetne *et al.* [33], Yamamoto and Matsuoka [34], and to a lesser extent Jabbarzadeh *et al.* [98]. The degree of flexibility of the fibre (straightening moment) was defined via the widely used material constants, Young's and shear moduli. This therefore links these *real world* material properties to a numerical simulation method which until now had always imposed the somewhat unrealistic *rigid* fibre condition.

3.3 Flexible Fibre Model

The flexible fibre used in this simulation is modelled by a chain of spheres (Figure 3.2). In this respect it is similar to models used by Skjetne *et al.* [33], Yamamoto and Matsuoka [34] and Jabbarzadeh *et al.* [98], and is also described in detail by Bird [23]. However the methods used to determine

internal moments and subsequent fibre shapes in this simulation are different to the methods used by those researchers. The spheres allow the use of existing hydrodynamic theory to calculate interaction forces between fibres, and also a provides a convenient means of subdividing the fibre into flexible segments.

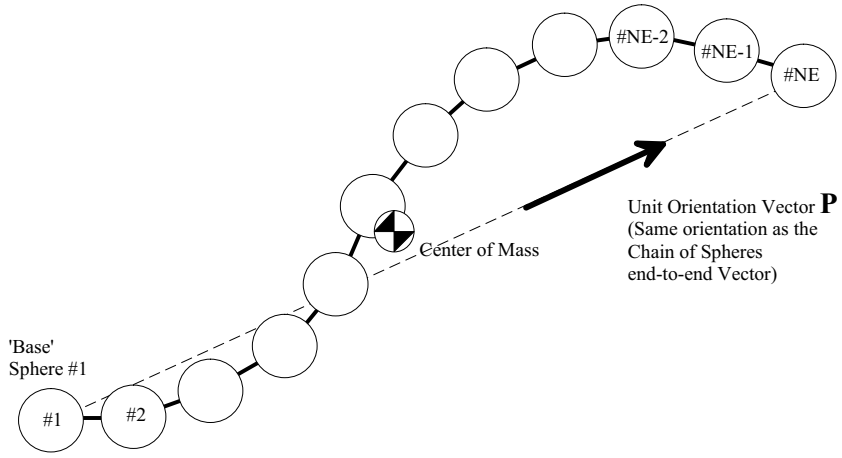

Figure 3.2: Chain-of-Spheres (Not drawn to scale)

External forces arise from viscous drag (including *long range* velocity disturbances from other distant spheres), and *short range* lubrication forces between close spheres. The spheres act as nodes along the length of the fibre through which these external influences can interact. The spheres are linked to each other by inextensible *connectors*. Both spheres and connectors are rigid however only the spheres generate, and are affected by external forces. The connectors only serve to transmit internal forces and maintain the configuration of the fibre and therefore do not interact with the fluid.

Within each sphere is a joint linking two connectors (Fig. 3.3). To model material flexure, the joint is assumed to be of circular cross section and of a predefined elastic modulus. The diameter at the joint is equal to that of a cylindrical rod of equal length and equivalent volume as the sphere-chain fibre. Each joint allows limited bending and torsion and when (angularly) deflected from equilibrium produces a restoring moment on the adjacent con-

nectors.

The main conditions imposed in this simulation are:

- The solvent is a Newtonian fluid.
- Velocity gradients are assumed to be homogeneous.
- Spheres and fibres are large enough so that Brownian motion is negligible.
- The suspension is assumed to meet the conditions set by Batchelor such that an ensemble average of the population to produce the required bulk properties is a valid procedure [11].
- De-coupling of flow and fibre orientation is valid.
- Spheres and fibres are force and torque free at all times. Flow rates are such that inertial effects are negligible.
- All fibres are identical in configuration. (Due to flexibility, fibres are not necessarily the same shape).

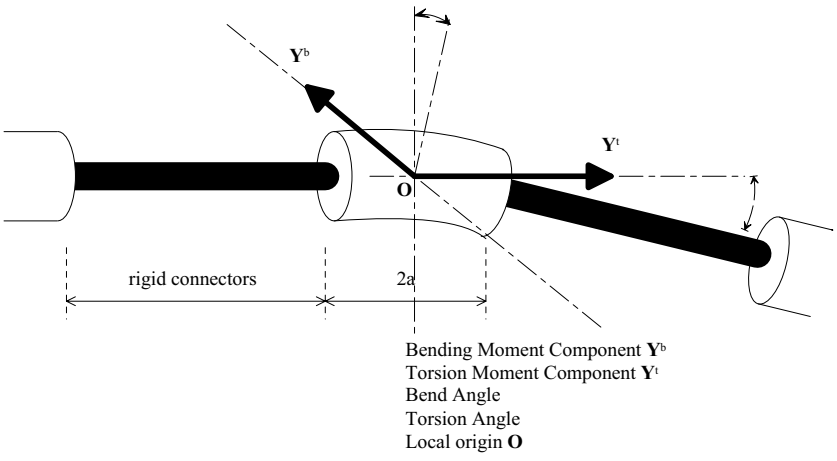

Figure 3.3: Joints linking connectors may bend and twist.

- At the stiffness and flow rates used in simulation, the fibres will remain nearly straight at all times.

3.3.1 Notation and Conventions

Standard tensor notation as reiterated by Bird [99] and others, is used throughout. As shown in Fig. 3.2, an end of the fibre is arbitrarily chosen as the *base* and spheres and connectors are numbered from that base. The indices and other naming conventions used in this chapter are listed in Table 3.1.

Parameters used throughout this chapter are chosen such that all results are non-dimensional, all lengths are relative to the bead radius $a = 1$.

3.3.2 Centre of Mass

The suspension moves relative to a fixed global origin. Global parameters are those that are in relation to this reference frame. Local terms are those which are relative to an individual fibre's centre of mass (COM). The centre of mass for a fibre, n, assuming all beads are the same dimension and mass m, is simply,

$$\mathbf{r}_{nc} = \frac{\sum_{\nu} m_\nu \mathbf{r}_{n\nu}}{\sum_{\nu} m_\nu} \tag{3.2}$$

where $\sum_{\nu}$ is the summation over all ν spheres within the fibre.

Fig. 3.6 shows the unit connector orientation vector $\mathbf{Q}_\nu$. As described by Bird [23], $\mathbf{Q}_\nu$ can be related to global and local sphere location vectors $\mathbf{r}_{n\nu}$ and $\mathbf{R}_{n\nu}$ with the connectivity relations as per eq. (3.3),

$$\begin{aligned} \mathbf{Q}_\mu &= \sum_{\nu} \mathbf{B}_{\mu\nu} \cdot \mathbf{r}_\nu, \\ \mathbf{R}_\nu = \mathbf{r}_\nu - \mathbf{r}_c &= \sum_{\mu} \tilde{\mathbf{B}}_{\nu\mu} \cdot \mathbf{Q}_\mu \end{aligned} \quad \text{where} \quad \begin{aligned} \mathbf{B}_{\mu\nu} &= \delta_{\mu+1,\nu} - \delta_{\mu\nu}, \\ \tilde{\mathbf{B}}_{\nu\mu} &= \begin{array}{ll} \frac{\mu}{NE} & \mu < \nu \\ -\left(1 - \left(\frac{\mu}{NE}\right)\right) & \mu \geq \nu \end{array} \quad \text{for} \end{aligned} \tag{3.3}$$

Notation	
Sphere number	$1 < \ldots \mu, \nu \ldots < NE$
Fibre number	$1 < \ldots m, n \ldots < NF$
Periodic reference cell coord.	i, j, k
... regarding Centre of Mass (COM)	c
Global position vector	$\mathbf{r}$
Local position vector from COM	$\mathbf{R}$
External Force vector	$\mathbf{F}$
External Moment vector	$\mathbf{M}$
Internal Tension vector	$\mathbf{X}$
Internal Moment vector	$\mathbf{Y}$
Connector Orientation unit vector	$\mathbf{Q}$
Unit normal to connector vector	$\mathbf{U}$
Orthogonal third unit vector to $\mathbf{Q}, \mathbf{U}$	δ_3
Fibre unit orientation vector	$\mathbf{P}$
Velocity vector	$\mathbf{V}$
Rotational velocity vector	$\mathbf{W}, \mathbf{w}$
Bending angle	θ
Torsion angle	ϕ
Oseen Tensor	$\mathbf{\Omega} = \frac{1}{8\pi\eta_s\lvert\mathbf{r}\rvert}\left\{\delta + \frac{\mathbf{rr}}{\lvert\mathbf{r}\rvert^2}\right\}$

Table 3.1: Notation and Conventions

3.3.3 Forces and Moments

Since the connectors do not interact at all with the solvent fluid, all interactions are between spheres only. One need not be concerned with distinguishing spheres of different fibres while determining forces. As far as the external force calculation is concerned, it can simply be regarded as a suspension of $NE \times NF$ spheres. Interactions between spheres are governed by the same laws regardless of whether they belong to the same fibre or different fibres. It is only *after* external forces are determined and internal tension through connectors are considered do the spheres become sub-units of fibres and move accordingly.

External: Viscous Drag and Long Range Hydrodynamic Effects

The drag force on sphere ν, of fibre n, in motion through a viscous Newtonian fluid is determined using Stokes law,

$$\mathbf{F}_{n\nu} = -\zeta \left[\mathbf{V}_{n\nu} - \mathbf{V}_{\infty}\right] \tag{3.4}$$

Stokes drag coefficient is given in the following form,

$$\zeta = 6\pi\eta_s a \tag{3.5}$$

where a is the sphere radius. At fibre n, sphere ν, the location is $\mathbf{r}_{n\nu}$ and the solvent velocity is $\mathbf{V}_{\infty}$. Assuming a homogeneous velocity gradient $\mathbf{K}$ tensor, $\mathbf{V}_{\infty}$ is given by Eq. (3.6),

$$\mathbf{V}_{\infty} = \mathbf{K} \cdot \mathbf{r}_{n\nu} + \mathbf{V}'_{n\nu} \tag{3.6}$$

The last term in Eq. (3.6) is the cumulative velocity disturbance at $\mathbf{r}_{n\nu}$ from the motion of $(NE \times NF) - 1$ other spheres in the suspension. Vector $\mathbf{r}_{m\mu n\nu} = \mathbf{r}_{n\nu} - \mathbf{r}_{m\mu}$ is the position vector from another sphere μ (fibre m) to the current sphere ν within fibre n. If sphere μ is producing a disturbance in the solvent (moving relative to the solvent) then sphere μ must itself be

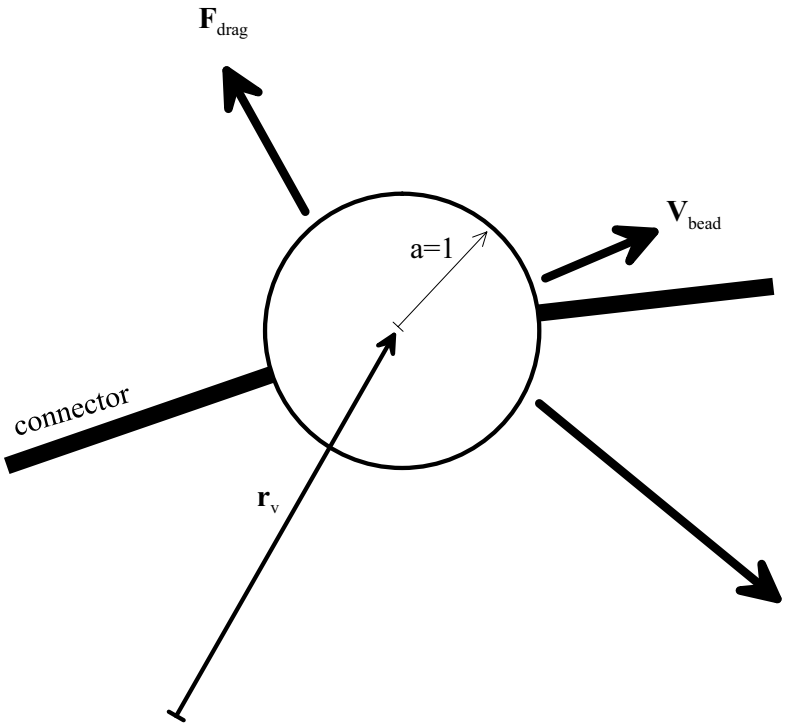

Figure 3.4: Drag force on a sphere in viscous fluid

experiencing a force, $\mathbf{F}_{m\mu}$. The velocity disturbance contribution at $\mathbf{r}_{n\nu}$ due to the *wake* of sphere μ is then determined using the Oseen tensor.

$$\mathbf{\Omega}_{m\mu n\nu} = \frac{1}{8\pi\eta_s \left|\mathbf{r}_{m\mu n\nu}\right|} \left\{ \delta + \frac{\mathbf{r}_{m\mu n\nu}\mathbf{r}_{m\mu n\nu}}{\left|\mathbf{r}_{m\mu n\nu}\right|^2} \right\} \tag{3.7}$$

The cumulative velocity disturbance from the other $(NE \times NF) - 1$ spheres is then,

$$\mathbf{V}'_{n\nu} = \sum_m \sum_\mu \mathbf{\Omega}_{m\mu n\nu} \cdot \mathbf{F}_{m\mu} \tag{3.8}$$

The effect from the long range velocity disturbance (or *wake*) is relatively small in magnitude however it has been shown to qualitatively alter the behaviour of the suspension [31] and therefore should be included to accurately model the suspension. Since this hydrodynamic effect takes contributions even from distant spheres, it is termed *long range* interaction. Substituting Eqs. (3.8) and (3.6) into (3.4), the force equation becomes,

$$\mathbf{F}_{n\nu} = -\zeta \left[\mathbf{V}_{n\nu} - \mathbf{K} \cdot \mathbf{r}_{n\nu} - \sum_m \sum_\mu \frac{1}{8\pi\eta_s \left|\mathbf{r}_{m\mu n\nu}\right|} \left\{ \delta + \frac{\mathbf{r}_{m\mu n\nu}\mathbf{r}_{m\mu n\nu}}{\left|\mathbf{r}_{m\mu n\nu}\right|^2} \right\} \cdot \mathbf{F}_{m\mu} \right] \tag{3.9}$$

External: Short Range Interaction: Lubrication Force

An additional component comes from fibre-fibre 'collisions' and by necessity occurs at very close range. The main practical concern when modelling close range interaction is to ensure that spheres do not unrealistically overlap each other and collapse into the same point in space. There are many approaches to ensure the separation between two bodies however, the basic requirement of symmetric reversibility in the Stokes fluid should be maintained. It is a basic feature of Stokes flow that the position of interacting hard spheres should return to their original positions if the flow was reversed - an apparent time-symmetry. A failure to return to the original position on reversing flow indicates an artificially created divergence from Stokes flow (i.e. simulation inaccuracy).

The use of lubrication forces (as opposed to repulsive or attractive potential methods) was seen by Yamane *et al.* [35] as a suitable method to maintain fibre and sphere separation, whilst maintaining the reversibility requirement. Fan *et al.* [31] also used this method. The use of lubrication forces is effective in these previous works and so is used here as well.

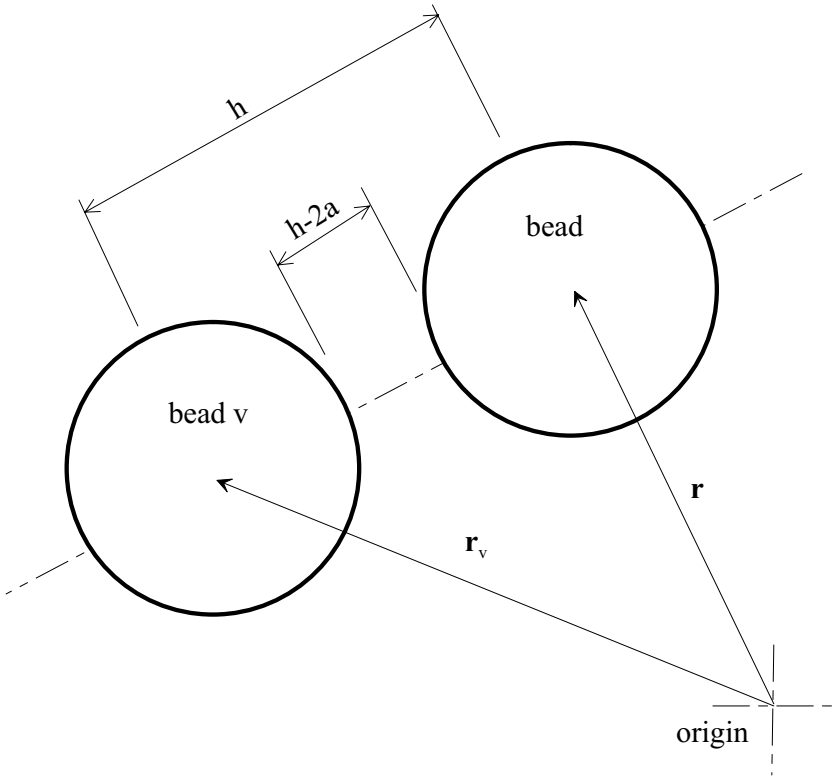

Figure 3.5: Lubrication between spheres; Two beads approaching each other

Karilla and Kim [100, Ch 11.2.2] produced a solution for lubrication force for two spheres in close proximity approaching each other. Lubrication forces are significant only when in close proximity, therefore in this simulation lubrication force only applies when the gap between the surface of two spheres $h - 2a$ is within $0.2a$ of each other, i.e., $h - 2a \leq 0.2a$ (where the distance between the sphere centres is h, and the distance $0.2a$ is assumed to be sufficient). Let $\mathbf{V}_{n\nu}$ be the velocity of bead ν, fibre n, and $\mathbf{V}_{m\mu}$ be the velocity

of bead μ, fibre m. If $\mathbf{r}_{\mu\nu} = \mathbf{r}_\nu - \mathbf{r}_\mu$ is the position vector from bead μ to bead ν, then the relative approaching or *squeezing* velocity component along the centreline between these beads is given by,

$$\mathbf{V}_{sqz} = \left[\frac{\mathbf{r}_{\mu\nu}}{|\mathbf{r}_{\mu\nu}|}\right]\left(\frac{\mathbf{r}_{\mu\nu}}{|\mathbf{r}_{\mu\nu}|}\cdot[\mathbf{V}_{n\nu} - \mathbf{V}_{m\mu}]\right)$$

Then the lubrication force is given to leading-term accuracy by,

$$\mathbf{F}_{\mu\nu} = -3\pi\eta_s\frac{a^2}{h-2a}\mathbf{V}_{sqz} \tag{3.10}$$

A negative value of the lubrication force implies that *overlapping* of beads has occurred. At *extremely* close range, Eq. (3.10) becomes inadequate and will cause unnatural asymptotically large forces. To counter this, the use of Eq. (3.10) is restricted to *near* contacts in the range, $\epsilon_{GAP} \leq h - 2a \leq 0.2a$, where ϵ_{GAP} is a very small positive number in the range which allows a stable numerical simulation to proceed. For *actual* contacts the rotation rate component of the fibre in the direction of the contact reduces to zero, hence stopping further overlap between the fibres. While this technically violates the Stokes reversibility condition, this situation was found not to occur often and did not noticeably alter results. By careful adjustment of ϵ_{GAP}, one can control the simulation so that this situation is rare or is eliminated entirely.

Internal: Connector Tension

Since the connectors are rigid and inextensible, the 'tension', $\mathbf{X}$ is simply the reactive force that opposes exactly the external forces acting in the direction of the connector. The connector orientation is described by the unit vector, $\mathbf{Q}$. Connectors are numbered in a similar convention as spheres. For every fibre there is always one more sphere than there are connectors. If spheres are numbered, $1 \leq \mu, \nu \leq NE$, and connectors, $1 \leq \mu, \nu \leq NE - 1$, the tensions in connectors are,

$$\mathbf{X}_v = \frac{\mathbf{Q}_\nu}{|\mathbf{Q}_\nu|^2}\sum_1^{NE}\begin{array}{ll} -\mathbf{Q}_\nu\cdot\mathbf{F}_\mu & \nu \geq \mu \\ +\mathbf{Q}_\nu\cdot\mathbf{F}_\mu & \nu < \mu \end{array} \text{ for } \begin{array}{c} 1 \leq \nu \leq NE-1 \\ 1 \leq \mu \leq NE \end{array} \tag{3.11}$$

Internal: Moments

When the forces are known the moments acting at each joint can then be calculated. For fibre, n, at joint, ν (at the centre of bead ν) the moment is simply equal to the moment balance generated by forces on spheres to either side of joint ν.

$$\mathbf{M}_\nu = \sum_\mu [\mathbf{r}_\mu - \mathbf{r}_\nu] \times \mathbf{F}_\mu \quad \text{for} \quad \nu = 1 \ldots NE \tag{3.12}$$

Eq. (3.12) however does not distinguish between the portion of the moment causing flexure and that causing whole-body rotation. If one used Eq. (3.12) to calculate the net moments '*left*' and '*right*' of the joint ν (Fig. 3.7), then these two moment components can be separated at each joint. '*Left*' and '*right*' are arbitrarily chosen and simply serves to distinguish from what side of a joint the moment was generated. In this case '*left*' is always the fibre end comprising bead 1, while the '*right*' side is the fibre end with bead NE. Fig. 3.8 demonstrates how all cases can be broken down into combinations of four basic cases. The four cases may be combined to produce all other scenarios *however they may only be combined in an additive fashion between flexure-causing and whole-body rotation causing cases*. Fig. 3.8 demonstrates two

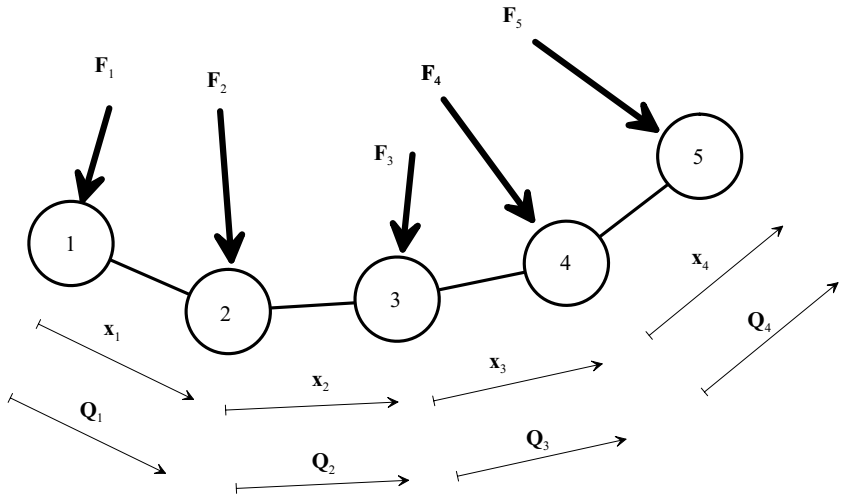

Figure 3.6: Connector vectors $\mathbf{Q}_\nu$ and tensions $\mathbf{X}_\nu$

examples for determining flexure and whole-body rotation causing moments.

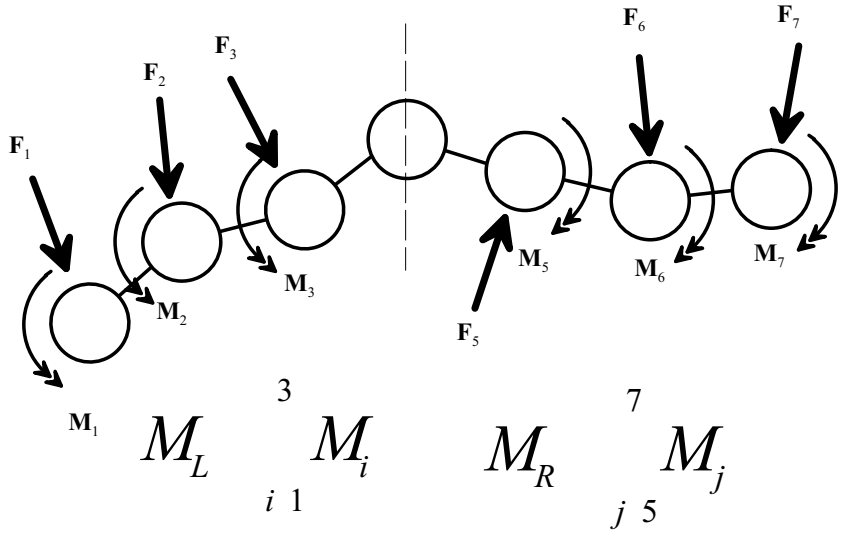

Figure 3.7: 'Left' and 'Right' moments

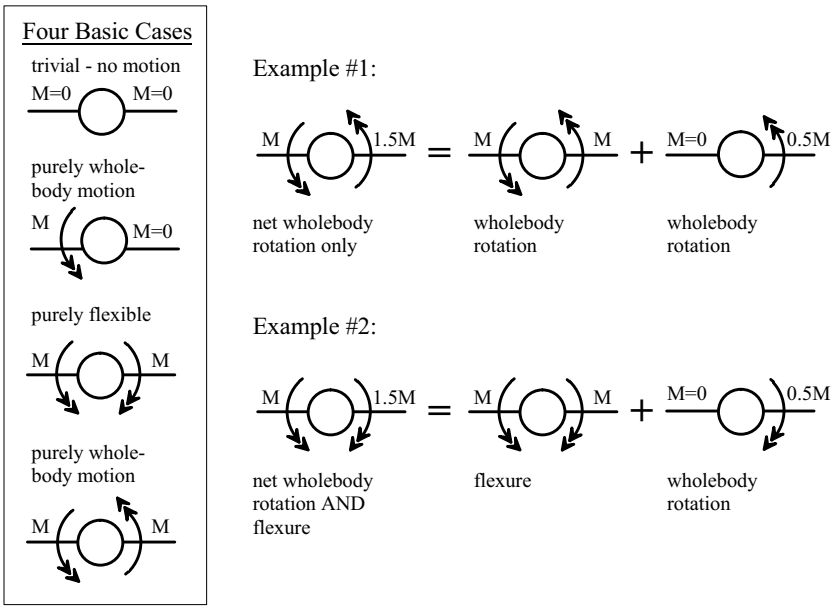

Figure 3.8: Four basic moment cases at a joint (*left*). Two examples using these cases are also shown (*right*).

The examples are one dimensional, however it is directly applicable for three dimensional moment vectors. Once flexure causing moments are determined for each joint, this moment can be decomposed into *bending* $\mathbf{Y}_\nu^b$ and *torsion* $\mathbf{Y}_\nu^t$ vector components (see Fig. 3.3). The bend and twist angles $\left(\theta^b, \phi^t\right)$ are calculated for each joint using Eq. (3.13).

$$\begin{array}{l} \left|\mathbf{Y}_\nu^b\right| = -k^b\left(\theta^b - \theta^{eq}\right) \\ \left|\mathbf{Y}_\nu^t\right| = -k^t\left(\phi^t - \phi^{eq}\right) \end{array} \quad \text{where} \quad \begin{array}{l} k^b = \frac{EI}{2a} \\ k^t = \frac{GJ}{2a} \end{array} \tag{3.13}$$

Eq. (3.13) includes the Young's and shear moduli. Finally given bending and twist angles, the adjacent connectors are then rotated to these calculated angles and the fibre shape is renewed.

3.3.4 Balancing Internal and External Moments

It is important to make the point that a truly flexible beam or fibre (such as those developed by Hinch [50] [51]) must develop an internal moment which is dependent on the motion of the body itself as well as any external forces and may not necessarily be balanced internally. Or put another way, a system of equations describing a truly flexible fibre must be a dynamic one, described by Eq. (3.14),

$$\rho\dot{x} - M'' = K \tag{3.14}$$

where ρ is fibre density, x is position along the fibre centreline, M is moment and K is distributed load on the fibre [101].

In this simulation the inertial component is neglected and therefore a truly dynamic system has been made static. However this simulation is limited to suspension flows taking place at a rate where inertial components are assumed to be negligibly small. The errors from omitting inertial components would likewise be small. Under these conditions this simulation may be viewed as a valid approximation to true flexible fibre behaviour.

The methods used are approximate solutions only. They are not obvious and so require some explanation. In the following sections it is explained

how contrary to first impressions, internal and external fibre moments do in fact balance.

Moment balances and fibre deformation

Central to this section is the premise that the fibre must be in equilibrium both internally and externally at all times. The fibre deformation is separated into 'external' and 'internal' aspects and each is found separately before combining the two.

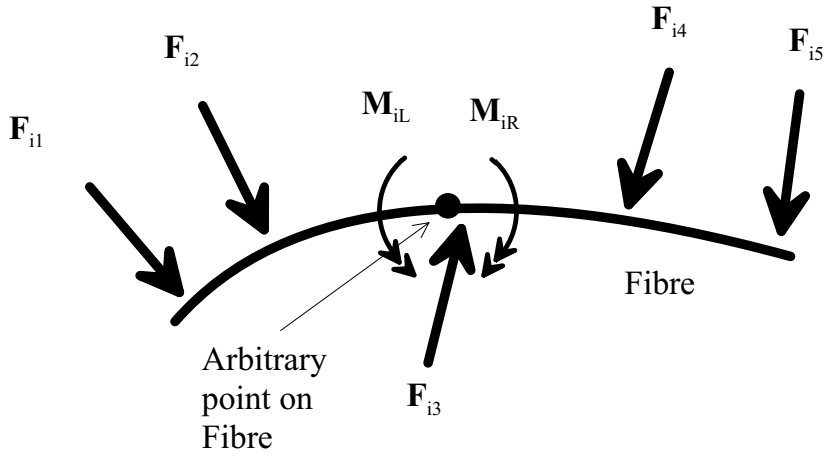

Figure 3.9: External forces produce 'internal' moments and deformation.

Consider a situation as shown in Fig. 3.9. Externally this fibre is in equilibrium therefore the response of this fibre to the applied forces $\mathbf{F}_{i1,2,3,4,5}$ is purely internal. For a fibre in equilibrium bending due to external loads, the internal moment either side of any point along its length must be balanced. The moments are equal and opposite on both sides of the point. Now consider Fig. 3.10 where there is a rigid body in a viscous fluid with several external forces applied. The external forces are $\mathbf{F}_{e1,2,3}$ and hence the resulting external moment sum is described by Eq. (3.15) (the far right term is used in discrete

case),

$$\left.\begin{array}{rcl} \mathbf{M}_{e1} & = & \mathbf{R}_1 \times \mathbf{F}_{e1} \\ \mathbf{M}_{e2} & = & \mathbf{R}_2 \times \mathbf{F}_{e2} \\ \mathbf{M}_{e3} & = & \mathbf{R}_3 \times \mathbf{F}_{e3} \end{array}\right\} \sum \mathbf{M}_e = \sum_j^{NE} \mathbf{R}_j \times \mathbf{F}_{e\_j} \tag{3.15}$$

For constant fibre rotation rate ω, Eq. (3.15) must be balanced by viscous drag (Eq. (3.16)),

$$\sum \mathbf{M}_e = \sum_j^{NE} \mathbf{R}_j \times \mathbf{F}_{e\_j} = \zeta\omega \tag{3.16}$$

where ζ is the rotational frictional drag coefficient about the Centre of Mass (COM) for the body.

At this stage note the fact that $\mathbf{F}_{i1,2,3,4,5}$ and $\mathbf{F}_{e1,2,3}$ are both external forces, causing exclusively internal moments, and exclusively external 'whole-body' rotations respectively.

Now consider a sphere-chain (as used in this simulation). Each sphere experiences external forces (hydrodynamic drag, lubrication and long range effects). Therefore the forces found in simulation $\mathbf{F}_{sim}$ are equivalent to the

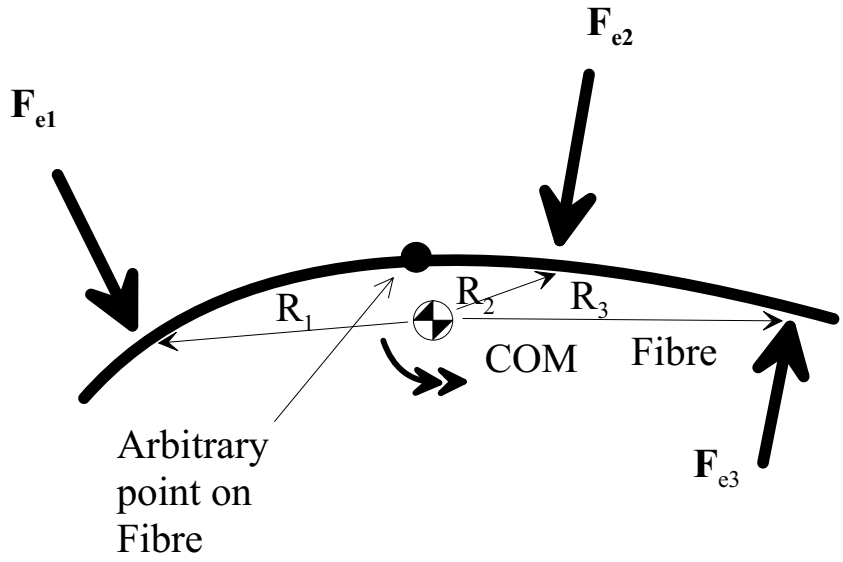

Figure 3.10: External forces produce 'external' wholebody motion.

combination of $\mathbf{F}_{i1,2,3,4,5...}$ and $\mathbf{F}_{e1,2,3...}$ acting together. At any sphere v, the force acting is $\mathbf{F}_{v\_sim} = \mathbf{F}_{v\_i} + \mathbf{F}_{v\_e}$. One now faces the task of distinguishing what proportion of each force found in simulation is $\mathbf{F}_i$ and what is $\mathbf{F}_e$. In other words, the aim is to determine the proportion of moments acting towards the internal moments (for fibre deformation), and towards the external moments (whole-body rotation). The approach used is to split the task into two approximate methods, tackling each separately.

Internal Moments

Three basic rules declared here are,

1. At any joint (sphere) the internal moment component 'left' and 'right' of that point must be equal and opposite hence maintaining internal moment balance.

2. There exists two species of forces. $\mathbf{F}_{internal}$ ($\mathbf{F}_i$ or $\mathbf{F}_{flex}$) causes purely internal bending and due to rule 1 must have an opposing partner(s) on the other side of point v on the fibre such that internal moments 'left' and 'right' balance. $\mathbf{F}_{external}$ ($\mathbf{F}_e$ or $\mathbf{F}_{rot}$) acts purely in producing whole-body rotation of the fibre.

3. Due to objectivity principles, internal forces/moments cannot be negated or subtracted by external forces/moments and vice versa.

Consider the bead-chain fibre in suspension. All forces acting on the beads are solved using Eqs. (3.9) and (3.10) with the methods described (see Section §3.3.3). By simply summing moments 'left' and 'right' of a particular bead v, the total 'left' and 'right' moments are known. For example, 'left' of joint v,

$$\mathbf{M}_L = \mathbf{R}_1 \times \mathbf{F}_1 + \mathbf{R}_2 \times \mathbf{F}_2 + \ldots + \mathbf{R}_{v-1} \times \mathbf{F}_{v-1} + \mathbf{R}_v \times \mathbf{F}_v \quad \text{ie, } \mathbf{M}_L = \sum_{j=1}^{v} \mathbf{R}_j \times \mathbf{F}_j \tag{3.17}$$

However recall that force is composed of an (as yet) unknown proportion of flexure-causing and rotation causing components,

$$\mathbf{F}_{v\_sim} = \mathbf{F}_{v\_i} + \mathbf{F}_{v\_e} \tag{3.18}$$

Therefore there also exists 'flexure causing' moments and 'rotation causing' moments,

$$\mathbf{M}_L = \sum_{j=1}^{v} \mathbf{R}_j \times [\mathbf{F}_{flex\_j} + \mathbf{F}_{rot\_j}] = \sum_{j=1}^{v} \mathbf{R}_j \times \mathbf{F}_{flex\_j} + \sum_{j=1}^{v} \mathbf{R}_j \times \mathbf{F}_{rot\_j} = \mathbf{M}_{L\_flex} + \mathbf{M}_{L\_rot}$$

likewise for the 'right' side,

$$\mathbf{M}_R = \sum_{j=v}^{NE} \mathbf{R}_j \times [\mathbf{F}_{flex\_j} + \mathbf{F}_{rot\_j}] = \sum_{j=v}^{NE} \mathbf{R}_j \times \mathbf{F}_{flex\_j} + \sum_{j=v}^{NE} \mathbf{R}_j \times \mathbf{F}_{rot\_j} = \mathbf{M}_{R\_flex} + \mathbf{M}_{R\_rot} \tag{3.19}$$

As a rule, the flexure-causing[3] component of the 'left' moment must be equal and opposite to the flexure-causing component of the 'right' moment, $\mathbf{M}_{L\_flex} = -\mathbf{M}_{R\_flex}$. Meanwhile the rotation-causing components of either side play no part at all in fibre bending. The remaining task is that of determining the magnitude of $\mathbf{M}_{L\_flex}$ and $\mathbf{M}_{R\_flex}$ and then determining the bending and twist angle at the joint. It is now clear that even in discrete cases the internal moment balance is in fact preserved since $\mathbf{M}_{L\_flex} = -\mathbf{M}_{R\_flex}$. The reason $\mathbf{M}_L \neq -\mathbf{M}_R$ is due to the inclusion of the 'whole-body' components. Although it appears that there is internal moment imbalance, this is not true. Internally the balance is preserved since $\mathbf{M}_{L\_flex} = -\mathbf{M}_{R\_flex}$.

In summary,

$$\mathbf{M}_L = \mathbf{M}_{L\_flex} + \mathbf{M}_{L\_rot} \quad \mathbf{M}_R = \mathbf{M}_{R\_flex} + \mathbf{M}_{R\_rot} \quad \mathbf{M}_{L\_flex} = -\mathbf{M}_{R\_flex} \tag{3.20}$$

Next, the separation of the components is described.

Consider a joint (sphere) with two opposing moments acting, $\mathbf{M}_L$ and $\mathbf{M}_R$ with unequal magnitudes. These moments may now be separated into flexure-causing and whole-body rotation components. Due to the third rule,

[3]Note that the terms 'flexure-causing' and 'internal' are used interchangeably as they refer to the same concept. Likewise, 'external', 'rotation-causing' and 'whole-body rotation' also refer to the same concept.

$\mathbf{M}_{L\_rot}$ and $\mathbf{M}_{R\_rot}$ may simply be combined into a single 'rotation' term. Objectivity laws and the 'no inertia' condition allow it to be neglected from any further consideration while determining internal deformations. The remainder must be balanced on 'left' and 'right' sides of a point on a fibre according to the first rule. The implication is that for a given $\mathbf{M}_L$ and $\mathbf{M}_R$ of unequal magnitude and opposing direction, the lesser of the two moments corresponds to the moment causing internal deformation. That is, at a joint v,

$$\text{if } |\mathbf{M}_{L\_v}| < |\mathbf{M}_{R\_v}| \text{ then } \mathbf{M}_{L\_v} = \mathbf{M}_{flexure\_v} \text{if } |\mathbf{M}_{R\_v}| < |\mathbf{M}_{L\_v}| \text{ then } \mathbf{M}_{R\_v} = \mathbf{M}_{flexure\_v} \tag{3.21}$$

Note that fibre deformation only occurs when $\mathbf{M}_L$ and $\mathbf{M}_R$ are *opposing*. When aligned they do not cause flexure. Rather they form a collaborative effort to increase whole-body rotation velocity. With Eq. (3.21) the internal moment may be calculated. Eqs. (3.13) may now be used to determine the bending and torsion deformation at the joint.

The whole-body rotation causing moment at the joint could also be extracted (this method is not used however to determine whole-body rotation in this simulation - see the following section). The difference between the greater and the lesser moment is equal to the moment at the joint contributing to whole-body fibre rotation,

$$\sum_{j=1}^{NE} \left\{ \begin{array}{l} \mathbf{M}_{R\_j} - \mathbf{M}_{L\_j} \text{ if } |\mathbf{M}_{L\_j}| < |\mathbf{M}_{R\_j}| \\ \mathbf{M}_{L\_j} - \mathbf{M}_{R\_j} \text{ if } |\mathbf{M}_{R\_j}| < |\mathbf{M}_{L\_j}| \end{array} \right\} = \mathbf{M}_{wholebody\_rotation} \tag{3.22}$$

Whole Body rotation

For this method, the following is assumed:

- The fibre is rigid during the whole-body rotation stage. The fibre is only flexible during internal moment considerations.

For a truly flexible fibre this assumption is not true. However the assumption that the fibre is always nearly straight allows some leniency. Also the use of

sufficiently small iterations in simulation minimizes errors in the approximation.

Since internal forces and moments must balance out from a whole-body viewpoint, Eq. (3.16) can also be written as,

$$\mathbf{M}_{rot} = \sum_{j=1}^{NE} \mathbf{R}_j \times \mathbf{F}_{total\_j} = \zeta \omega_\Delta \tag{3.23}$$

(including Eq. (3.18)). Therefore from the total force $\mathbf{F}_{total\_v}$ on each bead, v calculated in simulation, and with current bead position relative to the fibre Centre of Mass (COM) $\mathbf{R}_v$, the moment $\mathbf{M}_{rot}$ is now solved for.

$\mathbf{M}_{rot}$ is the moment causing deviational rotation velocity ω_Δ due to fibre interaction forces (Eq. (3.28)). Since $\mathbf{M}_{rot}$ is known through Eq. (3.23), ω_Δ is now solved for. However rotational frictional drag coefficient is not known, ζ nor is the vector direction for ω_Δ.

The assumption that the fibre is always nearly straight is resorted to once again. For an arbitrary curved fibre, the rotational velocity ω_Δ resulting from an applied moment $\mathbf{M}$ will not necessarily be in-line with the moment producing the rotation. That is, their unit vectors are not identical,

$$\frac{\mathbf{M}}{|\mathbf{M}|} \neq \frac{\omega_\Delta}{|\omega_\Delta|} \tag{3.24}$$

However if the chain of beads are nearly straight, and the beads are equally spaced, and of same shape and density, then the rotation vector will *approximately* align to the moment causing the rotation.

$$\frac{\mathbf{M}}{|\mathbf{M}|} \approx \frac{\omega_\Delta}{|\omega_\Delta|} \text{ conditionally} \tag{3.25}$$

Since vector $\mathbf{M}$ can be found (using Eq. (3.23)), the approximate direction of the deviational rotation of the fibre ω_Δ is known. We are now left with the task of finding $|\omega_\Delta|$.

Consider a rigid sphere-chain fibre rotating at the deviational rotation rate ω_Δ about the COM. Bead v has a linear velocity of, $\mathbf{V}_v = \omega_\Delta \times \mathbf{R}_v$. Using Eq. (3.25), $\mathbf{V}_v = \left(|\omega_\Delta| \frac{\mathbf{M}}{|\mathbf{M}|}\right) \times \mathbf{R}_v$. Hence that sphere experiences a

translational drag force of $\mathbf{F}_{drag\_v} = \zeta_s \left(|\omega_\Delta| \frac{\mathbf{M}}{|\mathbf{M}|} \right) \times \mathbf{R}_v$ (using Stokes viscous drag coefficient for a sphere, Eq. (3.5)). Converting the drag force into a moment about the COM, $\mathbf{M}_{drag\_v} = \mathbf{R}_v \times \mathbf{F}_{drag\_v} = \mathbf{R}_v \times \left[\zeta_s \left(|\omega_\Delta| \frac{\mathbf{M}}{|\mathbf{M}|} \right) \times \mathbf{R}_v \right]$. With Eq. (3.25), all beads of the fibre are summed taking only the moment components in the direction of the total moment. This can now be done with the knowledge that since total rotation is in-line with total moment, the non-aligned moments will cancel out (approximately). Hence we finally derive Eq. (3.31).

Final Moment Balance

Finally, internal and external moment equations are linked to complete the moment balance. Recall the wholebody rotation moment Eq. (3.22), and also Eq. (3.23) with Eq. (3.31). The equations are combined to form the final whole-body moment balance.

$$\begin{aligned} \sum_{j=1}^{NE} \left\{ \begin{array}{l} \mathbf{M}_{R\_j} - \mathbf{M}_{L\_j} \text{ if } |\mathbf{M}_{L\_j}| < |\mathbf{M}_{R\_j}| \\ \mathbf{M}_{L\_j} - \mathbf{M}_{R\_j} \text{ if } |\mathbf{M}_{R\_j}| < |\mathbf{M}_{L\_j}| \end{array} \right\} &\approx \mathbf{M}_{wholebody\_rotation} \approx \textstyle\sum_{j=1}^{NE} \mathbf{R}_j \times \mathbf{F}_{total\_j} \\ &\approx \sum_{\nu}^{NE} \left(\frac{\mathbf{M}_{total}}{|\mathbf{M}_{total}|} \cdot \left[\mathbf{R}_v \times \left[\zeta_s \left(|\omega_\Delta| \frac{\mathbf{M}_{total}}{|\mathbf{M}_{total}|} \right) \times \mathbf{R}_\nu \right] \right] \right) \frac{\mathbf{M}_{total}}{|\mathbf{M}_{total}|} \end{aligned} \tag{3.26}$$

Together with Eq. (3.20), the internal and external moment balance is observed for this system of equations.

3.3.5 Periodicity

Ideally the simulation would model a truly infinite suspension. In practise however, the direct simulation is limited to a *finite* representative population of fibres. From the finite representation, the results for an infinite suspension must be extrapolated. Extrapolating infinite results from a finite simulation is shown to be feasible and produce reasonable results, as seen in previous simulations by Yamane *et al.* [35] and Fan *et al.* [31].

A common approach to approximating an infinite suspension is to simulate only a finite suspension, but surround the simulation domain with

multiple 'copies' of itself on all sides (while maintaining the same suspension concentration). The simulation proceeds to calculate for the motion of only the finite number of fibres in the centre, but includes the long range hydrodynamic influence of *all* fibres, including the copies. Meanwhile, the added 'copies', which exactly mimic the simulated fibre motion, are assumed to move 'correctly', as if their trajectory had actually been calculated in simulation. This is not unreasonable as conditions are identical everywhere within an infinite suspension experiencing a homogenous linear shear gradient. The long range hydrodynamic influence felt by the few *actual* simulation fibres in the centre is similar to what would be felt in a truly infinite suspension, without the entire suspension actually having being simulated. This is a computationally cheap way of artificially increasing the size of the suspension. By increasing the amount of 'copies', the long range hydrodynamic effect on the simulation fibres approaches that of a truly infinite suspension. Since the long range hydrodynamic influence diminishes with distance (see the form of the Oseen Eq. (3.7)), the hydrodynamic effect approaches a steady magnitude as the number of 'copies' increases to infinity (This argument is used in the Ewald Summation method [69]).

Like earlier works from Yamane *et al.* [35] and Fan *et al.* [31], this simulation takes place in a cubic volume named the *reference cell*. The reference cell is of volume, $V = l^3$, where l is the length of a fibre. The volume fraction ϕ of the suspension is determined by the number of fibres and the sphere density (number of spheres per fibre). These parameters will be referred to as NF and NE respectively.

The method used in this work is similar to the Ewald summation method [69], with the added assumption that long range hydrodynamic effects are small in any case and decrease to insignificant magnitudes with distance. The fibre configuration within the reference cell is repeated in a periodic *lattice* as shown in Fig. 3.11. The number of repeating *layers* of cells surrounding the reference cell (in the centre) can be varied. For most simulation results in this work however, the *layer depth* is one cell deep, i.e. a $(3 \times 3 \times 3)$ lattice

of repeating cells surrounds the actual reference cell in the centre. While the Ewald summation [69] calculates the hydrodynamic effect from an infinite amount of reference cell 'copying', here it is assumed that one layer depth is sufficient. In this respect, the method used here is more crude, however as the hydrodynamic effect rapidly reduces with distance, the difference between one cell layer depth and more should be very small, if not insignificant. There is also an argument that hydrodynamic effects on a fibre from distant fibres are completely masked by the mass of fibres in between. Due to this 'masking effect', the inclusion of distant fibres would only increase the cost of the simulation with little difference to results.

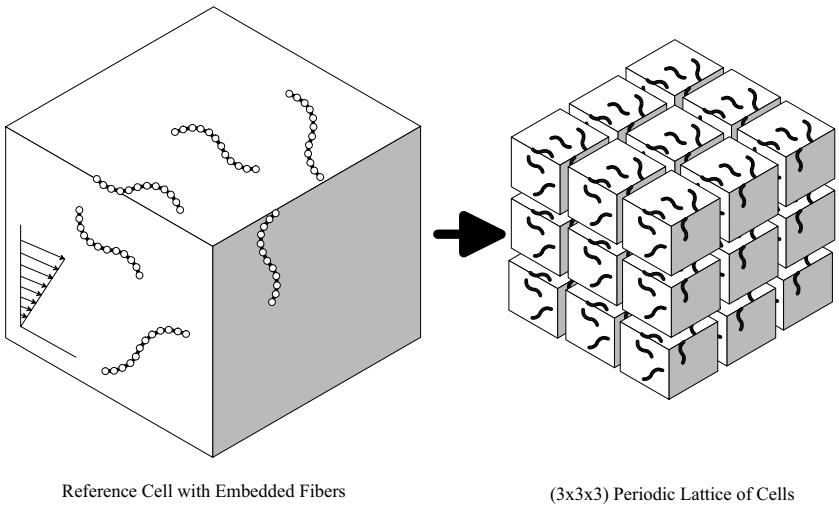

Figure 3.11: The reference cell and periodic repetition of the cell

Long range forces are assumed to apply only within a finite window of influence (see Fig. 3.12). On this basis, the cell depth one needs to simulate is limited. Within the window of influence around a sphere, the described interaction forces between spheres and fibres apply, however outside the window all forces are considered negligibly weak. The window depth may also be varied, and when combined with a suitable reference cell depth, the amount of interactions required to be simulated is controlled.

3.4 Simulation

The simulation proceeds in a fashion similar to Fan *et al.* [31]. The end-to-end unit vector of the sphere-chain is designated the 'fibre orientation' vector **P** and Eq. 3.28 is used to find the rotation rate of **P** for all simulation fibres. Once the suspension orientation is determined, a second step is employed to determine fibre shape. Lastly the viscosity and other bulk data are extracted through averaging over the fibre population.

The basic suspension information is established, such as number of fibres NF, number of beads NE, unit bead radius $a = 1$, fibre length l, and type and magnitude of flow, e.g., shear $\dot{\gamma}$ or extension $\dot{\epsilon}$. The initial fibre suspension is then created in the reference cell. Fibres are initially straight and beads are located at regular intervals along the fibre length. Fibres are oriented randomly and initial fibre velocity and rotation rate is set to be equal to that of the solvent local to the fibre. Care is taken to ensure that no fibres are overlapping before commencing simulation. In shear flow, the

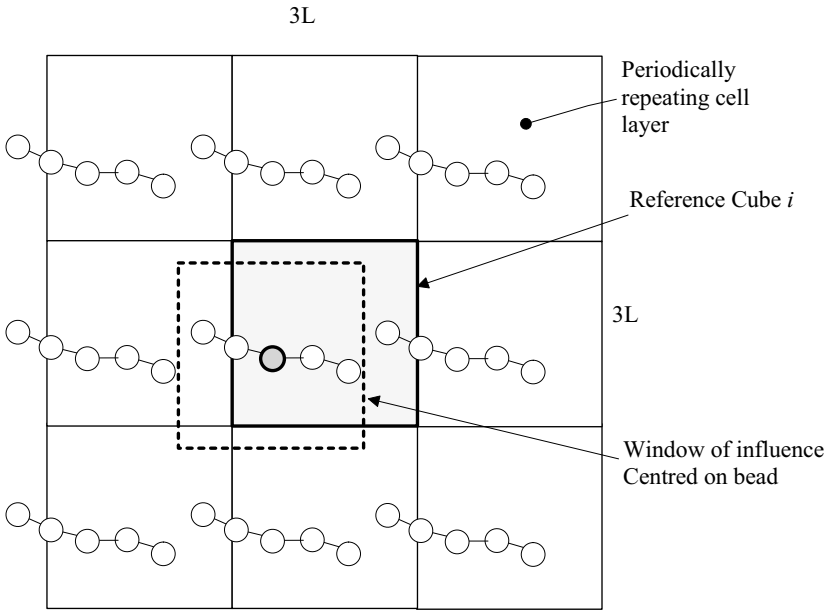

Figure 3.12: Window of influence centred about the sphere

simulation in run for the range, $0 \leq \gamma \leq 1000$, and for elongational flow, $0 \leq \gamma \leq 100 - 200$. The increment is set at $d\gamma = 0.01$, for a unit shear rate of $\dot{\gamma} = 1$.

At each iteration the fibre centre of mass $\mathbf{r}_{nc}$, end-to-end vector $\mathbf{P}$, global bead positions $\mathbf{r}_{n\nu}$, bead velocity $\mathbf{V}_{n\nu}$, external force $\mathbf{F}_{n\nu}$ and connector tension $\mathbf{X}_{n\nu}$ must be determined to fully understand the state of the suspension and determine the fibre motion for the next time step. Given bead velocities and fibre centre of mass, the velocity and new location for fibre Centre of Mass can be found,

$$\sum_{\nu}^{NE} \frac{\mathbf{V}_{n\nu}}{NE} = \dot{\mathbf{r}}_{nc} \qquad \mathbf{r}_{nc(\text{new})} = \mathbf{r}_{nc(\text{old})} + \dot{\mathbf{r}}_{nc} \cdot dt \tag{3.27}$$

The fibres net rotation rate $\mathbf{w}_{rotation}$ may be considered to be made of two components,

$$\mathbf{w}_{rotation} = \mathbf{w}_{\infty n} + \mathbf{w}_{\Delta\infty} \tag{3.28}$$

The fibre will have an undisturbed Jeffrey orbit rotation component $\mathbf{w}_{\infty n}$,

$$\mathbf{w}_{\infty n} \simeq \mathbf{P}_n \times \left[\frac{a_r^2}{a_r^2 + 1} \mathbf{K} \cdot \mathbf{P}_n - \frac{1}{a_r^2 + 1} \mathbf{K}^T \cdot \mathbf{P}_n \right] \tag{3.29}$$

Strictly speaking, Eq. (3.29) is inappropriately used since it neglects the rotation component parallel to vector $\mathbf{P}_n$ which would arise when the fibre is not axisymmetric. However for the flow conditions and moduli used in this simulation the flexible fibre will remain nearly straight and so the parallel component will be relatively small. This component is neglected in determining $\mathbf{w}_{\infty n}$ and therefore Eq. (3.29) is approximate only. The parallel component is not totally disregarded however. It will eventually be included as a component of the *deviational* rotation $\mathbf{w}_{\Delta\infty}$ to be determined next.

A fibre amongst its neighbours will also have a *deviational* component $\mathbf{w}_{\Delta\infty}$ due to inter-fibre interaction. We determine this component by considering the forces and moments on the fibre due to inter-fibre activity. From the interaction forces $\mathbf{F}_{nv}$ and current local bead positions $\mathbf{R}_{nv}$ the net moment

$\mathbf{M}_{nc}$ acting on fibre n about its centre of mass may be determined.

$$\sum_{\nu}^{NE} \mathbf{R}_{n\nu} \times \mathbf{F}_{n\nu} = \mathbf{M}_{nc} \tag{3.30}$$

It is assumed that the unit vector $\frac{\mathbf{M}_{nc}}{|\mathbf{M}_{nc}|}$ is equal to the unit vector of the *deviational* rotation rate $\frac{\mathbf{w}_{\Delta\infty}}{|\mathbf{w}_{\Delta\infty}|}$. This is a reasonable assumption since it is the moment on the fibre which causes the deviational rotation, and the fibre is always nearly straight. Having assumed the direction of the deviational rotation vector, one only needs to find the scalar magnitude $|\mathbf{w}_{\Delta\infty}|$ in Eq. (3.31), and then multiply this with the unit direction vector to completely determine the deviational component vector $\mathbf{w}_{\Delta\infty}$.

$$\mathbf{M}_{nc} = \sum_{\nu}^{NE} \left(\frac{\mathbf{M}_{nc}}{|\mathbf{M}_{nc}|} \cdot \left[\mathbf{R}_{n\nu} \times \left[\zeta \left(|\mathbf{w}_{\Delta\infty}| \frac{\mathbf{M}_{nc}}{|\mathbf{M}_{nc}|} \right) \times \mathbf{R}_{n\nu} \right] \right] \right) \frac{\mathbf{M}_{nc}}{|\mathbf{M}_{nc}|} \tag{3.31}$$

where

$$\left[\mathbf{R}_{n\nu} \times \left[\zeta \left(|\mathbf{w}_{\Delta\infty}| \frac{\mathbf{M}_{nc}}{|\mathbf{M}_{nc}|} \right) \times \mathbf{R}_{n\nu} \right] \right]$$

is the moment vector arising from the force on a single bead in the fibre. The unknown scalar $|\mathbf{w}_{\Delta\infty}|$ is determined numerically using Eq. (3.31). Therefore with Eq. (3.31) and the subsidiary Eqs. (3.28) - (3.30) the wholebody rotation rate is determined. The fibre may now be translated and rotated. Finally the methods of Section §3.3 are used to improve the estimate of the end-to-end vector $\mathbf{P}$ by then overlaying the sphere-chain and updating the deformed fibre shape in response to its environment. It is emphasised that this method is only valid when it is assumed the fibre will remain nearly straight at all times. Particles that are highly deformed such as in tight arcs, knots or loops cannot be properly modelled under these assumptions.

Once the new bead positions are established the new bead velocities can be calculated,

$$\mathbf{V}_{nv-new} = \frac{\mathbf{r}_{nv-new} - \mathbf{r}_{nv-old}}{\Delta t} \tag{3.32}$$

The new forces between beads are calculated using Eq. (3.9) and (3.10) for viscous drag, short and long range interactions. Finally the connector

tensions, suspension orientation and stress can be found using Eqs. (3.11), ensemble averaging and Eq. (2.11) respectively. The fibres are relatively stiff and deviate little from dead-straight, unlike the completely flexible threads used by Hinch [50] where higher order terms are required to adequately describe thread dynamics and calculate stresses. In the context of nearly straight fibres the use of the TIF equation is a valid approximation. When a fibre translates beyond the reference cell it is repositioned such that it continues its journey from the other side of the cell - re-entering the cell. Thus the volume fraction of the suspension is maintained. This procedure repeats for each iteration and information regarding the fibre orientation evolution, stress and viscosity can be extracted in each cycle.

Non-dimensionalised Young's and shear modulus used in simulation is related to real values with the following relations, $E_{sim} = \frac{E}{\dot{\gamma}\mu}$ and $G_{sim} = \frac{G}{\dot{\gamma}\mu}$ where $\dot{\gamma}$ is the shear rate and μ is the solvent viscosity. In the case of the 'imaginary soft fibre', the Poisson ratio is assumed to be $\nu = 0.35$ hence allowing the determination of equivalent G given modulus E.

The simulation was written in Fortran77 and was compiled and executed on a DEC Alpha workstation in the SyDCom[4] computing facility. Execution time for 100000 iterations ranges from several hours to several days or weeks depending on the volume fraction and periodic depth.

3.5 Results

Before presenting flexible fibre results, we first verify the validity of this simulation for the rigid fibre case. In the immediately following sections, the fibre joints are artificially forced rigid. The bend and twist angles are permanently set to zero deflection. As we will see when compared to previous known numerical results and experimental observations, the simulation results are a close qualitative and quantitative match. Following these rigid fibre verification tests, results for a lone flexible fibre and flexible fibre suspensions are

[4]Sydney University Distributed Computing Facility

presented and compared to previous results where available.

3.5.1 Verification: Rigid Fibre

Several different tests were performed to verify rigid fibre simulation results. Basic characteristics that must be reproduced in a simulation were nominated and then tested. For a lone rigid fibre in Newtonian shear flow,

- The fibre must execute a Jeffrey orbit as described by Eq. (2.2).
- The Jeffrey Orbital period must be predicted as described by Eq. (2.3).

Meanwhile for the suspension of rigid fibres, the following results were compared against known results.

- Relative viscosity η_r for simple shear flow $\dot{\gamma}$ against volume fraction ϕ.
- Relative viscosity η_r for simple extensional flow $\dot{\epsilon}$ against volume fraction ϕ.

The simulation data was compared to previous numerical results for shear by Fan *et al.* [31, Figs. 11 and 12] (which has been verified by other means [102]) and experimental results from Milliken *et al.* [103] and Bibbo [104]. Extensional flow results are compared to a semi-empirical equation by Batchelor [105] for rigid-rod suspensions.

Lone Rigid Fibre

Needless to say with the use of Eq. 3.29 within the simulation it is a foregone conclusion that an undisturbed rigid fibre in shear flow will execute the Jeffrey orbit at the correct orbital period for all aspect ratios and shear rates. Indeed this behaviour was observed in this simulation (as expected) for rigid undisturbed fibres over all aspect ratios and shear rates tested. One may now proceed with the knowledge that correct lone rigid fibre motion is successfully reproduced in this simulation.

Rigid Fibre Suspensions

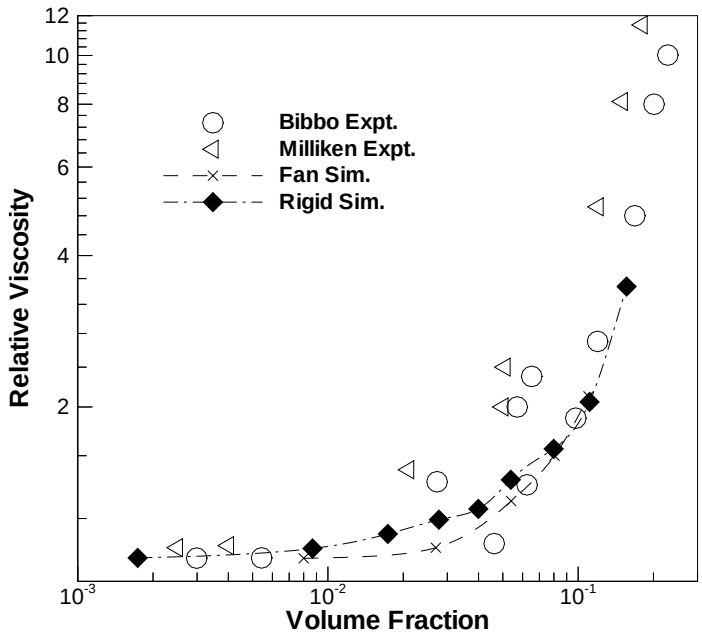

Figure 3.13: Rigid fibre relative viscosity in shear flow

Fig. 3.13 compares simulation viscosity (⧫) against Fan *et al.*'s numerical result (×) for varying volume fraction. The fibre aspect ratio is $a_r = 16.9$, there are $NE = 16$ beads per fibre, bead radius is $a = 1$, solvent viscosity is $\eta_s = 1$ and shear rate is $\dot{\gamma} = 1$. Milliken (◁) and Bibbo's (◯) experimental results are also plotted. Simulation viscosity shows a good qualitative match against those of Fan *et al.*. They also lie closer than Fan's result to the centre of the experimental data points produced by Bibbo, particularly in the mid-concentration ranges. Milliken found a generally larger viscosity over the volume fraction range, however his fibres were of a larger aspect ratio $a_r = 18$ and also it is believed the nature of his experiment produced overestimations for viscosity. Milliken uses Falling-ball rheometry [103] and it is suspected that an overestimate for viscosity may have been produced

from the strong elongational flow component that is expected in the wake of a sphere moving through viscous fluid. This concern has also been voiced by Fan *et al.* [31]. Quantitatively the simulation viscosity is marginally larger than Fan's result over the semiconcentrated region ($0.0035 < \phi < 0.0592$ for $a_r = 16.9$). In the dilute and concentrated regions the two results are very similar in magnitude. A feature not present in Fan's result is a very mild 'bump' (barely visible on the scale used in the graph) in the viscosity curve in the semi-concentration region from $10^{-2} \leq \phi \leq 10^{-1}$. This feature may be the same one as noted by Blakeney [89, Figure 2, page 327] in his experimental work on rigid rod suspensions which he attributed to an increase in 'mechanical interactions' between fibres (see Fig. 3.1). That is to say in this particular range of volume fraction the suspension is sparse enough to allow fibre rotations at a relatively unrestricted and high velocity, but dense enough that the likelihood of inter-fibre collision is high. This 'bump' region is apparently where these two opposing factors combine to cause the orientation dispersion to be at its greatest and hence for viscosity to reach a local maxima. Of course at higher volume fractions viscosity continues to increase in absolute magnitude however this could be attributed more to increasing concentration. This 'bump' can be looked upon as the volume fraction region where the contribution to suspension viscosity per fibre is at its greatest and is most efficiently made.

Fig. 3.14 compares simulation viscosity against Batchelor's semi-empirical viscosity equation in extensional flow [105]. This equation yields an estimate for Trouton ratio and is of the form,

$$\frac{\lambda_{trouton}}{\eta_s} = 3 + \frac{4}{3}\frac{\phi a_r^2}{\ln\left(\frac{\pi}{\phi}\right)} \tag{3.33}$$

where $\lambda_{trouton}$ is the Trouton viscosity, η_s is solvent viscosity, a_r is fibre aspect ratio and ϕ is volume fraction. In a review by Acrivos [39, chapter 15] this equation was judged to be 'very satisfactory' and so is deemed suitable to compare current results with. As we can see from Fig. 3.14, while the relative viscosity is somewhat overestimated over the whole breadth of volume

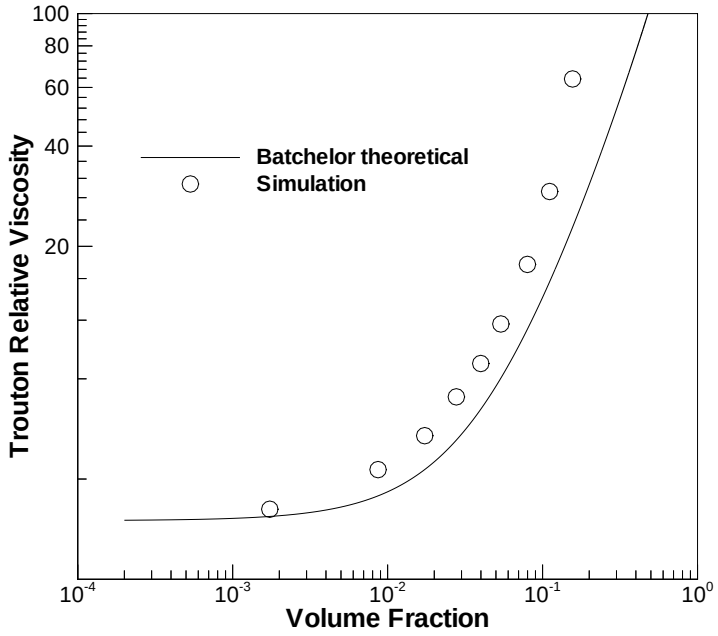

Figure 3.14: Rigid fibre relative viscosity in extensional flow

fraction, the qualitative match is clear. Fibres are rigid, with aspect ratio $a_r = 16.9$, sphere radius $a = 1$, spheres per fibre $NE = 16$, and extensional rate $\dot{\epsilon} = 1$.

For the most part then, the rigid fibre simulation accurately predicts known rigid fibre behaviour, both as individuals and interacting as groups in suspension. In the next section the rigid-joint restriction is removed and fibres are allowed to deform.

3.5.2 Flexible Fibre

There is little previous work on flexible fibres to compare findings with. Before looking at multiple fibres in suspension it is worthwhile looking at lone flexible fibre motion. In the following sections the results of two previous works by Hinch [50], and Skjetne *et al.* [33] in flexible fibres are reproduced. Following these verification tests we may then proceed with more confidence to the flexible fibre suspension results.

Lone Flexible Fibre Jeffrey's Orbital Drift

Skjetne *et al.* [33] reported on the simulated dynamics of a single flexible fibre in Newtonian shear flow. Amongst the many scenarios studied they report that flexible fibres will execute what initially is a Jeffrey orbit. However this orbit is not a stable one and will drift through orbital constants C. Also observed experimentally by Arlov *et al.* [106], C will tend to drift (for the most part) either to 0 or ∞, depending on the initial C value, with intermediate values also observed.

In Fig. 3.15 we can see clearly that orbital drift occurs in the simulation results (top) and is qualitatively similar to that produced by Skjetne *et al.* (bottom). The simulation fibre is $a_r = 16.9$, $NE = 16$, $a = 1$, $\dot{\gamma} = 1$ and is of a modulus equal to that for Vinylon (Young's modulus $E_{sim} = 5.2 \times 10^9$, shear modulus $G_{sim} = 1.9 \times 10^9$).

Fig. 3.16 shows the different rates of Jeffrey orbit drift between the rigid case and successively more flexible materials from glass fibre through

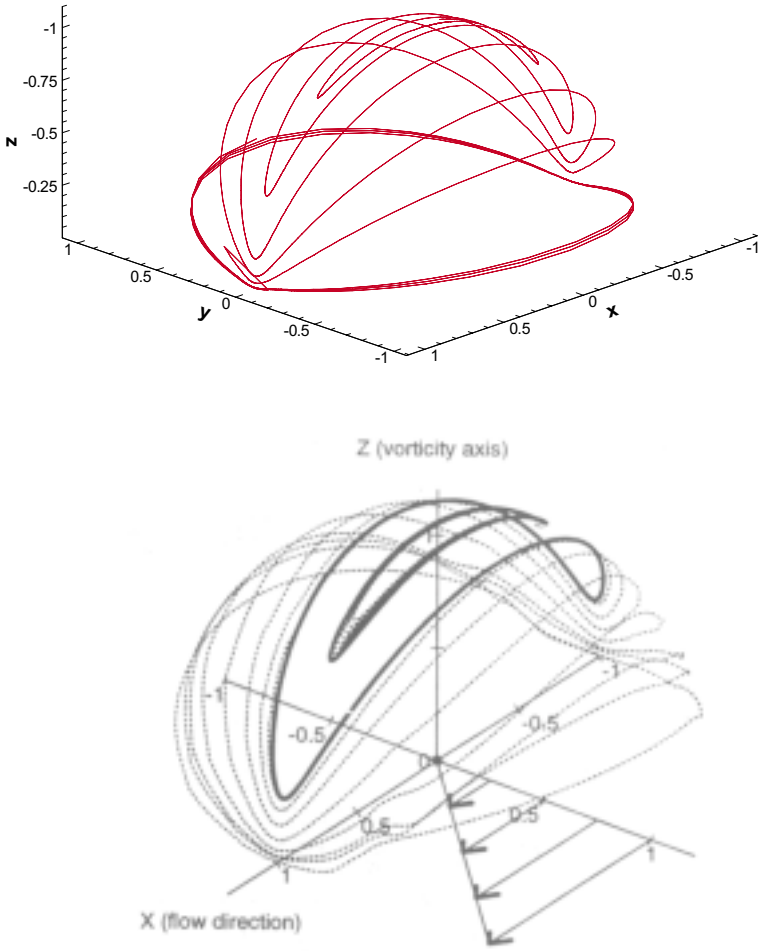

Figure 3.15: The Jeffrey orbit constant C is initially low. Over successive orbits the fibre drifts into the vorticity (z) axis. The result by Skjetne *et al.* (below) is reproduced in simulation (top).

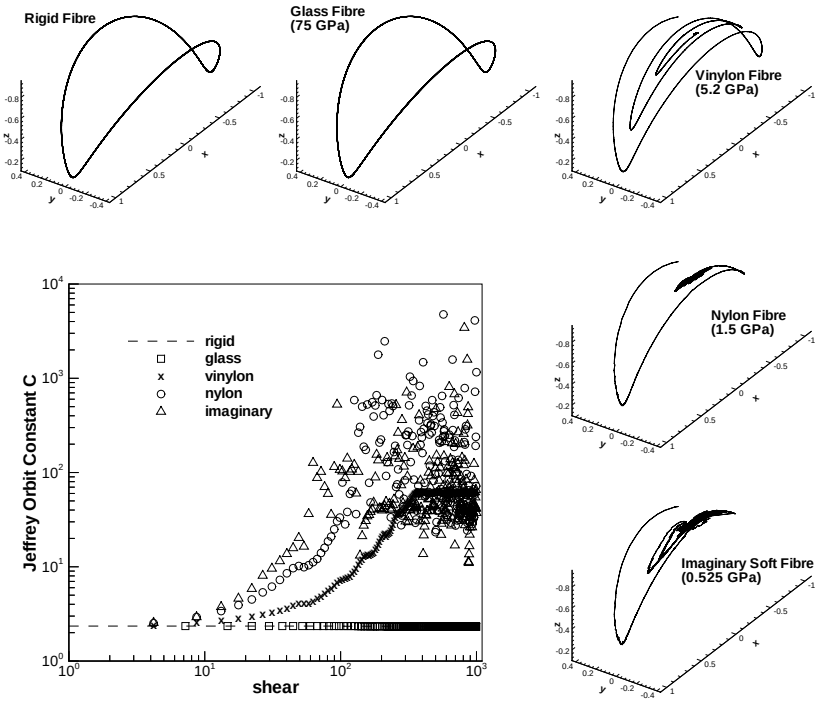

Figure 3.16: Comparison of orbit drift with decreasing stiffness Jeffrey orbit constants plotted against shear. Note the varying rate of increase in Jeffrey Orbit constant depending on fibre stiffness. Alignment to the vorticity (z) axis is not steady and the fibre orientation oscillates about that axis, particularly for the more flexible materials. The orbit constant ranges from $O(50) < C < \infty$ ($O(10^4)$ in numerical simulation) as indicated by the scatter of data points.

to nylon and an 'imaginary' soft fibre. The glass fibre ($\square$) is an order of magnitude stiffer than the other materials and behaves most like the rigid fibre ($--$). There is some divergence from the Jeffrey orbit but it is small and not visible at the scale shown. Vinylon ($\times$) executes several orbits with increasing orbit constant C until it is aligned with the vorticity (z) axis. The softer materials nylon ($\circ$) and 'imaginary' ($\triangle$) also show a spiralling into the vorticity axis but at proportionally faster rates. The softest 'imaginary' fibre does not complete a half orbit before it is aligned with the (z) axis. It is apparent that the rate of orbital drift towards the vorticity axis is inversely proportional to the elastic modulus of the material.

$$\frac{dC}{dt} \propto \frac{1}{E} \tag{3.34}$$

This behaviour of aligning to the vorticity axis is reminiscent of that observed in viscoelastic solvents. The Newtonian solvent with elastic fibre mimics the behaviour of a viscoelastic solvent with rigid fibre. This could possibly form the basis for a new model of viscoelastic fluids, but this is left for future exploration.

Single Flexible Fibre Straightening

One of the few theoretical works on flexible fibres was by Hinch [50, Fig. 3] where he looks at a flexible inextensible 'thread' in shear flow. The thread is of infinitesimal thickness ($a_r = \infty$) and there is no straightening tendency (Moduli $E = G = 0$). Given an initial shape and orientation in shear flow Hinch predicted the shape of the thread at successive values of shear. This result is reproduced with the current simulation.

Fig. 3.17 compares results by Hinch (left) against those produced in simulation (right). The thread is initially given a sinusoidal shape directed either with (Reversed 'S', or 'left facing') or against ('S' or 'right facing') the flow gradient and the evolving shape is calculated for shear values over the range, $\gamma = 1, 2, 3, 4, 5, 6$. The simulation fibre has $a_r = 16.9$, $NE = 16$, $a = 1$, $\dot{\gamma} = 1$. To correctly model a thread with no straightening tendency

the material moduli are set to zero ($E = G = 0$) and the beads are allowed to 'drift' with the flow. The qualitative match between theory and simulation is excellent. Because Hinch's thread has no thickness ($a_r = \infty$) the thread will straighten but will not continue its rotation beyond aligning to the shear direction. This result is expected for a fibre of infinite aspect ratio in shear and is predicted by Jeffrey's Eq. (2.2). The simulation however requires that a_r be finite and hence it is observed that the fibre straightens and aligns to the shear direction (as does Hinch's result) but then continues to rotate.

Flexible Fibre Suspension

The significant point made by Goto *et al.* [88] is that a more flexible fibre inclusion will result in a more viscous suspension. Using fibres of $a_r = 16.9$, $NE = 16$, $a = 1$, and a shear rate of $\dot{\gamma} = 1$ a series of simulation runs were performed for fibres of varying material stiffness. All materials used in simulation, and also those used by Goto *et al.*, Milliken *et al.*, and other

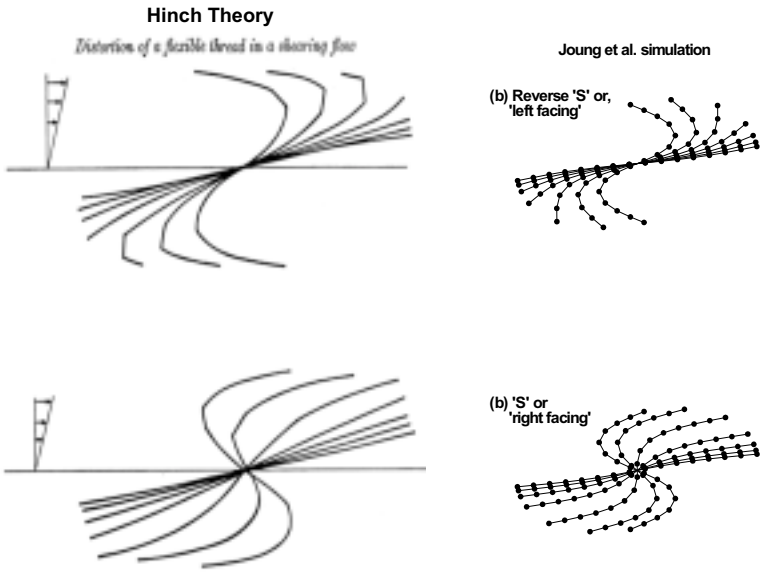

Figure 3.17: Distortion of a flexible thread in a shearing flow. Hinch (left) and Simulation (right)

researchers referred to here, are listed in order of their stiffness in Table 3.2.

Fibre Materials	**Modulus** $\left(E_{sim} = \frac{E}{\dot{\gamma}\mu}\right)$
'Rigid'	NA
Carbon [[88],[97]]	$235 - 245$
Glass [[88],[97]]	75
Vinylon [[88],[97]]	$5.2 - 8.0$
Polymethyl Methacrylate-Perspex [[103]]	$2.4 - 3.4$
Nylon [[88],[2],[97],[104]]	$1.5 - 2.5$
'Imaginary'	0.525

Table 3.2: Simulated material moduli

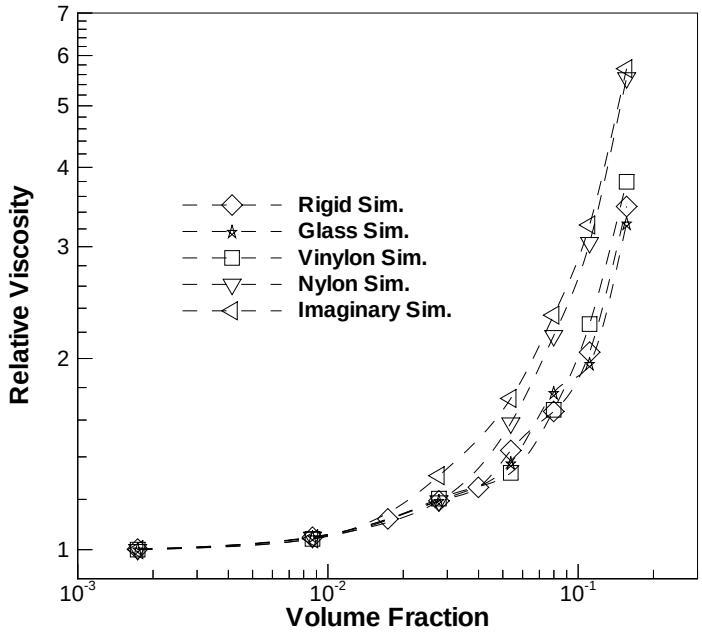

Figure 3.18: Viscosity versus volume fraction: flexible materials compared to rigid

Fig. 3.18 shows how the different materials used in simulation, Glass ($\star$), Vinylon ($\square$), Nylon ($\bigtriangledown$), Imaginary ($\lhd$) compare to rigid fibres ($\diamondsuit$). The differences appear to be quantitative only. Immediately we can see that the more flexible the material the greater the viscosity of the suspension. Glass being the stiffest of the simulated materials produces results only slightly greater than the rigid fibres over the whole volume fraction range (not noticeably different at the scale shown in Fig. 3.18). The most compliant materials Nylon and'Imaginary' both show significantly greater suspension viscosity than the rigid fibres (of the order $7-10\%$ greater than the rigid in the semiconcentrated to concentrated regions). These results are consistent with the experimental observations of Goto *et al.* [88]. Note that for lower volume fractions the difference in viscosity between materials becomes negligible. All materials match the rigid curve at lower volume fractions until a certain point when the curve diverges from the rigid fibre curve. This divergence point is dependent on the modulus of the material and determines the viscosity calculated at higher volume fractions. As modulus increases the divergence point moves towards the higher volume fraction.

Fig. 3.19 compares the experimental result of Bibbo for Nylon fibre ($\bigcirc$) against the simulated Nylon ($\blacktriangledown$) result. The simulated rigid curve ($\diamondsuit$) is also plotted. The experimental data is scattered particularly in the semiconcentrated region. This may be an indication of the increased inter-fibre activity at this concentration. We can see that the trajectory of the simulated Nylon curve ($\blacktriangledown$) follows experimental data well, and is a definite improvement over the equivalent rigid fibre result ($\diamondsuit$) especially at higher concentrations (see Fig. 3.19). It would seem that the differences between theoretical and experimental 'rigid fibre' results of past researchers may be accounted for when fibre flexibility is considered.

Stiffness Dependence of Suspension Viscosity

In Fig. 3.20 we plot the relative viscosity against the stiffness. For this example the fibres are always $a_r = 16.9$, $NE = 16$, $a = 1$ and shear rate

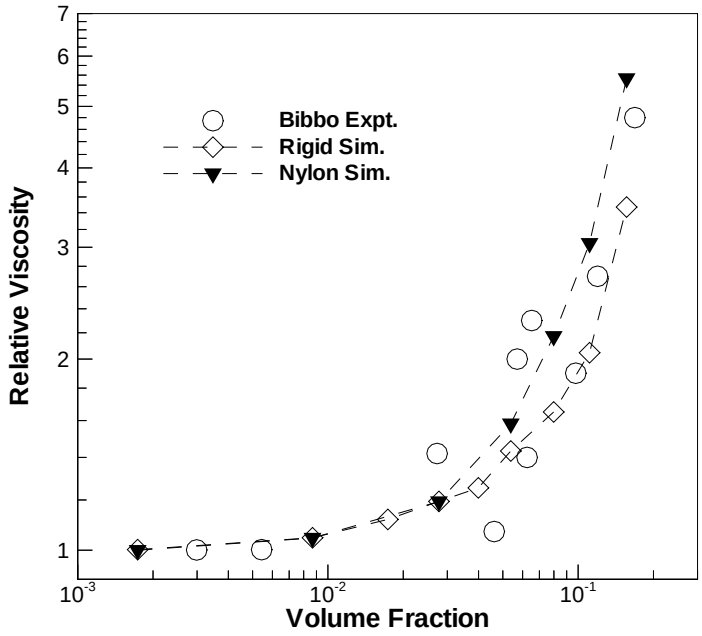

Figure 3.19: Nylon fibre compared to rigid and Bibbo experimental

is $\dot{\gamma} = 1$. The seven different curves represent constant concentration lines (NF = fibre number per reference cell) for $NF = 1, 5, 16, 31, 46, 64$ and 90. We can see that there is a distinct modulus 'band' in the range $10^9 < E_{sim} < 10^{10}$ within which the viscosity drops rapidly as stiffness increases for all concentrations tested. For the stiffness region $E_{sim} < 10^9$ suspension viscosity does not change significantly. For the region $E_{sim} > 10^{10}$ suspension viscosity again does not change significantly and in fact approaches the rigid fibre result.

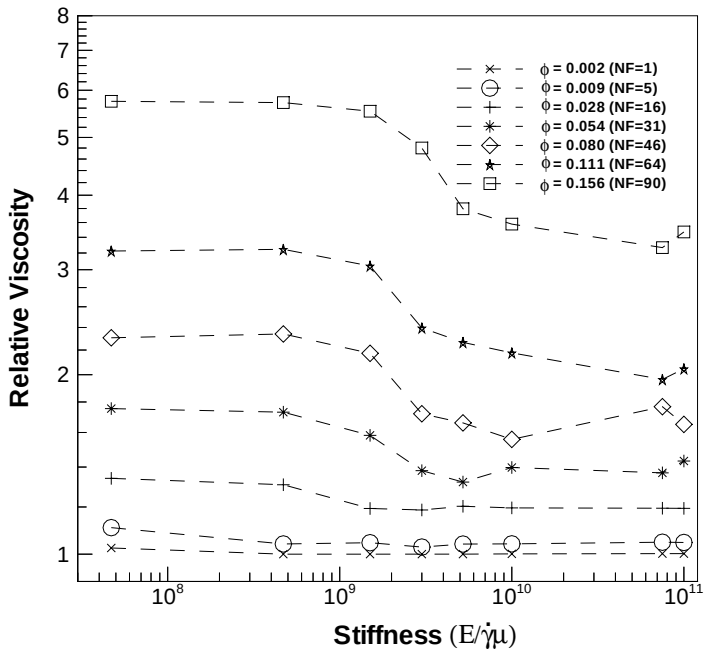

Figure 3.20: Relative viscosity versus stiffness - constant concentration lines

Fig. 3.20 also displays clearly the findings of Goto *et al.*'s experimental work - the suspension viscosity is indeed inversely related to the fibre stiffness. Further to Goto *et al.*'s conclusion we can also now state that this inverse relationship is valid only in a certain range of stiffness. When stiffness is high the suspension viscosity approaches a lower limit predicted by

the existing rigid fibre constitutive relations such as *TIF*. When stiffness is very low the suspension viscosity approaches an upper limit beyond which any further reduction in stiffness yields negligible further viscosity increase. The difference between the upper and lower viscosity limits is quite large. For example at $NF = 46$ ($\diamondsuit$), $\phi = 0.0798$ the upper viscosity limit is 41% greater than the lower limit viscosity. For $NF = 90$ ($\square$), $\phi = 0.156$ the upper limit viscosity is 65% greater in magnitude than the lower viscosity limit. We can see that the upper to lower viscosity difference increases as suspension concentration increases. With differences as great as this the use of 'rigid' fibres must be used with caution when accurate viscosity prediction is required.

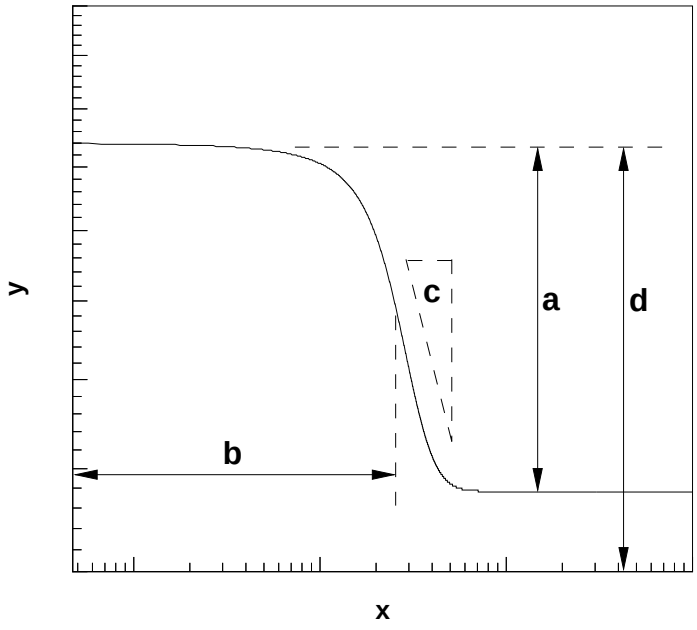

Figure 3.21: Curve fitting of viscosity versus fibre stiffness

This variation in viscosity with modulus may be fitted with the empirical

Eq. (3.35),

$$y = -\frac{a}{1 + e^{\frac{b-x}{c}}} + d \tag{3.35}$$

where a is the difference between the upper and lower $\eta_{relative}$ value, b is the displacement of the curve in the horizontal axis, c controls gradient and d is the maximum $\eta_{relative}$ value (Fig. 3.21). When terms are renamed to apply to the problem at hand, the equation becomes,

$$\eta_{flex} = \eta_{rigid} + \Delta\eta \left(1 - \frac{1}{1 + e^{\frac{E_{mean}-E}{c}}}\right) \tag{3.36}$$

There are three parameters in this equation $\Delta\eta$, E_{mean} and c which must be determined from data. From the simulation series shown in Fig. 3.20 these parameters are estimated to be,

$$\begin{aligned} \Delta\eta\left(\phi\right) &= 92.3853\phi^2 + 0.5677\phi + 0.0206 \\ E_{mean} &= 2.43 \times 10^9 \\ c &= 6.3 \times 10^8 \end{aligned} \tag{3.37}$$

where ϕ is volume fraction. Eq. (3.36) is then used to fit the simulation data as shown in Fig. 3.22.

Eq. (3.36) may be used as the basis of a method for predicting flexible fibre suspension viscosity. Given that the equivalent rigid fibre suspension viscosity (η_{rigid}) can be found through existing methods (e.g., TIF equation, or direct simulation) one only needs to know the fibre modulus, and the suspension volume fraction ϕ to the find the three new parameters (Eq. (3.37)) and hence estimate the flexible suspension viscosity using Eq. (3.36).

Interaction Coefficient

In their work, Fan *et al.* [31, Figs. 7 and 8] calculated with their direct simulation a numerical estimate for the interaction coefficient, C_i and compared this with experimental results from Folgar and Tucker [2, $a_r = 16$ Nylon fibres in Silicone Oil]. This comparison is repeated using this simulation where rigid fibres are now modelled by the chain of beads.

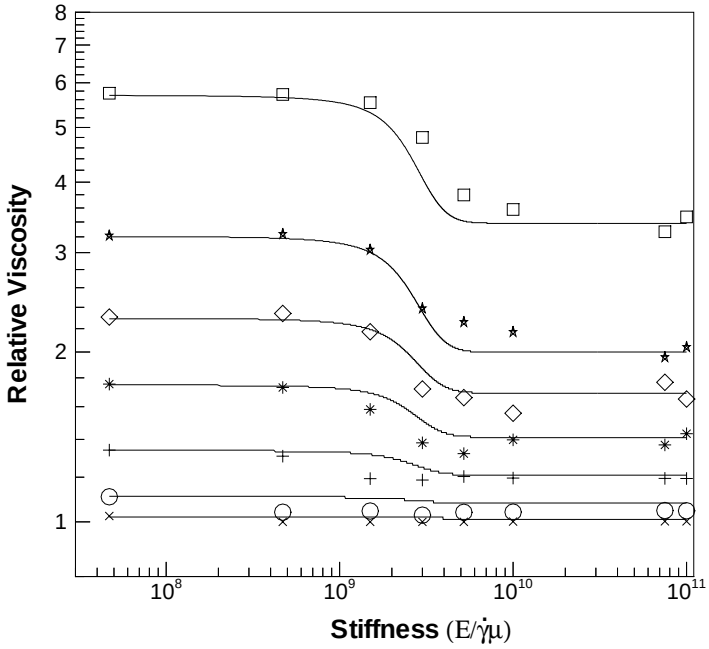

Figure 3.22: Viscosity estimate using curve-fitting

As discussed earlier (page 17), the Interaction Coefficient, C_i is a scalar term and operates in Eq. (2.8). However, recently there has been speculation that C_i may serve better as a tensorial term. If C_i is tensorial then the *Advani-Tucker* equation must be modified. When this is done the modified equation is,

$$\mathbf{C}\cdot\mathbf{PP}+\mathbf{PP}\cdot\mathbf{C}-2\mathbf{C}:\mathbf{PPPP}-\frac{2}{3}\mathbf{C}+\frac{2}{3}\mathbf{PP}\mathrm{tr}\left(\mathbf{C}\right)=\frac{1}{3\dot{\gamma}}\left(\ell\cdot\mathbf{PP}+\mathbf{PP}\cdot\ell^{T}-2\ell:\mathbf{PPPP}\right) \tag{3.38}$$

where in shear flow,

$$\mathbf{C}=\begin{bmatrix} C_{11} & C_{12} & C_{13} \\ C_{21} & C_{22} & C_{23} \\ C_{31} & C_{32} & C_{33} \end{bmatrix} \quad \ell=\dot{\gamma}\begin{bmatrix} 0 & 1-\zeta & 0 \\ -\zeta & 0 & 0 \\ 0 & 0 & 0 \end{bmatrix} \quad \zeta=\tfrac{1}{a_r^2+1}$$

The tensor $\mathbf{C}$ can be solved given the fibre orientation vectors $\mathbf{P}$ and their moments $\mathbf{PP}$ and $\mathbf{PPPP}$. In simulation we have a finite number of fibres and so ensemble averaging is used to approximate these tensors. Then $\frac{1}{3}trace(\mathbf{C})$ is used as the scalar equivalent C_i. In Fig. 3.23 the results from the simulation ($\triangle$) for a fibre $a_r = 16.9$, $NE = 16$, $a = 1$ and shear rate $\dot{\gamma} = 1$ are compared with Fan *et al.*'s latest numerical results ($\blacksquare, \blacktriangle, \blacktriangledown, \blacktriangleright, \blacktriangleleft$) and also experimental results by Folgar and Tucker ($\bigcirc$) for fibres with $a_r = 16$.

The simulation C_i values span approximately the same magnitude as the Folgar and Tucker experimental result. Furthermore it is noted that the simulation result also lies within Bay's experimentally determined range, $10^{-3} < C_i < 10^{-2}$ which is very encouraging. Fan *et al.*'s latest numerical results approximate the experimental result very well, particularly at higher volume fractions. The C_i range predicted by Yamane *et al.* is two orders of magnitude smaller than experimental results. It is noted that for all three groups of data, C_i tends to increase as concentration increases however the rate of change varies between the simulation and experimental results. The two results begin with a similar gradient for lower concentrations but the experimental curve maintains a higher gradient at higher volume fractions that the simulation.

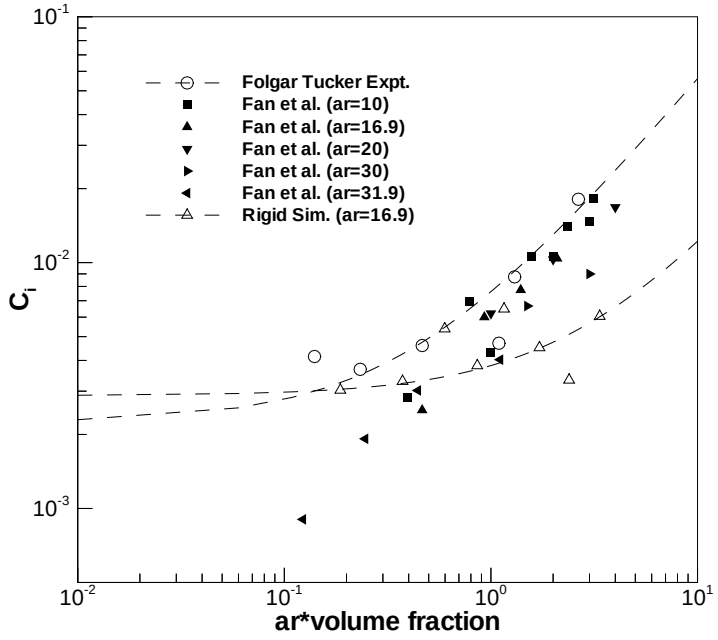

Figure 3.23: C_i comparison between rigid fibre simulation, Fan *et al.*'s simulation and Folgar and Tucker's experimental results

3.6 Conclusion

This chapter describes the creation of a numerical direct simulation of flexible fibres in Newtonian suspension, the associated theories and the results obtained from it. This simulation accounts for the interaction of fibres through both short and long range hydrodynamic interactions. For internal deformation the fibres are modelled as a chain of spheres joined with connectors. The connectors are allowed to rotate in relation to each other and therefore allow the deformation of the fibre as it interacts with the environment. As whole-body fibres, the simulation proceeds in a manner similar to that developed by Yamane *et al.* [35] and also used by Fan *et al.* [31]. The data produced may be used to calculate useful properties of the suspension such as bulk viscosity.

The simulation was created with the goal of achieving results on two levels. Firstly to reproduce the existing results of previous researchers in rigid fibre suspensions, and then to extend the findings to those of flexible fibres. The second goal was to improve the accuracy of viscosity prediction.

This simulation has been observed to reproduce the Jeffrey orbit, and the orbital period (as a function of aspect ratio) for lone undisturbed rigid fibres. The suspension viscosity is well predicted for the rigid fibre suspension as compared to experimental results [103][104][105], both in shear and extensional flow. For lone flexible fibres this simulation can reproduce results seen by Skjetne *et al.* [33] and Hinch [50] for orbital drifting and fibre straightening. Goto *et al.*'s conclusions on the relation of viscosity and flexibility are concurred with and elaborated on, and a method was developed to modify the existing rigid fibre viscosity result to an equivalent flexible fibre viscosity as a function of the fibres Young's modulus. It was shown that when fibre flexibility is accounted for, the suspension viscosity prediction is markedly improved. Finally the so called *Interaction Coefficient* C_i of Folgar and Tucker has been reproduced to a magnitude which is comparable to the experimental results and is in agreement with the latest numerical results of Fan *et al.*

Chapter 4

Viscosity of Curved Fibres in Suspension

4.1 Introduction

In this chapter we continue the development of the original simulation method first presented in Chapter 3. The work in this chapter is based on the paper by Joung *et al.* [107], a copy of which is also provided as additional material in the sleeve of this thesis.

The relationship between fibre shape and relative viscosity of a fibre suspension is explored further here. The numerical simulation was used to model non-Brownian *curved* rigid fibres in suspension under the influence of Newtonian shear flow. Curvature in the simulated fibres was taken to represent general deformities of real fibres in suspension. The simulation method was previously used by Joung *et al.* [87] to determine suspension viscosity for flexible fibres in suspension.

The results showed that when compared to the equivalent straight rigid fibre suspension, fibre curvature was found to contribute to a large increase in suspension viscosity. For typical semi-concentrated to concentrated suspensions, curved fibres were observed to produce viscosity increases of the order twice that of straight fibre suspensions. Results indicate that even a

small bend in the fibres may cause a large bulk viscosity increase. Suspension viscosity is therefore highly dependent on the quality control measures taken during sample preparation.

4.2 Background

In this work, as in Chapter 3, the main focus is on the viscosity of fibre suspensions since viscosity is important to the flow field development of molten plastics. As in [87], the same direct simulation method is used to observe the microstructural development of the fibre suspension in a shear flow and calculate suspension viscosity. In Chapter 3 however the simulation fibres were flexible and deformed in time and with flow conditions. In this chapter, the fibres are forced to be *rigid* but *curved*. Rigidity is enforced in order to eliminate fibre flexibility effects as a factor from results. This was the particular focus of 3. Curvature in the fibre is now introduced as a metaphor for general shape variations and deformities observed in real fibres. As shown in Fig. 4.1, deformity in fibre suspension is a real and commonly occuring event and the effects of it are studied here. Deformities of this kind are presumably produced in the laboratory by the method used to cut fibre samples. Deformations may also arise from fibre degradation over time, thermal variations (warpage), abrasions and other factors not usually addressed in theoretical and numerical works.

4.2.1 Shape Effects on Fibre Suspension Viscosity

The common approach in fibre suspension theory is to assume that fibres are rigid straight cylindrical rods. This assumption greatly simplifies the theory since a rigid straight cylinder is an easily defined geometry. In this way, complications arising from shape changes during flow may be avoided. It has been shown however that fibre shape is an important factor in the resultant suspension viscosity [90][25]. Nawab and Mason [91] observed experimentally that Nylon fibre suspensions could produce a measured viscosity three

times the order of theoretical predictions. They speculated that this difference might be a result of fibre curvature. Forgacs and Mason [93] showed that a slight curvature in the fibre would greatly alter fibre rotations. Kitano *et al.* [96] presented an empirical relationship between relative viscosity and volume fraction for various fillers such as glass and carbon fibres. Their results suggested that different materials would produce different suspension viscosities. It is reasonable to suppose that the varying filler stiffness (and hence shape deformation) was the cause for the viscosity variation. Likewise Goto *et al.* [88][97] looked experimentally at the relationship between fibre flexibility and suspension viscosity. They found that more flexible fibres produced relatively higher suspension viscosity than the equivalent stiffer fibre suspensions. Blakeney [89] found that slightly curved fibres (of the order $O(5°)$ end-to-end fibre axis tangent angle) could increase suspension viscosity by the order $10 - 15\%$ above that of a comparable straight fibre suspension. While we do not have the confidence to say yet that all straight rigid rod theories will generally under-estimate viscosity, the evidence does seem to imply that fibre deformity does contribute to a significant suspension viscosity increase over the equivalent straight fibre suspension. With this work we use a numerical basis to reproduce and describe this viscosity-curvature relationship.

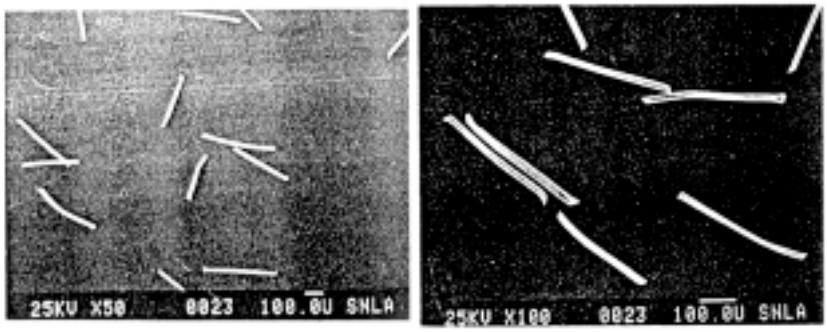

Figure 4.1: Photographs of Rayon fibres used by Milliken *et al.* [103, Fig. 2]

4.3 Numerical Simulation Method

4.3.1 Direct Simulation of Fibre Suspensions

The methods of Folgar and Tucker (Eq. (2.5)) and Advani and Tucker (Eq. 2.8) use stochastic components and so the fibre orientation should be seen as an orientation *probability*. Information of the motion of individual fibres in the suspension is not available with those methods. Direct simulation on the other hand is a very different method where the state of every fibre in suspension is known, and is determined through purely mechanistic theory. The trajectories of all suspension fibres are explicitly calculated numerically. Basic rules governing how fibres will translate, and interact with the suspending fluid and other fibres are defined. The fibres are then placed in a flow field and the position and orientation of every fibre is tracked with time. As fibres come in contact with obstacles or interact with another fibre, the rules governing the interaction behaviour determine how the fibre will react in that situation. As the simulation is run, many thousands or millions of interactions may take place and eventually structural evolution on a macroscopic level may be observed.

The direct numerical simulation used in this chapter was based on the simulation reported in Chapter 3. The numerical simulation reported in Chapter 3 was based on the work of Fan *et al.* [31] however the method was substantially modified to allow for flexible fibres instead of the standard cylindrical rigid fibre. The numerical method for the simulation discussed here is briefly reiterated in the following section, with additional detail concerning modifications relevant for the work in this chapter. It is advised that interested readers consult Chapter 3 for a complete description of the method.

4.3.2 Method

This simulation method is similar to that of Fan *et al.* [31]. Multiple fibres are placed in a simulation 'cell' containing a shear flow field. Each fibre is described by a unit vector **P**. Fibre centre of mass translation occurs in an affine manner. The rotation of **P** is described by Eq. 4.1, (this is another form of Jeffrey's equation).

$$\omega_\infty \approx \mathbf{P} \times \left[\frac{a_r^2}{a_r^2+1} \mathbf{D} \cdot \mathbf{P} - \frac{1}{a_r^2+1} \mathbf{D}^T \cdot \mathbf{P} \right] \tag{4.1}$$

Fibre interaction forces are calculated given their current relative position and velocity, and local flow conditions. These interactions include short range lubrication forces, and viscous drag with long range hydrodynamic effects. From these interaction forces, Fan *et al.* calculated an additional deviational rotation component which is added to that found using Eq. 4.1. All fibres are then translated and rotated for that timestep and the process is repeated for subsequent timesteps, thus the suspension evolves in simulation over time. Fan *et al.* use Ewald summation in their algorithm as a means of modelling for an infinite suspension.

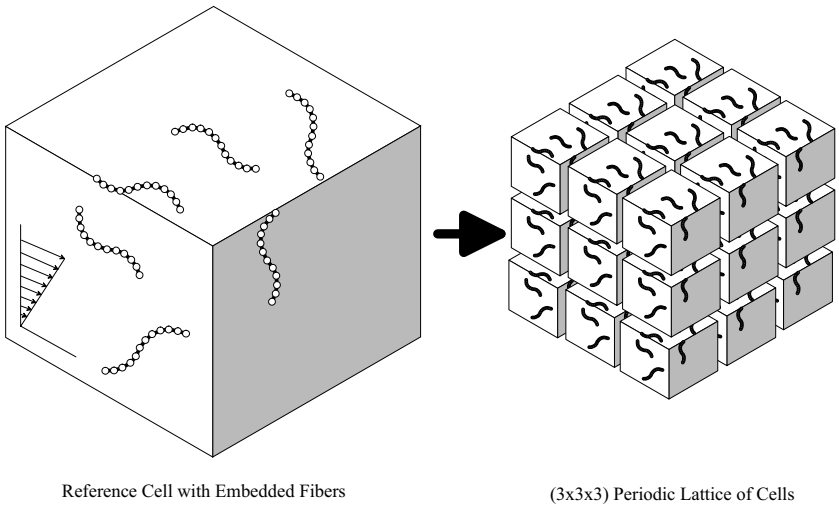

Figure 4.2: The reference cell and periodic repetition of the cell

The simulation reported in Chapter 3 is similar to Fan *et al.*'s [31], however the fibre model is changed and thus associated theories involving interaction forces are changed accordingly. Also an additional calculation is performed for fibre shape changes. Instead of Ewald summation to simulate an infinite suspension, duplicate cells are 'copied' on all sides of the simulation cell to create a lattice structure - see Fig. 4.2.

The rigid cylindrical rod of Fan *et al.* [31] is replaced with an inextensible chain of spheres linked with joints centered within each sphere, see Fig. 4.3. The joints have an elastic rotational stiffness which attempts to straighten

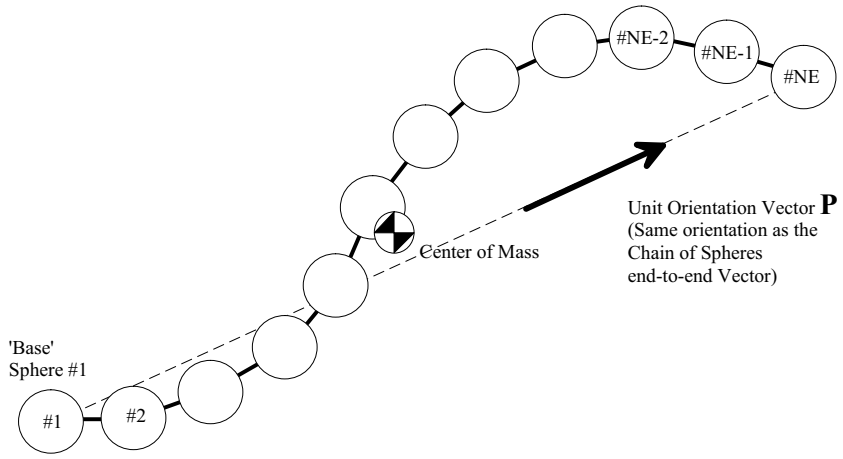

Figure 4.3: The Chain-of-Spheres fibre model used by Joung *et al.* (The deformation has been exaggerated for visualisation)

the joint if deflected. Internal bending moment $\mathbf{Y}^b_\nu$, torsion moment $\mathbf{Y}^t_\nu$, (see Fig. 4.4) and the bend and twist angles $\left(\theta^b, \phi^t\right)$ may be calculated for each joint using Eq. (4.2), given the Young's and shear moduli. θ^{eq} and ϕ^{eq} are the equilibrium bend and twist angle at the joint. For straight fibres $\theta^{eq} = \phi^{eq} = 0$.

$$\begin{aligned} \left|\mathbf{Y}^b_\nu\right| &= -k^b\left(\theta^b - \theta^{eq}\right) \quad \text{when} \quad k^b = \tfrac{EI}{2a} \\ \left|\mathbf{Y}^t_\nu\right| &= -k^t\left(\phi^t - \phi^{eq}\right) \quad \text{when} \quad k^t = \tfrac{GJ}{2a} \end{aligned} \tag{4.2}$$

Joint deflections are caused by fibre interaction forces. Fan *et al.* solved a slender body approximation for long range forces and a lubrication approx-

imation for close range interaction. In this simulation we do not use slender body approximation and instead apply long range interaction forces appropriate to spheres in viscous flow, as described in depth by Karilla and Kim [100]. For a moving sphere m, viscous drag force is described by Stokes Eq. (4.3),

$$\mathbf{F}_{visc\_m} = -6\pi\eta_s a \left[\mathbf{V}_m - \mathbf{V}_\infty\right] \tag{4.3}$$

where a is the sphere radius, $\mathbf{V}_m$ is sphere velocity and $\mathbf{V}_\infty$ is local fluid freestream velocity. Undisturbed freestream velocity $\mathbf{V}_\infty = \mathbf{D} \cdot \mathbf{r}_m + \mathbf{V}'_m$ is perturbed by the long range hydrodynamic effects of other suspension spheres via the $\mathbf{V}'_m$ term ($\mathbf{r}_m$ is the sphere position vector). This perturbation on a sphere m is the cumulative perturbation velocity from all other spheres n in the suspension, as described by Eq. (4.4),

$$\mathbf{V}'_m = \sum_n \mathbf{\Omega}_{mn} \cdot \mathbf{F}_n \tag{4.4}$$

where $\mathbf{F}_n$ is the drag force acting on all other suspension spheres n, and $\mathbf{\Omega}_{mn}$ is the Oseen tensor. The Oseen tensor is,

$$\mathbf{\Omega}_{mn} = \frac{1}{8\pi\eta_s \left|\mathbf{r}_{mn}\right|} \left\{\delta + \frac{\mathbf{r}_{mn}\mathbf{r}_{mn}}{\left|\mathbf{r}_{mn}\right|^2}\right\} \tag{4.5}$$

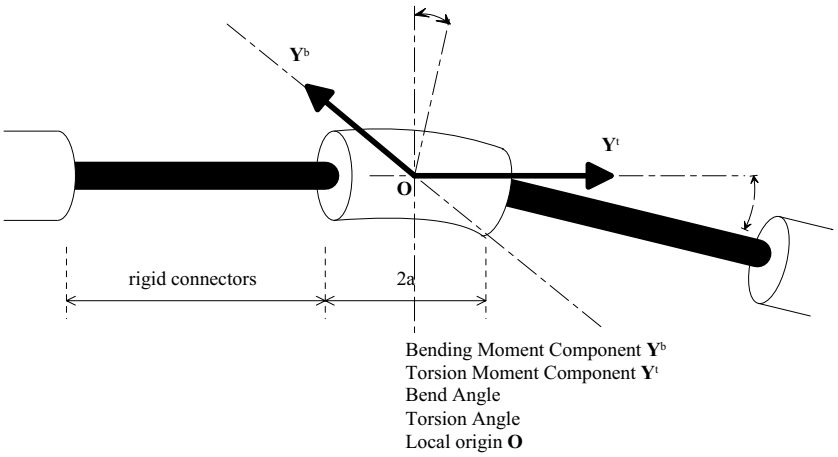

Figure 4.4: The joint linking connector segments

where $\mathbf{r}_{mn}$ is the relative position vector between spheres m and n in suspension.

Short range lubrication forces are calculated using Eq. (4.6)

$$\mathbf{F}_{lub\_mn} = -3\pi\eta_s \frac{a^2}{h-2a}\mathbf{V}_{sqz} \tag{4.6}$$

where $\mathbf{V}_{sqz}$ is the relative 'squeezing' velocity between spheres m and n given by,

$$\mathbf{V}_{sqz} = \left[\frac{\mathbf{r}_{mn}}{|\mathbf{r}_{mn}|}\right]\left(\frac{\mathbf{r}_{mn}}{|\mathbf{r}_{mn}|}\cdot[\mathbf{V}_n - \mathbf{V}_m]\right) \text{ and } h = |\mathbf{r}_{mn}|$$

The simulation proceeds as follows. The end-to-end vector of the bead-chain is taken to be the vector $\mathbf{P}$. Once the fibre rotation and translation rates are known, their new position and orientation are calculated for the current iteration as per the description above. Following this stage, the vector $\mathbf{P}$ is overlaid by the chain of beads. Since the interaction forces are known through Eqs. (4.3) and (4.6), an additional calculation based on Eq. (4.2) is performed to determine the deflection of the bead-chain along the fibre length. Hence at each timestep, fibres may also deform in response to flow conditions and interactions. Fibre deformation effectively results in another small rotation in the end-to-end orientation vector $\mathbf{P}$. Any bulk properties observed to change with stiffness moduli may thus be attributed to flexibility effects.

Finally a stress rule is required to calculate the bulk properties given the suspension microstructure. The total stress tensor is,

$$\sigma_{bulk} = \sigma_{solvent} + \tau_{fibre} \tag{4.7}$$

The solvent stress component is,

$$\sigma_{solvent} = -p\delta + \eta_s \cdot \dot{\gamma} \tag{4.8}$$

where p is hydrodynamic pressure. The remaining particle contributed stress τ_{fibre}, is appropriately expressed for fibre suspensions by the Transversely Isotropic Fluid equation (TIF) developed by Ericksen [9] and Hand [10]. An

improved version by Phan-Thien and Graham [53] (*TIF-PTG*) is,

$$\tau = 2\eta_s \left\{ \mathbf{D} + f(\phi, a_r)\mathbf{D}\colon \langle \mathbf{PPPP} \rangle \right\} \tag{4.9}$$

where,

$$f(\phi, a_r) = \frac{a_r^2 \phi \left(2 - \frac{\phi}{G}\right)}{4\left(\ln(2a_r) - 1.5\right)\left(1 - \frac{\phi}{G}\right)^2} \quad G = 0.53 - 0.013a_r \quad 5 < a_r < 30$$

From the stress tensor we find suspension relative viscosity η_{bulk} and the first and second normal stress difference coefficients, Ψ_1, Ψ_2 from the relations,

$$\tau_{yx} = \eta_{bulk}\dot{\gamma}_{yx} \quad \tau_{xx} - \tau_{yy} = \Psi_1 \left(\dot{\gamma}_{yx}\right)^2 \quad \tau_{yy} - \tau_{zz} = \Psi_2 \left(\dot{\gamma}_{yx}\right)^2 \tag{4.10}$$

4.3.3 Modifications for the Rigid Curved Fibre Simulation

The simulation as described above allows the joints along the sphere-chain to bend and twist. For the simulation reported here, the fibre is rigid and so the algorithms involved with joint bending are disabled and bend angle is fixed. Bend angle at each joint along the fibre was set equally such that the accumulated angle from one end to the other ranged from $2^\circ < \left[\theta_{fibre} = \sum_{joint=2}^{NoBeads-1} \theta_{joint}\right] < 40^\circ$. Fibres of varying curvature are shown in Fig. 4.5.

Each simulation 'run' contained fibres curved to the same degree. No mixed suspensions with varying curvature fibres were run. These fibres were simulated in shear flow and suspension viscosity was calculated using the TIF-PTG Eq. (4.9) over varying volume fractions and varying curvature angles.

Appropriate use of the TIF stress equation on curved fibres

In justifying the appropriateness of using the TIF stress Eq. (4.9) on these curved fibres, we appeal to the work of Hinch [50] for flexible, inextensible

threads. Hinch presented Eq. (4.11) for thread tension.

$$T = \mathbf{p} \cdot \mathbf{E} \cdot \mathbf{p} \frac{1}{2} \left(L^2 - s^2 \right) - 2\varepsilon \mathbf{p} \cdot \mathbf{E} \cdot \left(\int_{-L}^{s} \mathbf{y} - \frac{s+L}{2L} \int_{-L}^{L} \mathbf{y} \right) \tag{4.11}$$

where using the notation of Hinch, T is thread tension, L is half the fibre length, s is the length variable along the fibre centreline, ε is the magnitude of the deflection and $\mathbf{y}(s)$ is the shape function of the thread as a function of s.

Let us describe the arc of the curved fibre in this simulation with the fundamental mode shape $y(s) = \varepsilon \cos\left(\frac{\pi}{2L} s\right)$. If the fundamental mode shape is substituted into Eq. (4.11) and integrated, we get for the second term, $\frac{2L}{\pi} \sin\left(\frac{\pi}{2L} s\right) - \frac{2s}{L}$. Since the stress contribution from the fibre is proportional to the integral of tension along the entire fibre length, we may substitute $s = L$ into the resulting integral. The integral goes to zero, and hence the entire second term of Eq. (4.11) goes to zero. The first order $O(\varepsilon)$ effects on tension (and hence stress) for the curved fibre is zero. Therefore the errors associated with using the TIF equation on these curved fibres are sufficiently small as to be considered negligible (second order in deflection magnitude, $O(\varepsilon^2)$ or smaller).

While errors associated with the use of TIF may be acceptably small it is however acknowledged that many other theories used for this work were also intended only for straight rods. Therefore as in [87] our confidence in

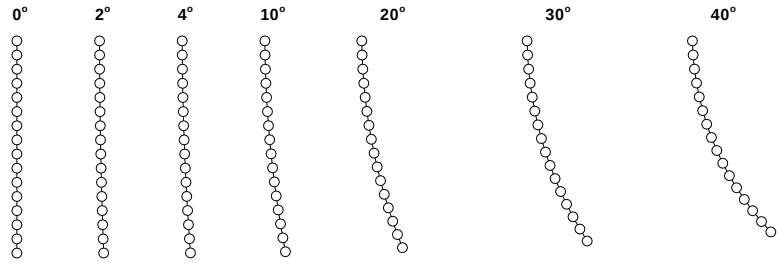

Figure 4.5: Curved Chain-of-Sphere fibres. Curve angle from $2° < \theta_{fibre} < 40°$

the results decreases as fibres increasingly deviate from dead-straight. In the Results section §4.4, one should note that as curvature increases, our estimate for viscosity will become inaccurate. This should be kept in mind particularly while reviewing Figs. 4.8 and 4.10. However by the same token the inaccuracies reduce to zero with curvature and so the pronounced effects shown in Figs. 4.8 and 4.10 for *low* curvature are not invalidated by the 'nearly straight' fibre assumption.

4.3.4 Conditions

The main conditions imposed on this simulation are,

- The solvent is a Newtonian fluid.
- Velocity gradients are homogeneous.
- Beads and fibres are of dimensions such that Brownian effects are negligible.
- The suspension is assumed to meet conditions set by Batchelor [11] such that an ensemble average of the fibre population is a valid procedure to produce the required bulk properties.
- Flow field and fibre orientation are de-coupled.
- Beads and fibres are force and torque free at all times. Flow rates are sufficiently slow that inertial effects are negligible.
- All fibres are identical in connectivity configuration *and* shape.

To elaborate on the fourth condition, Batchelor [11, Section §3] assumes the state of some quantity can be adequately estimated from a single sufficiently extensive realization. Hence an ensemble average over some region in space may be taken to be equivalent to the integral average of the same quantity over any spatial coordinate with respect to which the quantity is statistically stationary. It is assumed in this work that the dimensions of the reference

simulation cell are sufficiently large, and the number of fibres used in simulation are sufficiently great, so as to allow valid averages for stress, viscosity or any other quantity derived from averaging. Furthermore it is assumed that any quantity derived by averaging within the reference cell is representative over the entire infinite suspension since the quantity is assumed statistically stationary in space.

On the second and fifth conditions, it has been shown that the presence of particles in a flowing fluid will alter the development of the flow field (Lipscomb *et al.* [108]). In this simulation it is assumed that fluid velocity field is unaffected by the motion and orientation of fibres. The errors associated with this assumption would presumably decrease as fibre concentration is reduced. In light of Lipscomb *et al*'s work this assumption however is not entirely correct. These effects have not been considered at this time and thus it must also be assumed that the main focus of this chapter, the viscosity-curvature phenomenon discussed in Section §4.4 is independent of the flow-fibre de-coupling assumption.

4.3.5 Simulation initial conditions

As shown in Fig. 4.3, one end of the fibre is arbitrarily chosen as the 'base' and beads and connectors are numbered from that base. Parameters used throughout this work are chosen such that all results are non-dimensional, all lengths are relative to the bead radius $a = 1$.

The basic suspension information is established before commencing. These include terms such as the number of fibres, number of beads, unit bead radius $a = 1$, fibre length, and type and magnitude of flow, e.g., shear flow, with shear rate $\dot{\gamma}$, or extension with extensional rate $\dot{\epsilon}$.

The initial fibre suspension is then placed in the reference cell. Fibres are oriented randomly and initial fibre velocity and rotation rate is set to be equal to that of the freestream fluid in the locality of the fibre. Care is taken to ensure that no fibres are overlapping before commencing the simulation. For shear flow the simulation is typically run for, $0 \leq \gamma \leq 1000$. The increment

is $d\gamma = 0.01$, with a unit shear rate of $\dot{\gamma} = 1$. For each iteration, information such as the fibre centre of mass, end-to-end vector $\mathbf{P}$, global bead positions $\mathbf{r}_m$, bead velocity $\mathbf{V}_m$, and external force $\mathbf{F}_m$ are determined. From this information the suspension orientation state is known and hence the bulk properties can be calculated.

When a fibre translates beyond the reference cell it is repositioned so that it continues its motion from the other side of the cell. That is, the fibre re-enters the cell immediately after it has exited, hence maintaining the suspension volume fraction.

The simulation was written in Fortran77 and was compiled and executed on a Digital Alphastation 500 in the SyDCom[1] computing facility. Execution time for 100000 iterations ranged from several hours to several days or weeks depending on the volume fraction and periodic depth.

4.4 Results

In this section the results for curved rigid fibre suspensions are presented. Viscosity data is presented as a function of curvature for varying concentrations. The fibres used are always of aspect ratio $a_r = 16.9$ to allow comparison with equivalent experimental data by Bibbo [104], and numerical data by Fan *et al.* [31]. The number of spheres in a fibre is always $NE = 16$, and bead radius $a = 1$. The suspension concentration is controlled by varying the number of fibres within the reference cell. The suspension is sheared at the rate $\dot{\gamma} = 1$ with solvent viscosity normalized to $\eta_s = 1$. End-to-end curvature of the fibres range from $2^\circ \leq \theta_{fibre} \leq 40^\circ$. Although the use of Eq. (4.1) is increasingly inaccurate at curvatures as large as 40°, results at this curvature magnitude are included in the results for completeness. While the viscosity trends as curvature increases to 40° may be interesting for speculative purposes, the reader should be cautious about making definite conclusions at these larger angles.

[1]Sydney University Distributed Computing Facility

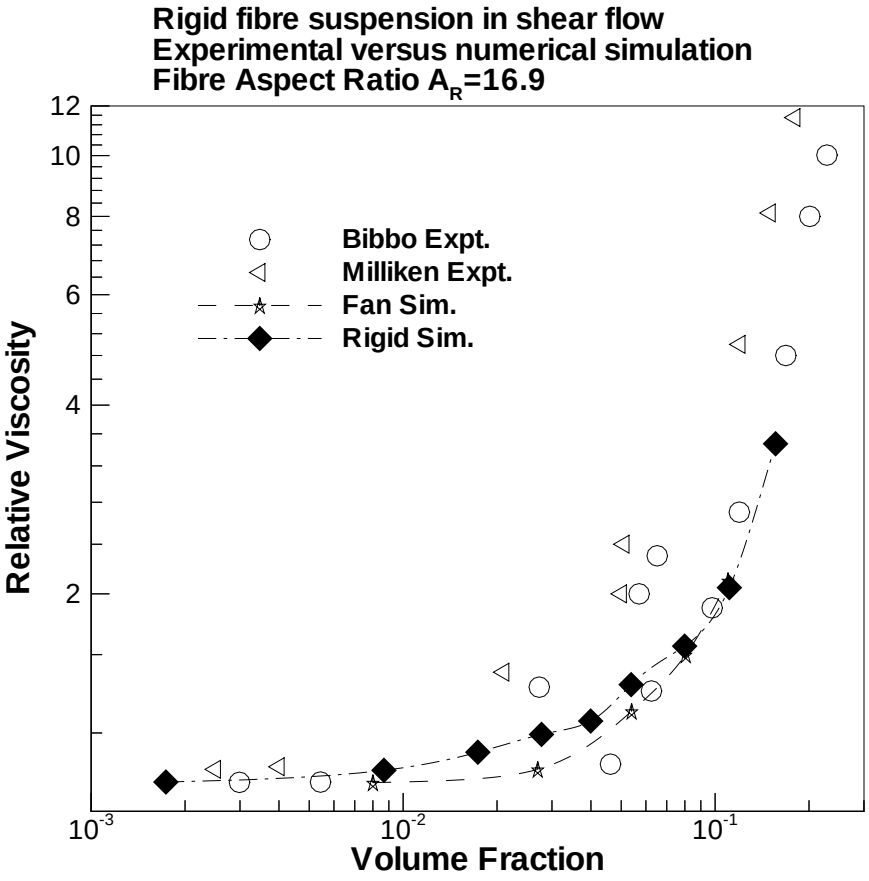

Figure 4.6: Experimental versus numerical simulation comparison for straight rigid $a_r = 16$ fibres. Bibbo (◯) and Milliken *et al.* (◁) results are experimental while Fan *et al.* (★) and the current results (⧫) are numerical simulation results.

4.4.1 Curved Fibre Suspension - η_{bulk} sensitivity to curvature

Fig. 4.7 compares the same 'straight' fibre simulation result against progressively more curved fibre simulation results. This result is in agreement

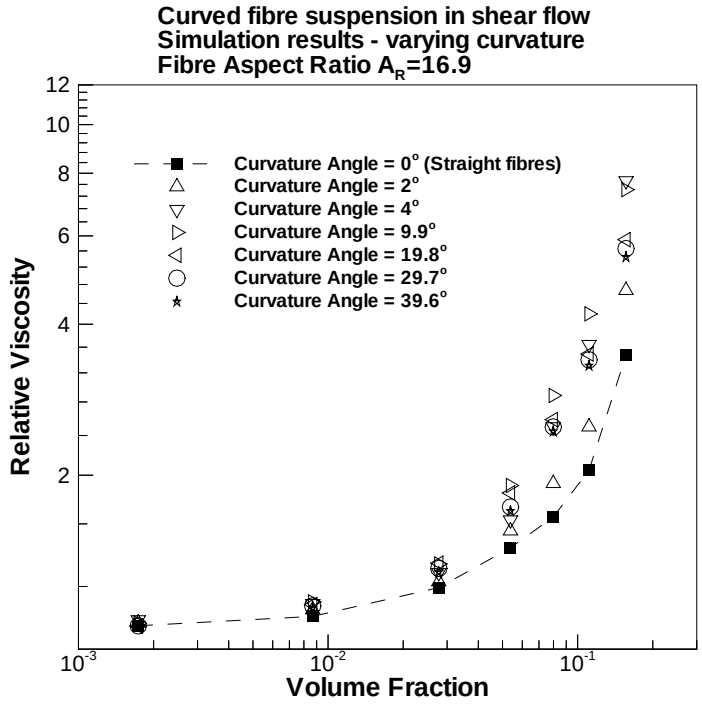

Figure 4.7: Simulation results for varying fibre curvature. Curved fibre suspensions (hollow symbols) consistently result in higher viscosity than straight fibres (■).

with the earlier premise that curvature in the fibre is a significant contributor to the elevation in viscosity over straight fibre suspensions. Over the entire volume fraction range and for all curvatures tested, there is a large increase in the viscosity. Furthermore, the curved fibre viscosity magnitude is in fact quantitatively improved when compared with the experimental results of Bibbo (◯) (compare with Fig. 4.6).

Fig. 4.7 does not reveal the relationship between suspension viscosity and fibre curvature. In Fig. 4.8, relative viscosity is plotted against fibre

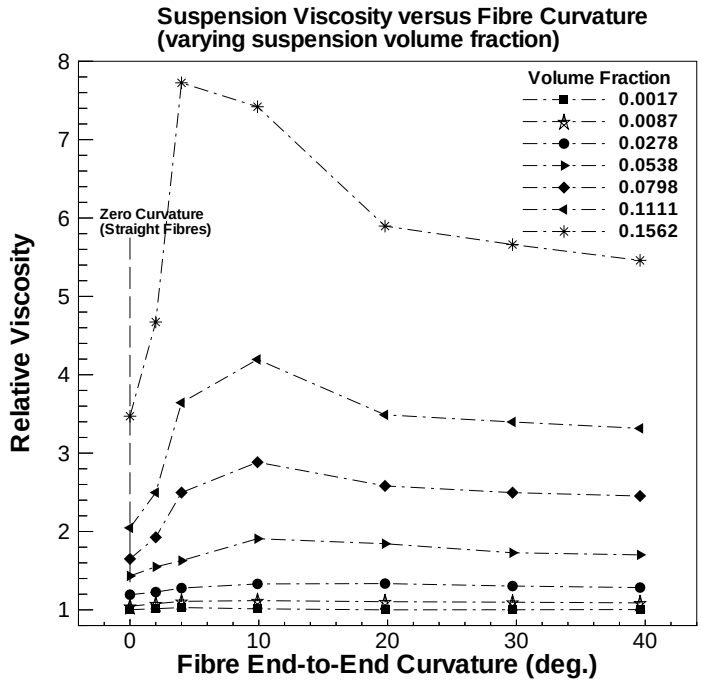

Figure 4.8: Suspension relative viscosity versus fibre end-to-end curvature, for varying suspension volume fractions. The fibres are rigid with $a_r = 16.9$, Number of beads per fibre = 16. The suspension contains a population of 100% identically curved fibres.

curvature for varying suspension concentrations. The viscosity data features a peak for rather small curvature angles in the range $5^\circ < \theta_{fibre} < 10^\circ$. Beyond this, viscosity reduces in magnitude and appears to converge to a value much larger than for straight fibres (although we can expect results to become inaccurate at large curvatures).

Fig. 4.8 reveals a peculiar phenomenon where viscosity rises rapidly for very small curvature angles. The gradient of curves in Fig. 4.8 at zero fibre curvature is non-zero and is in fact quite steep. It is also noted that the proportional increase in viscosity, as curvature deviates from 'dead-straight', is more pronounced for higher volume fractions. For example the highly concentrated fibre suspension of volume fraction $\phi = 0.1562$ (symbol (⋇) in Fig. (4.8)) has a relative viscosity of $\eta_r \approx 3.5$ when fibre curvature is $\theta_{fibre} = 0^\circ$ (dead straight), but for a small curvature of $\theta_{fibre} = 4^\circ$, relative viscosity jumps to $\eta_r \approx 7.7$. The relative viscosity is approximately twice the magnitude of the 'dead-straight' result and for the same curvatures, this order increase is approximately consistent over all the tested volume fractions. This magnitude of viscosity increase is reminiscent of Nawab and Mason's [91] observed experimental viscosity of order three times the theoretical predictions (as discussed in Section §4.2). Fibre deformations may very well have played an important part in their result.

This result demonstrates the extreme sensitivity of the suspension viscosity to fibre shape imperfections. For a seemingly small shape distortion, the effect on viscosity is dramatic. Suspension viscosity appears to reach a maximum at a very small curvature. Beyond this critical curvature angle the viscosity reduces markedly again. This behaviour would pose the following problem to experimental researchers attempting to produce accurate reproducible viscosity results. First, great care must be taken so that fibre samples are well prepared. Tolerance to bent fibres and other deformation is low and consequences of using imperfect fibres are severe. Yet as we can see from a snapshot of a typical suspension by Milliken *et al.* [103] (Fig. 4.1), small curvatures are not uncommon despite the care taken by Milliken in

preparing fibre samples. Second, results cannot be improved much by simply removing the most extremely bent fibres from the sample. As we have seen, the greatest effects occur for curvatures of only $5° < \theta_{fibre} < 10°$. One would have to undertake the much more arduous task of removing all fibres with curvature beyond say, 1°. Last, one can expect more flexible fibre materials to deform more than stiffer ones. Therefore, for consistency, stiffer fibres are preferable to more flexible fibres. Likewise for fibres of greater aspect ratio (whereby the tendency to flex is greater than for shorter stout fibres), stiffer fibres are preferable when consistently reproducible viscosity is desirable.

4.4.2 Viscosity-Curvature Curve Fitting

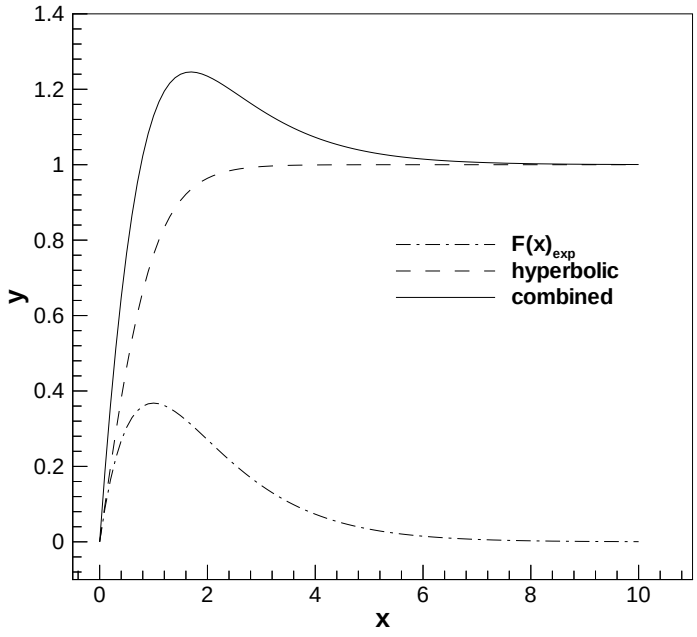

Figure 4.9: The $F(x)_{\text{exp}}$ and hyperbolic components, and the combined result

The data as presented in Fig. 4.8 cannot be fitted easily by a low order least square polynomial fit. Instead it is better described with a combination

of hyperbolic and $F(x)_{\exp}$ functions (where $F(x)_{\exp}$ is of the form $F(x)_{\exp} = xe^{-x}$). Fig. 4.9 shows the two individual components and the resultant sum of these two parts. The resulting empirical equation fitted to the simulation data is,

$$\eta_{bulk}(\theta_{fibre}, \phi) = \epsilon\theta_{fibre}e^{\left(-\alpha\theta_{fibre}-\zeta\right)} + \delta\frac{e^{\beta\theta_{fibre}} - e^{-\beta\theta_{fibre}}}{e^{\beta\theta_{fibre}} + e^{-\beta\theta_{fibre}}} + \gamma \tag{4.12}$$

where the coefficients, α, β, γ, δ, ϵ and ζ are functions of volume fraction ϕ in the range, $0 \leq \phi \leq 0.16$,

$$\begin{gathered}
\alpha(\phi) = \tfrac{0.0007}{\phi} + 1.2\phi + 0.005, \\
\beta(\phi) = 4.2828\phi^2 - 0.1138\phi + 0.0022, \\
\gamma(\phi) = 8904.6471\phi^4 - 1716.2639\phi^3 + 118.8461\phi^2 + 5.2429\phi + 0.9922, \\
\delta(\phi) = -747.8328\phi^3 + 237.5086\phi^2 - 8.4300\phi + 0.3531, \\
\epsilon(\phi) = \tfrac{0.01}{\phi} - 1.5\phi + 2, \\
\zeta(\phi) = 153.3682\phi^2 - 61.5718\phi + 5.8786.
\end{gathered} \tag{4.13}$$

Eq. (4.12) fits most of the simulation data well as can be seen in Fig. 4.10. One should note that fibre aspect ratio and bulk properties are related. Therefore the constants presented in Eq. (4.13) are applicable only for fibres with aspect ratio $a_r = 16.9$. The actual form of the viscosity-curvature relationship for all fibre aspect ratios and curvatures is yet to be found. This curve fit is presented simply as a glimpse into the true nature of this relationship.

We may expect that at any time in shear flow a certain proportion of fibres are permanently bent. A certain percentage may also acquire bends due to mechanical interaction or thermal gradients (warpage). The steep gradient of the viscosity-curvature curve at low curvature angle reveals the sensitivity of suspension viscosity to even the slightest curvature in fibres. The wide scatter in existing experimental viscosity data may well be caused by minor fibre shape imperfections.

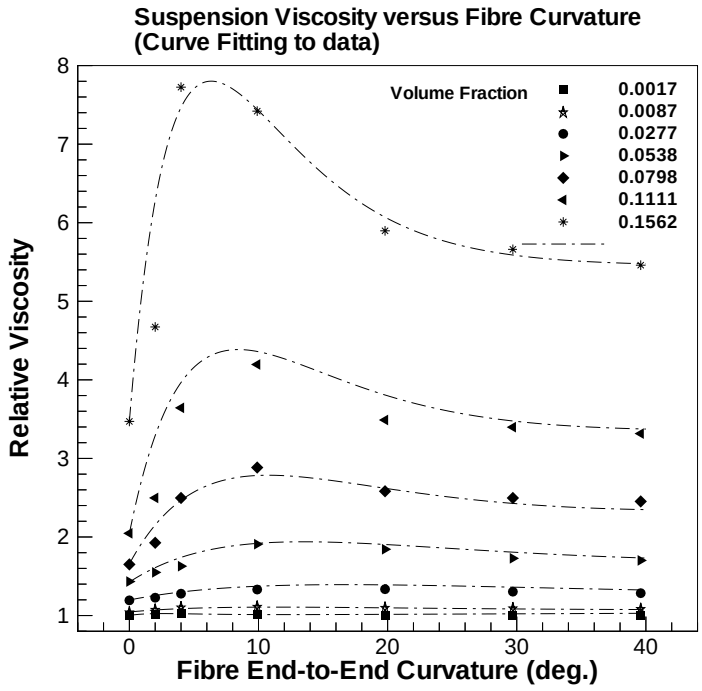

Figure 4.10: Curve fitted equation plotted with simulation results ($a_r = 16.9$). The computations were not continued beyond 15% volume fraction because of excessive computational time required

4.5 Discussion and Conclusion

This work studied the importance of fibre shape in sheared fibre suspensions. The initial hypothesis was that small deformities in the fibres of a suspension can produce a noticeable effect on suspension viscosity. In this work, fibres were directly simulated in Newtonian shear flow for varying volume fraction and varying fibre curvature θ_{fibre}, and the bulk viscosity was observed.

It was found that there was a rapid and large increase in bulk viscosity as fibre curvature was increased. The viscosity - curvature relationship can be fitted to a single Eq. (4.12) given volume fraction and fibre curvature (for fibre aspect ratio $a_r = 16.9$ only).

The curious form of the curvature-viscosity relationship (Fig. 4.10) leads one to ask the obvious question of why this happens. The answer is unknown, but a speculative discussion is offered. It is acknowledged that fibre alignment is central to the resulting viscosity of a fibre suspension. Briefly, fibre misalignment increases interaction activity and encourages further misalignment. The resulting suspension is more resistant to flow and so a viscosity increase is measured. When a single infinite aspect ratio fibre has aligned to shear direction it presents *no* profile in the shear direction. Theoretically it will remain aligned indefinitely. A curved fibre however does present a profile in the shear direction. The more curved a fibre, the larger the profile seen in the shear direction. Therefore regardless of aspect ratio it does not remain aligned indefinitely. Curved fibres in suspension will not exhibit as strong a tendency to remain aligned to shear flow as does a straight fibre suspension. Curved fibres are less able to pack neatly into dense aligned structures than straight fibres. Therefore a curved fibre suspension has a propensity to misalignment and hence we see a viscosity increase with curvature. This cannot however explain the subsequent viscosity decrease beyond approximately $\theta_{fibre} = 10^\circ$ curvature angle. It is yet to be seen whether the behaviour in that region also reflects a truly physical phenomenon or is merely the result of theoretical or numerical inadequacy.

The implications are of particular importance to experimenters in fibre

suspensions. It would appear that the viscosity (and possibly other bulk properties) are highly sensitive to the quality control maintained in preparing the fibre samples. The rapid increase in bulk viscosity as seen in Fig. 4.10 shows that even a small deviation from 'dead straight' fibres, or the use of highly flexible fibres, or highly elongated fibres (large aspect ratio fibres are more prone to bending) will result in large deviations in bulk property. Further, one simply cannot remove the most deformed from the fibre samples in the hope of reducing this viscosity increase. From the results shown in Fig. 4.10, it appears that the fibres which contribute most to the increase are those with a relatively mild curve of the order $O(5^\circ$ to $10^\circ)$.

Summary: Part II

In **Part II** the first of two new direct simulation methods was presented. The fibre simulation was based on the new 'Chain-of-Spheres' fibre model. Part II clearly shows the ability of this method to accurately estimate suspension bulk viscosity. We have seen estimations for viscosity over a range of volume fractions and also over a range of fibre stiffness.

The ability to account for fibre deformation proved to be particularly useful as it allowed for the simulation of particular details of fibre motion, for example, orbital drift to vorticity axis, 'S' shape configurations and shape evolution with shear, which have so far only been implied by theory, and seen before only in other flexible fibre direct simulations. The viscosity predictions were seen to more accurately match equivalent experimental data when fibre flexibility was accounted for.

The relationship between fibre stiffness, and bulk viscosity was characterized for the first time using this method. Lastly we have seen an indication as to the level of sensitivity of suspensions to fibre shape imperfections. The suspension viscosity was noted to approximately *double* as only mild curvatures of 4° were introduced.

In **Part III**, we move away from the prediction of bulk properties and focus closer on the motion of individual particles. A new, more capable simulation method is presented featuring the ability to model the motion of particles of arbitrary shapes, within arbitrarily complex flow fields.

Part III

Three Dimensional Fibre Simulation

Chapter 5

Single Particle Dynamics in Shear Flow

5.1 Introduction

Part III (Chapter 5 to 7) describes a new direct simulation created for the modelling of *arbitrarily shaped* particles in Newtonian fluid. To date, particle shapes used in simulation have been restricted to simple axially symmetric cylinders, ellipses, spheres or discs. Like the simulation used in Part II, the new simulation method is based on the Stokes law for viscous drag on a sphere, and uses spherical 'subunits' as the building blocks of greater complex structures. Within this framework, arbitrarily shaped particle structures may be designed and created with little effort.

In this chapter, the simulation is used to study the single particle dynamics of various shapes in Newtonian shear flow. Known and unknown shape-dependent particle behaviour is demonstrated, and when available, is tested against existing theories or observations.

In Section §5.2, a modification and extension of the sphere-chain style of simulation is described. This new simulation is similar to the PSM of Yamamoto and Matsuoka (referred to in Section §2.2.1). The main difference is the extended linkages allowed for each subunit sphere. Each sphere

may be linked to a maximum of 30 other spheres. Previous simulations allowed subunits only two bonds each (i.e. end-to-end) effectively allowing only thread-like structures to be made (with the exception of Yamamoto *et al.*'s four bonded spheres in [34] and [72]). With the increased number of bonds allowed, truly three dimensional particle structures may be constructed. For example, many filler particles are planar in form. Planes and various other shaped particles were chosen for investigation. Irregular, non-symmetrical particles may be simulated as easily as conventional spheres, ellipsoids, cylindrical fibres and oblate discs. The motion of these familiar shapes in shear flow will be revisited, as well as a brief look at the motion for some new complex particle shapes. This 3D sphere-chain simulation is also capable of modelling fibre dynamics embedded within realistic complex flow fields. The focus of the work in Chapters 6 and 7 is on fibre flow through two complex flow fields.

5.2 Numerical Method

While multi-body style simulations are generally very powerful, the specificity of some model designs described in Section §2.2.1 restricts them to a very limited range of applicability. For example, the *ball-and-socket* model of Skjetne *et al.* [33] was designed in part to reduce the numbers of subunits required to assemble a given length of particle. This design however limited possible particle shapes to end-to-end linked chains only. It is also computationally expensive to keep track of all the necessary parameters in a ball-and-socket based simulation, see for instance, the discussion in §5.2.5 on calculating intraparticle torque.

From a programmer's perspective, the scope for applying the simulation to a wide variety of problems diminishes rapidly as the model specificity increases. Sphere-based models have an inherent isotropy, and sphere-based hydrodynamics have a simplicity which allows scope for expansion. This is evident from the numerous PSM variants Yamamoto *et al.* have published.

It was a secondary aim in this work to produce a simulation whose range of application was as wide as this genre allows. To this end, this current simulation is also sphere-based and wherever possible, complexity and specificity in theory or algorithm are minimized or substituted with simpler, or at least more widely applicable alternatives.

It will be shown subsequently how complex and realistic particle motion can arise from quite simple theories and algorithms, based on the application of as little as three simple rules for viscous drag, internal force and internal torque between linked spheres.

5.2.1 The 3D Particle

For the purposes of this discussion, the suspension particles will be referred to as *particles*, and the spherical building blocks used to construct particles as *subunits*. Particles of different shapes, bond arrangements or mechanical characteristics are said to belong to different *species*. Within the particle, subunits may be positioned in space arbitrarily. Unlike Yamamoto *et al.*'s PSM, subunits are not bonded by direct contact, but instead by 'elastic'[1] bonds over short distances (any distance is in fact possible however physical limitations apply, see Section §5.2.5). Subunits are allowed a maximum of 30 *bonds*, to any other subunits within the particle. Only subunits interact with each other or with the suspension medium. One is not concerned with subunit-bond or bond-bond intersections during particle design. By the careful arrangement of subunits and bonds, arbitrarily shaped 3D particles may be conceived in a manner akin to the design of spaceframe structures.

An example of a basic particle shape is the torus shown in Fig. 5.1. In this case, the torus is constructed from a hexagonal cross section. Six subunits occupy each perimeter node of the hexagon, with a seventh at the centre. The cross section is rotated at 30° intervals through a circular revolution to

[1] Although bonds have a finite stiffness and are based on elastic theory, the bond stiffness of particles used in this thesis are always set to 'high' values. It is assumed in this thesis that particles are always approximately 'rigid'. See Section §5.2.3

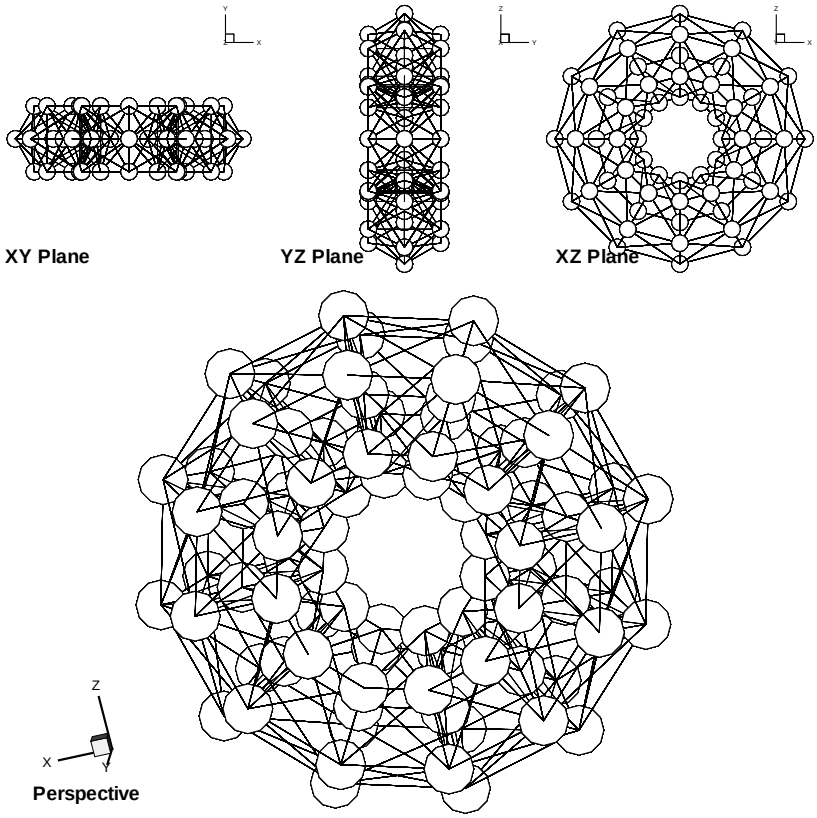

Figure 5.1: 3D Torus model, 84 spheres (spheres are not drawn to scale)

produce the torus shape. In the primitive shown in Fig. 5.1, the radius of revolution is twice the section radius. Coordinates of each subunit correspond to the nodal positions of the 3D framework. Each subunit's relationship to the larger structure is completely described by 94 parameters. These are, its individual identification number, its coordinates (relative to a local origin), identification numbers of other subunits with which it shares a bond (maximum 30), and each bond's non-dimensional Stiffness[2] (E_{sim}) and Shear Moduli (G_{sim}). For example, for a subunit i, 94 parameters as shown in Eq. (5.1) are required.

$$\left\{ \begin{array}{c} \textit{for bead } i: \\ ID_i, \\ (x,y,z)_i, \\ [ID_1, ID_2, \ldots, ID_{29}, ID_{30}]_i, \\ [E_1, E_2, \ldots, E_{29}, E_{30}]_i, \\ [G_1, G_2, \ldots, G_{29}, G_{30}]_i \end{array} \right\} \tag{5.1}$$

Hence to fully describe the structure and mechanical characteristics of the torus consisting of 84 subunits, an (84×94) *primitive* matrix is sufficient.

Each particle used is represented by a primitive matrix of this type. There is no limitation to the size of the primitive matrix (apart from those relating to computational resources and solution time), nor to the combination of different particle species in the same simulation run (e.g. heterogenous suspensions are possible). Particle mechanical strength may be modified by altering the Stiffness or Shear moduli (E_{1-30} and G_{1-30}) on a bond-by-bond basis within the primitive matrix[3]. As there is no concern over overlapping of bonds, it is conceivable that one may for example repeat bonds between

[2] Although bonds have a finite stiffness and are based on elastic theory, the bond stiffness of particles used in this thesis are always set to 'high' values. It is assumed in this thesis that particles are always approximately 'rigid'. See Section §5.2.3

[3] Although bonds have a finite stiffness and are based on elastic theory, the bond stiffness of particles used in this thesis are always set to 'high' values. It is assumed in this thesis that particles are always approximately 'rigid'. See Section §5.2.3

the *same* pair of subunits (ID_{1-30}) to locally double the material rigidity, or perform a combination of the two methods. The particles are then scaled, rotated and translated to an arbitrary initial position prior to simulation.

In the case of suspensions (multiple particles in the one simulation), the individual primitive matrices of each particle are compiled into a single global subunits matrix with globally re-numbered subunit ID_i. The simulation then treats the global subunits matrix in the same way it would a single primitives subunit matrix. In a heterogenous suspension for example, if there are 50 particles of species M, each with 25 subunits, and 100 particles of species N, each with 84 subunits, then the global subunits matrix will be of dimension, $([50 \times 25_{species\ M} + 100 \times 84_{species\ N}] \times 94)$. During simulation, the global subunits matrix is updated at each timestep to reflect the positions of each subunit. The global subunits matrix is an important internal dataset since it reflects the microstructure of the suspension. Contents of this matrix are extracted and stored in datafiles for postprocessing. In order to approximate a reasonably uniform material density and structural isotropy within particles, it is recommended that subunits are positioned, and their bonds made in regular patterns such as BCC or FCC configurations.

5.2.2 Non-Dimensionality

The radius and mass of the constituent subunits are by default $a = 1$ and $m = 1$, unless stated otherwise. All scales are made dimensionless. Subunit radius is taken as the unit length scale for all lengths in this simulation. Simulation moduli E_{sim} and G_{sim} are non-dimensionalised in a similar manner to the simulation in Part II, i.e. $E_{sim} = \frac{E}{\dot{\gamma}\mu}$ and $G_{sim} = \frac{G}{\dot{\gamma}\mu}$. Bulk viscosity is normalised against the solvent viscosity. All forces and torque are taken in their non-dimensional form, using non-dimensional components. The 'timescale' is correlated with non-dimensional shear.

5.2.3 'Rigid' Particles and Bond Stiffness

In most cases presented in this simulation, the bonds were made very stiff so that the simulation particles could be considered approximately, 'rigid'. The elastic theory is therefore only used in order to maintain internal rigidity and particle shape. While the simulation is technically capable of modelling flexible particles, particle flexibility is a complication which will not be studied in detail at this time. There are a few 'flexible' particle cases included in later results, however these results should been viewed separately from the rest of the results presented. They are included only for illustrative purposes for the interested reader.

Although the effect of particle flexibility is not studied at this time, the structure of the particles *are* based on elastic theory. Future studies involving flexibility (e.g. the effects of flexibility on orientation, dynamics and viscosity) is desirable, however these aspects are too complex to be studied here. Therefore, in lieu of substantial alteration to algorithms, it was decided that the simulation would remained unchanged, with the potential to model flexible particles in the future. For the purposes of this thesis, the particle 'rigidity' is maintained via the use of high stiffness moduli. In the following sections on force and torque (Section §5.2.5), the reader should be mindful that the internal forces and torques play very little part in the salient simulation results apart from maintaining the particle shape.

5.2.4 Inertia and Reynolds Number

The fluid is always assumed to be creeping flow. Therefore the fluid inertia is assumed to be negligible. Particle inertial effects however may apply, since the mass of subunits are non-zero. Proudman and Pearson [109] expanded the Navier-Stokes equations with inertial effects to obtain a highly accurate prediction for drag force around the sphere with a low Reynolds number. At a Reynolds number of 0.05 the drag predicted by the creeping flow Stokes law is only 2 percent less than the Proudman and Pearson expansion [110].

Many readers conform to the often referred to magnitude of $Re \lessapprox 10^{-4}$. By Happel and Brenners observation however, higher Re situations need not be immediately disqualified as inaccurate. '*The exact Reynolds number above which the neglect of fluid inertia constitutes a poor approximation depends, in the final analysis, on the accuracy required.*' [110, pp. 42]. A variation of the order 2% or even slightly larger, is perfectly acceptable in many cases, including those seen in this chapter. When more than a single characteristic dimension is used, Happel and Brenner note that Reynolds numbers significantly greater than unity are possible without inertial effects being appreciable. Also, they note that phenomena arising from inertia are lost in the creeping motion assumption. It is argued that the continued use of the Stokes drag force law in the low Reynolds number range is perfectly acceptable for this simulation. In any case, in later results (e.g. see Section §5.3.4), the effect of various Re values for simulation particles will be studied. In this study, appropriate Re ranges will be determined for minimised inertial effects. It will be shown that particles used throughout Part III of this thesis are mostly unaffected by inertial effects.

While inertial effects are not the main focus of this work, Eqs. 5.2 and 5.3 include the inertial terms and so the equations of motion are capable of accounting for inertial effects. Some subunits in the results reported in this chapter may experience conditions where Reynolds numbers are higher than $Re = 10^{-4}$. Reynolds numbers however generally remain in the low Reynolds number range (e.g. $Re_{low} < 1$). In fact, some preliminary results to come show that higher Reynolds numbers are sometimes experienced without results noticeably deviating from equivalent creeping flow based theory.

5.2.5 Equations of Motion

The simulation discussed in this chapter is posed at the level of the spherical subunit and not the particle itself. Particle motion, orientation and deformation arise only as a consequence of the cooperative movement of the group of subunits. The movement of subunits are influenced by the flow field of

the suspending medium, interparticle interactions, and intraparticle bonds to other subunits. These influences are manifested as forces and torques on subunits from which the simulation calculates a trajectory over successive timesteps. Forces and torques between subunits are calculated on a cumulative pairwise basis. As is customary in Stokesian Dynamics [75], the additivity of pairwise interactions is assumed in order to improve computational time. The equations of motion are based on Eqs. 2.16 and 2.17, and include inertial components. They are restated here as Eqs. (5.2) and (5.3) for convenience.

$$m\frac{d\mathbf{v}}{dt} = \left(\mathbf{F}^h\right)_{viscous} + \left(\sum \mathbf{F}^i\right)_{intraparticle} + \left(\sum \mathbf{F}^p\right)_{interparticle} \tag{5.2}$$

$$\left(\frac{2}{5}ma^2\right)_{sphere}\frac{d\mathbf{w}}{dt} = \left(\mathbf{T}^h\right)_{viscous} + \left(\sum \mathbf{T}^i\right)_{intraparticle} + \left(\sum \mathbf{T}^p\right)_{interparticle} \tag{5.3}$$

It is worthy to note that of most existing multi-body simulation variants, a great deal of complexity is associated with accounting for the relative orientation between subunits - to solve for the torque components of Eq. (5.3). Past simulations usually required subunit-fixed local orientation vectors to be updated with each timestep in order to determine relative angular deflections and subsequent intraparticle torque (see Eqs. 5.10b, 5.10c and Figs. 5.3b, 5.3c). The trigonometric manipulation required is computationally expensive and prone to inaccuracy relative to other intrinsic operations. If it were possible to avoid solving Eq. (5.3) in favor of an alternative method, then the complexity of coded algorithms would be significantly streamlined and simulation time would be improved.

In the following sections, the method used for viscous, intraparticle and interparticle force and torque will be detailed. It will be shown how all components of Eq. (5.3) are eliminated or replaced with alternate methods. The resulting simulation method solves instead a streamlined version of the force Eq. (5.2) only. The reader is reminded to recall from Section §5.2.3 that except for the Stokes viscous drag force, these calculations are only used in this chapter to maintain particle shape, and hence internal flexibility is

mostly eliminated as a significant factor in any results.

Viscous Force and Torque

A spherical body moving through a Newtonian fluid experiences a drag force and torque resisting that motion (Fig. 5.2a). In this simulation, subunits are spherical and so, the drag force and torque on subunit i may be expressed by Stokes law for drag on a sphere, Eq. (5.4) and (5.5) respectively.

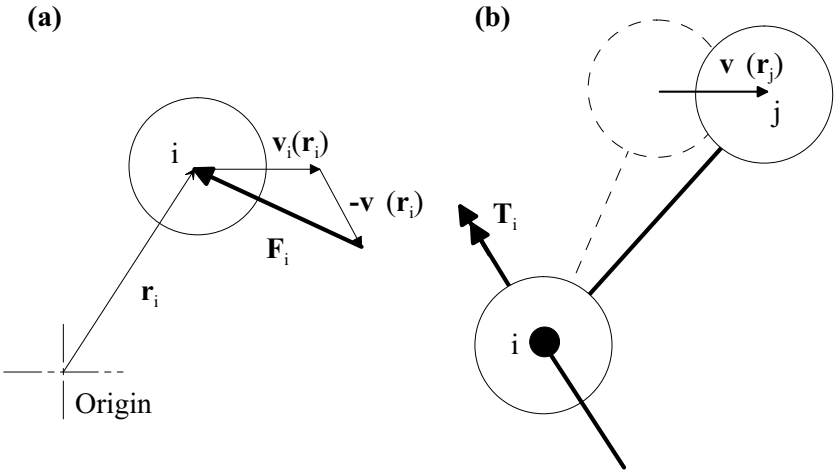

Figure 5.2: (a) Drag force on a sphere, (b) The rotation of the ij bond due to the drift of sphere j is equivalent to the rotation of the same ij bond due to an imposed torque on sphere i (excluding the extension of the ij bond).

$$\mathbf{F}_i^h = -6\pi\eta a \left(\frac{d\mathbf{r}_i}{dt} - \mathbf{v}_\infty(\mathbf{r}_i) \right) \tag{5.4}$$

$$\mathbf{T}_i^h = -8\pi\eta a \left(\frac{d\theta_i}{dt} - \mathbf{w}_\infty(\mathbf{r}_i) \right) \tag{5.5}$$

$\mathbf{v}_\infty(\mathbf{r}_i)$ and $\mathbf{w}_\infty(\mathbf{r}_i)$ are linear and angular fluid velocity at subunit i's global position, $\mathbf{r}_i$. θ_i is subunit i's current orientation. a is the spherical subunit radius and η is the fluid viscosity.

The force Eq. (5.4) is used as shown in the simulation, however the torque Eq. (5.5) is not. For all intents and purposes, a sphere that is rotated

is identical to the original unrotated sphere. The only discernible change while rotating this system of linked spheres is the orientation of the bonds to neighboring subunits. Assuming $\frac{d\mathbf{r}_j}{dt} - \mathbf{v}_\infty(\mathbf{r}_j) = \mathbf{0}$, Eq. (5.4) is used to calculate the *drift* of the neighboring subunit j. Ignoring for the time being the radial ij bond length change, the resulting orientation of the ij bond *due to the drift* of subunit j is equivalent to that found by directly rotating the rigid ij dumbbell about i with torque $\mathbf{T}_i^h$ from Eq. (5.5) (see Fig. 5.2*b*). Eq. (5.5) may be done away with all together as its effect is implied by the relative drift of neighboring subunits as calculated from Eq. (5.4). This reasoning depends on three conditions, (1) the Newtonian flow velocity field $\mathbf{v}_\infty$ varies linearly and mildly over the length scale of ij bonds, (2) the subunits are ideal non-slipping spheres where the centre of resistance is equivalent to the centre of mass, and (3) At some other stage, the radial ij bond length change is compensated for. This compensation comes in the form of an intraparticle extensional bond stiffness rule (Section §5.2.5). With reasonable particle designs (Section §5.2.1), these conditions will be met for most cases. The $\left(\mathbf{T}^h\right)_{viscous}$ component of Eq. (5.3) may thus be entirely eliminated from the simulation.

Long Range Hydrodynamic Interaction

In Eq. 5.4, the freestream velocity term, $\mathbf{v}_\infty$ is composed of the *undisturbed* macroscopic freestream velocity, $\mathbf{V}_\infty = \mathbf{K}\cdot\mathbf{r}$ (where $\mathbf{K}$ is the velocity gradient tensor and $\mathbf{r}$ is the position in the flow), and a long range wake disturbance accumulated from the motion of other spheres in the suspension, $\mathbf{V}'$. That is Eq (5.6),

$$\mathbf{v}_\infty = \mathbf{V}_\infty + \mathbf{V}' \tag{5.6}$$

As in Eqs. (3.7) and (3.8) in Part II, the Oseen tensor is used in this instance to determine the velocity disturbance at a sphere n due to the wake from another sphere m. Eqs. (5.7) and (5.8) are restated here for convenience.

$$\mathbf{\Omega}_{mn} = \frac{1}{8\pi\eta\left|\mathbf{r}_{mn}\right|}\left\{\delta + \frac{\mathbf{r}_{mn}\mathbf{r}_{mn}}{\left|\mathbf{r}_{mn}\right|^2}\right\} \tag{5.7}$$

$$\mathbf{V}'_n = \sum_m \mathbf{\Omega}_{mn} \cdot \mathbf{F}_m \tag{5.8}$$

Eqs. (5.7) and (5.8) are substituted into Eq. 5.6 to obtain $\mathbf{v}_\infty$, including the small influence of long range hydrodynamic interactions. In simulation the forces from the previous iteration are used in Eq. (5.8).

In the results section, data will be presented for simulation runs with and without hydrodynamic long range interaction. While long range hydrodynamic interaction *is* by default implemented here (unless stated otherwise), the computational load added by including this feature is highly prohibitive. At very high concentrations, other researchers [21][23] have shown hydrodynamic interaction to be significant. The results in this chapter however show very little difference with or without hydrodynamic interaction, apart from a massive increase in CPU time with the interaction included.

Similar numerical works by Fan *et al.* [31] and the work in Part II include hydrodynamic interaction. It should be noted that the various peculiar particle motions observed in those works are almost identically reproduced in this simulation - with long range interaction *disabled*. There is strong circumstantial evidence against including the long range hydrodynamic interaction. From the result comparisons with and without long range interaction in the sections to come, it could be concluded that very little new knowledge is gained by its inclusion, and the computational cost is too severe. While it remains included in this simulation, its automatic inclusion in simulations of this type should be further reviewed.

Intraparticle Force and Torque

Intraparticle force and torque may be categorized further into those arising from extensional, bending and torsional stiffness (Fig. 5.3). Bond Stiffness is controlled by the non-dimensional Extensional and Shear Moduli, E_{sim} and G_{sim} respectively. Each bond within a particle is assigned an independent extensional and shear stiffness modulus via the particles primitive matrix, as discussed in Section §5.2.1. For the purposes of calculating forces and

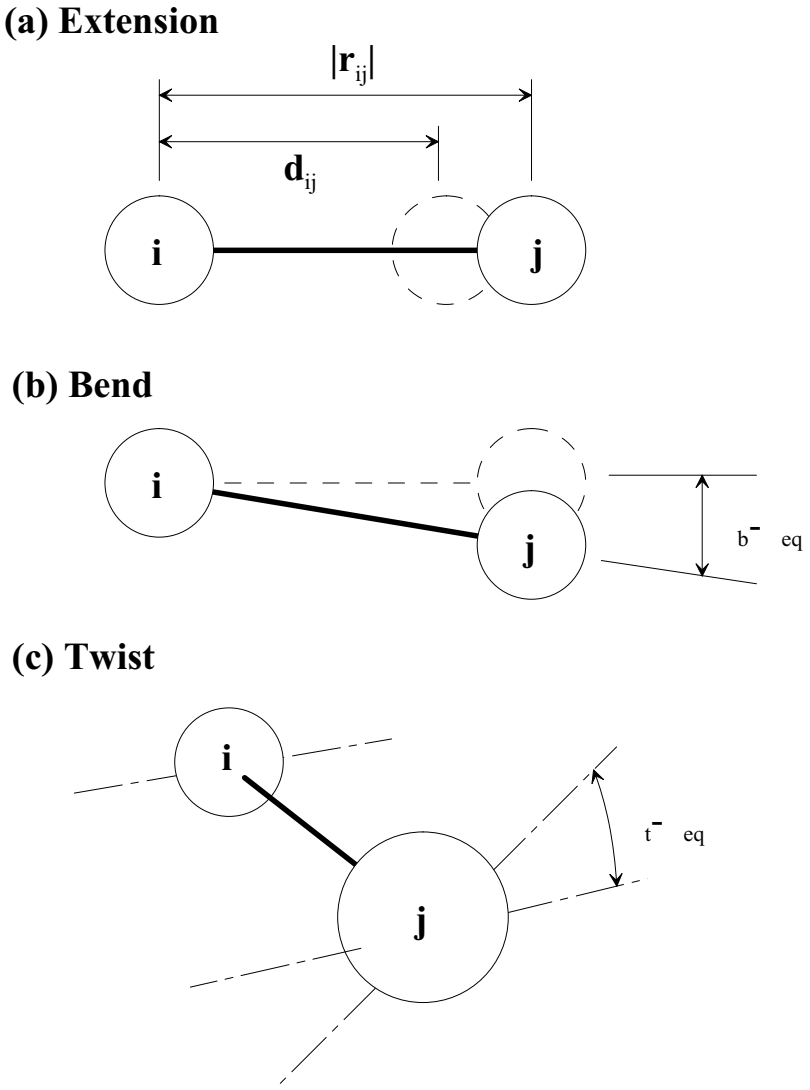

Figure 5.3: (a) Extension, (b) Bending and (c) Torsion in a bond between subunit i and j

torques, bonds are assumed to deform like an elastic cylindrical beam of cross sectional radius a (the non-dimensional spherical subunit radius). Stiffness coefficients for the cylindrical beam are thus able to be defined as shown in Eq. (5.9).

$$\begin{aligned} k^e_{ij} &= \tfrac{\pi a}{2} E_{sim} \quad \textit{(a) stretching stiffness} \\ k^b_{ij} &= \tfrac{\pi a^3}{8} E_{sim} \quad \textit{(b) bending stiffness} \\ k^t_{ij} &= \tfrac{\pi a^3}{4} G_{sim} \quad \textit{(c) twisting stiffness} \end{aligned} \tag{5.9}$$

Intraparticle force and torque are linearly related to extensional and angular deflection by Eqs. (5.10a, 5.10b and 5.10c).

$$\begin{aligned} F^e_i &= k^e_{ij}(|\mathbf{r}_{ij}| - d_{ij}) \quad \textit{(a) extension force} \\ T^b_i &= k^b_{ij}\,(\theta_b - \theta_{eq}) \quad \textit{(b) bending torque} \\ T^t_i &= k^t_{ij}\,(\phi_t - \phi_{eq}) \quad \textit{(c) twisting torque} \end{aligned} \tag{5.10}$$

In simulation, extensional force on a subunit is calculated using Eq. (5.10a). d_{ij} is the equilibrium ij bond length. $|\mathbf{r}_{ij}| = |\mathbf{r}_j - \mathbf{r}_i|$ is the instantaneous ij bond length calculated from the known positions of subunits $\mathbf{r}_i$ and $\mathbf{r}_j$ at each timestep. A component of subunit i's response to the extensional force F^e_i is the correction for the drifting ij bond length change, found to be necessary in Section §5.2.5.

As already discussed, it is the intention that all torque based calculations be eliminated or replaced by alternative methods. Eqs. (5.10b) and (5.10c) are not used in this simulation. The computational overhead required to maintain and update θ_b, θ_{eq}, ϕ_t, and ϕ_{eq} in simulation is high and best avoided. In Yamamoto *et al.*'s PSM, Klingenberg *et al.*'s particle level simulation, and the flexible fibre simulations of Part II, fibre cross sections were one dimensional and hence bond bending and torsion *were* a necessary consideration for realistic particle modelling. Without it, subsections of a fibre-like particle could rotate freely about their bonds, acting unrealistically to relieve internal stresses and alter particle dynamics. In the spaceframe-like particle constructions used in this simulation, the particles' torsional and bending stiffness are inherent in the highly crossbraced 3D structure. The bending and torsion equations are no longer strictly necessary to provide

bending and torsional stiffness in the structure. There are however occasions where rotational bond stiffness is still desirable (e.g. Fig. 5.4). In Fig. 5.4*a*,

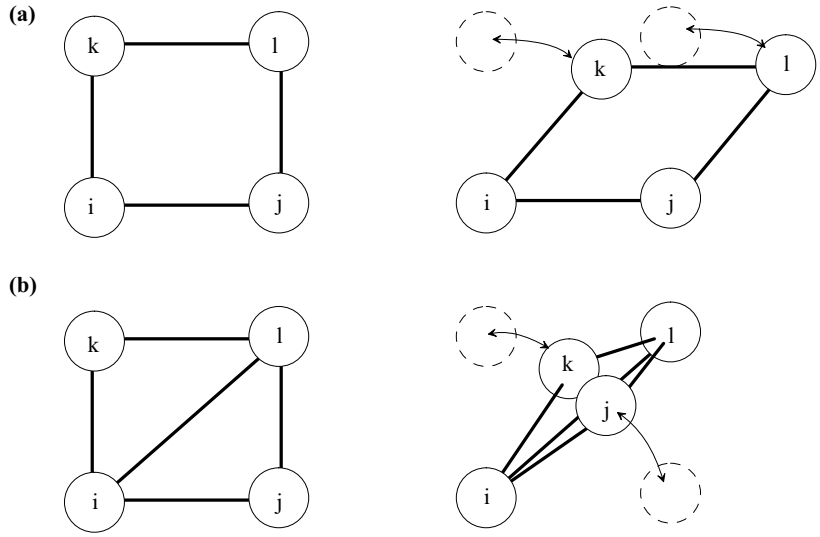

Figure 5.4: Rotational bond stiffness stops (*a*) skewing and (*b*) folding.

the structure is susceptible to skewing as there is no rotational bond stiffness at the node points (*i*,*j*,*k*, and *l*). If a cross brace *il* bond is now added (Fig. 5.4*b*), the structure is still susceptible to folding in the third dimension. While this simulation is intended primarily for the modelling of 3D particles, the inclusion of some rotational stiffness allows compatibility with the 2D and 1D models of earlier implementations.

Torsion is comparatively insignificant and is omitted in this simulation, but bending is included. Bending Eq. (5.10*b*) is not used directly however. Instead it is turned into an *equivalent* force. In Fig. 5.5*a*, the linear velocity of subunit j due to a rigid-body rotation of dumbbell ij about i (rotational velocity $\mathbf{w}_{irel} = \mathbf{w}_\infty - \mathbf{w}_i$) is equal to the cross product, $\mathbf{v}_{jrigid} = \mathbf{w}_{irel} \times \mathbf{r}_{ij}$. However, since dumbbell ij is not rigid, the actual linear velocity of subunit j is $\mathbf{v}_{ij} = \mathbf{v}_j - \mathbf{v}_i$. $\mathbf{v}_{ij}$ may be broken down into components parallel ($\mathbf{v}_{ijpar}$) and perpendicular ($\mathbf{v}_{ijper}$) to $\mathbf{r}_{ij}$. The difference, $\mathbf{v}_{ijdeform} = \mathbf{v}_{jrigid} - \mathbf{v}_{ijper}$ may be taken to be the velocity component of j due purely to bending deformation

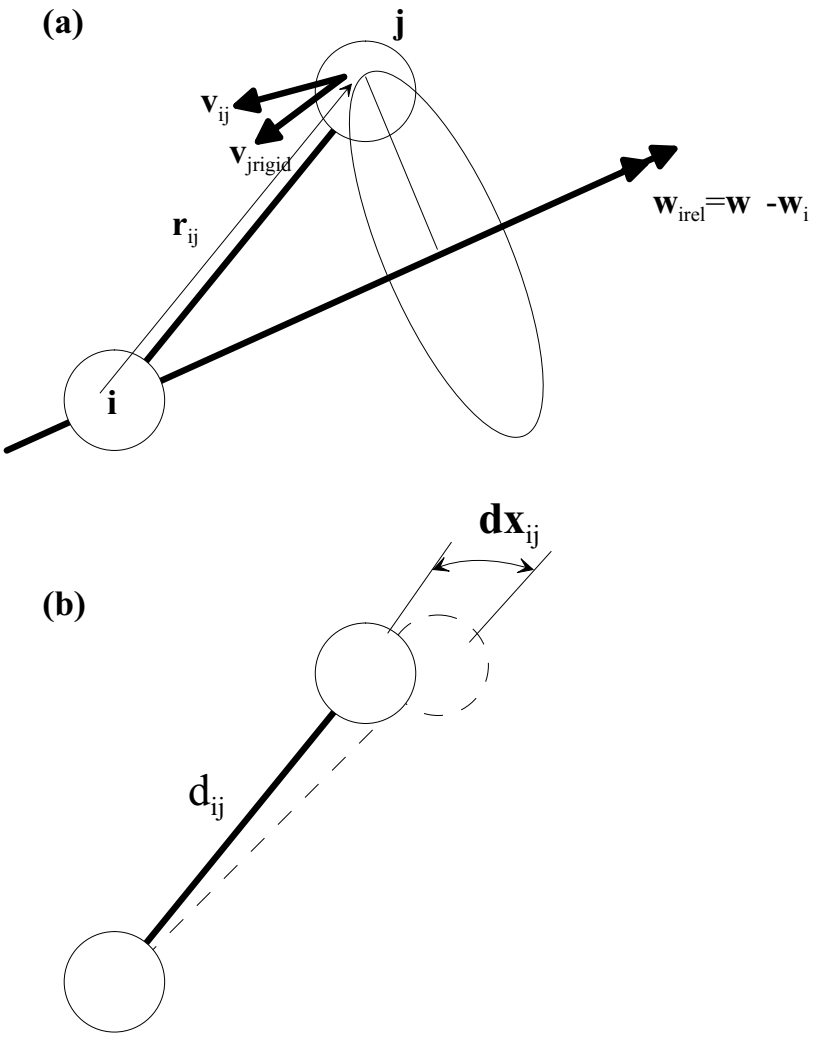

Figure 5.5: (a) Rigid-body bending versus actual bending (b) Bending deflection

(extensional deformation is dealt with separately by Eq. (5.10a)). Over a non-dimensional simulation iteration $d\gamma$, this velocity difference is equivalent to a linear deflection $\mathbf{dx}_{ij} = dt \cdot \mathbf{v}_{ijdeform}$. All bonds themselves are assumed to efficiently transfer forces and torques to the linked subunits at their bond roots. The linear deflection $\mathbf{dx}_{ij}$ over a moment arm d_{ij} will result in a bending moment at the root of the ij bond, at i. If the angular deflection α is always assumed to be small, approximately satisfying the relationship $\tan(\alpha) = \frac{|\mathbf{dx}_{ij}|}{d_{ij}}$, then substituting into Eq. (5.10b), the bending moment at i is $T_i^b = k_{ij}^b(\alpha)$. Acting over the moment arm d_{ij}, this is equivalent to a force on subunit j of $\mathbf{F}_j^b = -\frac{T_i^b}{d_{ij}} \frac{\mathbf{dx}_{ij}}{|\mathbf{dx}_{ij}|}$. The bending moment experienced at subunit i produces the same outcome as an equivalent position-correcting force on subunit j of the form described by Eq. (5.11),

$$\mathbf{F}_j^b = -\frac{k_{ij}^b}{d_{ij}} \tan^{-1}\left(\frac{|\mathbf{dx}_{ij}|}{d_{ij}}\right) \frac{\mathbf{dx}_{ij}}{|\mathbf{dx}_{ij}|} \tag{5.11}$$

where $\mathbf{dx}_{ij}$ is expressed by Eq. (5.12).

$$\mathbf{dx}_{ij} = dt \cdot [[\mathbf{w}_{irel} \times \mathbf{r}_{ij}] - [\delta - \mathbf{r}_{ij}\mathbf{r}_{ij}] \cdot \mathbf{v}_{ij}] \tag{5.12}$$

For each subunit i, the bending moment is calculated using Eq. (5.10b). The bending moment is converted into an *equivalent* force using Eq. (5.11) which is applied not to i but subunit j.

Interparticle Force and Torque

Interparticle forces and torques are those which act between different particles. While interparticle forces may arise for many varying reasons, in this simulation only the short range repulsive forces required to prevent particle overlap are considered. Kim and Karilla [100, Ch. 11.2.2] described lubrication forces between two spheres in close proximity (Fig. 5.6).

The lubrication force Eq. (5.13) describes the force acting on a subunit i and is used to maintain particle separation in suspension in a reversible manner.

$$\mathbf{F}_{im}^p = 3\pi\eta \frac{a^2}{h - 2a} \mathbf{V}_{jn-im}^{sqz} \tag{5.13}$$

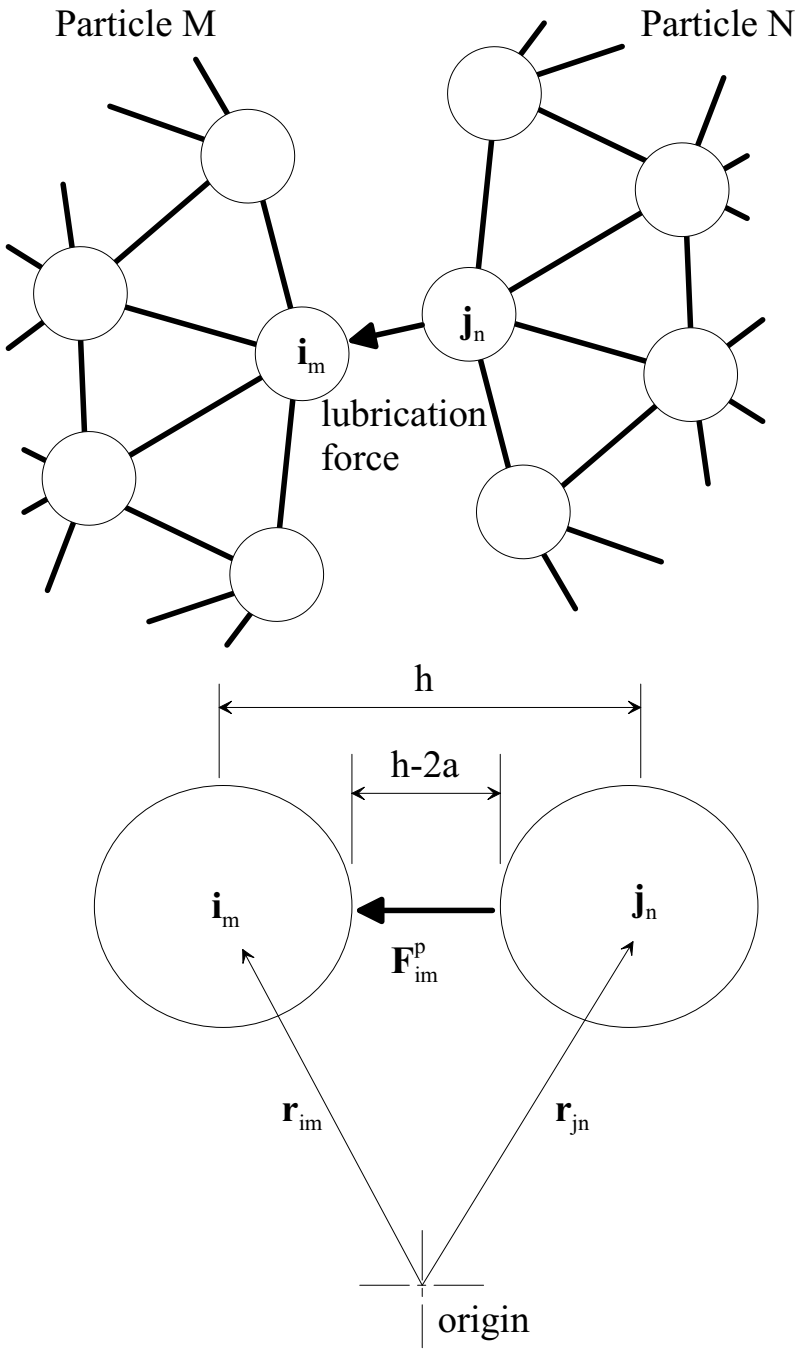

Figure 5.6: Interparticle lubrication force between subunit i of particle m and subunit j of particle n

In Eq. (5.13), a is the subunit radius and h is the centre distance between subunit i of particle m and subunit j of particle n. $\mathbf{V}^{sqz}_{jn-im}$ is the *squeezing velocity* or the component of the relative velocity at which subunit j of particle n approaches subunit i of particle m as expressed in Eq. (5.14).

$$\mathbf{V}^{sqz}_{jn-im} = \left[\frac{\mathbf{r}_{jn} - \mathbf{r}_{im}}{|\mathbf{r}_{jn} - \mathbf{r}_{im}|}\right] \cdot \left(\left[\frac{\mathbf{r}_{jn} - \mathbf{r}_{im}}{|\mathbf{r}_{jn} - \mathbf{r}_{im}|}\right] \cdot (\mathbf{v}_{jn} - \mathbf{v}_{im})\right) \tag{5.14}$$

This force is only required at close range when overlap is imminent. For this work, Eq. (5.13) is included in the force summation when the distance between subunits is in the range $h - 2a < L^{lub}$ where $L^{lub} = 2a$. One should choose the upper range limit (in this case, $2a$) such that for a given $\mathbf{V}^{sqz}_{jn-im}$ upon the activation of $\mathbf{F}^{p}_{im}$, there is sufficient time for the particle contact surface velocities to equalize before actual contact. While Yamane *et al.* [35] and Fan *et al.* [31] use a cutoff of $0.2a$, their cutoff was appropriate only in the context of their single body fibre models. A larger L^{lub} is required here to allow for the transmission of internal forces to affect particle level velocity change. As the force magnitude in Eq. (5.13) is inversely related to subunit separation, the simulation outcomes should be reasonably insensitive to L^{lub} as it is increased. It is assumed that interparticle forces $\mathbf{F}^{p}$ always act through the subunit's centre of mass, thus producing no associated torque. It is also assumed that any interparticle torques are negligible. Therefore $(\sum \mathbf{T}^{p})_{interparticle}$ of Eq. (5.3) is eliminated.

Eq. (5.13) and variants of it, have been successfully used in previous simulations by Yamamoto *et al.* [82], Ross and Klingenberg [84], Yamane *et al.* [35] [32] and Fan *et al.* [31].

Final Equations of Motion

The general equations of motion (5.2) and (5.3) were in Sections §5.2.5 through to §5.2.5. The torque Eq. (5.3) is eliminated in this process. The final equation of motion is expressed by Eq. (5.15) which is integrated in simulation to determine each subunit's instantaneous velocity and position

with shear.

$$m_i \frac{d\mathbf{v}_i}{dt} = -6\pi\eta a \left(\frac{d\mathbf{r}_i}{dt} - \mathbf{v}_\infty(\mathbf{r}_i)\right)_{viscous} + \left[\left(\begin{array}{c}\text{bonds}\\ \text{only}\\ \sum\limits_j\end{array} k^e_{ij}\left[|\mathbf{r}_{ij}| - d_{ij}\right]\right)_{extension} - \left(\begin{array}{c}\text{bonds}\\ \text{only}\\ \sum\limits_j\end{array} \frac{k^b_{ji}}{d_{ji}} \tan^{-1}\left(\frac{\mathbf{dx}_{ji}}{d_{ji}}\right)\frac{\mathbf{dx}_{ji}}{|\mathbf{dx}_{ji}|}\right)_{bending}\right]_{intraparticle} + \left(\begin{array}{c}\text{only when}\\ h-2a<0.2a\\ \sum\limits_j\end{array} 3\pi\eta\frac{a^2}{h-2a}\mathbf{V}^{sqz}_{j-i}\right)_{interparticle} \tag{5.15}$$

5.2.6 Flow Condition

The suspending medium is a Newtonian fluid. Temperature effects, phase changes, or free surfaces are not considered. The flow field is assumed to develop independently of the particle motion. Although Lipscomb *et al.* [108] showed that the decoupling of particle motion and flow field development is increasingly inaccurate at higher concentration, most other direct simulation works also neglect this. In any case, all cases presented in this thesis are dilute. It is therefore assumed that a decoupled flow field is acceptable here.

If the entire flow domain is subject to the same flow condition (e.g. simple shear flow) then a tensorially defined flow is convenient and computationally efficient. The velocity gradient tensor components, $\frac{\partial v_i}{\partial x_j}$ are specified prior to commencing simulation. From this, all other commonly used flow terms are generated, e.g. deformation rate tensor, $\dot{\gamma} = \nabla\mathbf{v} + \nabla\mathbf{v}^T$, $\mathbf{D} = \frac{1}{2}\dot{\gamma}$, $\mathbf{K} = \nabla\mathbf{v}^T$, vorticity tensor, $\omega = \nabla\mathbf{v} - \nabla\mathbf{v}^T$, local velocity, $\mathbf{v}_i(\mathbf{r}_i) = \mathbf{K}\cdot\mathbf{r}_i$ and rotation rate, $\mathbf{W}_i = \frac{1}{2}\left[\nabla\times\mathbf{v}_i(\mathbf{r}_i)\right]$. Given the known position of subunits in simulation $\mathbf{r}_i$, the fluid velocity and other flow terms can be determined for use in the equations of motion (Section §5.2.5).

For the shear flow simulations presented here, the flow direction is always in the positive (x) direction. The shear gradient is along the (y) axis. The shear magnitude is always $\dot{\gamma} = 1$. Along the (z) axis, the (xy) flow field planar sections are identical. The flow conditions described apply over an infinite domain and so wall effects are not considered here.

5.2.7 Simulation Procedure

The parameters in Table 5.1 are the default values used unless stated otherwise.

Parameters	
Subunit Radius	$a = 1$
Subunit Mass	$0.1 < m < 1.0$
Non-dimensional Solvent Viscosity	$1.0 < \eta < 10$
Lubrication Cut-off distance	$L^{lub} = 2a$

Table 5.1: Parameters and default values

As mentioned earlier, the time variable is directly correlated with non-dimensional shear deformation. Due to the non-dimensionalizing process, the simulation may be measured against shear γ. Shear deformation is an important global variable which must be set prior to commencing. Deformation variables included the initial shear γ_i, ending shear γ_e, and increment $d\gamma$. Usually $\gamma_i = 0$, while $d\gamma$ was in the range $0.0001 < d\gamma < 0.001$ depending on the accuracy required. Ending shear γ_e is case dependent but must be large enough to allow certain particle dynamic phenomenon to evolve and become evident ($100 < \gamma_e$ was usually sufficient but will be stated individually for each case when necessary).

In the following study of individual particle motion, a single particle of a nominated species was used. The particle (and its member subunits) may be subject to scaling and rotation. Once the initial orientation was set, it was translated to its initial position (usually the origin). Each subunit was

imparted with an initial velocity (by default, velocity was equal to that of the local fluid which it displaced).

Once the simulation commenced, the equations of motion of Section §5.2.5 were solved. After solving Eq. 5.15 for all subunits, the subunit accelerations were integrated using the simple trapezoidal method to determine subunit velocity, and new position in space (Eq. 5.16).

$$\begin{aligned} V_{\gamma+d\gamma} &= V_\gamma + \tfrac{1}{2}d\gamma(a_{\gamma-d\gamma} + a_\gamma) \\ x_{\gamma+d\gamma} &= x_\gamma + \tfrac{1}{2}d\gamma(V_{\gamma-d\gamma} + V_\gamma) \end{aligned} \tag{5.16}$$

where a is linear acceleration, V is linear velocity, and x is position of the subunit in space. Knowing this, the global subunits matrix was updated for each iteration. Relevant data were collected and output to a datafile for postprocessing prior to the next iteration. The simulation continued in $d\gamma$ increments until the ending point γ_e or other termination condition was met.

The simulation results presented in Section §5.3 were computed on Intel $x86$ processor based computers (Intel Pentium II and III generation) running Microsoft Windows and RedHat Linux operating systems. The simulation source code was written in ANSI standard Fortran77 and compiled using Intel Fortran 95 Compiler for Linux v6 and Digital Visual Fortran v6 Compiler. CPU times for single particle simulation runs ranged from minutes, through to several days for suspensions, depending on the size of the global subunits matrix produced and the shear range set, $d\gamma$ and γ_e.

5.3 Results - Single Particle Dynamics

In the immediately following section, the simulation performance is compared in reproducing some known particle dynamic behaviour in a series of verification tests. Afterwards, more single fibre dynamics are detailed. Finally, results for particles of non-standard shapes and structural characteristics are presented.

5.3.1 The Rigid Rod-like Particle - Jeffrey Orbit

Experimental and theoretical results for rod-like particles are readily available. The dynamics of the rod-like particle is chosen as the topic of interest in this section. The results gathered in this study will be compared to previous known results as a means of verifying the performance of this simulation. From this comparison, one may gauge the accuracy of subsequent results obtained using this simulator.

Fig. 5.7 depicts a typical rod-like particle used in this section. Similar

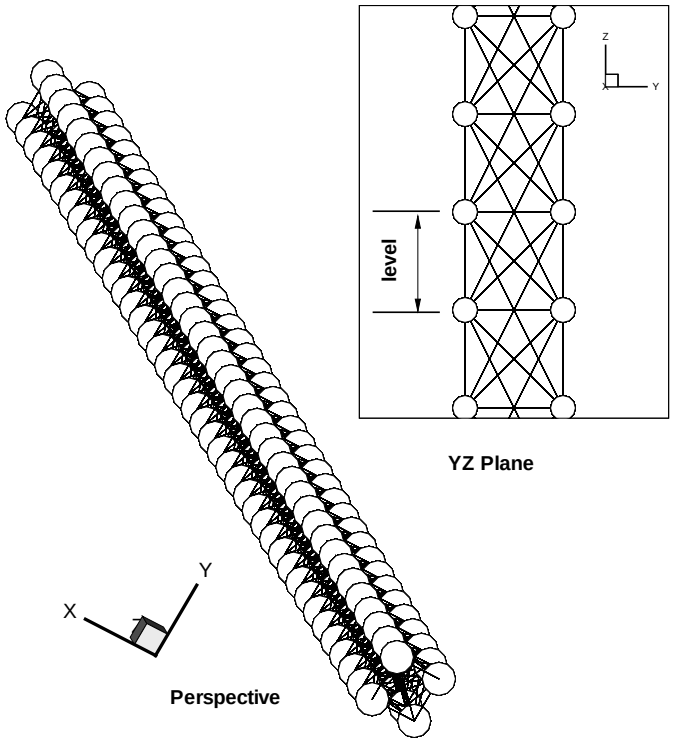

Figure 5.7: The Rod-like particle used to simulate Jeffrey orbit. The particle shown has 40 levels, each 6 units tall, square cross-sectional sides are 6 units between sphere centres. Sphere radius is $a = 1$ (Spheres are not drawn to scale)

rod-like particles of varying aspect ratio may be constructed by stacking subunit levels of the same square cross-section. The square cross-section was

chosen because it is 'mass-balanced' about the axis of revolution. It maintains this property while using only the 4 nodes for the cross section. While a more 'circular' section could have been used (e.g. hexagon, octagon) this requires more spheres and ultimately increases the simulation size. Mass balance is important in this study since it ensures the sectional centre of resistance is always coincident with the axis of revolution, and thus particle dynamics are close to that of a truly axi-symmetric body. In Fig. 5.7 the species shown has 40 levels of subunits, each level is 6 units tall. Spheres in the cross-section are $3\sqrt{2}$ units from the centroid (i.e. the corners of the square cross-section are at local coordinates $(3,3)$, $(-3,3)$, $(-3,-3)$, and $(3,-3)$). The sphere radius is $a = 1$.

To calculate an aspect ratio, a fibre diameter must first be known. Since this fibre has a square cross-section, a diameter must be *approximated*. A possible 'diameter' taken could be $2 \times 3\sqrt{(}2)$ (i.e. the square cross-section diagonal), giving the fibre an aspect ratio of $a_r \approx 28.3$. However, a more appropriate approximation is to use the diameter for a circle section equivalent in area to the square section, i.e. $l^2_{sqr.side} \equiv \pi r^2_{eqv.circle}$. Hence $r_{eqv.circle} = \frac{l_{sqr.side}}{\sqrt{\pi}}$. This approach gives the slightly higher approximation for aspect ratio of $a_r \approx 35.4$. The 'equivalent circle' area approach is the method used to estimate aspect ratio.

Each subunit in a 'level' is bonded to all four subunits of the neighbouring levels, above and below it, as well as the subunits within its own level. The result is a regular, highly interconnected pattern of linkages forming the particle structure. Bond non-dimensional Extensional and Shear Moduli are set in simulation, to a relatively high value of $E_{sim} = 8000$ and $G_{sim} = 8000$, so the particle will exhibit a high degree of rigidity. For the following results, 22 different aspect ratio fibres were tested in shear flow. The number of 'levels' and the corresponding aspect ratio are listed in Table 5.2.

Single particles of varying aspect ratio are placed (alone) in a simulation reference cell of Newtonian sheared fluid. The centre of mass of the particle coincides with the global origin. The initial orientation of the particle is

Levels	Aspect Ratio	Re_{max}
2	1.8	0.0095
3	2.6	0.0143
4	3.5	0.0191
5	4.4	0.0239
6	5.3	0.0286
7	6.2	0.0334
8	7.1	0.0382
9	8.0	0.0430
10	8.9	0.0477
12	10.6	0.0573
14	12.4	0.0668
16	14.2	0.0764
18	16.0	0.0859
20	17.7	0.0955
25	22.1	0.1194
30	26.6	0.1432
35	31.0	0.1671
40	35.4	0.1910
70	62.0	0.3342
100	88.6	0.4775
140	124.1	0.6685
180	159.5	0.8594

Table 5.2: The square cross-section fibre. 'Levels', corresponding Aspect Ratio, and the maximum Reynolds number estimated for the spheres at fibre-end during shear flow rotation

always in the (xz) plane, with an inclination of 60° from the (z) axis towards the (x) axis. With this configuration, the initial Jeffrey orbital constant is always $C_{initial} = 0.08$. The flow velocity is in the (x) direction varying linearly with (y). Shear rate is of magnitude $\dot{\gamma} = 1$.

Sphere mass is $m = 0.1$ and solvent viscosity is $\eta_{sim} = 5$. Assuming the region of the fibre near the centre of mass is nearly stationary (much lower Reynolds numbers here), and the ends of the fibre experience the greatest velocities, the Reynolds number will be greatest for the spheres at the *ends* of the fibre. Reynolds number is $Re = \frac{\rho V l}{\eta}$. ρ is the density of the sphere itself, i.e. $\rho = \frac{m}{\frac{4}{3}\pi a^3}$. Assume a fibre tumbling purely in the shear plane. Maximum velocity for the rotating fibre is assumed to occur at the fibre end when oriented perpendicular to the shear direction. Maximum velocity is thus approximately, $V_{max} \approx \dot{\gamma} \cdot \frac{L_{fibre}}{2}$, where L_{fibre} is the fibre length. The characteristic length is equivalent to the sphere radius, $l \equiv a$.

As seen in Table 5.2, the estimated maximum Reynolds number that any subunit within the fibre could experience, is always in the 'low Reynolds number' range, certainly less than 1 for all fibres tested. Recall Happel and Brenner's conclusion that Stokes law drag on a sphere is not much different in magnitude to low Reynolds number drag [110]. Furthermore fibres closer into the centre of mass will always experience lower Reynolds number conditions. The high rigidity of the internal bonds means that any subunit trajectory inaccuracy (due to inertial effects) will be mostly negated by the bonding influence of the majority of other lesser inertia-affected subunits. The trajectory of subunits at the ends of the fibre cannot deviate far from an equivalent inertialess result - in spite of the higher Reynolds number that a few 'end subunits' are experiencing. All fibres tested are therefore not greatly affected by inertia, and results should be directly comparable with inertia-less Jeffrey theory predictions.

The Jeffrey orbit is characteristic of the motion of a rigid fibre in shear and hence its appearance is the first indicator of a correct simulation. In Fig. 5.8 the simulated Jeffrey orbit is plotted for the $a_r = 35.4$ particle. In Fig.

5.8 the particle itself has been superimposed over the Jeffrey orbit plot for better visualization. In this figure, a single subunit acts as a tracer and its trajectory is recorded over several orbits. The wobbles in the orbital path indicate the spin of the particle about its main axis of revolution during the orbit.

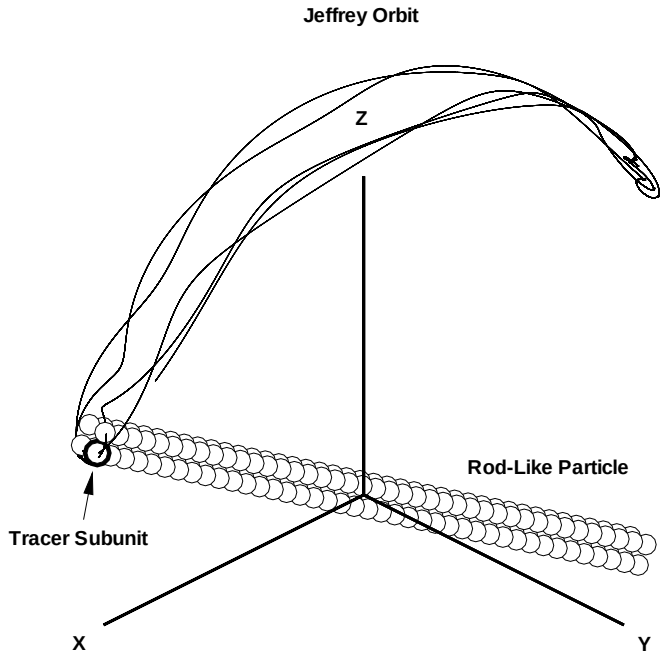

Figure 5.8: Simulated Jeffrey orbit for the $a_r = 35.4$ fibre, with the trajectory of the fibre end plotted

$$T_{orbit} = \frac{2\pi}{\dot{\gamma}} \left(a_r + \frac{1}{a_r} \right) \tag{5.17}$$

The Jeffrey orbital period for the ellipsoid is given by Eq. (5.17). The correction factor, λ_{corr} is traditionally used to obtain an *effective* aspect ratio, $a_e = \lambda_{corr} a_r$ correcting for the effects of shape difference between ellipsoids and cylindrical rods. Trevelyan and Mason [24] have experimentally estimated this correction to be $\lambda_{corr} = 0.7$. Given Eq. (5.17), the theoretical orbital period versus aspect ratio relationship for the ellipsoid is shown in

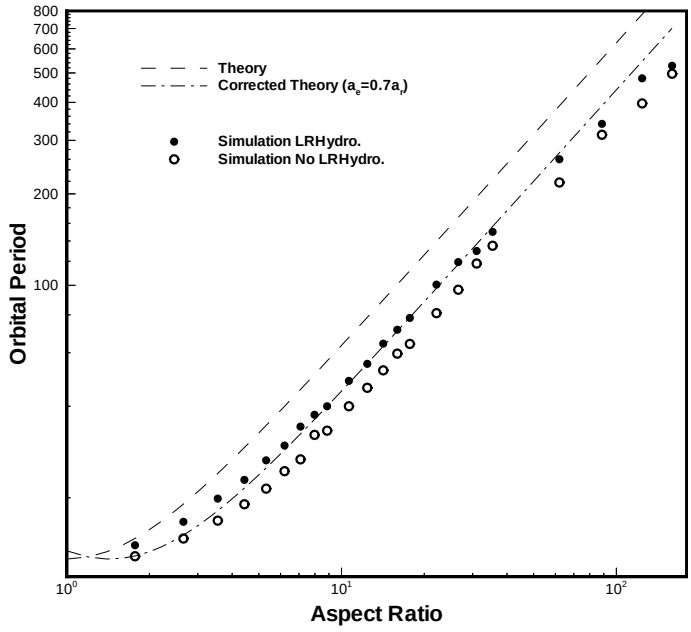

Figure 5.9: Jeffrey orbital period vs particle aspect ratio. theory (-), and corrected theory (- ·) compared with Simulation results with long-range hydrodynamic interaction (•), and also without (○) hydrodynamic interaction

Fig. 5.9. In this figure the theoretical relationship (Eq. (5.17)) is plotted (Theory (-)), as well as Trevelyan and Mason's corrected theory (- ·) where effective aspect ratio with $\lambda_{corr} = 0.7$ is used. Finally the simulation data points are plotted as black circles (•). Also included are data points from an equivalent series of simulation runs, where long-range hydrodynamic interaction was disabled (∘). That is, the $\mathbf{V}'$ in Eq. (5.6) was removed, and hence the summation in Eq. (5.8) was *not* done for that case. Since most simulation data points are in the range $2 < a_r < 20$ the graph is plotted in log axes to reveal more detail in the lower regions. It is clear the simulated data matches the corrected theory very well over almost the entire tested aspect ratio range. It is also interesting to note that there is a small quantitative difference between the two series of simulation runs, but no qualitative difference. The simulation orbital period with long-range hydrodynamic interaction enabled (•) is on average 15.1% greater in magnitude than the simulation without. Long-range hydrodynamic interaction appears to have the effect of marginally increasing orbital period over the entire aspect ratio range. However there appears to be no other qualitative difference, e.g. the shape of the Jeffrey orbit and the different fibre orientations were all unchanged. Finally, the largest deviation from theory occured at the highest aspect ratios (Fibres with 140 and 180 'levels', i.e. $a_r = 124.1$ and $a_r = 159.5$). Reasons for this divergence will be discussed shortly.

One may now refine Trevelyan and Mason's correction factor λ_{corr} using this simulation data. The exercise was undertaken whereby over the likely range $0.65 < \lambda_{corr} < 0.75$, the area difference under the 'period versus aspect ratio' curve was compared and minimized, relative to the simulation data (the (•) case). In Fig. 5.10, the root square of the area difference is plotted against the λ_{corr} range. Since the data points for $a_r = 124.1$ and 159.5 in Fig. 5.9 diverge excessively, these two points are omitted from the calculation. The minimum as indicated in Fig. 5.10 represents a refined value for λ_{corr} based on the simulation results. The refined shape correction factor between ellipsoid and the rod-like particle is estimated to be $\lambda_{corr} = 0.7124$. This

value is used in the following section involving particle spin.

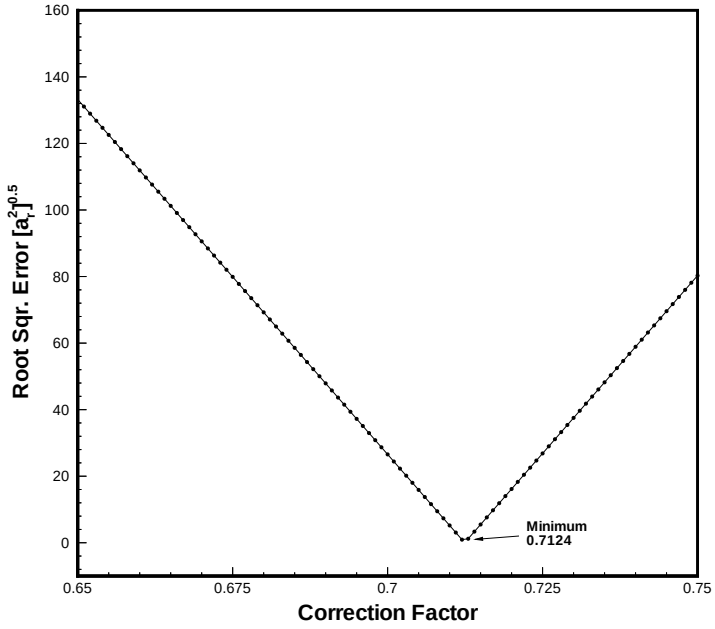

Figure 5.10: The minimum error between theoretical and (•) simulated data occurs when the shape correction factor is $\lambda_{corr} = 0.7124$.

Fibre Spin

As seen in Fig. 5.8, the wobble of the tracer subunit over the Jeffrey orbital path is an indication of the particle's spin about its main axis of revolution. In Fig. 5.11, the (y) axis trajectory of the tracer subunit, when plotted against shear, (γ) reveals both high and low frequency regular oscillations indicating spin and orbital rotation cycles respectively. Particle spin is a behaviour that has not been revealed by numerical simulation until now. It is the use of full 3D particles with finite width which permits this result. Particle motion was theoretically analyzed at length by Anczurowski and Mason [90]. Indeed, included in their work is a derived expression for the

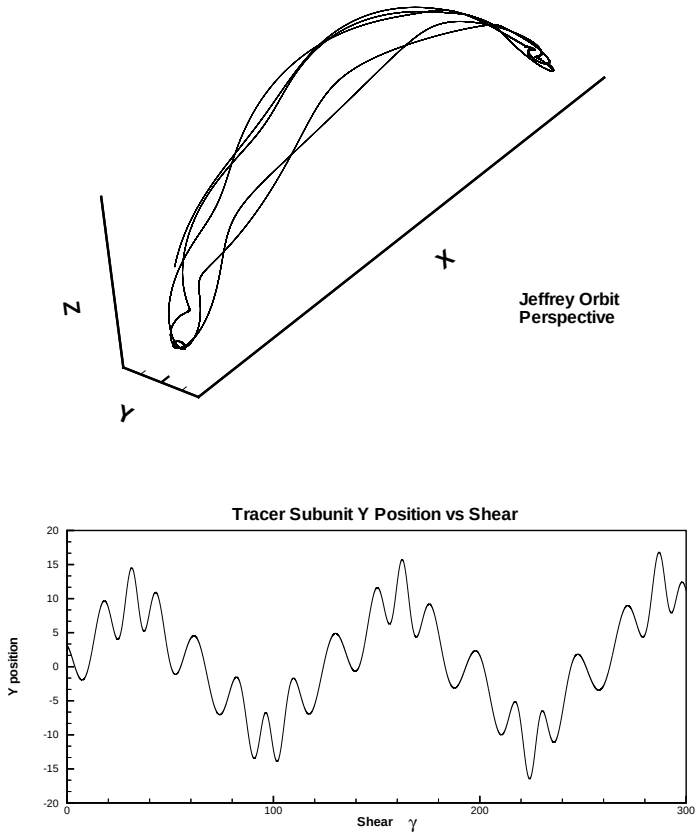

Figure 5.11: Jeffrey orbit with wobbles indicating particle spin - the (y) axis trajectory of the tracer subunit reveals a high frequency oscillation representing complete spins (n), and low frequency oscillations representing orbital cycles.

axial spin of a cylinder within the orbital period. It is this expression which for convenience will be paraphrased here and also used for comparison with simulation data.

The theoretical number of complete spins for an elongated cylinder ($a_r > 1$) is expressed by Eq. (5.18),

$$n = gK(k) \tag{5.18}$$

$$g = \frac{a_r^2 + 1}{\pi a_r \left(C^2 a_r^2 + 1\right)^{\frac{1}{2}}} \tag{5.19}$$

$$k = \sqrt{\frac{C^2\left(a_r^2 - 1\right)}{C^2 a_r^2 + 1}} \tag{5.20}$$

where g is given by Eq. (5.19), and $K(k)$ is the complete elliptic integral of the first kind of modulus k, given by Eq. (5.20). The complete elliptic integral of k may be approximated by the series expansion as shown in Eq. (5.21).

$$K(k) = \frac{\pi}{2}\left\{1 + \left(\frac{1}{2}\right)^2 k^2 + \left(\frac{1\cdot 3}{2\cdot 4}\right)^2 k^4 + \left(\frac{1\cdot 3\cdot 5}{2\cdot 4\cdot 6}\right)^2 k^6 + \ldots\right\} \tag{5.21}$$

Using this method, the theoretical relationship between particle spin per orbital period (n) and effective aspect ratio (assuming $\lambda_{corr} = 0.7124$) is shown in Fig. 5.12 by the solid line. The equivalent simulation data was obtained from output data, simply by dividing the number of higher frequency oscillations (spin), by the number of low frequency spatial oscillations (orbits) over the same shear interval (see Fig. 5.11 *bottom*). The spin results are plotted in Fig. 5.12. The Corrected theoretical result is the solid line (-), the simulation with long-range hydrodynamic interaction is (•), and the simulation without the long-range interaction is (∘). Again as most of the aspect ratios are in the range from $2 - 20$, log axes are used to reveal detail in this range. We can see that over the range $12 < a_r < 100$ the simulated particle spin (with long-range hydrodynamic interaction (•)) is reasonably well predicted compared to the theory despite a general under-estimation to a small degree. It should be noted that the differences at low a_r are accentuated by the log

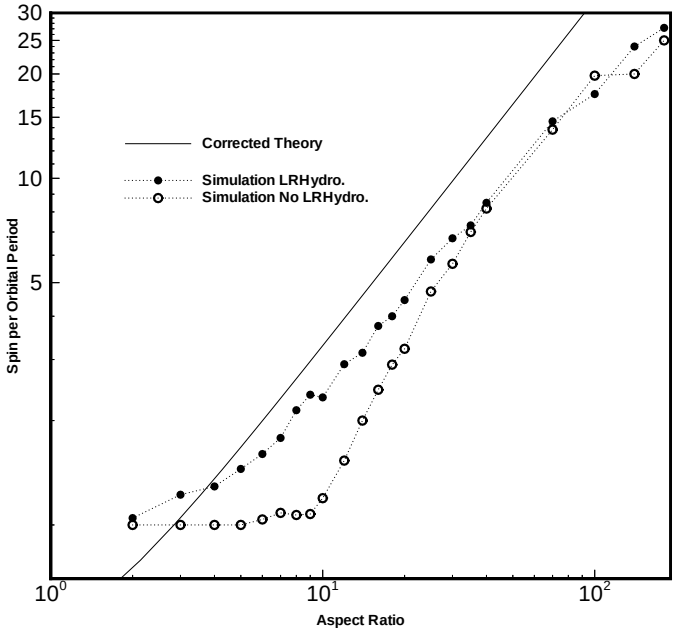

Figure 5.12: particle spins per orbital period (n) versus effective aspect ratio. Corrected Theory versus Simulation, both with long-range hydrodynamic interaction ($\bullet$) and without ($\circ$)

scaling. The error generally *increases* with aspect ratio. The simulation series without long-range interaction (∘) generally performs slightly worse than those with interaction enabled. Long-range hydrodynamic interaction appears to improve the spin prediction performance for lower aspect ratio fibres, but becomes less effective with increased aspect ratio where fibres contain more interacting subunits. As with Fig. 5.9, the divergence with theory occurs most with the largest aspect ratio particles ($a_r = 124.1$ and 159.5), and there is also anomalous behaviour over the low aspect ratio range from $3 < a_r < 12$.

It is believed that the less accurate low a_r prediction is due to the fact that in this range, the simulated particle shape is actually more like a cube than a rod. The assumption that these shapes are like cylinders becomes increasingly significant in the accuracy of calculated aspect ratio. $r_{eqv.circle} = \frac{l_{sqr.side}}{\sqrt{\pi}}$ is still used as the effective particle 'radius' when in fact the cross section is square (one would construct a more detailed cylindrical particle species in this case - Section §5.2.1). It is probable that the error in predictions up to $a_r = 12$ in Fig. 5.12 is due to this error in 'aspect ratio' calculation, and also reflects the different dynamics of cuboids to cylinders and ellipsoids. In the limiting case of $a_r \to 1$, there is no Jeffrey orbit as such, and as aspect ratio approaches 1, spins also approach 1. That is, spin and orbit rates converge until the particle simply 'spins' with the rotational rate of the local fluid. This reveals a limitation in the simulation in that it does not represent particle dynamics well when there are too few subunits used in the construction of the particle. Like any other form of numerical discretization, the accuracy improves with finer divisions.

At the other end of the a_r range, it was observed that the particles exhibited noticeable deformation, despite the large stiffness constants used. It was shown in Part II, that even small deformations and flexibility in rod-like particles causes an erratic, irregular orbital motion and presumably also divergent spin rate. For realistic rod-like particles subject to flexibility and deformation, one should expect the eventual divergence from a theory which

relies on the rigidity of particles. As the aspect ratio increases, the particle becomes more slender and for the same stiffness moduli, will become increasingly susceptible to bending deflection and/or buckling. In this light, the result for high a_r is not altogether unexpected.

CPU solve time and long-range interaction

The simulation with long-range hydrodynamic interaction included (•), clearly produced results closer to theoretical prediction. The main difference between the simulations with (•), and without (○) however are mostly quantitative.

In Fig. 5.9 the only real difference is an approximately consistent elevation in orbital period magnitude of 15% across the a_r range. In Fig. 5.12 the inclusion of long-range hydrodynamic interaction did appear to improve the quality of the spin prediction somewhat (in the range $3 < a_r < 12$), however at these low a_r, the difference is accentuated by the log scaling. The difference in spin rate over the whole a_r range is *roughly* an even increase in spins per orbit.

The difference in computational solution time, with and without long-range interaction is however highly significant. In Fig. 5.13, the CPU solution times for both simulation series are compared. The simulations were run on four different computers. They were Intel PII 233Mhz and 366Mhz, and Intel PIII 800Mhz and 850Mhz. All had sufficient memory so that the simulation could run mostly in RAM (minimal memory swapping to harddisk). To allow better comparison, the CPU times were normalised to represent the solution to a simulation shear of $\gamma = 300$ at increment $d\gamma = 0.0003$ (a quite small increment, hence the rather large timescale in Fig. 5.13). As shown in Fig. 5.13, the simulations with long-range interaction (•) take far longer to finish, compared to those without interaction (○). As a_r increases, the CPU times (in minutes[4]) for the two different simulation series, quickly separate to an

[4]CPU time is independent of other solution parameters and does not need to be non-dimensionalised

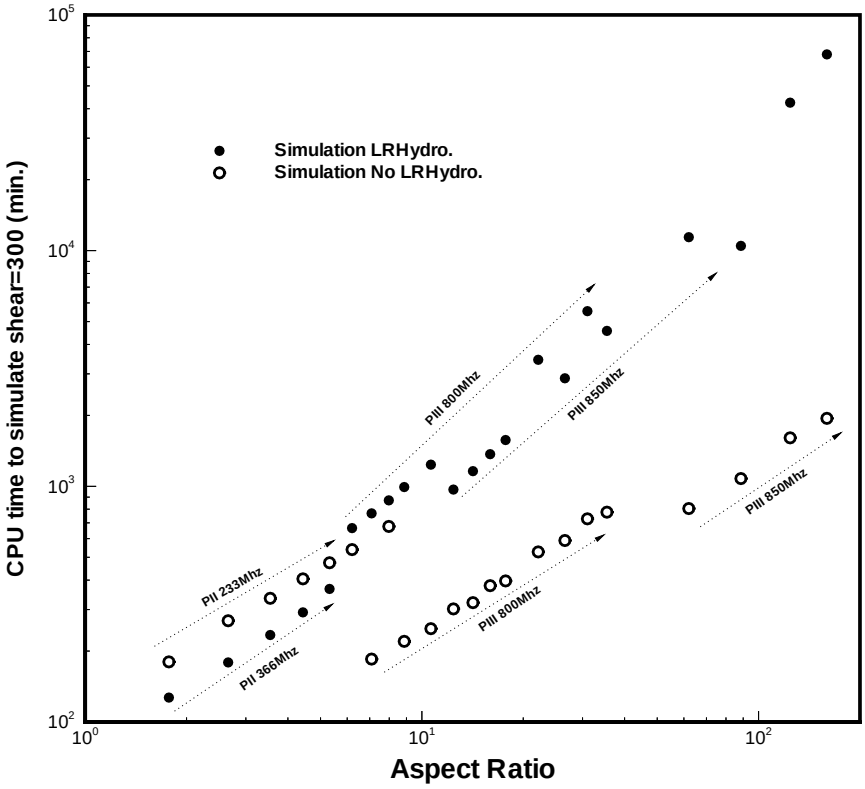

Figure 5.13: CPU solution times, with (•) and without (○) hydrodynamic interaction enabled. Hydrodynamic interaction calculations severely increase solution time. The difference in solution time is very large and grows quickly towards an order of magnitude separation.

order of magnitude difference.

When qualitative information only is sought, such as studies on orientation and flow conditions etc, or only a rough idea on particle velocity and spin, there is little to be gained by insisting on using the full long-range hydrodynamic simulation method. The increase in CPU solution time is very high and the added information is of only limited value. The difference only seems to be a small improvement in the prediction of particle rotation and spin rate.

In summary, the simulation has been shown to faithfully simulate the important case of the rigid rod-like particle in shear flow. The Jeffrey orbital motion was reproduced well with accurate orbital period prediction as compared to theory. The simulation's ability to predict particle spin was demonstrated, and the spin-rate compared reasonably well with the theoretical prediction. It was argued that including long-range hydrodynamic interaction (through the Oseen tensor) was highly costly computationally, and was of only limited benefit. Finally the data from this section was used to refine Trevelyan and Mason's ellipsoid-to-rod shape correction factor, $\lambda_{corr} = 0.7124$. In the following section, the rigidity of the particle is relaxed and the effects of flexibility are compared to known flexible particle behaviour.

5.3.2 The Flexible Rod-Like Particle

As mentioned earlier, this simulation was presented as a rigid particle simulation. The contribution of the particle deformation theory was minimised since the stiffness moduli were usually set very high and the near-rigidity assumption was assumed. The simulation particles presented in this thesis are considered 'rigid' and therefore particle flexibility was effectively eliminated as an important factor in the results. It is not impossible however to soften this condition and approximate flexible particles. While confidence for results of 'flexible' particles is not as high as for rigid particles, it is interesting nevertheless to observe some flexible particle results as a preview of possible

future directions this method could take. In this section, the flexible rod-like particle is studied. This section should be viewed in isolation from the rest of the results section.

Hinch described the deformation of a flexible thread in flow in his two papers, [50] and [51]. In these works, the thread is an inextensible two dimensional entity with no bending stiffness. The inextensible thread is initially positioned in an S-shaped configuration across a shear flow gradient. Hinch determined from a theoretical basis, the drifting thread's shape in 1γ shear deformation intervals from $0 < \gamma < 6$ when the thread ends face into, and also away from the direction of flow. In Fig. 5.14(*far left*) the thread, reproduced from Hinch [50] is shown. Since Hinch's result was analytically derived,

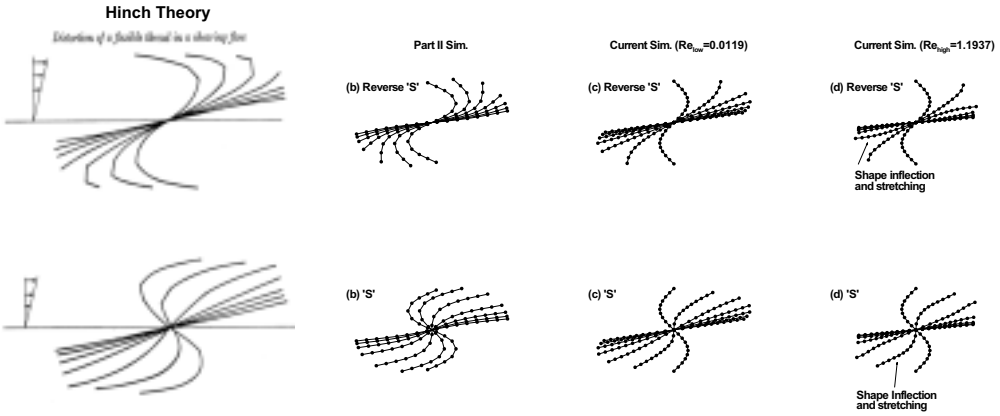

Figure 5.14: (*far left*) The thread of Hinch is initially positioned in an S shape across a shear gradient and allowed to drift with the flow. The configuration of the thread over successive shear-steps from $\gamma = 0$ to $\gamma = 6$ are superimposed; (*centre left*) In Part II, simulated Hinch's thread with a flexible fibre simulation; (*centre right*) The current simulation reproduces the the same scenario well for the low Reynolds number case ($m = 0.1$, $\eta_{sim} = 10.0$, $E_{sim} = 5000$, $G_{sim} = 0$, $Re_{max} = 0.0119$); (*far right*) The current simulation shows inertia related shape differences for higher Reynolds number case ($m = 1.0$, $\eta_{sim} = 1.0$, $E_{sim} = 2000$, $G_{sim} = 0$, $Re_{max} = 1.1937$).

comparison against it is a useful test of the fidelity of a simulations particle deformation model. In Part II, Hinch's scenario was used as a verification result for the first flexible fibre simulator. In that work, the thread was

modelled using 16 subunit beads linked together with 'inextensible' bonds (high $E_{stretch}$) exhibiting no resistance to angular deflection ($E_{bending} = 0$). Given an initial S-shape (sinusoid) both facing into and against the shear flow, the result of Hinch was successfully reproduced with great accuracy. In Fig. 5.14(*centre left*) the simulation results from Part II are redrawn for convenience.

The Hinch scenario was repeated once again as verification of the deformation model used in this current simulation (Fig. 5.14(*centre right*) and (*far right*)). In a manner similar to Part II, the inextensible thread was now modelled by a 21 subunit chain. Bond stiffness modulus was set to a high value, $E_{sim} = 5000$ (and also $E_{sim} = 2000$) to approximate inextensibility in the thread. The bending force (Eq. 5.11) is also disabled for this particle. The 21 subunits are initially positioned in a sinusoidal arrangement, facing into and against a shear flow gradient of magnitude $\dot{\gamma} = 1$. Two different simulations were run, one for a low Reynolds number case ($Re = 0.0119$), and one for a larger Reynolds number ($Re = 1.1937$) where inertial effects may take effect. The different Reynolds number cases were achieved by varying the values for non-dimensional simulation viscosity and subunit mass ($m = 0.1$ and $\eta = 10.0$, or $m = 1.0$ and $\eta = 1.0$). In Fig. 5.14(*centre right* and ((far right))) the new simulation results are shown superimposed in 1 shear deformation intervals from $0 < \gamma < 6$, consistent with results by Hinch and from Part II.

On comparing results, one finds that for the low Reynolds number case (*centre right*), the current simulation reproduces previous results well. At each 1γ interval the corresponding thread shape between the Hinch result, 'Part II' result, and current low Re simulation (*centre right*) result can be clearly identified, and the evolution of the shape is very similar. The current simulation at higher Reynolds number (*far right*) does not match the theoretical result as well as the 'Part II' result or the current low Reynolds number result, particularly for the thread shapes at shear $\gamma = 1$ and $\gamma = 2$. For the higher Reynolds number case, the inertial influences on subunits

are not great, but noticeable. Massive subunits with initial velocity tend to 'overshoot' their position relative to inertialess, or low Reynolds number counterparts. Hence the shape inflections along the thread contour (compare the $\gamma = 2$ shapes) are reasonably explained and reflect the presence of inertial components in the equations of motion.

As a final exercise on this topic, a fully three dimensional rod-like particle was tested in the same Hinch scenario. In Fig. 5.15 the fully 3D rod-like

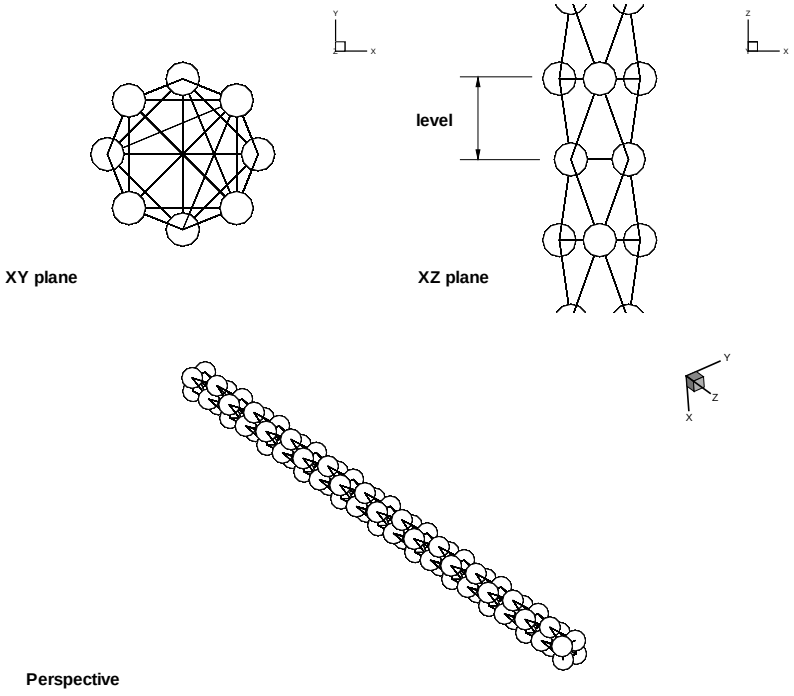

Figure 5.15: Rod-like particle used in the Hinch inextensible thread scenario

particle species used for this exercise is shown. This particle species is similar to the one shown in Fig. 5.7 since the cross section of this species is also square. This time however every second cross section level is axially rotated by 45°. This configuration maintains the axial symmetry but allows a slightly denser subunit packing, more diagonal cross bracing links within structure and subsequently a more accurate model of a cylindrical rod in deflection than

the elongated cuboid. The particle should be highly flexible so a relatively low stiffness modulus was used, $E_{sim} = G_{sim} = 400$. The particle was initially positioned lying across the shear gradient along the (y) axis. Unlike the 2D species, this particle's original shape is straight. The S-shape however is seen to develop from the flow conditions during its motion. In Fig. 5.16,

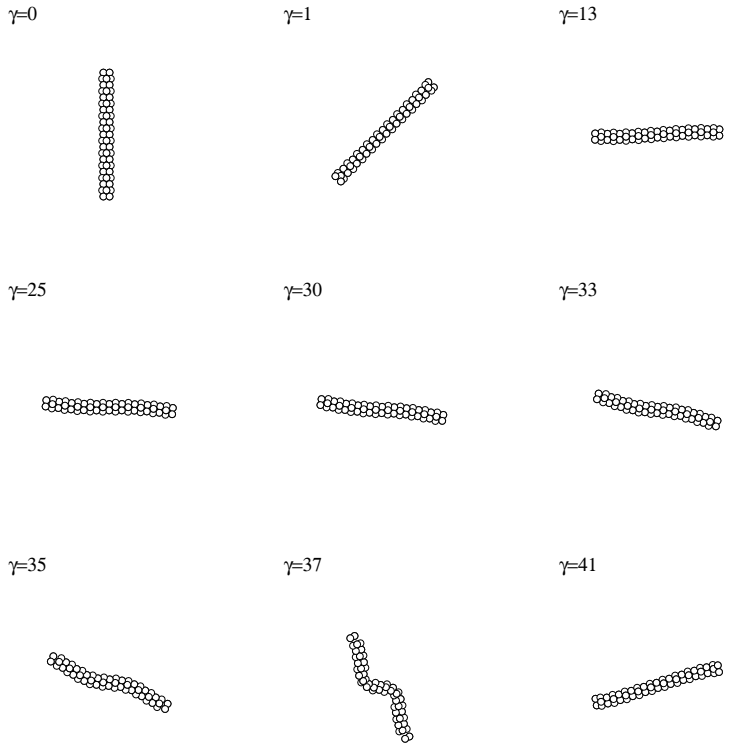

Figure 5.16: Simulated rotation and deformation of a highly flexible 3D rodlike particle in shear flow. The characteristic S-shape seen in Hinch's inextensible thread is induced by the flow. (Subunit diameter not drawn to scale).

we see simulation snapshots of the particle rotation in the (xy) plane for select times. For the 2D subunit-chained particle, orientation rotation stops once it aligns with the shear (x) direction. This is characteristic motion for a particle of infinite aspect ratio (zero width) predicted by Jeffrey's theory. For the 3D particle with finite width however, the particle is able to rotate

past the shear direction, continuing to tumble in the shear (xy) plane. In Fig. 5.16 we see selected snapshots over three quarters of a revolution (i.e. 270°). The 3D particle is highly flexible and due to flow vorticity quickly adapts the characteristic S-shape. During periods when particle orientation is aligned to shear, particle stiffness and extensibility in shear restores the original straight particle shape. Unlike the 2D particle, the 3D particle will continue rotating in this manner indefinitely.

5.3.3 The Plate-Like Particle

The simulation of plate-like particles is rare and to date only Yamamoto and Matsuoka [72] are believed to have accomplished this numerically with their PSM simulations. Experimentally, there are notable studies on the orbital rotation of oblate discs by Trevelyan and Mason [24], Goldsmith and Mason [26] and Anczurowski and Mason [90]. While oblate discs have aspect ratios $a_r < 1$ it is observed in these experimentally derived works that the orientation of the main axis of revolution still obeys the Jeffrey Eq. (2.2). For this section, plate-like particle species were created and compared with the theoretical prediction for oblate ellipsoid orientation in shear flow. Fig.

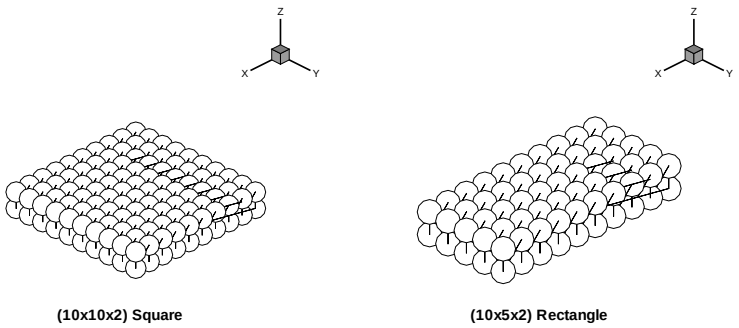

Figure 5.17: The $(10 \times 10 \times 2)$ square plate (*left*) and the $(10 \times 5 \times 2)$ rectangular plate (*right*). (xy) plane view. (Subunit diameter not drawn to scale)

5.17 shows two example 3D plate-like particle species used in the simulation.

The square plate (Fig. 5.17 (*left*)) is a 200 subunit particle made of two (10×10) interlinked layers, while the rectangle (Fig. 5.17(*right*)) uses 100 subunits in a double (10×5) layer. For the results following, the subunit bond stiffness was set to a high stiffness value of $E_{sim} = 5000$. The particle is placed at the global origin and subjected to Newtonian shear flow. The main 'axis of revolution' **n** of the square plate is located at the centre and points perpendicularly from the plate surface (Fig. 5.18). For the simulated data,

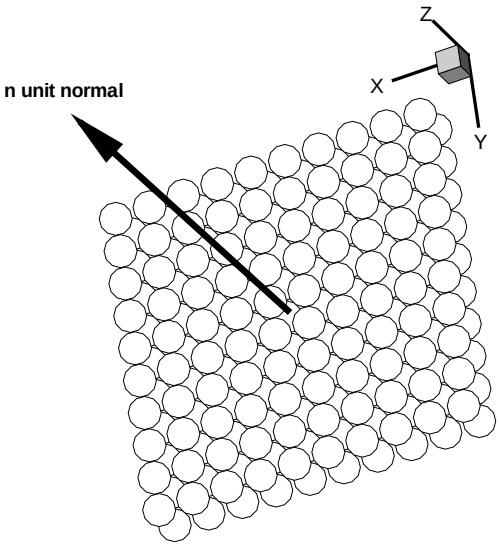

Figure 5.18: The orientation axis for the square plate is defined by vector **n** located at the centre of the plate and directed perpendicularly from the surface.

the initial orientation of the particle is always such that the plate edges are parallel to the constant (x) and constant (y) planes, and unit vector **n** is 60° from the (z) axis pointing towards the (x) axis, lying in the (xz) plane, i.e. the initial orientation (Jeffrey orbital constant value) is $C = 0.1732$. Since

the square plate width is 9 times the thickness, the aspect ratio is $a_r = \frac{1}{9}$. When particle aspect ratio is lower than 1 the Jeffrey theory predicted that the Jeffrey orbit changes orientation from one with a tendency to linger in the shear direction, to one tending to cross the shear direction (see Fig. 5.19). While an elongated particle has a preference for alignment in shear direction, a platelike particle has a tendency to align such that its largest face is parallel to the shear planes of the flow. One may interpret both these cases as attempts by the particle to minimize the sectional profile presented to the flow freestream. In Fig. 5.19, we see the theoretical plot based on

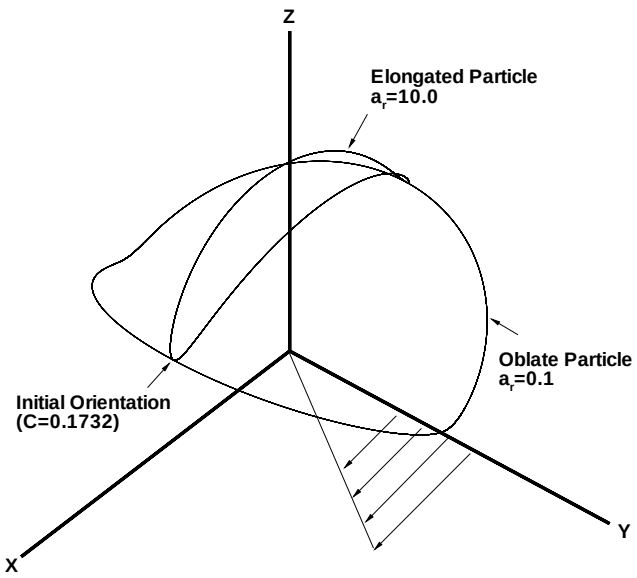

Figure 5.19: For the same orbital constant C, the Jeffrey orbit will differ depending on whether $a_r > 1$ or $a_r < 1$.

Eq. (2.2) for example oblate ($a_r = 0.1$) and elongated ($a_r = 10$) particles. Although the initial orientation of $\mathbf{n}$ is the same, there is a large change in

orbital shape as a_r makes the transition from being greater than, to being less than 1. This is a phenomenon that any simulation of this kind should be capable of reproducing. In Fig. 5.20, snapshots are provided of the output from the current simulation.

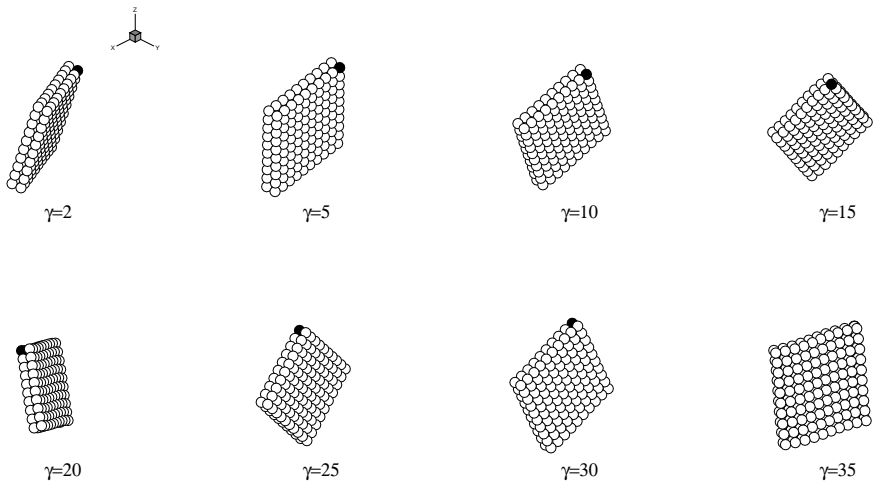

Figure 5.20: Snapshots of simulated plate motion. Subunit '1' is coloured black for better visualisation. ($m = 0.1$, $\eta_{sim} = 10.0$, $E_{sim} = G_{sim} = 5000$, $Re = 0.0107$)

The square particle is seen to rotate about the (z) vorticity axis much like a truly axi-symmetric disc. A majority of time is spent with the plate face parallel to the (xz) shear plane as expected. This motion has also been derived theoretically by Anczurowski and Mason [90], been observed experimentally by Goldsmith and Mason [26, Fig. 2, plate 1], and previously numerically simulated by Yamamoto and Matsuoka [72]. In Fig. 5.21, the simulated motion of the unit normal vector **n** is plotted against the equivalent theoretical result. The relevant parameters are, $C = 0.1732$, $a_{r\ sim} = \frac{1}{9}$, $a_{r\ theory} = \frac{1}{10}$, $\dot{\gamma} = 1$, $\eta_{theory} = 1$, $\eta_{sim} = 10$, $m = 0.1$, and $Re_{max} = 0.0107$. The simulation compares very well against the theoretical result. There is a very slight drift in C compared to the theoretical closed orbit. This is most visible at the y axis extremities, as pointed out in Fig. 5.21. This difference is most likely due to a small amount of deformation and/or residual

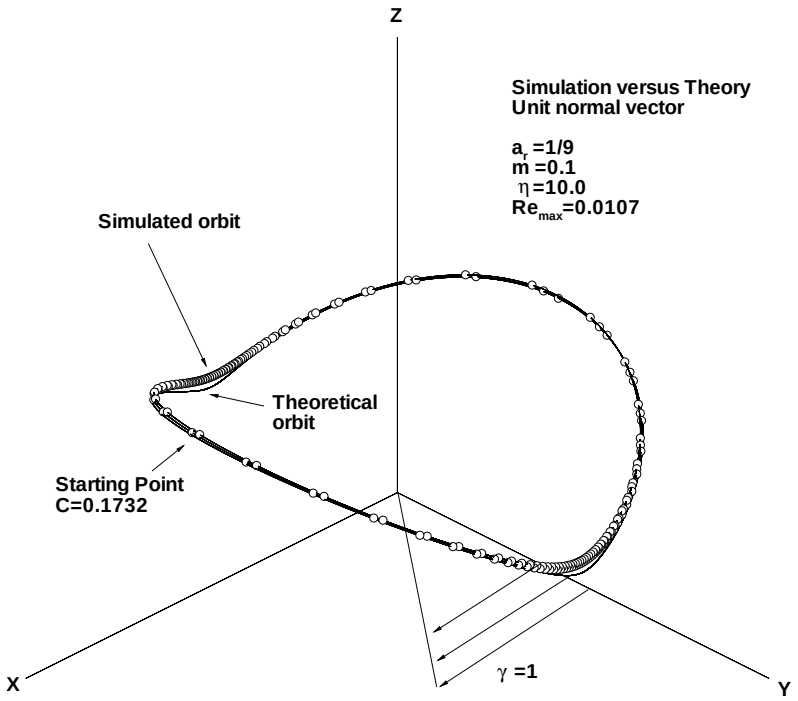

Figure 5.21: Jeffrey orbits are compared for the theoretical oblate disc (Theory (−)), against the simulated square plate (◯).

inertial effect. The overall difference however is insignificant. The maximum Re_{sim} experienced by subunits in this simulation was approximately 0.01. Simulation particles like this square, with Re_{max} in this order of magnitude or smaller, are clearly quite adequate in approximating inertial-less particles. This is also consistent with the 'low Reynolds number' arguments of Happel and Brenner [110] as discussed in Section §5.2.4.

5.3.4 Orbit Constancy of the Plate-Like Particle

Under different combinations of subunit mass and solvent viscosity, the plate-like particles were seen to drift from the Jeffrey predicted orbits by varying degrees. The most likely causes for drift in the orbit are due to particle flexibility, and from inertial effects. Since internal stiffness was set very high in all cases, the flexibility issues are effectively eliminated.

The remaining cause for drift is due to particle inertia. In the non-dimensional simulation, one can obtain a measure of the strength of the inertial effects by correlating against Reynolds number on subunits within the particle. In this section, the Reynolds number on subunits are correlated with observed orbital constant C drift. From this, a range of suitable Reynolds numbers on subunits can be estimated such that inertial effects in simulation may be minimised.

In Fig. 5.22, the tracer path with shear for the #1 numbered subunit (corner subunit) of the plate-like particle is compared side-by-side for a high Reynolds number ($Re_{max} = 1.0743$), and a low Reynolds number ($Re_{max} = 0.0107$) particle. Observing Re_{max} for only the corner subunit is sufficient since the corner subunits experience the greatest relative velocity and hence the highest Re and inertial effects. The subunits closer to the centre of mass and rotation move with less velocity and experience less inertia effects. We only need be concerned with the maximum Re since deviation from Stokes law in a low Reynolds number flow is directly proportional to Re [110]. All other flow parameters and initial particle position (orbital constant $C = 0.1732$) are identical between simulation runs. It can be seen that for a high

Reynolds number (high inertia) particle, the larger planar face of the square particle quickly aligns parallel to the (xy) shear gradient plane, minimizing its sectional exposure to the freestream flow. The particle motion quickly settles to one of pure spin with the orientation axis **n** aligning to the vorticity (z) axis without further rotation. On the other hand, when Reynolds number is low (low inertial effects) the same particle shape reverts to the theoretically predicted Jeffrey orbit for an oblate disc. In Fig. 5.23, the orbital motion of the perpendicular unit vector **n** is shown over a range of inertial conditions $0.0011 < Re_{max} < 53.7148$, (initial $C = 0.1732$ always). It is clear that as Re_{max} increases, the orbital motion degenerates from the Jeffrey theoretical prediction to one where the orientation vector **n** becomes completely aligned with the vorticity axis.

For the various simulation cases $0.0011 < Re_{max} < 53.7148$, in Fig 5.24, we can observe the drift C of the particle with shear γ. For the range $6.4458 < Re_{max} < 53.7148$, C rapidly drops to zero, i.e. the particle rapidly begins spinning in the vorticity axis. This is clearly inertia affected rotation. For $Re_{max} \leq 1.0743$, C is relatively constant (oscillatory but not drifting), i.e. the particle demonstrates the Jeffrey predicted orbit. Inertia does not drastically affect the motion in this range. For the case $Re_{max} = 0.0011$,

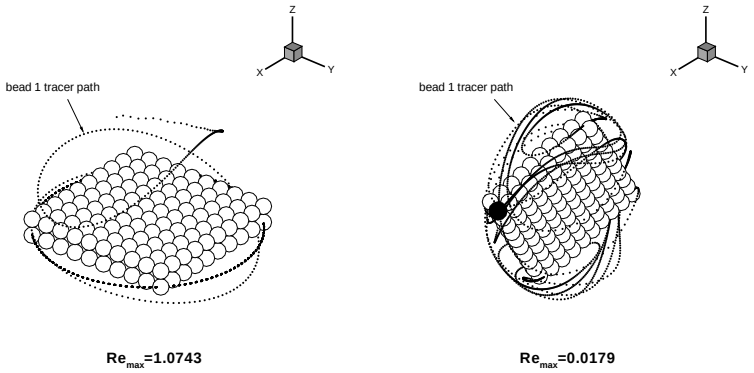

Figure 5.22: Starting from identical flow conditions and initial positions, the plate-like particle orientation varied greatly depending on the Re_{max} on the tracer sphere.

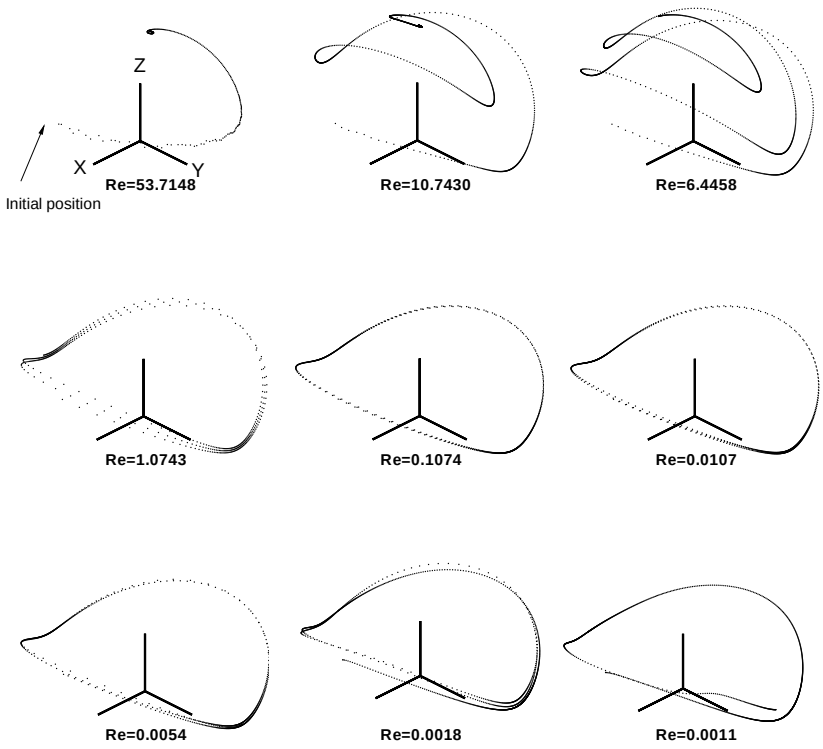

Figure 5.23: As Re_{max} increases, the orbital motion degenerates from one which closely follows the theoretical prediction to one where orientation vector **n**, completely aligns with the vorticity axis.

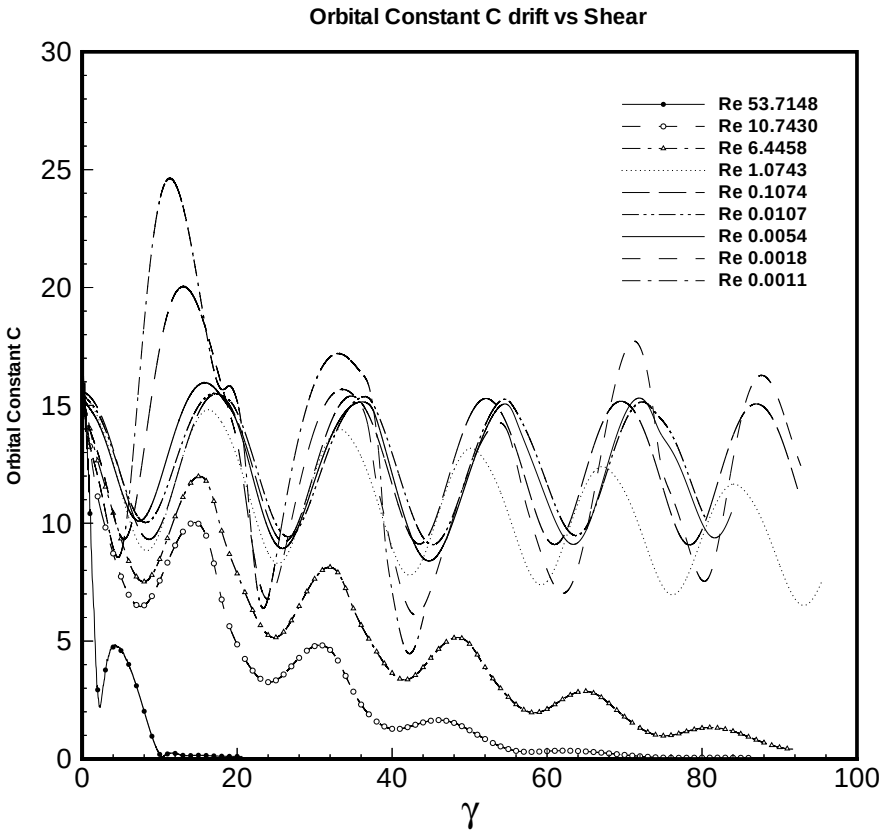

Figure 5.24: Orbital constant C versus shear γ for various Re_{max} square plate particles

the subunit mass was so small in magnitude that numerical errors became significant in the equation of motion Eq. (5.15).

If the linear gradient of each curve, $\frac{dC}{d\gamma}$ in Fig. 5.24 is plotted against Re_{max}, we obtain Fig. 5.25. It is clear in Fig. 5.25 that C drift is nearly

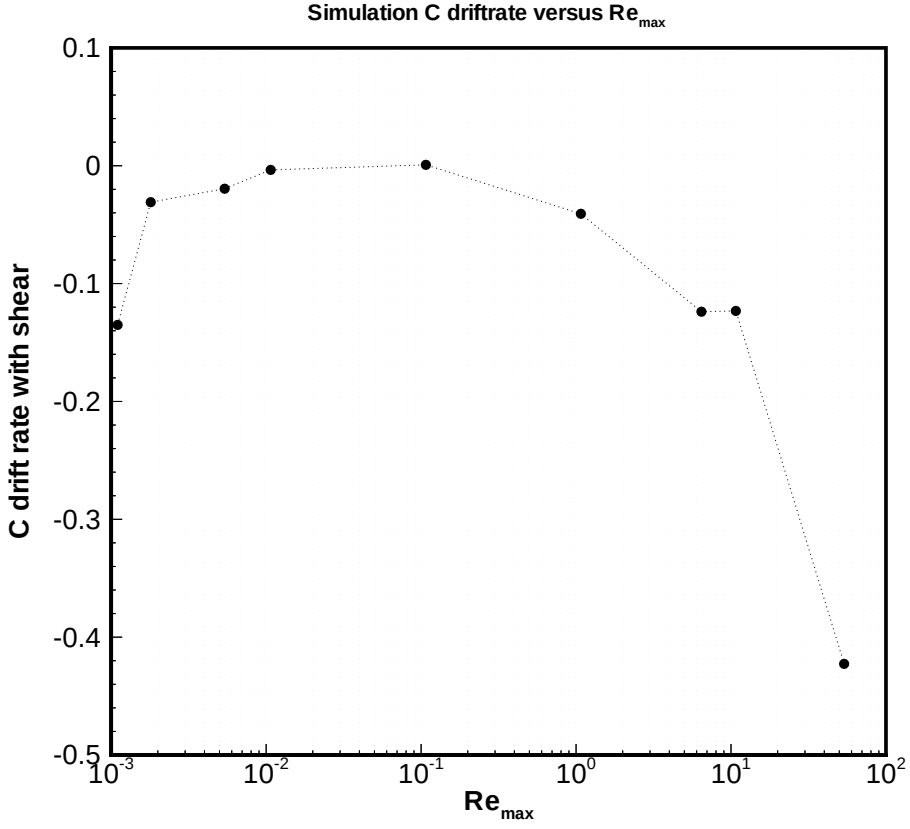

Figure 5.25: The Orbital drift rate $\frac{dC}{d\gamma}$ versus Re_{max} shows a range of Re_{max} where $dC/d\gamma$ is minimised, and hence inertial effects are at a minimum.

zero in the range $0.002 \lessapprox Re_{max} \lessapprox 1.0$, and hence inertial effects on orbital motion are minimised. The behaviour in the range $Re_{max} \lessapprox 0.002$ is affected by numerical effects (simulation results are not obtained from this Re range). So long as the subunits in similar simulation particles are approximately in the range, $0.002 \lessapprox Re_{max} \lessapprox 1.0$, inertial effects should be negligible.

Preferred Orientation

Whether a non-interacting ellipsoid would achieve any preferred orbit has been a topic of discussion since Jeffrey first published his work [4]. Jeffrey himself speculated that orbital constants would tend towards those corresponding to a minimum energy dissipation, $C \to 0$ for $a_r > 1$, and $C \to \infty$ for $a_r < 1$ (i.e. **n** for an oblate ellipsoid tends to rotate without spin purely in the shear plane, while for the elongated rod **n** aligns to the vorticity axis and spins without rotation). Eisenschitz [111] disagreed, believing that all particles would maintain their initial orbit. Various experimental observations agree with neither (but more with Eisenschitz than Jeffrey). Trevelyan *et al.* [24] reported inconclusive results, where C was seen to increase in some instances, decrease in others, or vary erratically. Goldsmith *et al.* [26] found no tendency to drift at all, and Anczurowski *et al.* [90] also reported discs remaining in their initial orbital constant.

The results of this simulation agree more with Eisenschitz and the experimental observations of Goldsmith *et al.* and Anczurowski *et al.*. The observed inertia dependent drift in C shown in this section however suggests that the agreement must be qualified for real life particles which possess a certain mass. Under shear conditions, viscous resistance over the broad plate surface induces a substantial axial spin on the particle, on top of the predicted **n** rotation. As particle inertia increases, the orbit is shown to be increasingly affected by inertia, causing the orbital constant C to tend towards zero at faster rates. When inertial effects are reduced, the particle is shown to increasingly agree with Eisenschitz and comply with Jeffrey's theoretical Eq. (2.2). None of the experimental results, nor the numerical results from Yamamoto *et al.*'s PSM or the current work agree with the Jeffrey 'minimum energy dissipation' idea.

The inertial effect is shown to be a deciding factor in the preferred particle orientation for plates. To ensure agreement with the Jeffrey theory, inertia must be controlled. Jeffrey's theory is an inertialess one, and so these results highlight the difference with and without inertia. The results from Fig. 5.25

show that so long as subunits experience low $Re_{max} \lessapprox 1.0$, and preferably $Re_{max} \lessapprox 0.1$, inertial effects should be rendered insignificant.

It should be noted that depending on the inertia of the particle, the observed drift may take many orbits to become apparent. All particles with mass in a Newtonian fluid will eventually drift, however with careful consideration, parameters can be selected such that inertia is effectively negligible for the time period to be studied in simulation.

5.3.5 Other shapes

In this section, the shear flow dynamics of other particle shapes are presented. No previous results are believed to exist for comparison so this section will merely report qualitatively on the observed dynamics found. The species tested were the rectangular plate (Fig. 5.17*right*), the torus (Fig. 5.1), small and large 'balls', and the limp Pom-Pom. The limp Pom-Pom is another case where flexibility is permitted and so should be reviewed in isolation to the others. The Newtonian fluid is always in shear flow ($\dot{\gamma} = 1$).

A discussion on rod-like particle orientation usually involves measurements of C and the motion of the orientation vector $\mathbf{n}$. The information to be conveyed here however is intended merely to be illustrative of the rotational behaviour observed. Also, some particle shapes here are not adequately described with single vectors or orientation parameters. Therefore for the following particles, instead we plot the paths of 'tracer' subunits in three dimensional space. The particle itself in its final configuration (at $\gamma_{end} = 300$) is finally superimposed on the tracer plot for better visualisation of the shape and motion.

Rectangle

The rectangular plate is constructed in the same way as the square plate described earlier ($E_{sim} = G_{sim} = 5000$). The rectangle (Fig. 5.26) in shear flow was seen to align parallel to the (xy) shear plane increasingly rapidly as Re_{max} increased. This is consistent with the behaviour of the square plate

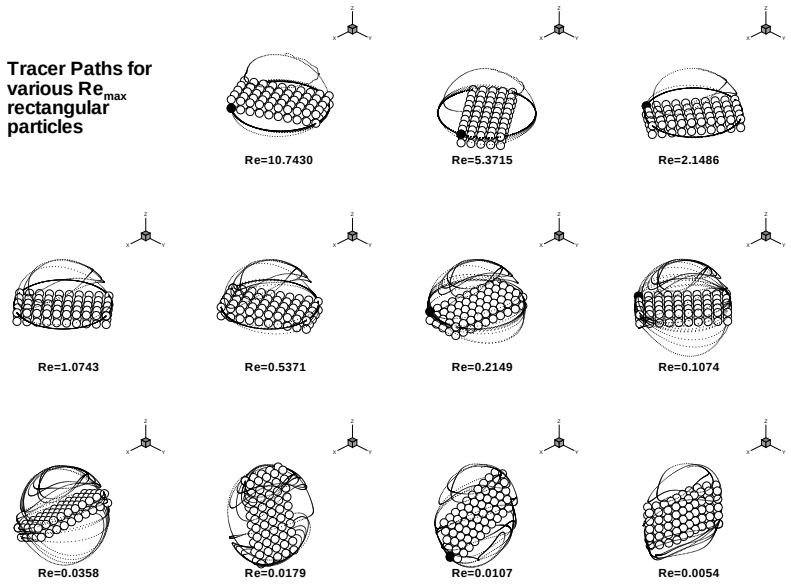

Figure 5.26: The rectangular particle prefers an (xy) shear plane ($C = 0$) orbit for high Re_{max}. For low Re_{max} orbits, the motion becomes irregular and does not follow a closed orbital path like the square plate.

under similar circumstances. At the lower Re_{max} however, the rectangular plate shows a tendency for extended periods of 'rolling' about its longer axis (see Fig. 5.26 $Re_{max} = 0.0179$), interspersed with erratic Jeffrey-like orbits and intermittent reversals in orientation. Unlike the rod or disc, the rectangle is not axi-symmetric and so with each orbit is unable to maintain any stable C orbit. These observations for the rectangular plate are entirely consistent with observations described by Yamamoto and Matsuoka [72].

Yamamoto and Matsuoka also simulated 'logrolling' of rod-like particles with their PSM. They discussed the theoretical possibility of a stable vorticity-aligned 'logrolling' suspension state under certain low shear conditions. Yamamoto and Matsuoka speculated that 'logrolling' had not been seen in simulations only because low aspect ratio particles were never tested ($a_r < 20$). According to Yamamoto and Matsuoka, a low particle aspect ratio was an important factor for 'logrolling' to occur.

Yamamoto and Matsuoka's view on 'logrolling' may well be correct. This opinion is backed by the current result, and also those seen for low a_r shapes like balls (Section §5.3.5), and the pom-pom (Section §5.3.5). The ball shaped particle ($a_r \approx 1$) spins purely about the vorticity axis. In this case 'spin' could be seen as a type of 'logrolling'. The limp pom-pom result shows that particles with little or no propensity to maintain any particular shape would be moulded by the flow into a vorticity logrolling ovoid (i.e. a spheroid extended along the axis of spin). The default preference of any particle is to 'logroll' about vorticity until that preference is superseded by stronger influences, e.g. the preference for rigid rods to align to the streamline. The topic of course requires more study than can be offered here and so we shall depart from this subject and leave it open for other researchers.

Torus

The torus (Fig. 5.1, $E_{sim} = G_{sim} = 2000$) was expected to behave in a similar manner to the square plate and oblate disc. In Fig. 5.27, the torus in fact showed a rather different response. Over the range of inertial conditions

tested ($0.0233 < Re_{max} < 1.8608$) the torus invariably preferred alignment with the (xy) shear plane. For $Re_{max} = 1.8608$ the alignment was rapid and was indicative of strong inertial forces. For $Re_{max} = 0.3722$ and 0.1861, the torus attempted several square plate-like orbits, however again it quickly returned to the xy plane. Since in some respect the torus is similar in shape to a plate or disc, this is not surprising. At $Re_{max} = 0.0233$ the torus deformed into a roughly ellipsoidal shape and aligned along the shear direction. This is like the behaviour of flexible red blood cells observed under similar conditions by Goldsmith [112].

Small and Large Balls

In Figs. 5.28 and 5.29 are the tracer paths of small and large 'balls' in shear flow ($E_{sim} = G_{sim} = 5000$). The balls were roughly isometric, the smaller 'ball' actually being a diamond shape and the larger, a rounded cube. As neither shape presented any significant cross sectional variation to the flow during rotation, both particles settled on rotating entirely about

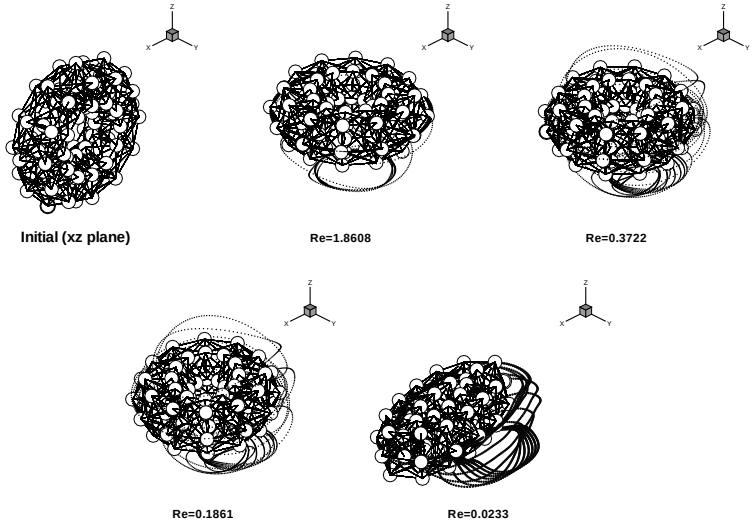

Figure 5.27: The torus was seen to show a strong preference to align parallel to the (xy) shear plane regardless of the inertial conditions.

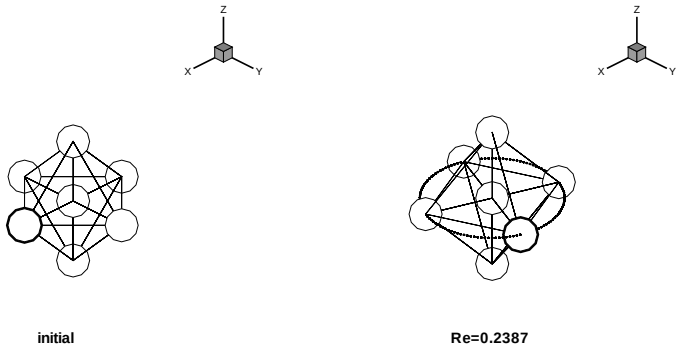

Figure 5.28: The small ball (7 subunit body centred diamond) rotated entirely about the (z) vorticity axis.

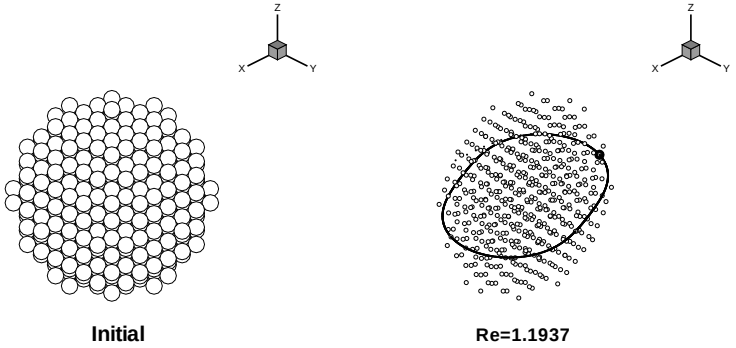

Figure 5.29: The big ball (514 subunit rounded cuboid) also reverted to pure spin about the (z) vorticity axis. The subunit size (*right*) is reduced for better view of the tracer path.

the (z) vorticity axis. It is also noted that like the torus, there was a slight tendency to elongate into an ellipsoid aligned in the shear direction. Since E_{sim} was higher here, and the ball structures are more highly cross linked, the deformation was not as great as for the torus.

Pom-Pom

The Pom-pom is a partially 2D structure since the pom-pom branches are not full 3D structures but merely linear chains (Fig. 5.30). The particle internal stiffness in the central cubic area was $E_{sim} = G_{sim} = 2000$, while along the branches there is no cross bracing and hence the branches are completely flexible, similar to the Hinch thread (Section §5.3.2). The results here therefore should be considered separately from the other particles, as with all other particles where flexibility was allowed (recall Section §5.2.3). The central core is a cuboid but while the 8 branches are nearly inextensible,

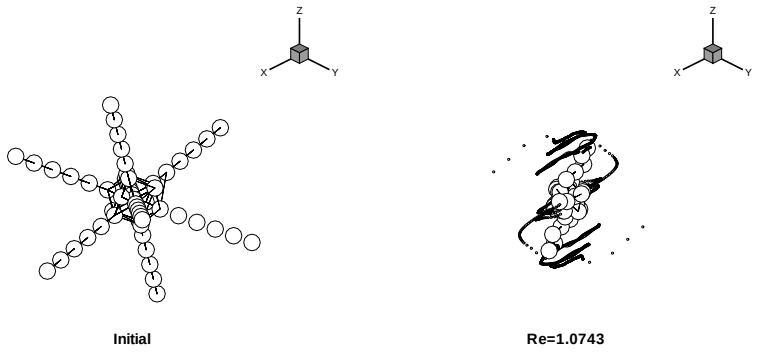

Figure 5.30: The limp Pom-pom is seen to roll into a central mass rotating with the (z) vorticity axis.

they are flexible in bending. The Pom-pom is 'limp' except for its cuboid core, and branches are free to drift and entangle in the flow. In shear flow we see that the pom-pom branches wind around the core forming an ovoid, but generally irregularly structured mass twisted about the (z) vorticity axis. Once this final elongated shape coalesced, the shape did not change any

further and simply spun about the (z) vorticity axis for the remainder of the simulation time.

5.4 Summary and Conclusions

This chapter reported on a new method for the direct simulation of particles suspended in Newtonian fluid. The method allowed for the modelling of arbitrarily shaped three dimensional particles. The new particle simulation was then subjected to verification tests in order to gauge its ability to reproduce known particle dynamic behaviour. Finally the simulation was run for several important and common particle shapes and the particle dynamics of these species were reported.

Rod-like particles exhibited the theoretically predicted Jeffrey orbit with a preference to linger in the (x) shear aligned orientation. The orbital period and spin rate was in good agreement with previous theoretical, numerical and experimental studies. Flexible rod-like particles were shown to exhibit deviant spiralling Jeffrey orbits in agreement with previous numerical works. For the case of semi-rigid multibody particle simulations, it was argued that including long-range hydrodynamic interaction was sometimes unnecessary for qualitative results. Plate-like particles were shown to rotate in either a Jeffrey theory predicted orbit, or to revert to an orientation state parallel to the (xy) shear plane. The latter state was due to the effects of particle spin and inertia. The effects of inertia in simulation were however shown to be easily controllable. By modifying simulation parameters such that the largest Re experienced by a constituent subunit was less than about $Re_{max} < 1.0$, or preferably $Re_{max} < 0.1$, inertial effects were made negligible. This range of Re_{max} of course varies from particle to particle however particles of similar mass or shape should respond in a similar way to Re_{max}.

Following the verification tests for rod and plate motion, the simulation was then tested in shear for a range of other representative shapes from the elongated rectangular plate to the centrally concentrated balls and pom-pom.

The rectangular plate moved in an irregular manner sometimes spinning with vorticity about its longer axis reminiscent of the log-rolling of liquid crystal particles, other times exhibiting Jeffrey-like orbits like an elongated rod, and sometimes reverting to the (xy) shear plane spin like a square plate. As a particle's mass distribution became more centrally concentrated (torus & balls) the particle motion was shown to revert to pure spin about the (z) vorticity axis regardless of the simulation viscosity. These centrally concentrated particles do not present any significant variation in profile to the freestream flow as it rotates. In lieu of a strong orientation, the orientation of the torus and ball is dominated by the flow vorticity hence the observed vorticity spin preference. Finally the limp pom-pom showed a tendency to coalesce into an irregular elongated mass and spin purely in the vorticity axis. The results presented here are but a few particle shapes of interest. We have now established that the method described here can credibly reproduce a wide range of particle dynamics.

In the following chapters, the simulation is extended beyond the simple shear flow regime by embedding the particles within realistic complex flow fields. In Chapter 6, we study the effects of varying flow gradients and inertia on the trajectory of particles. The cylindrical Couette flow field is used to demonstrate the ability of the simulation method to numerically recreate inertially driven particle migration. In Chapter 6, we study the rod-like fibre as it travels through a diverging channel. The evolution of fibre orientation during the shear to extension transition will be studied in detail. Through comparison and analysis of previous theoretical treatments of this situation, the deficiencies of existing 2D fibre theories will be demonstrated and new fibre dynamics based on the full 3D particle model will be described.

Chapter 6

Particle Simulation in a Complex Flow Field

6.1 Introduction

This chapter is the second of three on the direct simulation of arbitrarily shaped particles in Newtonian flow. The method described in the Chapter 5, is now expanded with the ability to embed particles within a complex flow field.

The new simulation is used to study the effects of non-linear shear gradient and inertia on particle migration in a cylindrical Couette flow field. While analytic solutions for the Couette flow field are available, it is done this way here (as a presolved FE field) as a demonstration of the simulation in a familiar flow situation. More complicated flow fields can be also be used, as is done in Chapter 7.

This chapter reports on the development of a variation on the work in Chapter 5. The simulation particles are now allowed free movement, embedded in a realistic flow field. Because the simulation method is capable of modelling particle dynamics in a non-linear shear gradient, we chose to test this ability for the case of a rod-like particle in a common non-linear flow field - the cylindrical Couette flow field.

In the following sections, fibre motion in a cylindrical Couette flow will be described. The simulation method will be briefly re-iterated with new information on the method of embedding within a pre-solved finite element mesh. Finally the results will be presented and discussed.

6.2 Particle Migration

Phillips *et al.* [81] is often referred to as the basis of many subsequent suspension migration theories. The key mechanism for particle migration in shear flow, according to their theory, arises from the imbalance in the frequency of irreversible interparticle collisions on the side of the particle experiencing the higher shear rate, as compared to the side with lower shear rate. The reaction of the particle to this imbalance is to translate normal to the shearing plane in the direction of lower collision. Since the interaction is irreversible the displacement does not return to zero once the colliding particle has moved on. According to Phillips *et al.*, this is the basic mechanism of migration. Furthermore, as more particles move to regions of less collision frequency, a concentration gradient develops, causing a viscosity gradient which also contributes to the migration.

This theory however does not account for the migration of lone particles which have also been observed in experiments. There must be other conditions where particle migration may take place, which do not depend on interparticle interaction. For example under certain conditions, inertia may contribute to individual particle migration [113]. The lateral force arising from the 'Slip-Spin' behaviour of a spinning sphere in a viscous medium was studied by Rubinow and Keller [114]. The observed 'tubular pinch effect' for suspension tube (Poiseuille) flows suggests an inertially induced migration away from the tube axis balanced by a repelling wall-effect near the tube wall. The result is a particle concentration peak located approximately $0.6 \times$ radius from the tube walls [115]. Observations of deformable blood cells in tube flows suggest that particle shape and deformation also play a part in

migration [112][116].

With the new capability for embedding complex flow fields, the simulation method is suited to particle dynamics in non-linear flow conditions, and is also capable of accounting for particle shape and inertia. The cause for the migration in the results of this chapter are already well known. It is clearly inertia-induced migration (results will show particle drift in reponse to an increase in Re on subunits). We present these results only to demonstrate this simulation's ability to reproduce this behaviour.

6.3 Numerical Method

The numerical method was described in detail in Chapter 5. The method used is mostly unchanged apart from the extensions described in the following sections (§6.3.2). The reader is referred to Section §5.2.5 in Chapter 5 for a full description of the numerical method used.

6.3.1 The 3D Particle

An example of a simulation rod-like particle is shown in Fig. 6.1. This rod-like particle was used to obtain the simulation results for this chapter. In this case, the rod-like particle is constructed from a square cross section. With each *level* (see Fig. 6.1(xz)*plane view*), the square section is rotated by 45° about the main (z) axis. This arrangement allows for slightly tighter packing of subunits and more diagonal bonds than if the rotations were not made. The bending characteristics are closer to a true cylindrical rod than the equivalent cuboid rod-like particle. The width of the fibre square cross-sections are 3 (i.e. the corners of the square cross-section are at local coordinates $(1.5, 1.5)$, $(-1.5, 1.5)$, $(-1.5, -1.5)$, and $(1.5, -1.5)$), and there are 20 levels, each of height 3. Sphere subunit radius is 1. The fibre 'diameter' is based on an equivalent circular cross section i.e. $l^2_{sqr.side} \equiv \pi r^2_{eqv.circle}$, hence, $r_{eqv.circle} = \frac{l_{sqr.side}}{\sqrt{\pi}}$ as in Chapter 5. Aspect ratio is then calculated based on this equivalent radius, i.e. $a_r = 17.72$.

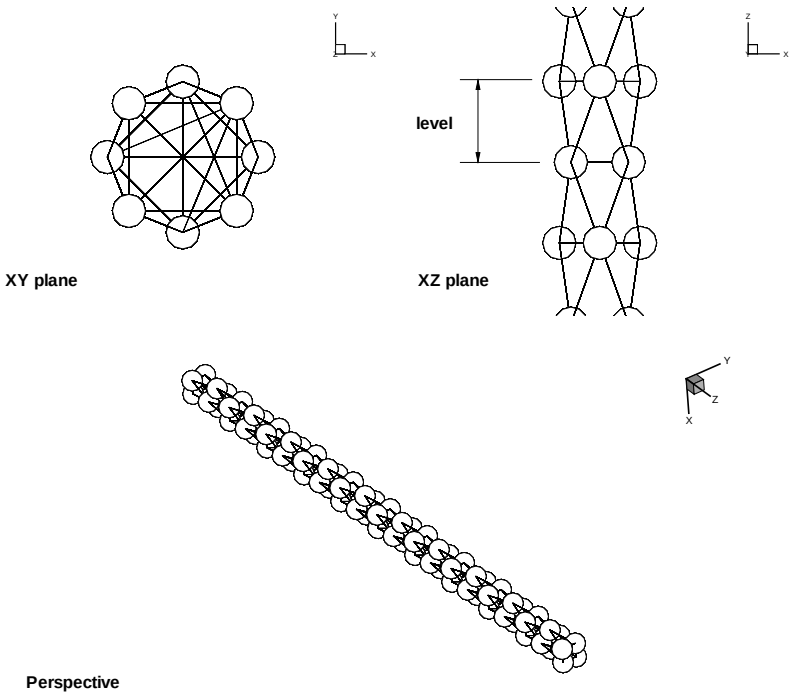

Figure 6.1: 3D rod-like particle, 84 spheres (spheres are not drawn to scale)

Each subunit is linked to every other subunit in the same level, and also the level above and below. The resulting structure is a highly regular cross-linked, rod-like shape. Coordinates of each subunit correspond to the nodal positions of the 3D framework. Each subunit's relationship to the larger structure is completely described by 94 parameters. These are, its individual identification number, its coordinates (relative to a local origin), identification numbers of other subunits with which it shares a bond (maximum 30), and each bond's non-dimensional Stiffness moduli (E_{sim}) and Shear (G_{sim}). For the subunit i, 94 parameters are required, as shown in Eq. (6.1).

$$\left\{ \begin{array}{c} \textit{for bead } i: \\ ID_i, \\ (x,y,z)_i, \\ [ID_1, ID_2, \ldots, ID_{29}, ID_{30}]_i, \\ [E_1, E_2, \ldots, E_{29}, E_{30}]_i, \\ [G_1, G_2, \ldots, G_{29}, G_{30}]_i \end{array} \right\} \tag{6.1}$$

To fully describe the structure and mechanical characteristics of the rod-like particle consisting of 84 subunits, a (84×94) *primitive* matrix is sufficient.

Each particle used in simulation is represented by a primitive matrix. There is no limitation to the size of the primitive matrix apart from those relating to computational resources and solution time. Particle mechanical strength may be modified by altering the Stiffness or Shear modulus (E_{1-30} and G_{1-30}) on a bond-by-bond basis within the primitive matrix. The particles are then scaled, rotated and translated to an appropriate initial position prior to simulation.

6.3.2 Embedding particle within a FE flow field

In this extension to the method, the simulation is now allowed to take place embedded within a pre-solved finite element flow field. The Finite Element PDE solver *FastFlo* ver3.0 was used to pre-solve the non-dimensionalized

momentum Eq. (6.2) (2D incompressible Navier-Stokes).

$$\frac{\partial \mathbf{v}}{\partial t} + (\mathbf{v} \cdot \nabla)\,\mathbf{v} + \nabla p - \frac{1}{Re}\nabla \cdot [\nabla \mathbf{v}] = \mathbf{0} \tag{6.2}$$

Fluid Reynolds numbers were in the range $0.001 < Re < 0.005$ approximating creeping flow. An Operator Splitting algorithm was used to solve the convection and diffusion terms in two separate stages per convergence iteration. This method is an established one and as it is not crucial to the particle simulation, it will not be elaborated further here. A full description is in [117, Ch. 20]. *Fastflo* is used to generate the velocity v_i, and velocity gradient $\frac{\partial v_i}{\partial x_j}$ fields which are imported into the particle simulation. FE meshes in *FastFlo* are composed of 2D 6-node 7-point quadrature triangle elements, as shown in the example in Fig. 6.2. The meshes are unstructured and auto-generated by

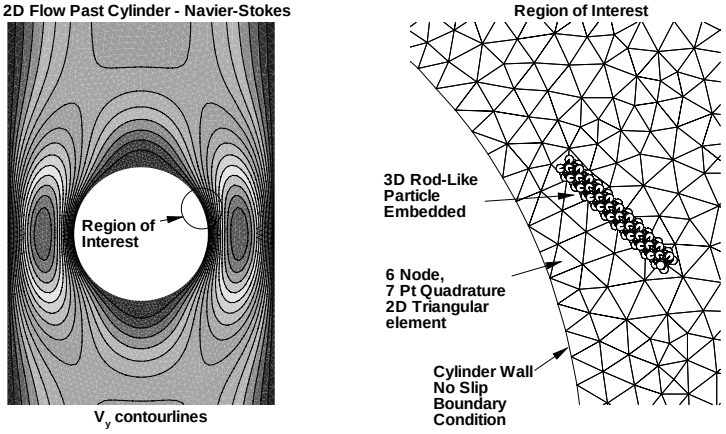

Figure 6.2: The FE solution data for Navier-Stokes flow imported and used in the particle simulation. (Fibres are not drawn to scale)

FastFlo given the flow domain and boundary conditions. The characteristic dimensions of the FE solution are independent of the simulation's characteristic dimensions, e.g. the characteristic length in the couette solution is the inner cylinder radius, while in the particle simulation, it is the subunit radius a. The velocity field must be appropriately scaled to suit the particle

simulation and the various dimensions after scaling are correctly reconciled for an appropriate particle simulation to proceed.

The simulation extracts the local flow velocity and velocity gradients of each subunit by referring to the imported FE data. After the correct element is identified, the flow data is interpolated from the basis functions for the triangular element. Unlike previous single-body particle works, this particle simulation maintains its validity when the flow field is *non-linearly* varying over the length scale of the particle. This is because the local flow conditions around a particle are sampled multiple times at the coordinates of each individual constituent subunit. The flow linearity requirement is not entirely eliminated, but is now limiting only over the length scale of subunits, not entire particles.

Since the particle simulation is fully three dimensional, the 2D FE flow field is extruded into the (z) axis once imported into the particle simulation. Along the (z) axis, the (xy) flow field planar sections are identical. Therefore, while $\frac{\partial v_x}{\partial x}$, $\frac{\partial v_x}{\partial y}$ and $\frac{\partial v_y}{\partial x}$, $\frac{\partial v_y}{\partial y}$ gradients are possible, velocity and velocity gradients in the (z) axis direction are reduced to zero. The simulation may easily be modified to import truly 3D meshes, but this will be left for future extensions. Wall effects are not considered at this time. Temperature effects, phase changes, or free surfaces are also not considered.

6.3.3 Simulation Procedure

Infinite flow domains are not permitted and so limits are imposed on the space within which particles may exist in this simulation. The global maximum and minimum range is specified prior to simulation, $\{X_{min}, Y_{min}, Z_{min}\}$ and $\{X_{max}, Y_{max}, Z_{max}\}$, producing a large cuboid as the allowable simulation domain. In relation to the imported FE flow field, the FE mesh must exist entirely within this allowable domain. If particles stay within the FE domain, then they should never travel beyond the particle simulation limits.

Once the simulation commences, the equations of motion of Section §5.2.5 are solved and the positions of subunits are updated for each iteration. Rel-

evant data is output to a datafile for post-processing. The simulation continues in $d\gamma$ increments until the ending deformation γ_e or other termination condition is met.

The simulation results and also the FE flow field data used in Section §6.4 were computed on Intel $x86$ processor based PCs running MS-Windows Operating Systems, and RedHat Linux v7.3 operating systems. The simulation source code was written in ANSI standard Fortran77 and compiled using Intel Fortran 95 Compiler for Linux v6, and Digital Visual Fortran v6 Compiler.

6.4 Results Inner Rotating 2D Couette

6.4.1 Couette flow field

The 2D Navier-Stokes flow field (Eq. 6.2) was solved by Finite Element method in *Fastflo*. The characteristic length, and inner cylinder radius was $R_i = 1$, while the outer stationary cylinder was of radius $R_o = 3.717$, as shown in Fig. 6.3. These proportions were chosen to be consistent with other well cited earlier works that used these same proportions [81][118][119]. For the non-dimensional FE solution the rotation rate of the inner cylinder is $\Omega_{anticlockwise} = 1$. The generally unstructured mesh was concentrated as a function of radius with the smallest triangular elements at the inner cylinder surface. In all 4000 corner nodes, and 7744 triangular elements were used. A non-slip, no flux surface boundary condition was applied and the solution was iterated until a convergent result was obtained. The resulting flow field was one of concentric circular velocity paths with the highest velocity and shear rate at the inner cylinder surface. The velocity and shear rate reduces non-linearly to zero at the outer cylinder boundary.

After the FE velocity field is obtained, it is scaled by a factor 269. This is the ratio between the Couette flow's characteristic length r_i, and the particle simulation's characteristic length a. This made the scaled inner Couette radius 269 times larger than the particle simulation characteristic length, i.e.

$r_i = 269a$. The scaled inner radius was approximately 4.3 and 76.8 times the fibre length and diameter respectively (see Fig. 6.3). In the process, the FE field is scaled to dimensions roughly of the scales seen in the lab, and finally suitable for the particle simulation.

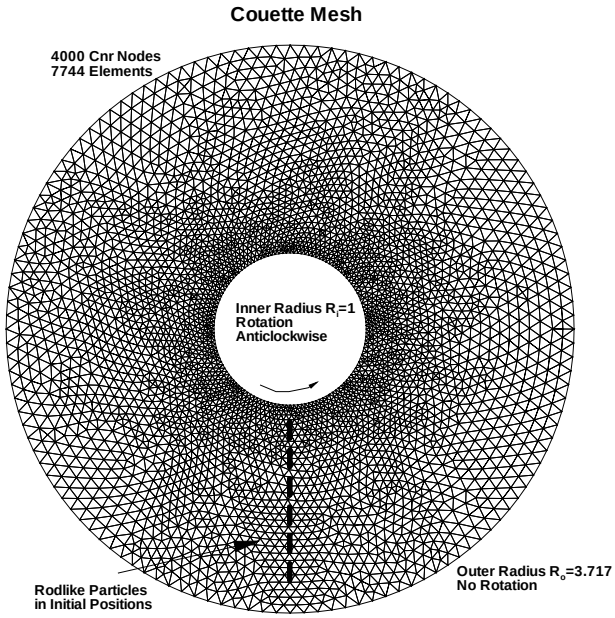

Figure 6.3: The cylindrical Couette FE mesh with six fibre particles in their initial positions

This velocity field was used in the simulation with embedded rod-like particles (as seen in Fig. 6.1). Three different series of simulations were run with varying particle parameters. (1) In the first, particles are 'rigid' ($E_{sim} = G_{sim} = 8000$), with parameters such that subunits are experiencing low Reynolds number flow conditions. (2) In the second, particles are 'flexible' ($E_{sim} = G_{sim} = 400$), with parameters such that subunits are experiencing low Reynolds number flow conditions. (Note, the reader is reminded that all results for flexible particles should only be viewed as qualitative in-

formation, and in isolation from other simulation results. See Section §5.2.3) (3) In the third, particles are 'rigid' ($E_{sim} = G_{sim} = 8000$), with parameters such that subunits are experiencing High Reynolds number flow conditions.

Three rod-like particles were arranged initially radially outward at distances $radii = 0.368, 0.568, 0.868$ from the centre. (For the high Reynolds number case, six particles were used, initially located at $radii = 0.368$, 0.468, 0.568, 0.668, 0.768, 0.868) The particles were placed at these radial intervals to experience flow conditions at the various radial distances from the moving inner cylinder surface. Since this is an inertial particle simulation, and fluid velocities range according to radius from the centre, the initial Re_{max} varies depending on the initial radial position of each fibre. The estimated initial Re_{max} for each fibre's subunit #1 is listed in Table 6.1. By 'Radial Position'

Radial Position $1 < r < 3.717$	Low Re Sim.	High Re Sim.
1.3680	1.5381	76.9071
1.7398	–	48.0669
2.1115	0.6088	30.4424
2.4833	–	20.8290
2.8550	–	12.8179
3.2639	0.1282	6.4089

Table 6.1: Approximate subunit Re numbers in Couette flow

(in Table 6.1) it is meant the radius from the centre of the Couette device, and is given relative to the inner cylinder radius $r_i = 1$.

The tracer subunit positions on each fibre are recorded against shear deformation. Shear deformation is taken to be the shear of the fluid at the non-slip inner cylinder surface. The simulation shear ranges from $\gamma_i = 0$ to $\gamma_e = 1000$, with $d\gamma = 0.0002$. The inner cylinder therefore executes 159.1 anticlockwise revolutions during the simulation.

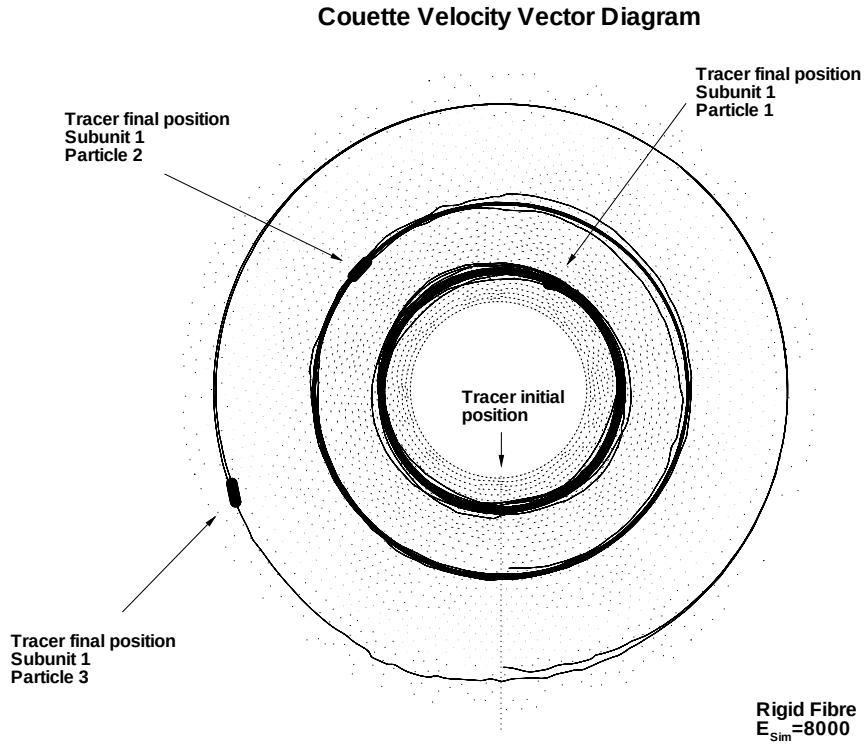

Figure 6.4: 'Rigid' fibres in low Reynolds number Couette flow. Tracer paths are plotted.

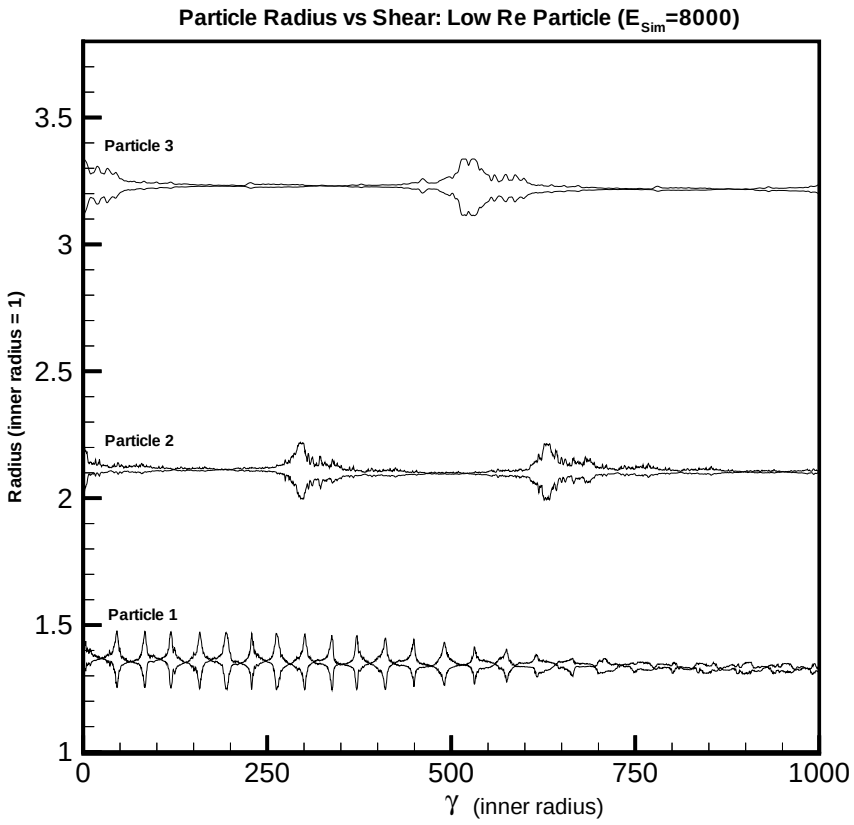

Figure 6.5: 'Rigid' fibres in low Reynolds number Couette flow. The radius of tracers from the Couette centre are plotted against γ.

6.4.2 Rigid Fibre, Low Re

In Fig. 6.4, the tracer paths for subunits #1 of each fibre are plotted over the range $0 < \gamma < 1000$. The result is as expected. Fibres are seen to tumble occasionally as in shear flow, and tracers move in concentric circles of roughly the same radius about the Couette.

In Fig. 6.5, the radial position of tracers are plotted against γ. Radius generally does not change indicating that fibre motion is in concentric circles, as expected. The 'pulses' in this figure indicate fibre tumbling as it travels around the Couette. In the locality of the fibre, the flow is roughly shear flow and so Jeffrey-like orbits are expected. The 'pulses' drop in frequency with radius since shear rates decrease with radius.

6.4.3 Flexible Fibre, Low Re

In Fig. 6.6, the tracer paths for subunits #1 of each fibre are again plotted over the range $0 < \gamma < 1000$. The result is again as expected. Fibres are seen to tumble occasionally as in shear flow, and tracers move in concentric circles of roughly the same radius about the Couette.

In Fig. 6.7, the radial position of tracers are plotted against γ. Radius again does not change much indicating that fibres move in concentric circles. The 'pulses' with γ indicate tumbling in the fibre as it travels around the Couette. The 'pulses' also decrease in intensity with γ. On closer inspection of the data, it was revealed that fibres slowly transformed from head-over-heel tumbling, to axis rolling in the vorticity axis. This is a known behaviour of flexible fibres in shear.

It must be concluded that flexibility alone does not appear to contribute to any particle migration. This is a point that is revisited in Section §6.4.5.

6.4.4 Rigid Fibre, High Re

In Fig. 6.8, we see the tracer path for subunit 1 of particle 1 (the inner most particle at initial $r = 1.3680$). The position of the six fibres at the simulation

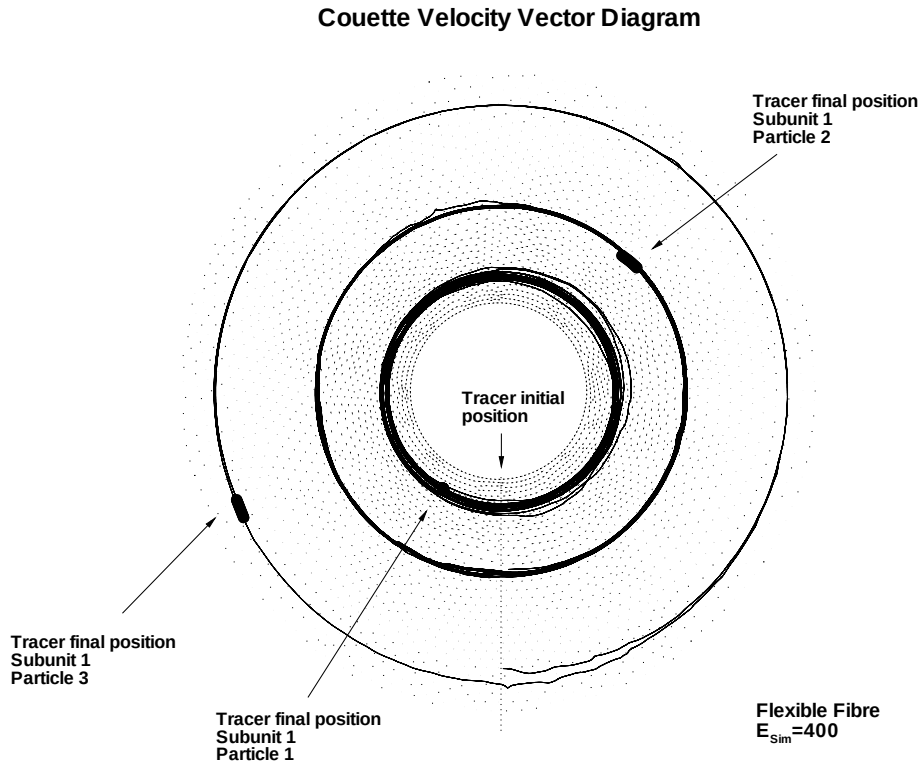

Figure 6.6: 'Flexible' fibres in low Reynolds number Couette flow

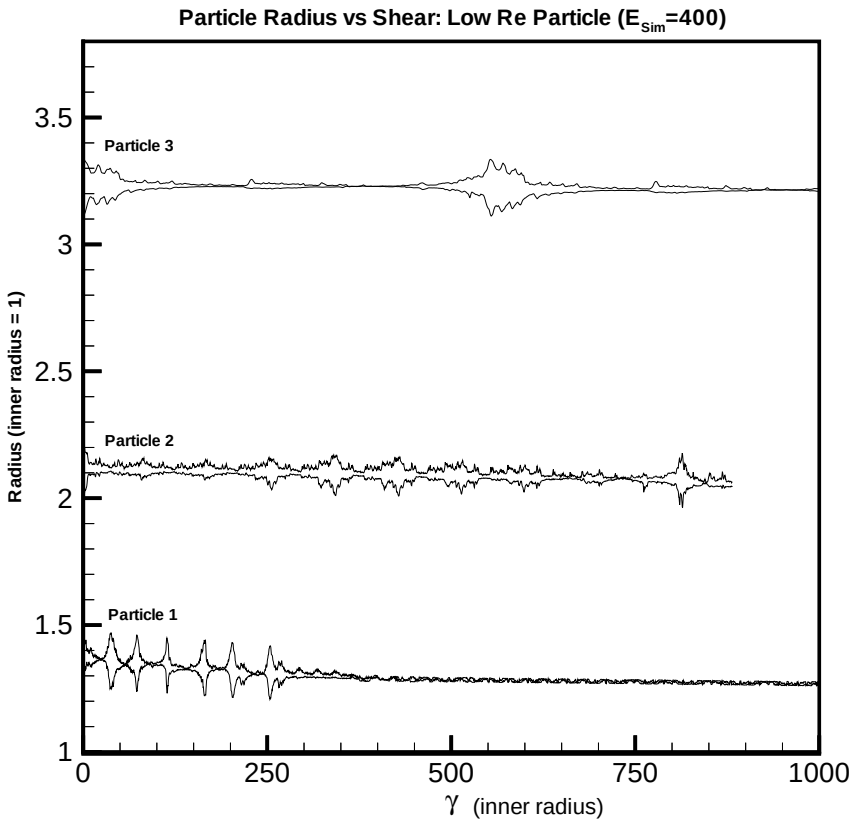

Figure 6.7: 'Flexible' fibres in low Reynolds number Couette flow. The radius of tracers from the Couette centre are plotted against γ.

end $\gamma_e = 1000$ is also drawn for better visualisation. The tracer path and the particles are superimposed over a velocity vector field. The tracer path

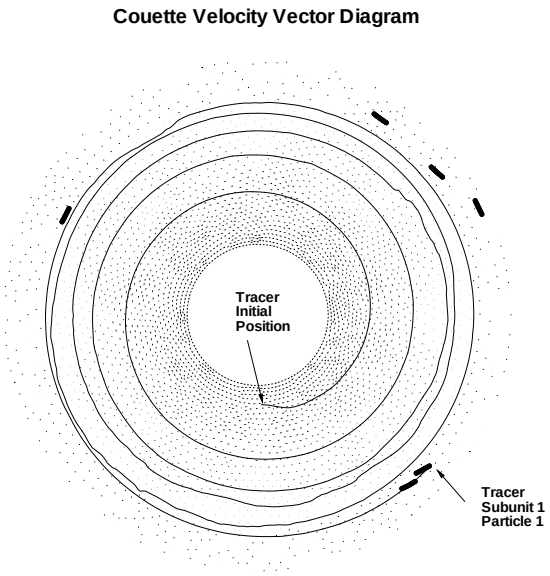

Figure 6.8: 'Rigid' fibres in high Reynolds number Couette flow. A clear drift has taken place for all six fibres.

shows a clear spiralling outward. The inner most fibre subunit was initially experiencing a very high $Re_{max} \approx 76.9071$. Since, all other flow and particle conditions are unchanged, the drift is clearly inertia induced. The rate of drift diminishes with radius.

In Fig. 6.9, the tracer radial distance is plotted for all six fibres. While the drift rate diminishes with radius, and hence shear rate, it is likely that the driving force behind the drift is mostly inertial, and not shear-induced migration. In the following section however, we will explore the shear flow aspect of migration further.

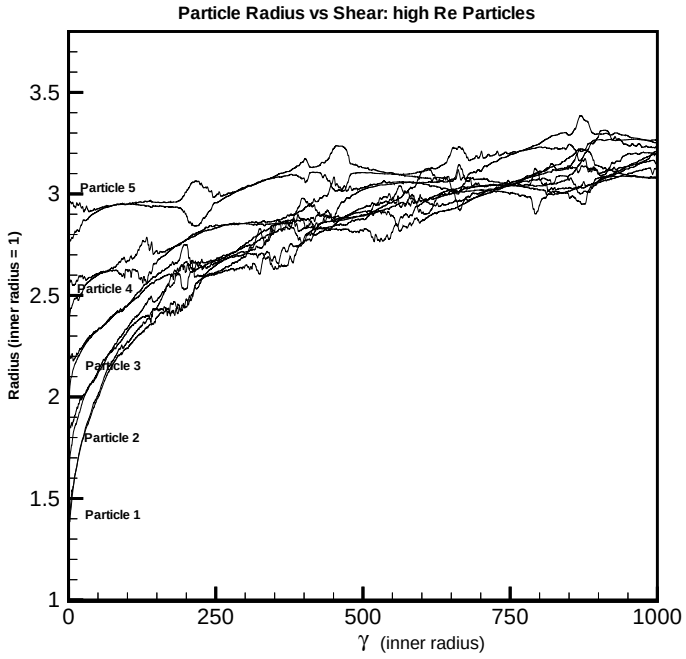

Figure 6.9: 'Rigid' fibres in high Reynolds number Couette flow. The radius of tracers from the Couette centre are plotted against γ. The drift rate is linked to radial distance, and hence the shear rate in the region. The particles prefer an orientation aligned with the local flow direction, however an end-over-end tumble can also be seen at approximately regular time intervals.

6.4.5 Flexible High Re Particles in a non-linear 2D shear flow field

In this section, particle migration is studied, in relation to the combined influences of high inertia and non-linear shear rates. High Re is a requisite for drift as is evident in the previous sections, or it at least accelerates drift rate. The non-linear shear gradient is of particular interest however and is the main focus of this section.

In the previous sections, the flow streamlines were circular so while cross streamline migration ('drift') was clearly apparent, it was not clear whether the drift was entirely and exclusively due to inertial forces, or whether the non-linear shear gradient also made a contribution.

Here, two different particles are simulated in a highly non-linear shear gradient flow. (Note, it is not important exactly what type of flow is used. So long as the shear gradient is highly non-linear, if particle migration is observed, a relationship between non-linear shear gradient and particle migration will be evident.)

To eliminate some factors such as inertia (around a curved path), this time the flow domain is not curved, but straight. The flow takes place in a 2D infinite channel. The FE mesh is a 1×1 square, see Fig. 6.10. The flow velocity is from left to right. The shear gradient used is highly non-linear. The velocity profile is according to Eq. 6.3. Prior to importing into the particle simulation, the velocity field is scaled by a factor 150. That is, the characteristic length of the mesh was 1, but was scaled by 150 relative to the particle simulation characteristic length $a = 1$.

$$v_x = y^4 \tag{6.3}$$

Eq. 6.3 is used as the velocity profile. It is emphasised again that for this test it is *not* important what type of profile is used, or even whether it represents a realistic flow. The salient feature is that it is non-linear, and (it will be seen in the Results section that) the particle migrates. Since it is a straight streamline, the particle's momentum is in the (x) direction. Any resulting

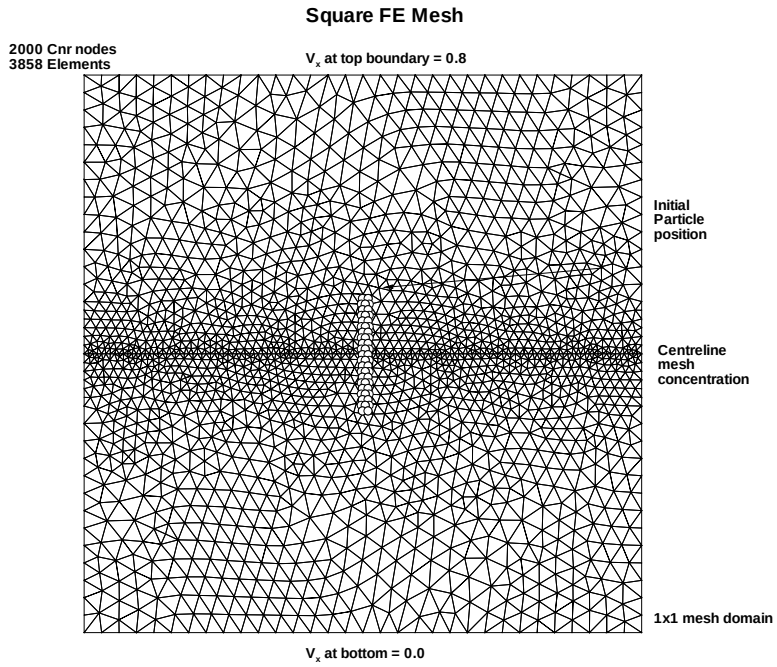

Figure 6.10: The channel flow FE mesh and rod-like particle in its initial position

particle migration (not in the (x) direction) must then be due mostly to the non-linear shear gradient. Inertial effects due to flow around a curved streamline are avoided using this channel flow situation.

The fibre is initially positioned vertically oriented (along y axis). The tracer subunit at the 'top' of the fibre experiences the greatest initial velocity. It also experiences the largest Re of approximately $Re_{max} = 4.641$ (Since scaled velocity at that point is approximately $v_x = 19.44$, subunit mass $m = 1$, viscosity $\eta_{sim} = 1$, and characteristic length is $a = 1$, also $E_{sim} = G_{sim} = 150$).

The FE mesh and the fibre initial position is as shown in Fig. 6.10. The unstructured FE mesh features 3848 triangular elements (2000 corner nodes in total). The particle is placed in the centre of the mesh and since for the majority of the simulation it will travel from left to right along the centreline, a mesh concentration is placed along that line. When the particle exits the right of the domain, the simulation automatically repositions it on the left side of the mesh to re-enter. The flow field thus approximates an infinitely long 2D channel. The simulation runs over the shear range from $\gamma_{initial} = 0$ to $\gamma_{end} = 500$ with increment $d\gamma = 0.005$.

In Fig. 6.11, the initial and final positions of the rod-like particle are shown, with the tracer paths for subunits at either end of the particle. The tracer path 'folds' over the flow domain since it exited to the right, and re-entered from the left twice during the simulation run. The result shows a clear drift towards the low shear region in agreement with the previously know observations of shear induced particle migration. This is also true for the rectangle in the same situation (see Fig. 6.12 $Re_{max} = 2.6183$, $a = 1$, $m = 1$, $\eta_{sim} = 1$, $E_{sim} = G_{sim} = 1000$). The particle momentum is directed predominantly along the (x right) direction, and the particle translation path is not constantly curved (as was the case with the Couette flow field). There is no interaction between any other particles (except intra-particle interactions amongst the subunits). By elimination, this drift must be attributed to the non-linear shear gradient, and inertial effects. Recall that as shown in Section

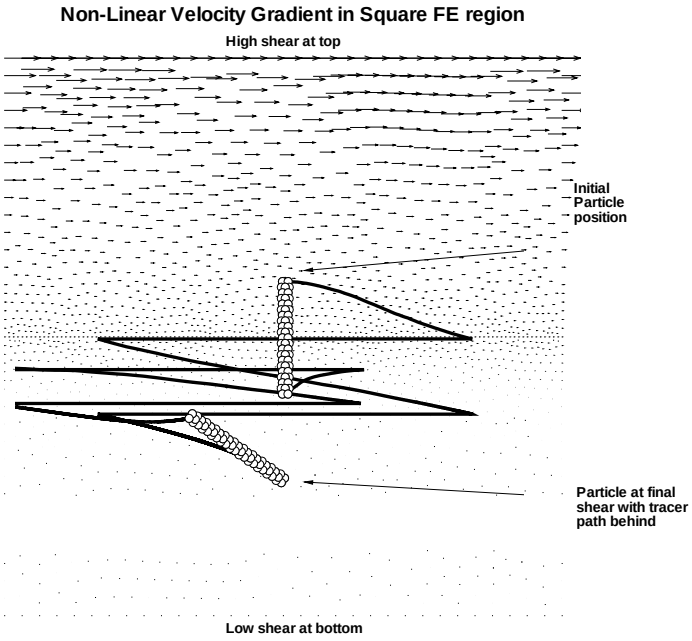

Figure 6.11: The initial and final particle positions with tracer paths. The tracer path folds over twice as the particle exits to the right, and re-enters from the left at two occasions within the duration of the simulation run. The figure is superimposed over a velocity vector diagram of the flow field.

§6.4.3, flexibility alone does not appear to contribute to particle migration. Therefore we may eliminate particle flexibility here.

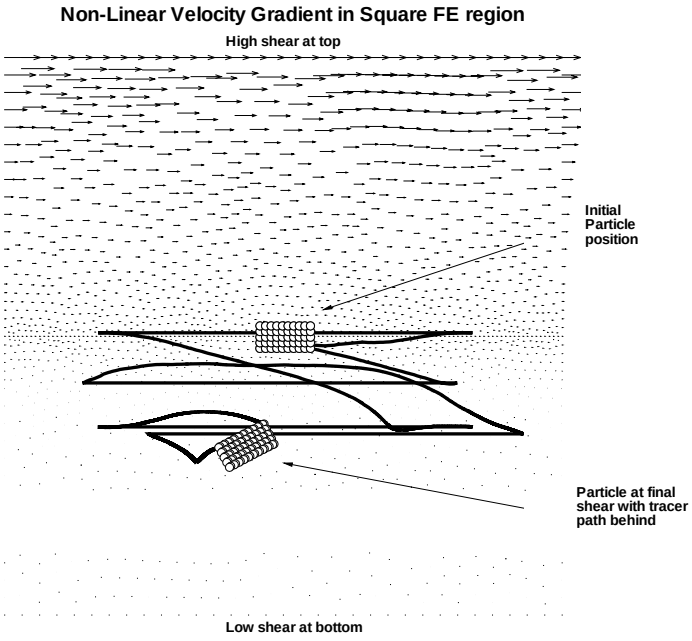

Figure 6.12: The $10 \times 5 \times 2$ rectangular particle in the channel flow. Tracers indicate the path of subunits during flow. Initial Reynolds number experienced was $Re_{max} = 2.6183$.

6.5 Summary and Conclusions

In this chapter, the simulation method was extended with the ability to embed the particle simulation within a pre-solved finite element flow field. The simulation was capable of accurately reproducing particle dynamics including particle inertia and arbitrary particle shape in a realistic non-linear complex flow field.

The capabilities were tested with a demonstration in simulation of fibres embedded in a 2D cylindrical Couette flow. A high Re rod-like particle was shown to migrate across streamlines in the highly non-linear shear environment of Couette flow. The migration seen here did not depend on the traditional migration theory of Phillips *et al.* [81], but was due to the effect of particle inertia, and non-linear shear flow gradient. Results for a high Re, $10 \times 5 \times 2$ rectangular particle in a non-linear shear flow also indicate a relationship between particle inertia and migration. Flexibility in particles however was shown not to play a significant part in migration.

Chapter 7

A Study of Short Fibre Orientation in Diverging Flow

7.1 Introduction

This chapter is the last of three on the direct simulation of arbitrarily shaped particles in Newtonian flow.

In this chapter the earlier theoretical work by Vincent and Agassant [120], and numerical work by Yamamoto and Matsuoka [73] are revisited. Results are presented here on the prediction of fibre orientation in a 2D diverging flow. Comparison is made with aspects of the results in [120] and [73], and the different methods by which the results were obtained are evaluated.

The orientation dynamics of the elongated fibre is known for both pure shear and pure elongation flow. The diverging channel flow is interesting because it features both a shear dominated Poiseuille flow and a gradual transition to an elongation dominated flow. The diverging channel flow is used to demonstrate the ability of this simulation to reproduce fibre orientation within realistic flow fields which contain elements of both shear and elongation.

The results for the 3D particle simulation are noticeably different to the theoretically derived work of Vincent and Agassant, where the fibre is as-

sumed to be sufficiently described as a 2D orientation vector. It is argued here that the current result is superior to Vincent and Agassant's because of its use of a truly 3D particle geometry. It is argued that the differences between the results implies a deficiency in the 2D orientation vector based theory.

While there are many variations of the theory based on Jeffrey's work, they are all bound by the same assumptions and limitations inherited from the original concept. The suspended Jeffrey ellipsoid was reduced to two defining characteristics; (1) Unit vector $\mathbf{P}$, the vectorial representation of main axis orientation, and (2) the location of the centre of mass. While this may be a perfectly adequate representation for the often used rigid cylindrical rod in linear shear flow field, there are some aspects of this approach that may not accurately portray a real fibre.

One such example is the fact that the vectorial director representation does not truly account for the fibre's width (shape). The Jeffrey theory includes a *shape correction factor* λ, which scales rotational velocity to compensate for the effect of shape difference between the ellipsoid and a cylinder-like fibre. λ however is only a scaling factor and does not qualitatively alter particle dynamics, according to the particle shape. The vector $\mathbf{P}$ is merely a two dimensional mathematical representation and has length but no actual width (Fig. 7.2*a*). A finite width, or otherwise varied shape, may cause a noticeable difference in the particle dynamics in certain conditions. Researchers such as Brenner [121][110] have provided analytic formulae of hydrodynamic resistance coefficient for various candidate particle shapes, e.g. spheroids, prolate spheroids, long slender axisymmetric bodies etc. These formulae however are limited to those particular shapes only. To simulate for non-axisymmetric, irregular, or other various shapes, new resistance coefficients would have to be created.

Another example of possible inaccuracy is the fact that the flow conditions $\mathbf{D}$, ω and $\mathbf{v}$ are only 'sampled' at a single point (the fibre centre of mass) while the fibre in reality occupies a finite volume in space over which flow

conditions may vary. This reduces accuracy in particle dynamics modelling when flow conditions are not linear (i.e. not symmetrical) over the length scale of the particle.

The current simulation method is not based on the theory of Jeffrey [4], and so provides an independent method with which one may compare results. Instead of being represented by a vectorial director, fibres in this simulation are multi-body constructions of linked spheres (see Fig. 7.2*c*). The fibre structure is fully three dimensional and hence has finite dimensions (width) unlike its vectorial counterpart. In the following sections it will be shown how results obtained from the 3D fibre model have some qualitatively different features compared to the 2D vectorial model. It will be argued that these results may be more realistic and the difference in results are due to the ability of this simulation to account for finite particle dimension, and non-linear flow gradients within the length scale of the fibre.

7.2 Background

Vincent and Agassant [120] provided a theoretical analysis of the fibre orientation in the diverging channel flow. With theory based on the fibre dynamics of Jeffrey [4], Vincent and Agassant predicted the orientation as a fibre travelled through a diverging channel (Fig. 7.1).

In the diverging channel, the flow field exits the narrow channel with a Poiseuille profile. As fibres prefer alignment with the shear direction, it is justified to assumed the fibres enter the divergence closely aligned with the streamline. The magnitude of shear reduces and elongational components increase in the divergent region, causing the fibre to tend towards a transverse orientation. Depending on the local region within the divergence, the relative magnitude of shear and elongation flow components vary in intensity and hence so does the preference for transverse orientation. The result is a pattern of fibre orientations as shown in Fig. 7.1.

Vincent and Agassant obtained a similar result using their theoretical

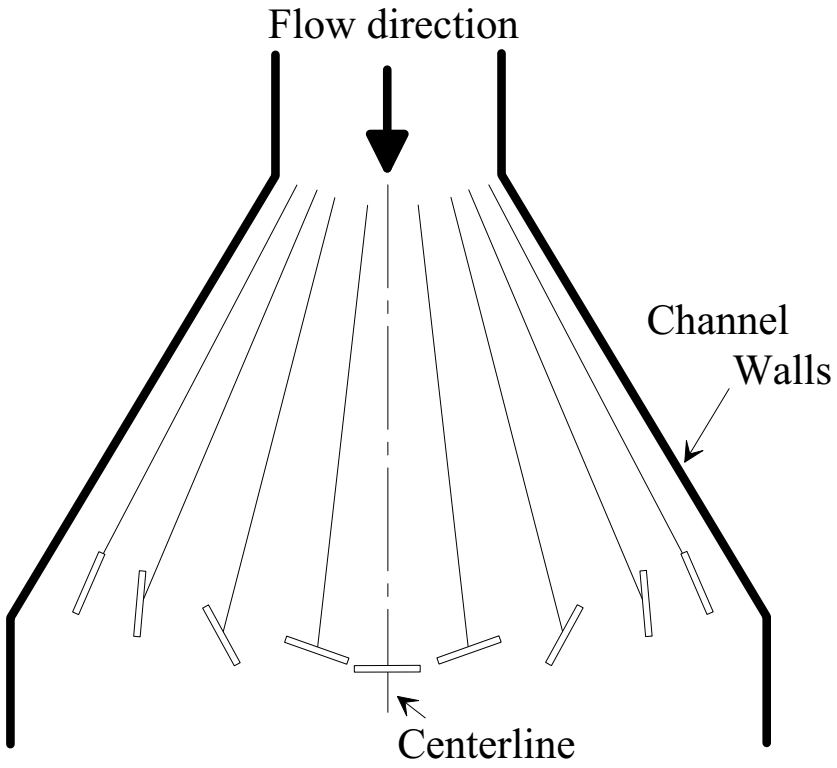

Figure 7.1: For a diverging channel flow the elongated fibre orients itself transversely to the streamline. The degree of its orientation ranges from almost complete perpendicular alignment along the centreline where elongational flow is strongest, to near streamline alignment near the channel walls where shear flow is strong.

analysis. They also found however that the *final* orientation varied proportionally with the degree of the *initial* orientation when it entered the divergence. This conclusion will be examined with results from the current simulation. It will be asserted that in creeping, or near-creeping flows, the final orientation of the fibre is dependent mostly on the flow geometry, and *not* initial fibre orientation. This is an indication of the different outcomes achieved when a 3D particle model is used, as compared to the 2D vectorial director model.

Yamamoto and Matsuoka [73] attempted a numerical solution of the same problem. Their 'Particle Simulation Method' (PSM) was closely related to the current simulation and was also capable of including particle inertia, particle flexibility, and 'sampling' of flow conditions at multiple points (instead of at the centre of particle mass only). Like the current method, the simulation particle was constructed from subunit spheres. Yamamoto and Matsuoka's PSM linked spheres in an end-to-end configuration with extensible and rotateable bonds (Fig. 7.2*b*). The bond stiffness was controllable allowing variable bond stiffness. The end-to-end bonding configuration allowed elongated chains of spheres or 'fibre-like' particles to be simulated. In [73], they embedded their simulation fibre in a presolved FE flow field. The two dimensional diverging channel was used and compared to Vincent and Agassant's work. In [73, Fig. 13], the comparison between Vincent and Agassant's theory and the PSM simulation was shown to be close.

While Yamamoto and Matsuoka's PSM is related to the current simulation, there is one important difference. The PSM fibre geometry remains essentially only two dimensional. While each subunit sphere *has* a finite radius, the radius is only relevant in the force-torque calculations. In terms of particle geometry, the subunits are essentially infinitely small points lined up in a straight line, and when viewed along the axis the 'cross-section' is reducible to a single dimensionless point. It retains the vectorial **P**-like characteristic of having a finite length but no width. In the particular geometry and relative length scales used here, finite width is an important factor which

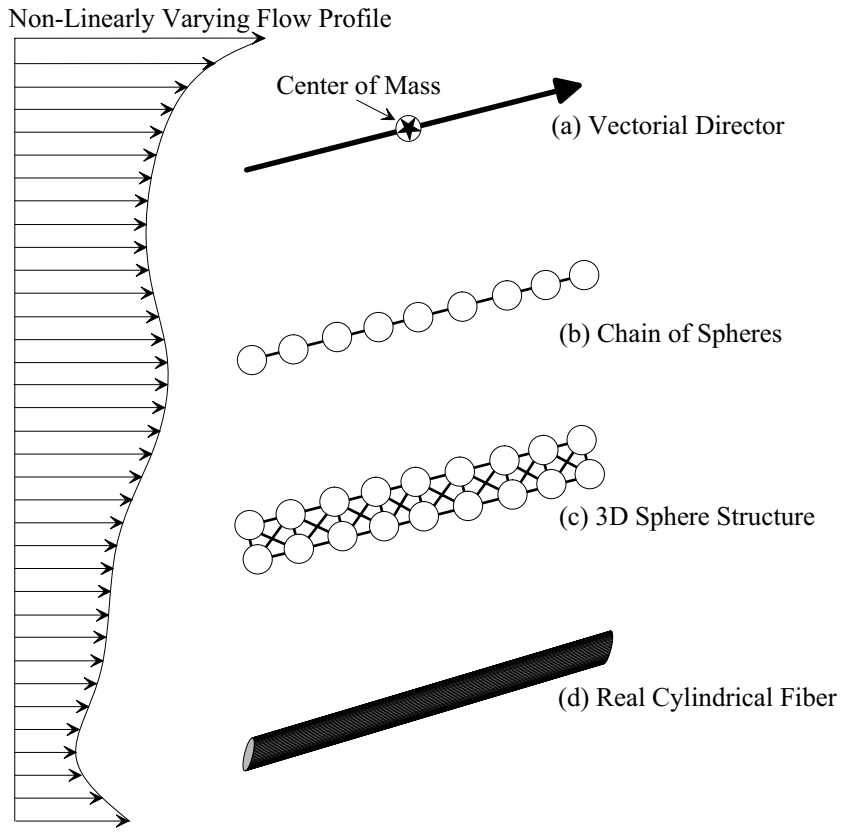

Figure 7.2: The various means of modelling the elongated fibre. (a) the 2D *vectorial director* samples flow conditions only at the centre of mass, and can only represent a rigid fibre. (b) *Chain of Spheres* - samples the flow condition at each sphere's centre of mass and allows flexibility. When the chain of spheres is aligned to the flow, the profile presented to the streamline is infinitely small. (c) *3D Sphere Structure* - also samples flow condition at each sphere's centre of mass but spheres are now distributed in three dimensions. The structure allows flexibility and non-linear flow condition to be correctly accounted for, even when fully aligned to the streamline since it has finite width. (d) The real cylindrical particle.

greatly affects the final outcome. In these particular circumstances, the stiffened 'chain-of-sphere' fibre of Yamamoto and Matsuoka is only marginally better than the single vectorial director of Vincent and Agassant, and not accurate enough to display the same particle dynamics shown using the full 3D model.

7.3 Numerical Method

The numerical method was described in detail in Chapter 5. In Chapter 6, a description was added for the modifications allowing embedded simulations in FE meshes. The method is essentially unchanged since Chapter 6.

7.3.1 Simulation Procedure

The equations of motion (5.15) (Chapter 6, Section §5.2.5) were solved and the positions of subunits were updated for each iteration in shear $d\gamma$. Relevant data was processed and output to a datafile for post-processing prior to the next iteration.

7.3.2 Flow Geometry

The flow geometry used here was identical to that used by Vincent and Agassant [120] and also the numerical work of Yamamoto and Matsuoka [73]. The diverging channel scenario is such a case that the particular combination of shear and extensional flows illustrate the differences between 2D and 3D models very well.

In Fig. 7.3 the Finite Element mesh is shown with embedded rod-like particles positioned at the exit of the narrow channel before the diverging flow begins (flow was from left to right). The unstructured mesh consisted of 4000 corner nodes and 7572 triangular elements. The average element size reduced with proximity to the channel walls (the regions of highest shear).

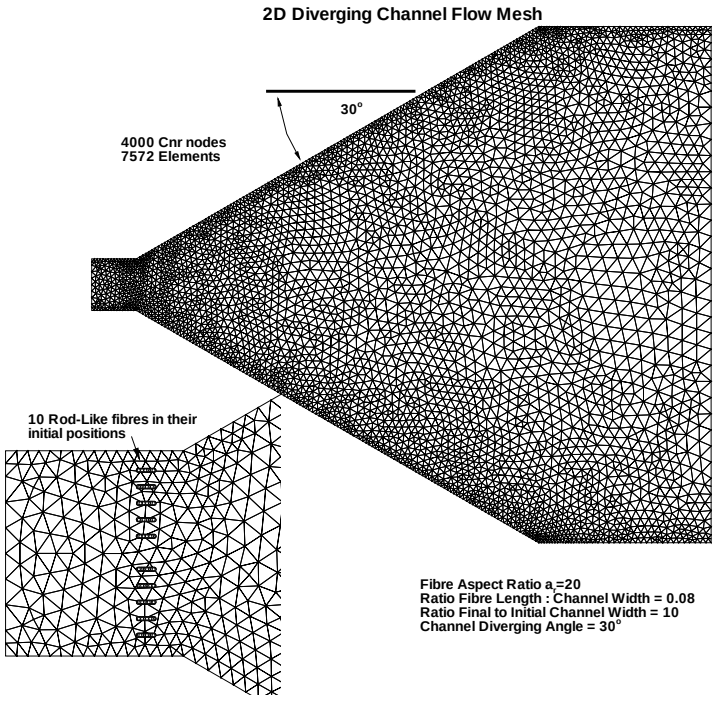

Figure 7.3: The 2D Diverging flow mesh used in simulation with rod-like particles drawn in the inset

The fluid was a Newtonian fluid based on the 2D incompressible Navier-Stokes Eq. (6.2). To approximate near-creeping flow, Eq. (6.2) was solved using $Re_{fluid} = 0.001$. The flow field was pre-solved to steady state by the Finite Element method using the commercial PDE solver, *Fastflo* v3.0. The incoming flow profile was defined by the FE boundary condition and was in the form of 2D Poiseuille channel flow as specified by Eq. 7.1,

$$\begin{aligned} v_x &= V\left(1 - \tfrac{y^2}{w^2}\right) \\ v_y &= 0 \end{aligned} \tag{7.1}$$

where $w = 1$ was the half-width of the narrow channel. The origin was located at the entering flow boundary at the channel centreline. Entering non-dimensional maximum centreline velocity was $V_{enter} = 1$. The channel diverged at 30° from the centreline, and the ratio of final to initial channel width was 10 : 1. Prior to use in the particle simulation, the FE flow field (characteristic length w) was scaled by 375, i.e. $w = 375a$, to make the flow field an appropriate scale relative to the particle simulation's characteristic length a. This scaling factor was arbitrarily set, but was selected such that the relative dimensions of flow to particle were of the order seen in [120] and [73].

The embedded rod-like particle used here had an aspect ratio, $a_r = 17.72$. This was the same rod fibre used in Chapter 6 (Vincent and Agassant used $a_r = 20$ fibres). The scaling was such that the fibre length was 0.08 the length of the narrow channel width (this ratio was 0.025 in [73]). Particle stiffness was high ($E_{sim} = G_{sim} = 3000$) to approximate a rigid fibre.

A single fibre was placed at the exit of the narrow channel along an initial 'trajectory' line β (see Fig. 7.4*a*). It should be noted that the term 'trajectory' is a misnomer as angle β is not necessarily the direction of the streamline at that point. The angle β merely refers to the angle subtended by the centreline and the line extending from the origin to the initial position of the fibre at the narrow channel exit. For want of a better term however, this line will continue to be referred to as 'trajectory'.

In this series of simulations, trajectories of $\beta = 0°$ and $\beta = 15°$ were used.

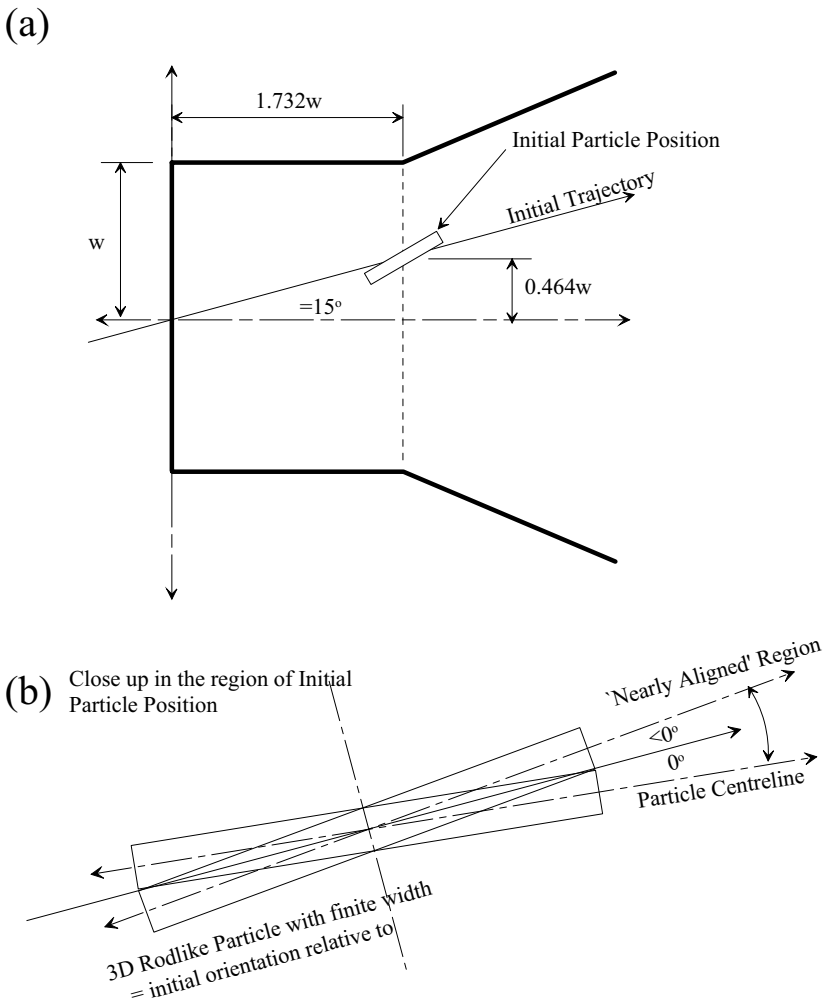

Figure 7.4: (a) The initial position and orientation for fibres along the $\beta = 15°$ trajectory line. (b) For fully 3D particles the finite particle width causes a region of 'stable alignment' which can alter the resulting orientation through the divergence.

The fibre was positioned at the mouth of the narrow channel, at coordinates $(x = 1.732w, y = 0.464w)$, so that the initial trajectory was $\beta = 15°$. Another series was also run where $(x = 1732w, y = 0)$, for $\beta = 0°$. Initial particle velocity was equal to the local freestream velocity. The scaled velocity profiles in the narrow channel varied depending on the initial y position. In this case, simulation fibres at initial position $\beta = 15°$ started with an initial and maximum $Re_{max} \approx 0.1874$. Fibres at $\beta = 0°$ started with an initial and maximum $Re_{max} \approx 0.2387$. Velocities downstream of this point reduce rapidly as do Re on the particles. Previous chapters show that inertial effects have a negligible effect on particle dynamics at these Re_{max} magnitudes.

Finally, the fibre was oriented relative to the trajectory β by an orientation angle θ. This angle is the 'initial orientation' which will be studied and compared with other results later. $\theta < 0°$ when the leading end of the fibre is above the trajectory line, and $\theta > 0°$ when the leading end of the fibre points below the trajectory line. When $\theta = 0°$ the fibre is in line with the trajectory line β. A range of θ from $-10° \leqslant \theta \leqslant +30°$ was used in the same way as Vincent and Agassant [120].

The orientation angle of the fibre relative to the global framework α ($\alpha = 0°$ on the channel centreline) is the subtraction of θ from β, that is, $\alpha = \beta - \theta$. In the results section, the variation of α as the fibre travels through the divergence is plotted.

While the flow field is a two dimensional field (extruded in the third dimension), the particle simulation itself is three dimensional. Therefore if the particle orientation moves out of the (xy) plane, α refers to the *apparent* orientation as seen from an observer looking perpendicularly upon the (xy) plane. In Chapter 5, we saw that particles usually require a large number of rotations before any out-of-plane (z) orientation developed. We shall see in this scenario that fibres do not have the opportunity to complete even half a revolution before the simulation has ended. In all results, the apparent orientation was virtually identical to the actual orientation.

The simulation results and also the FE flow field data to be discussed in

Section §7.4 were computed on Intel $x86$ processor based PCs running MS-Windows Operating Systems, and RedHat Linux v7.3 operating systems. The simulation source code was written in ANSI standard Fortran77 and compiled using Intel Fortran 95 Compiler for Linux v6, and Digital Visual Fortran v6 Compiler for Intel/Windows.

7.4 Results: 2D Diverging Channel

In Fig. 7.5 the simulated fibre is shown at various γ (between $0 < \gamma < 1000^{+}$, increment $d\gamma = 0.0002$) as it travels along the $\beta = 15°$ trajectory. The different versions show the fibre motion for varying initial fibre orientations, $\theta = -10°$, $-5°$, $-1°$, $+1°$, $+5°$, $+7°$, $+10°$, $+15°$, $+18°$, $+20°$, $+30°$. Fig. 7.6 is the equivalent plot for the trajectory $\beta = 0°$ (fibre initially on the centreline), and varying initial orientation, $\theta = +1°$, $+5°$, $+10°$. In Fig. 7.7, the fibre orientation angle α is plotted against γ.

For Fig. 7.7(*left*) three groups of data were observed. The first group of fibres ($-10° < \theta < +7°$) rotated slowly anticlockwise and ended pointing approximately $\alpha_{final} \approx 145°$ away from the centreline direction (direction of flow along centreline). The fibre started initially aligned at $\alpha_{initial} = \beta - \theta_{initial}$ to the centreline. There was then a relatively short period where fibre orientation moved from $\alpha_{initial}$ towards conformation with the master curve. This is represented by the mismatching individual curves for $\gamma < 1000$. For the remainder of the flow $1000 < \gamma < 4000$ the fibre executed a slow anticlockwise rotation at nearly the same rate for all individual cases. This is presumably the preferred local shear direction in that particular region of the flow.

The second group ($+15^{o} < \theta < +30^{o}$) underwent a similar anti-clockwise rotation, however the whole curve was shifted $\Delta\alpha = -180°$ indicating the fibre initially executed a rapid reversal (*end-over-end tumble* in the *clockwise* direction first) before the same slow anticlockwise rotation as was seen in the first group. This initial reversal is due to the relatively steep $\theta_{initial}$ of

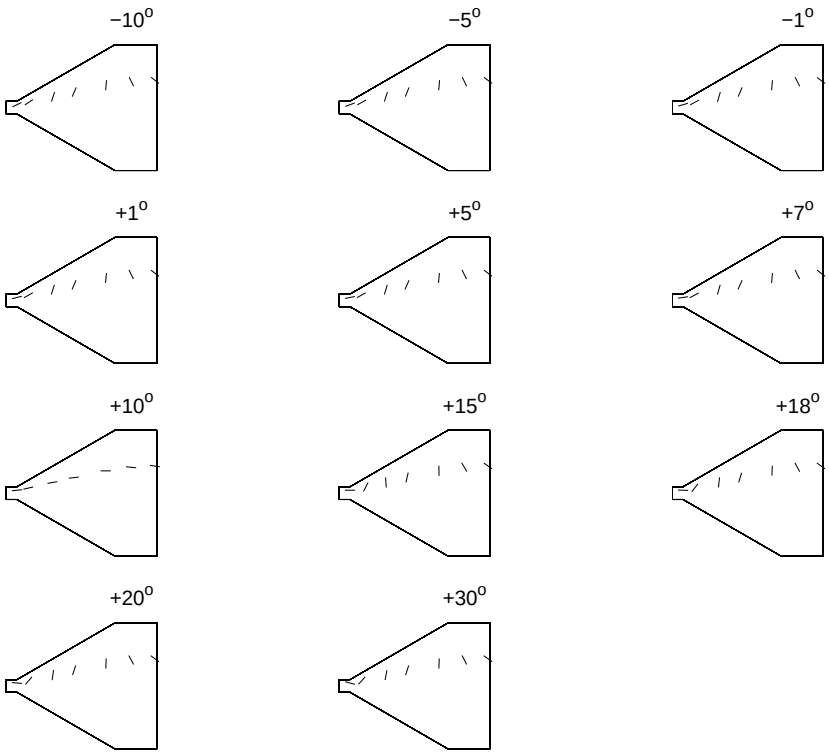

Figure 7.5: Simulation results showing fibre orientation at selected γ for the trajectory $\beta = 15°$ and varying orientation, θ. With the exception of $\theta = +10°$ all others appear nearly identical (The fibre is represented here with a line with length 5 times the true scale length for better visualisation).

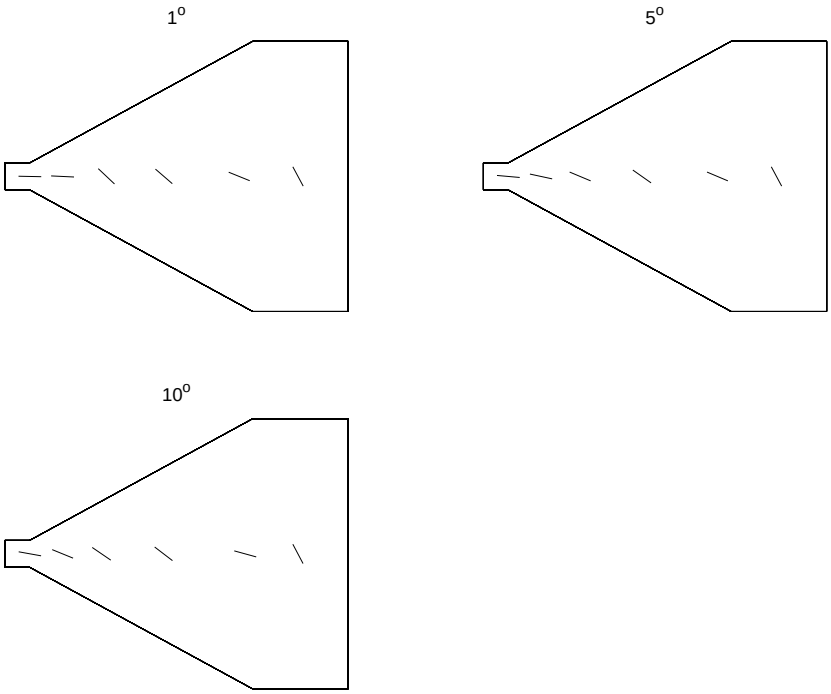

Figure 7.6: Fibres in channel flow at selected γ. Fibres are on the centreline trajectory $\beta = 0°$, for varying initial orientation $\theta = +1°, +5°, +10°$.

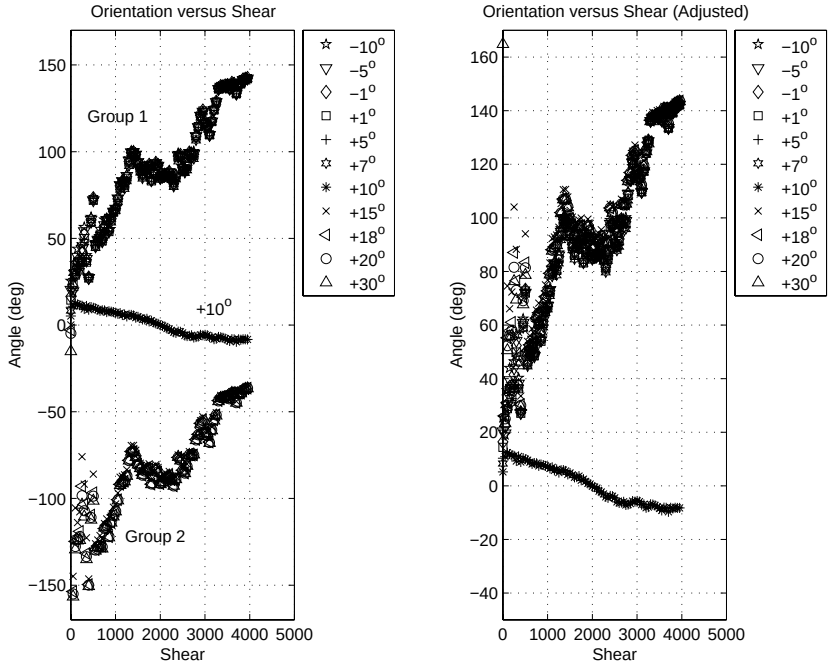

Figure 7.7: (*left*) Fibre orientation angle α versus shear for various initial $\theta_{initial}$. (*right*) The same plot, α versus shear, with the $+180°$ correction for fibres that executed an initial reversal. It is clear that the initial fibre orientation is irrelevant to the progress of α with γ with the exception of $\theta = +10°$, indicated by the $(*)$ symbol. (α is the orientation of the fibre relative to the centreline, $\alpha = \beta - \theta$).

the fibre combined with the relatively strong extensional flow regime in the region immediately entering the divergence. In Fig. 7.7(*right*) the initial reversal was adjusted by shifting these plots up by $\Delta\alpha = +180°$. Once the adjustment was made, it was seen that all data curves (except $\theta = +10°$, symbol $(*)$) collapsed approximately into one master $\alpha\,(t)$ curve. Finally, in regards to the first and second groups of data, one may notice that the mean gradients, $\frac{d\alpha(t)}{dt}_{mean}$ for the first group (Fig. 7.7(*left*)) are slightly steeper than $\frac{d\alpha(t)}{dt}_{mean}$ for the second 'reversed' group (This is also indicated by the different levels for the two plateau regions in Fig. 7.8). This is due simply to the fact that the fibres that executed an initial reversal, ended their clockwise rotation with a new orientation $\alpha\,(t) + 180°$ which happened to be closer to the final $\alpha_{final} \approx 145°$ than the non-reversed fibres for the same γ period. The reversed fibres subsequently required less anticlockwise rotation over the remaining γ to achieve the same α_{final}. Hence $\frac{d\alpha(t)}{dt}_{mean}$ is marginally lower than the non-reversed fibre group.

The third group consists of the single $\theta = 10^o$ data (Fig. 7.7, symbol $(*)$). This third group will be discussed in Section §7.4.1.

7.4.1 2D Director Based Theory versus Full 3D Methods

Figs. 7.5 and 7.7 in particular are of interest since the equivalent theoretical results of Vincent and Agassant [120, Fig. 11] predicted that fibres along the same β trajectory would result in a *smoothly varying* α_{final} of magnitude proportional to the initial $\theta_{initial}$. Furthermore the rotation of the fibre with time could be either clockwise or anti-clockwise, depending on whether $\theta_{initial} < 0°$ or $\theta_{initial} > 0°$, and the rate of rotation was dependent on the magnitude of $\theta_{initial}$. Fig. 7.5 and 7.7 appear to contradict this prediction, indicating instead that apart from a narrow range around $\theta = +10°$ $(*)$ (for the $\beta = 15°$ case only), the fibre orientation over the whole γ range follows *nearly the same* $\alpha(\gamma)$ *curve and* $\frac{d\alpha}{d\gamma}$ *regardless of initial* $\theta_{initial}$. Furthermore this rotation was *always anti-clockwise*, regardless of whether $\theta_{initial}$ was greater

than or less than 0^o.

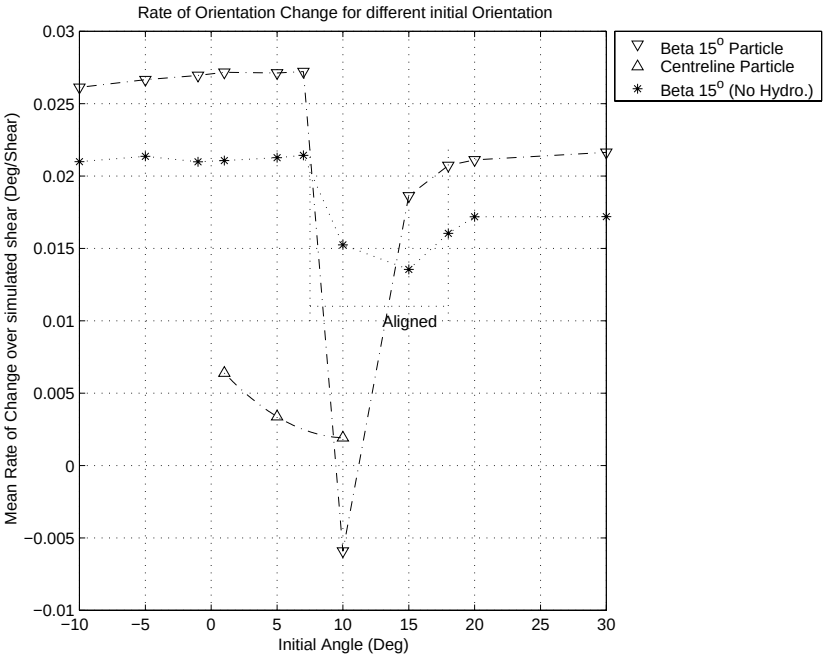

Figure 7.8: The rate of change of orientation, $\frac{d\alpha}{d\gamma}$ plotted against $\theta_{initial}$ (recall $\alpha = \beta - \theta$). There are three distinct bands of angular rate, (1) a plateau region $\alpha < 8°$, (2) a second plateau region $\alpha > 18°$, and (3) a narrow transition band of altered fibre dynamics, $8^o < \alpha < 18°$ (Data for simulation series *without* long-range hydrodynamic interaction is also plotted $(*)$).

At first glance, this result might suggest a problem in the current simulation since Vincent and Agassant's result [120] was correctly derived. Yamamoto and Matsuoka's PSM [73] also reproduced Vincent and Agassant's result. Both [120] and [73] however did not specifically allow for the fact that a real fibre has finite width and in some cases, e.g. a non-linear flow, the fibre width has a non-negligible effect on fibre orientation. It is argued that the differences between 2D and full 3D fibre models are highlighted in the low flow-rate diverging channel scenario. It is argued that in this situation, sampling the flow field at a *single* point (the fibre's centre of mass) is not adequate in accurately determining the orientation of the fibre if one uses orientation rules based on vectorial directors and linear flow gradient. Issues

such as flow and configuration reversibility are not necessarily true in this situation. One must take into consideration the non-linearity of the flow field over the characteristic subunit length either by refining the flow dependent rules of orientation accordingly, or alternatively taking multiple flow condition samples and solving for coordinated multibody motion as is done in the current simulation.

The fibre width plays a key role in the fibre's rotation direction. A 2D fibre-director may execute both clockwise and anti-clockwise rotation depending on $\theta_{initial}$. This is because the 2D theory does not include an anti-clockwise (for $\beta > 0°$ trajectories only) viscous drag moment arising from drag across the fibre width. For any 3D finite width particle on any trajectory where $\beta > 0°$, the prevailing rotation will be anti-clockwise regardless of $\theta_{initial}$ because that is the rotation of the fluid (and vice versa for $\beta < 0°$ trajectories). When $\theta_{initial}$ was severe enough, the fibres were observed undergoing a short period of clockwise rotation until the fibre reached the flows shear direction in the locality of the fibre. It then however quickly reverted back to anti-clockwise rotation for the remainder of the motion.

Consider a finite dimension 3D fibre represented in Fig. 7.4*b* as an elongated rectangle. It has a small range of $\pm\Delta\theta$ rotation where overall fibre length (corner-to-corner) could be seen to *increase* slightly with small $\Delta\theta$. This range of orientation could be viewed as a special range where altered, or non-Jeffrey-like fibre dynamics could occur. The 2D fibre-director theory is not applicable here. While this range is very small, it is quite significant since a cylindrical fibre in shear spends a great majority of its time in precisely this near-aligned orientation range. Depending on the aspect ratio, a rod-like particle in shear may easily spend over 90% of the time nearly-aligned to the streamline [31][87]. This is arguably an unacceptable amount of time for which a 2D director based theory may *not* be applicable. For the rod-like fibre species used in this simulation, the length is 14.3 times longer than its maximum width. This makes this small θ range approximately $\Delta\theta \approx \pm 4°$. Since $\beta = 15°$ and $\alpha = \beta \mp \Delta\theta$, the range of $\alpha_{altered}$ is

approximately $11° < \alpha < 19°$. This mostly coincides with the range captured in simulation ($8° < \alpha_{sim} < 18°$) where the $\frac{d\alpha}{d\gamma}$ curve underwent its 'change between plateaus' in Fig. 7.8.

Fig. 7.8 is certainly peculiar, however it should be noted that it was not generated under particularly obscure circumstances or conditions. This plot is reproducible under varying conditions. A simulation series without the long-range hydrodynamic interaction was also run and similar results were obtained (see the $(*)$ datapoints in Fig. 7.8). That simulation series was run with greatly different increment $\mathrm{d}\gamma = 0.01$ (as opposed to 0.0002 for the current results), and with $Re_{max}^{\beta=15°} = 0.9370$, and $Re_{max}^{\beta=0°} = 1.1937$ (as opposed to 0.1874 and 0.2387 respectively). Despite these differences, the distinctive shape of the plot in Fig. 7.8 is present regardless. It is put that these results reflect a real phenomenon, and it is observed here only because of the use of a 3D fibre model.

On these results it is argued that while Vincent and Agassant's theoretical work [120] was correct (within its own limitations), the assumption that a fibre is like a 2D vector $\mathbf{P}$ is not entirely accurate. It is argued that the current simulation results are in fact correct, or rather *more correct*, and that the differences between a 2D and 3D model can cause a noticeable divergence in the outcome under certain non-trivial circumstances.

7.5 Summary and Conclusions

In this chapter, the new particle simulation method is applied to a study of fibre orientation in a 2D diverging channel. For comparison, an earlier theoretical result is referred to of the same scenario studied by Vincent and Agassant [120], and a numerical result studied by Yamamoto and Matsuoka [73].

At first glance the current simulation appeared to have reproduced the expected result well. The range of orientation seen in Figs. 7.5 and 7.6 qualitatively matched the expected results (Fig. 7.1). On closer inspection

behavioural peculiarities were noticed which indicated a divergence from Vincent and Agassant's prediction. The current results showed that after an initial period of adjustment, the 3D fibre rotated at an orientation rate $\alpha = f(\gamma)$, mostly independent of its initial orientation. For a given initial trajectory β, the fibre finished in approximately the same final orientation regardless of $\alpha_{initial}$. α_{final} appeared only to be dependent on the domain geometry, fibre geometry and flow conditions (velocity, viscosity etc.). When the rate of rotation was plotted for a range of initial orientations, a distinctive relationship was apparent. Two 'plateau' regions in the $\alpha - \theta$ plot clearly indicated fibres moving at a rotation rate mostly independent of initial orientation (Fig. 7.8).

Based on simple reasoning in Section §7.4.1 the 3D method was predicted to show altered non-Jeffrey-like particle dynamics in a narrow orientation range, which would not be seen in a 2D method. The altered region is seen in Fig. 7.8 in the range between $8° < \theta_{initial} < 18°$ (only for the case $\beta = 15°$). This region, predicted by simple reasoning, appeared to be verified by numerical simulation. The range of altered dynamics depends on the fibre aspect ratio and is only revealed with 3D particle models which directly account for details of the fibre's geometry. It was a basic assumption of the vectorial method that a 3D fibre can be represented by the two dimensional vector. Given these results, it is argued that this assumption may not always be true.

Part IV

Conclusion

Chapter 8

Conclusion

8.1 Summary

The main goal of this thesis was to gain a better understanding of the microstructural dynamics within a flowing fibre-filled suspension, and from it derive useful information of bulk property. These aims were achieved through the use of the Direct Simulation numerical method. The direct simulation method itself is open to many different approaches. In this thesis, fibres were represented by multi-bodied constructions of spheres. Spheres were the building blocks used to form greater structures. These structures were initially elongated chains-of-spheres (Part II) and were taken to represent rod-like fibres. These particle constructions were then extended into truly three dimensional structures (Part III), allowing for an arbitrary range of particle shapes to be observed in flow fields. In the development of these algorithms and models, the method itself was refined and improved.

In Chapter 3, the Chain-of-Spheres simulation was used to extract detailed information about the suspension including fibre orientation and bulk viscosity. The simulation was shown to quantitatively predict non-dimensional bulk viscosity with good precision over a range of volume fractions. When the fibres were allowed to deform in the flow, it was observed that semi-concentrated to concentrated suspensions exhibited a viscosity increase of

the order $7 - 10\%$ greater than the equivalent rigid fibre suspension tested. This result is in agreement with experimental work by Goto *et al.* [88] and Blakeney [89]. The existence of a relationship between bulk viscosity and particle stiffness was established. This result shows that fibre material stiffness can play an important part in the final viscosity value found. Furthermore it implied that real fibre suspension viscosities may be underestimated by rigid fibre theories.

It was apparent from the results of Chapter 3, that matters relating to fibre shape and deformation could play an important part in the rheology of the suspension. This needed to be explored further, and was done so in Chapter 4. In Chapter 4, particular attention was paid to the influence of fibre shape on relative viscosity. The original chain-of-spheres simulation was modified to model for *rigid*, but deliberately *curved* fibres. Curvature in the fibre was taken to represent the general deformities that a real fibre may endure. When compared to the equivalent straight rigid fibre suspension, fibre curvature was found to contribute to an even greater increase in bulk viscosity. Greater than those seen for Chapter 3. Curved fibre suspensions were observed to be experiencing viscosity increases of the order twice that of straight fibre suspensions. It was apparent that even small fibre deformities could affect microstructural development such that the bulk viscosity markedly increased. With such a sensitivity to fibre shape, this result has some important implications. One must consider the quality of fibre inclusions when repeatability of suspension measurements is required. When consistent material performance is necessary in fibre composites, the experimenter is highly dependent on the quality control measures taken during sample preparation.

In Chapter 5, the older method of Part II (Ch. 3 and 4) was significantly extended. Any complexity in particle shape severely complicates theory development. Theories for some time were mostly restricted to axially symmetric cylinders, ellipses, spheres and discs. Up to Chapter 4, the Chain-of-Sphere simulation was used where the particle shape was limited

to simple linear chains. The new simulation reported in Chapter 5, was capable of modelling greater complex particle structures, within complex flows generated separately using Finite Element methods. In Chapter 5, the simulation was used to study the dynamics of various particle shapes in shearing Newtonian fluid. In this chapter, it was demonstrated that the method could reproduce basic known fibre behaviour, such as the Jeffrey orbit. The three dimensional simulation was capable of revealing greater details of the motion such as the correct orbital periods, and a good approximation of spin during orbit. From this, the ellipsoid-to-cylinder shape correction factor, ($\lambda_{corr} = 0.7124$) of Trevelyan and Mason [24] was verified to great accuracy by this completely different approach. Other particle shapes were also observed in motion. Complex behaviour and configurations were observed, such as the apparent log-rolling of the rectangular plate, and the ovoid shape of the collapsed limp Pom-Pom. The results showed that this simulation is capable of a highly accurate reproduction of the micro-dynamics of different shaped particles.

In Chapter 6, the three dimensional simulation was developed further. The particles were now embedded in a complex FE flow field. It was possible to model particle motion through flow regions with complicated and varying non-linear flow gradients. The case of a rod-like particle in a cylindrical Couette flow field was used to demonstrate this capability and explore an interesting real-life scenario. Inertia induced particle migration in non-linear shear gradients was explored. Rod-like particles with high inertial forces were observed migrating to the outer rim of the Couette device. Particles with high Re were also shown to migrate across streamlines in highly non-linear straight channel flow.

Finally in Chapter 7, the case of fibre orientation in a 2D diverging flow was explored. Like the Couette cylinder, the diverging flow was also chosen for the unique and varying flow types shown in different regions of the flow. The orientation dynamics of the rod-like fibre is already well known for simple flows, from the work of Jeffrey. The diverging channel flow however

featured both a shear dominated Poiseuille flow at the entrance, and a gradual transition to an elongation dominated flow. This variation was used to demonstrate the ability to determine orientation as a fibre travelled through this rapidly evolving flow environment.

The simulation results show detailed differences to results by Vincent and Agassant [120], and by Yamamoto and Matsuoka [73]. The final orientation of fibres travelling through the divergence are *not* particularly influenced by the initial orientation when it entered the divergence. This is different to the above researchers, who argued that initial orientation determined the final orientation. Vincent and Agassant [120], and Yamamoto and Matsuoka [73] both use a two dimensional fibre model. It is argued that in the diverging channel scenario, the two dimensional model cannot include the secondary contributions of particle width and non-linear shear gradients over the length scales of the subunits.

8.2 Conclusions and Final Remarks

Fibre suspensions are interesting materials which may yield interesting opportunities for study at all levels, from the microscopic field of view, through to the macroscopic. The study of the broader, measureable parameters such as bulk viscosity and stress is the traditional realm of the rheologist. With the current advances in computer power however, new numerical approaches are possible, and the detailed, comprehensive understanding of the dynamics of microstructure and its relation to observed phenomena is feasible. The methods developed in this thesis show that fibre suspensions can be accurately modelled at the microscopic level, and successfully extrapolated into the macroscopic level. Particularly important bulk parameters such as viscosity, extensional viscosity, interaction coefficient C_I, shape correction factor λ, and orbital constant C were calculated and were shown to agree with other works where available.

A priority while undertaking this research was to improve the capabilites

of the method. This task was difficult because this method is currently underdeveloped. There were relatively few previous examples of innovation in this field to compare with. Compared to the large research efforts directed towards other more established numerical methods, the worker in this field is destined to take far greater leaps into the dark with every addition. The simulation of Part II was refined through streamlining of existing methods, and new innovations in model design. By the end of Part III, we saw developments including the ability to model for particles of arbitrary shape, embedded within complex flows of the users design.

It is hoped that future researchers may gain from these additions and be encouraged to extend the potential of this method further.

8.3 Future Directions

As mentioned, this method is still relatively underdeveloped. There is much that can be improved, and one need only look at the caveats and assumptions used throughout this thesis to see where the main deficiencies lie. Recommended future developments should be in the following areas;

- The simulation of particles in *viscoelastic* fluids.
- Coupling of the dynamics of particles, with the flow field development.
- Three dimensional complex flow fields (by Finite Element method or any other method).
- Parallelisation of algorithms: The algorithms of this work are excellent candidates for parallelisation. The improvement in solution time through parallel algorithms may allow whole bulk flows, with truly microscopic resolution to be achieveable now, without any need for improvements in computer speed.
- Improved constitutive equations are required to cater for multibody constructed particles.

- Improved particle flexibility models are desirable.

Bibliography

[1] G. Potsch and W. Michaeli, *Injection Molding - An Introduction*, Hanser Pub, 1995.

[2] F. Folgar and C. L. Tucker, *Orientation Behavior of Fibers in Concentrated Suspensions*, Journal of Reinforced Plastics and Composites **3**, 98 (1984).

[3] R. Zheng, N. McCaffrey, K. Winch, H. Yu, and P. Kennedy, *Predicting Warpage of Injection Molded Fibre-Reinforced Plastics*, Journal of Thermoplastic Composite Materials **9**, 90 (1996).

[4] G. Jeffrey, *The Motion of Ellipsoid Particles Immersed in a Viscous Fluid*, Proceedings of the Royal Society of London **A102**, 161 (1923).

[5] S. G. Advani and C. L. Tucker, *The Use of Tensors to Describe and Predict Fibre Orientation in Short Fibre Composites*, The Journal of Rheology **8**, 751 (1987).

[6] X. J. Fan, *Rheology of Semiconcentrated Fibre Suspension in the Oldroyd-B Fluid*, Acta Mechanica Sinica **8**, 295 (1992).

[7] R. Larson, H. Hu, D. Smith, and S. Chu, *Brownian Dynamics Simulations of a DNA Molecule in an Extensional Flow Field*, Journal of Rheology **43**, 267 (1999).

[8] N. Phan-Thien and R. Zheng, Macroscopic modelling of the evolution of fibre orientation during flow, in *Flow-Induced Alignment in Com-*

posite Materials, edited by D. Guell and T. Papathanasiou, chapter 3, pages 77–111, Woodhead Publishing Ltd, Cambridge UK, 1997.

[9] J. L. Ericksen, *Anisotropic Fluids*, Archive for Rational Mechanics and Analysis **4**, 231 (1960).

[10] G. L. Hand, *A Theory of Anisotropic Fluids*, Journal of Fluid Mechanics **13**, 33 (1961).

[11] G. K. Batchelor, *The Stress System in a Suspension of Force-Free Particles*, Journal of Fluid Mechanics **41**, 545 (1970).

[12] R. Zheng, P. Kennedy, N. Phan-Thien, and X.-J. Fan, *Thermoviscoelastic Simulation of Thermally and Pressure Induced Stresses in Injection Moulding for the Prediction of Shrinkage and Warpage for Fibre-Reinforced Thermoplastics*, Journal of Non-Newtonian Fluid Mechanics **84**, 159 (1999).

[13] P. Kennedy, *Flow Analysis of Injection Molds*, Hanser Publisher, 1995.

[14] R. S. Bay, *Fibre Orientation in Injection Molded Composites: A Comparison of Theory and Experiment*, PhD thesis, Department of Mechanical Engineering. University of Illinois USA, 1991.

[15] W. Kuhn, *Uber Die Gestalt Fadenformiger Molekule in Losungen*, Kolloid Zeitschrift **68**, 2 (1934).

[16] H. A. Kramers, *Het Gedrag Van Macromoleculen in Een Stroomende Vloeistof*, Physica **11**, 1 (1944).

[17] H. Giesekus, *Elasto-Viskose Flussigkeiten, Fur Die in Stationaren Schichtstromungen Samtliche Normalspannungskomponenten Verschieden Gross Sind*, Rheologica Acta **2**, 50 (1962).

[18] H. Giesekus, *Die Elastizitat Von Flussigkeiten*, Rheologica Acta **5**, 29 (1966).

[19] J. G. Kirkwood and J. Riseman, *The Instrinsic Viscosities and Diffusion Constants of Flexible Macromolecules in Solution*, Journal of Chemical Physics **16**, 565 (1948).

[20] J. G. Kirkwood and J. Riseman, *Errata: The Intrinsic Viscosities and Diffusion Constants of Flexible Macromolecules in Solution*, Journal of Chemical Physics **22**, 1626 (1954).

[21] B. H. Zimm, *Dynamics of Polymer Molecules in Dilute Solution: Viscosity, Flow Birefringemence and Dielectric Loss*, Journal of Chemical Physics **24**, 269 (1956).

[22] P. E. Rouse, *A Theory of the Linear Viscoelastic Properties of Dilute Solutions of Coiling Polymers*, Journal of Chemical Physics **21**, 1272 (1953).

[23] R. B. Bird, O. Hassager, R. C. Armstrong, and C. F. Curtiss, *Dynamics of Polymeric Liquids - Volume 2 Kinetic Theory*, volume 2, John Wiley and Sons, 1977.

[24] B. J. Trevelyan and S. G. Mason, *Particle Motions in Sheared Suspensions. I. Rotations*, Journal of Colloid Science **16**, 354 (1951).

[25] F. P. Bretherton, *The Motion of Rigid Particles in a Shear Flow at Low Reynolds Number*, Journal of Fluid Mechanics **14**, 284 (1962).

[26] H. L. Goldsmith and S. G. Mason, *Particle Motions in Sheared Suspensions XIII The Spin and Rotation of Disks*, Journal of Fluid Mechanics **12**, 88 (1962).

[27] G. I. Taylor, *The Motion of Ellipsoidal Particles in a Viscous Fluid*, Proceedings of the Royal Society of London **103**, 58 (1923).

[28] P. G. Saffman, *On the Motion of Small Spheroidal Particles in a Viscous Liquid*, Journal of Fluid Mechanics **1**, 540 (1956).

[29] Y. Iso, D. L. Koch, and C. Cohen, *Orientation in Simple Shear Flow of Semi-Dilute Fiber Suspensions 1. Weakly Elastic Fluids*, Journal of Non-Newtonian Fluid Mechanics **62**, 115 (1996).

[30] J. Azaiez, *Constitutive Equations for Fiber Suspensions in Viscoelastic Media*, Journal of Non-Newtonian Fluid Mechanics **66**, 35 (1996).

[31] X. Fan, N. Phan-Thien, and R. Zheng, *A Direct Simulation of Fibre Suspensions*, Journal of Non-Newtonian Fluid Mechanics **74**, 113 (1998).

[32] Y. Yamane, Y. Kaneda, and M. Doi, *The Effect of Interaction of Rodlike Particles in Semi-Dilute Suspensions under Shear Flow*, Journal of the Physical Society of Japan **64**, 3265 (1995).

[33] P. Skjetne, R. F. Ross, and D. J. Klingenberg, *Simulation of Single Fiber Dynamics*, Journal of Chemical Physics **107**, 2108 (1997).

[34] S. Yamamoto and T. Matsuoka, Dynamic simulation method for particle dispersed systems, in *Proceedings of the 14th Annual Meeting of the Polymer Processing Society. International Conference on Polymer Processing*, pages G2–07 305–306, Polymer Processing Society, 1998.

[35] Y. Yamane, Y. Kaneda, and M. Doi, *Numerical Simulation of Semi-Dilute Suspensions of Rodlike Particles in Shear Flow*, Journal of Non-Newtonian Fluid Mechanics **54**, 405 (1994).

[36] S. G. Advani and C. L. Tucker, *A Numerical Simulation of Short Fibre Orientation in Compression Molding*, Polymer Composites **11**, 164 (1990).

[37] S. G. Advani and C. L. Tucker, *Closure Approximations for Three-Dimensional Structure Tensors*, Journal of Rheology **34**, 367 (1990).

[38] E. Ganani and R. L. Powell, *Suspensions of Rodlike Particles: Literature Review and Data Correlations*, Journal of Composite Materials **19**, 194 (1985).

[39] D. J. Jeffrey and A. Acrivos, *The Rheological Properties of Suspensions of Rigid Particles*, AIChE Journal **22**, 417 (1976).

[40] N. Y. Kuzuu and M. Doi, *Nonlinear Viscoelasticity of Concentrated Solution of Rod-Like Polymers*, Polymer Journal **12**, 883 (1980).

[41] L. G. Leal, *The Slow Motion of Slender Rod-Like Particles in a Second-Order Fluid*, Journal of Fluid Mechanics **69**, 305 (1975).

[42] A. Ait-Kadi and M. Grmela, *Modelling the Rheological Behaviour of Fibre Suspensions in Viscoelastic Mdeia*, Journal of Non-Newtonian Fluid Mechanics **53**, 65 (1994).

[43] L. Leal and E. Hinch, *The Effect of Weak Brownian Rotations on Particles in Shear Flow*, Journal of Fluid Mechanics **46**, 685 (1971).

[44] L. G. Leal and E. J. Hinch, *The Rheology of a Suspension of Nearly Spherical Particles Subject to Brownian Rotations*, Journal of Fluid Mechanics **55**, 745 (1972).

[45] E. J. Hinch and L. G. Leal, *Constitutive Equations in Suspension Mechanics, Part 2. Approximate Forms for a Suspension of Rigid Particles Affected by Brownian Rotations*, Journal of Fluid Mechanics **76**, 187 (1976).

[46] E. J. Hinch and L. G. Leal, *The Effect of Brownian Motion on the Rheological Properties of a Suspension on Non-Spherical Particles*, Journal of Fluid Mechanics **52**, 683 (1972).

[47] L. G. Leal and E. J. Hinch, *Theoretical Studies of a Suspension of Rigid Particles Affected by Brownian Couples*, Rheologica Acta **12**, 127 (1973).

[48] E. J. Hinch and L. G. Leal, *Time-Dependent Shear Flows of a Suspensions of Particles with Weak Brownian Rotations*, Journal of Fluid Mechanics **57**, 753 (1973).

[49] G. Batchelor, *Slender-Body Theory for Particles of Arbitrary Cross-Section in Stokes Flow*, Journal of Fluid Mechanics **44**, 419 (1970).

[50] E. J. Hinch, *The Distortion of a Flexible Inextensible Thread in a Shearing Flow*, Journal of Fluid Mechanics **74**, 317 (1976).

[51] E. J. Hinch, *The Deformation of a Nearly Straight Thread in a Shearing Flow with Weak Brownian Motions*, Journal of Fluid Mechanics **75**, 765 (1976).

[52] J. S. Cintra and C. L. Tucker, *Orthotropic Closure Approximations for Flow-Induced Fiber Orientation*, Journal of Rheology **39**, 1095 (1995).

[53] N. Phan-Thien and A. L. Graham, *A New Constitutive Equation for Fibre Suspensions: Flow Past a Sphere*, Rheologica Acta **30**, 44 (1991).

[54] X. Fan, N. Phan-Thien, and R. Zheng, *Simulation of Fibre Suspension Flows by the Brownian Configuration Field Method*, Journal of Non-Newtonian Fluid Mechanics **84**, 257 (1999).

[55] H. C. Ottinger, *Stochastic Processes in Polymeric Fluids - Tools and Examples for Developing Simulation Algorithms*, Springer-Verlag Berlin Heidelberg, 1996.

[56] J. Sun, N. Phan-Thien, and R. I. Tanner, *An Adaptive Viscoelastic Stress Splitting Scheme and its Applications: AVSS/SI and AVSS/SUPG*, Journal of Non-Newtonian Fluid Mechanics **65**, 75 (1996).

[57] J. Sun, M. D. Smith, R. C. Armstrong, and R. A. Brown, *Finite Element Method for Viscoelastic Flows Based on the Discrete Adaptive Viscoelastic Stress Splitting and the Discontinuous Galerkin Method:*

DAVSS-G/DG, Journal of Non-Newtonian Fluid Mechanics **86**, 281 (1999).

[58] N. Phan-Thien, T. Tran-Cong, and A. L. Graham, *Shear Flow of Periodic Arrays of Particle Clusters: A Boundary-Element Method*, Journal of Fluid Mechanics **228**, 275 (1991).

[59] X.-J. Fan, N. Phan-Thien, and R. Zheng, *Complete Double Layer Boundary Element Method for Periodic Suspensions*, Zeitschrift fur angewandte mathematik und Physik ZAMP **49**, 167 (1998).

[60] F. Qi, N. Phan-Thien, and X. Fan, *Effective Moduli of Particulate Solids: Completed Double Layer Boundary Element Method with Lubrication Approximation*, Zeitschrift fur angewandte Mathematik und Physik ZAMP **51**, 92 (2000).

[61] F. Qi, N. Phan-Thien, and X. J. Fan, *Effective Moduli of Particulate Solids: Lubrication Approximation Method*, Zeitschrift fur angewandte Mathematik und Physik ZAMP **52**, 1 (2001).

[62] S. Nasseri, N. Phan-Thien, and X. Fan, *Lubrication Approximation in Completed Double Layer Boundary Element Method*, Computational Mechanics **26**, 388 (2000).

[63] S. Nasseri and N. Phan-Thien, *Hydrodynamic Interaction Between Two Nearby Swimming Micromachines*, Computational Mechanics **20**, 551 (1997).

[64] M. Loewenberg and E. J. Hinch, *Collision of Two Deformable Drops in Shear Flow*, Journal of Fluid Mechanics **338**, 299 (1997).

[65] D. Doraiswamy, *The Origins of Rheology: A Short Historical Excursion*, Journal of Rheology - Rheology Bulletin **71** (2002).

[66] G. K. Batchelor, *Transport Properties of Two-Phase Materials with Random Structure*, Annual Review of Fluid Mechanics **6**, 227 (1974).

[67] B. J. Alder and T. E. Wainwright, *Phase Transistion for a Hard Sphere System*, Journal of Chemical Physics **27**, 1208 (1957).

[68] G. E. Moore, *Cramming More Components Onto Integrated Circuits*, Electronics **38**, 114 (1965).

[69] P. P. Ewald, *Die Berechnung Optischa und Elektrostatischer Gitterpotentiale*, Annalen Der Physik **64**, 253 (1921).

[70] J. F. Brady, R. J. Phillips, J. C. Lester, and G. Bossis, *Dynamic Simulation of Hydrodynamically Interacting Suspensions*, Journal of Fluid Mechanics **195**, 257 (1988).

[71] S. Yamamoto and T. Matsuoka, *Dynamic Simulation of Fiber Suspensions in Shear Flow*, Journal of Chemical Physics **102**, 2254 (1995).

[72] S. Yamamoto and T. Matsuoka, *Dynamic Simulation of a Platelike Particle Dispersed System*, Journal of Chemical Physics **107**, 3300 (1997).

[73] S. Yamamoto and T. Matsuoka, *Dynamic Simulation of Microstructure and Rheology of Fiber Suspensions*, Polymer Engineering and Science **36**, 2396 (1996).

[74] T. Nomura, S. Yamamoto, and T. Matsuoka, Numerical simulation method for fracture of fibers in injection molded composites, in *Proceedings of the 7th International Conference on Numerical Methods in Industrial Forming Processes*, page poly3, 2001.

[75] G. Bossis and J. F. Brady, *Dynamic Simulation of Sheared Suspensions. 1. General Method*, Journal of Chemical Physics **80**, 5141 (1984).

[76] J. F. Brady and G. Bossis, *The Rheology of Concentrated Suspensions of Spheres in Simple Shear Flow by Numerical Simulation*, Journal of Fluid Mechanics **155**, 105 (1985).

[77] I. L. Claeys and J. F. Brady, *Suspensions of Prolate Spheroids in Stokes Flow. Part 1. Dynamics of a Finite Number of Particles in an Unbounded Fluid*, Journal of Fluid Mechanics **251**, 411 (1993).

[78] I. L. Claeys and J. F. Brady, *Suspensions of Prolate Spheroids in Stokes Flow. Part 2. Statistically Homogeneous Dispersions*, Journal of Fluid Mechanics **251**, 443 (1993).

[79] I. L. Claeys and J. F. Brady, *Suspensions of Prolate Spheroids in Stokes Flow. Part 3. Hydrodynamic Transport Properties of Crystalline Dispersions*, Journal of Fluid Mechanics **251**, 479 (1993).

[80] X. Fan, N. Phan-Thien, and R. Zheng, *Simulation of Fibre Suspension Flow with Shear-Induced Migration*, Journal of Non-Newtonian Fluid Mechanics **90**, 47 (2000).

[81] R. J. Phillips, R. C. Armstrong, R. A. Brown, A. L. Graham, and J. R. Abbott, *A Constitutive Equation for Concentrated Suspensions That Accounts for Shear-Induced Particle Migration*, Physics of Fluids A - Fluid Dynamics **4**, 30 (1992).

[82] S. Yamamoto and T. Matsuoka, *A Method for Dynamic Simulation of Rigid and Flexible Fibers in a Flow Field*, Journal of Chemical Physics **98**, 644 (1993).

[83] S. Yamamoto and T. Matsuoka, *Dynamic Simulation of Flow-Induced Fiber Fracture*, Polymer Engineering and Science **35**, 1022 (1995).

[84] R. F. Ross and D. J. Klingenberg, *Dynamic Simulation of Flexible Fibers Composed of Linked Rigid Bodies*, Journal of Chemical Physics **106**, 2949 (1997).

[85] C. F. Schmid and D. J. Klingenberg, *Mechanical Flocculation on Flowing Fiber Suspensions*, Physical Review Letters **84**, 290 (2000).

[86] C. F. Schmid, L. H. Switzer, and D. J. Klingenberg, *Simulations of Fiber Flocculation: Effects of Fiber Properties and Interfiber Friction*, Journal of Rheology **44**, 781 (2000).

[87] C. G. Joung, N. Phan-Thien, and X. J. Fan, *Direct Simulation of Flexible Fibers*, Journal of Non-Newtonian Fluid Mechanics **99**, 1 (2001).

[88] S. Goto, H. Nagazono, and H. Kato, *The Flow Behavior of Fiber Suspensions in Newtonian Fluids and Polymer Solutions. 1. Mechanical Properties*, Rheologica Acta **25**, 119 (1986).

[89] W. R. Blakeney, *The Viscosity of Suspensions of Straight, Rigid Rods*, Journal of Colloid and Interface Science **22**, 324 (1966).

[90] E. Anczurowski and S. G. Mason, *The Kinetics of Flowing Dispersions. II. Equilibrium Orientations for Rods and Discs (Theoretical)*, Journal of Colloid and Interface Science **23**, 522 (1967).

[91] M. A. Nawab and S. G. Mason, *Viscosity of Dilute Suspensions of Threadlike Particles*, Journal of Physical Chemistry **62**, 1248 (1958).

[92] J. M. Burgers, *Second Report on Viscosity and Plasticity*, Nordemann, New York , 113 (1938).

[93] O. L. Forgacs and S. G. Mason, *Particle Motions in Sheared Suspensions. X. Orbits of Flexible Threadlike Particles*, Journal of Colloid Science **14**, 473 (1959).

[94] C.-M. Tchen, *Motion of Small Particles in Skew Shape Suspended in a Viscous Fluid*, Journal of Applied Physics **25**, 463 (1954).

[95] M. Doi and N. Y. Kuzuu, Nonlinear elasticity of rodlike macromolecules in condensed state, in *Reports on Progress in Polymer Physics in Japan*, volume 22, 1979.

[96] T. Kitano, T. Kataoka, and T. Shirota, *An Empirical Equation of the Relative Viscosity of Polymer Melts Filled with Various Inorganic Fillers*, Rheologica Acta **20**, 207 (1981).

[97] S. Goto, H. Nagazono, and H. Kato, *The Flow Behaviour of Fibre Suspensions in Newtonian Fluids and Polymer Solutions II. Capilliary Flow*, Rheological Acta **25**, 246 (1986).

[98] A. Jabbarzadeh, J. Atkinson, and R. Tanner, *Nanorheology of Molecularly Thin Films in N-Hexadecane in Couette Shear Flow by Molecular Dynamics Simulation*, Journal of Non-Newtonian Fluid Mechanics **77**, 53 (1998).

[99] R. B. Bird, R. C. Armstrong, and O. Hassager, *Dynamics of Polymer Liquids - Volume 1 Fluid Mechanics*, volume 1, John Wiley and Sons, 1977.

[100] S. Kim and S. Karilla, *Microhydrodynamics Principles and Selected Applications*, Butterworth Series of Chemical Engineering, Butterworth Heinemann, 1991.

[101] L. D. Landau and E. M. Lifshitz, *Theory of Elasticity*, volume 7 of *Course of Theoretical Physics*, Pergamon Press, second edition, 1970.

[102] X. J. Fan, N. Phan-Thien, and R. Zheng, *Simulation of Fibres Suspension Flows by the Brownian Configuration Field Method*, Journal of Non-Newtonian Fluid Mechanics **84**, 257 (1999).

[103] W. J. Milliken, M. Gottlieb, A. L. Graham, L. A. Mondy, and R. L. Powell, *The Viscosity-Volume Fraction Relation for Suspensions of Rod-Like Particles by Falling Ball Rheometry*, Journal of Fluid Mechanics **202**, 217 (1989).

[104] M. A. Bibbo, *Rheology of Semi-Concentrated Fiber Suspensions*, PhD thesis, Chemical Engineering, Massachusetts Institute of Technology, 1987.

[105] G. K. Batchelor, *The Stress Generated in a Non-Dilute Suspensions of Elongated Particles by Pure Straining Motion*, Journal of Fluid Mechanics **46**, 813 (1971).

[106] A. P. Arlov, O. Forgacs, and S. Mason, *Particle Motions in Sheared Suspensions 4: General Behaviour of Wood Pulp Fibres*, Svensk Papperstidning **61**, 61 (1958).

[107] C. G. Joung, N. Phan-Thien, and X. J. Fan, *Viscosity of Curved Fibers in Suspension*, Journal of Non-Newtonian Fluid Mechanics **102**, 1 (2002).

[108] G. G. Lipscomb, M. M. Denn, D. Hur, and D. Boger, *The Flow of Fibre Suspensions in Complex Geometries*, Journal of Non-Newtonian Fluid Mechanics **26**, 297 (1988).

[109] I. Proudman and J. R. A. Pearson, *Expansions at Small Reynolds Numbers for the Flow Past a Sphere and a Circular Cylinder*, Journal of Fluid Mechanics **2**, 237 (1957).

[110] J. Happel and H. Brenner, *Low Reynolds Number Hydrodynamics with Special Applications to Particulate Media*, Martinus Nijhoff Publishers, 1986.

[111] R. Eisenschitz, *Die Viscositat Von Suspensionen Langgestreckter Teilchen und Ihre Interpretation Durch Raumbeanspruchung*, Zeitschrift fur Physikalische Chemie. Abteilung A, Chemische Thermodynamik, Kinetik, Elektrochemie, Eigenschaftslehre **A158**, 78 (1932).

[112] H. L. Goldsmith, *Red Cell Motions and Wall Interactions in Tube Flow*, Federation Proceedings **30**, 1578 (1971).

[113] A. Karnis, H. L. Goldsmith, and S. G. Mason, *The Flow of Suspensions Through Tubes. V. Inertial Effects*, Canadian Journal of Chemical Engineering **44**, 181 (1966).

[114] S. I. Rubinow and J. B. Keller, *The Transverse Force on a Spinning Sphere Moving in a Viscous Fluid*, Journal of Fluid Mechanics **11**, 447 (1961).

[115] B. P. Ho and L. G. Leal, *Inertial Migration of Rigid Spheres In a Two-Dimensional Unidirectional Flows*, Journal of Fluid Mechanics **65**, 365 (1974).

[116] W. S. J. Uijttewaal, E.-J. Nijhof, and R. M. Heethaar, *Lateral Migration of Blood Cells and Microspheres in Two-Dimensional Poiseuille Flow: A Laser Doppler Study*, Journal of Biomechanics **27**, 35 (1994).

[117] Commonwealth Scientific and Industrial Research Organisation (CSIRO), Compumod Pty Ltd Distributors, Level 13, 309 Pitt St, Sydney, 2000, *Fastflo Tutorial Guide*, 3 edition, 1999.

[118] C. A. Stover, D. L. Koch, and C. Cohen, *Observations of Fibre Orientation in Simple Shear Flow of Semi-Dilute Suspensions*, Journal of Fluid Mechanics **238**, 277 (1992).

[119] L. A. Mondy, H. Brenner, S. A. Altobelli, J. R. Abbott, and A. L. Graham, *Shear-Induced Particle Migration in Suspensions of Rods*, Journal of Rheology **38**, 444 (1994).

[120] M. Vincent and J. F. Agassant, *Experiental and Theoretical Study of Short Fiber Orientation in Diverging Flows*, Rheologica Acta **24**, 603 (1985).

[121] H. Brenner, *Rheology of a Dilute Suspensions of Axisymmetric Brownian Particles*, International Journal of Multiphase Flow **1**, 195 (1974).

[122] R. S. Brumbaugh, *Ancient Greek Gadgets and Machines*, Thomas Y. Crowell Company, 1966.

[123] A. Neuburger, *The Technical Arts and Sciences of the Ancients*, Methuen and Company, 1969, Translated by Henry L. Brose from original text Die Technik des Altertums.

[124] I. of the History of the Natural Sciences, *Ancient China's Technology and Science*, Foreign Languages Press, Beijing, 1983.

[125] F. Gies and J. Gies, *Cathedral, Forge, and Waterwheel: Technology and Invention in the Middle Ages*, Harper Perrenial Publishers, 1994.

Appendix A

Additional Material

A.1 Simulation Source Code

The latest source code for the 'Chain-of-Spheres' simulation (Part II) and the '3D Particle' Simulation (Part III), along with assorted datafiles and other code can be found in the CD-ROM included at the back of this thesis. The 'Chain-of-Spheres' simulation and associated files are found at:

`CDROM:/01-Chain_of_Spheres/01-Source_Code_Stable/f409`

The '3D Particle' simulation and associated files are found at:

`CDROM:/02-3D_Particle/01-Source_Code_Stable/F55116`

The two simulations were written in ANSI standard Fortran77 and compiled using the Digital Fortran Compiler. Simulations were executed on various machines. These include DEC/Compaq Alpha processor based workstations running UNIX and Linux operating systems, and Intel $x86$-based PCs running both Linux and Windows.

A.2 Electronic Version of Thesis

Electronic versions of this thesis (Postscript, *Adobe PDF*, and LaTeX 2_ε) are available in various formats on the attached CD-ROM at:

`CDROM:/04-Thesis`

Appendix B

Pre-Rheology

B.1 Introduction

This is a brief history of some lesser known ancient technologies which might be considered to have a rheological flavour. Rheology as a distinct and recognised science did not exist prior to the early 1900's. It took more than one and a half millennia of 'promising starts' and gadgeteering in pre-16th century Europe before mostly theological pre-occupations finally gave way to the new empirical sciences and technologies. This history takes place mostly prior to the Rennaissance. The following passage is by no means complete, and is intended only for the historically inclined reader.

B.2 Pre-Rheology

Evidence for mankind's interest in Rheology and technology of flow can be found as far back as the ancients (e.g. [122][123][124][125]). The clepsydra is perhaps the most cited device from antiquity. Essentially nothing more than a vessel with a small hole in the bottom, time could be measured by the rate at which water leaked from it. The accuracy was mediocre, as the rate of flow diminished with the water level. However it was the first time-measuring innovation since the ancient sundial, and an example of the utilization of fluid property in a measuring instrument of practical use by mankind. The me-

chanician, Ctesibius (270 B.C.) refined the clepsydra further by eliminating the variation in water pressure as water level reduced. An overflow design was invented by which the water level in the vessel was maintained with a continuous water input supply and an overflow design to remove any excess (Fig. B.1). The clepsydra could then be used continuously and indefinitely as a time measurer, corrected only intermittently with astronomical time-keeping. Ctesibius also contributed to the knowledge of Alexandria with inventions based on the compressibility of air and water [122][123]. The

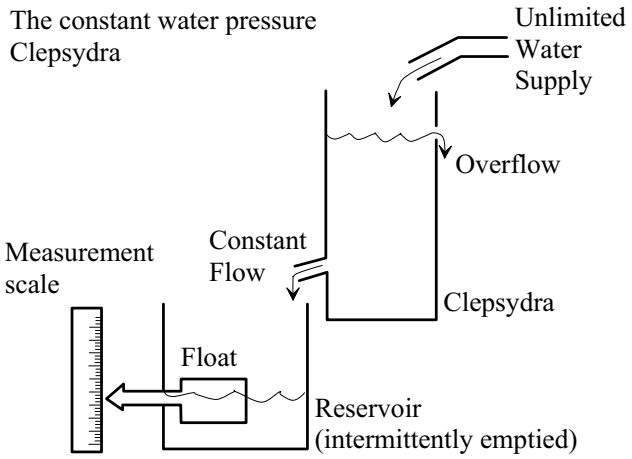

Figure B.1: The constant water pressure clepsydra of Ctesibius 270 B.C.

clepsydra was the first of a series of improvements on the concept of the 'water clock', culminating in the octogonal Tower of the Winds, (see Fig. B.2) created by Andronicus of Rhodes in the first century A.D. for the agora of Athens[1]. The Tower of the Winds was a public timekeeper and weather station with a water mechanism at its core. It featured a large ornamental dial, marking the hours with hands attached to rotating drums connected to floats. Heron of Alexandria (1st century A.D.), taught by the designs of Ctesibius, added his own knowledge of the power of fire and steam to develop the first steam engine (Fig. B.3). Heron created numerous ingenious gadgets and devices demonstrating a deep understanding of fluid mechanics, such as

[1]The Agora was the business centre of ancient Athens

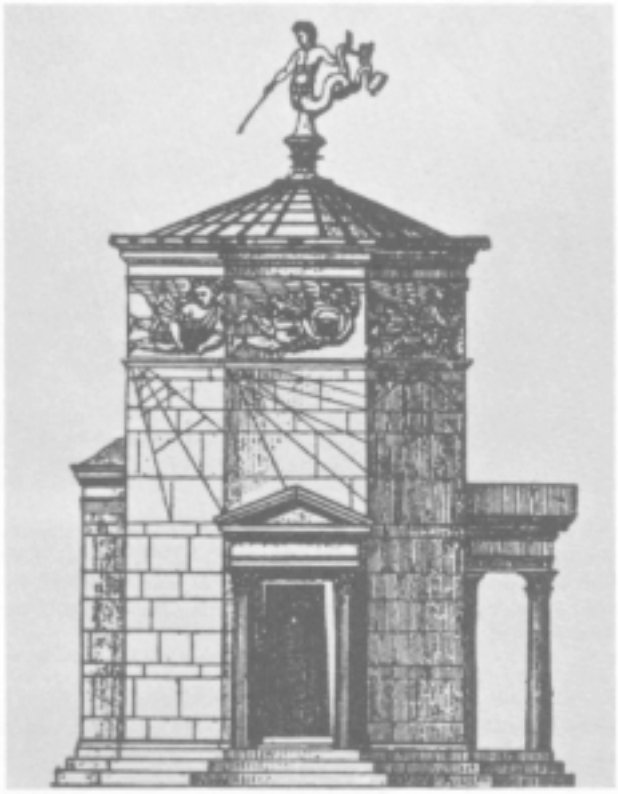

Figure B.2: The *Tower of the Winds* water clock. from [122]

the ability to siphon, and many other fluid responses to pressure, heat and flow [122]. Also related to water time keeping, the Han Dynasty astronomer Zhang Heng (2nd century A.D.) invented a water driven celestial globe based on an independently invented clepsydra. The celestical globe revolved with the diurnal motion of the skies above him [124] (Fig. B.4).

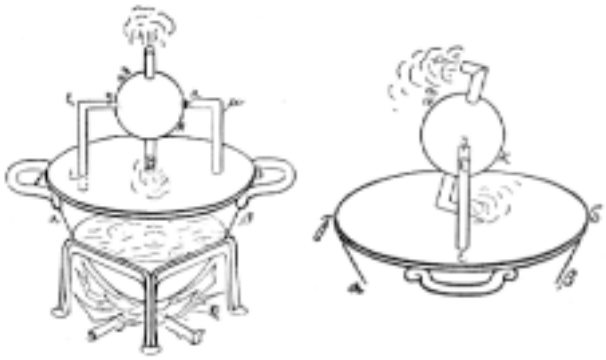

Figure B.3: The steam engine, or *Aeolipile* invented by Heron of Alexandria. From [123]

On the topic of water transport, Archimedes of Syracuse (3rd century B.C.) invented the screw for pumping water to a higher level. Three Kingdoms Dynasty inventor Ma Chun (260 A.D.) invented the Chinese equivalent square-pallet chain pump. This was a conveyor-belt like device with buckets linked in a belt. Power was provided by a man on a treadmill, an animal, and then eventually water power. Siphoning was also used in ancient China's Eastern Han Dynasty (25-220 A.D.) as a means of irrigation. In 1044 A.D. Zeng Gongliang is recorded using a large siphon to draw water over a hill using a long bamboo pipe. It is unclear what method of suction he used to initiate the siphoning over such a distance [124].

In the Eastern Han Dynasty (25-220 A.D.), oil (or *Shiyou*, literally *rock oil*) was found in a spring flowing out of a mountain south of Yanshou County of Jiuquan. When collected in a pot it changed from a brownish yellow to black and so was also called *shiqi* (*rock laquer*). Not only was it found to burn with an extremely bright flame but was also an excellent lubricant for axles and bearings [124]. In the Eastern Mediterranean early in the Byzantine

Roman period, military engineers of Constantinople devised a petroleum based naval weapon known as the *Greek Fire*. Discharged from tubes off the ships prows during close combat, ignited fluid was propelled under pressure onto the walls of enemy ships like a modern flame thrower. The problem with the Naphtha (petroleum distillate) available was that it would not adhere to the enemy ship walls easily, and would disperse rapidly once it fell into the water. An unknown inventor thickened the Naphtha with resin and sulfur. Like modern Napalm, the resulting formula did not disperse in water, nor could it be easily put out with water, continuing to burn enemy ships hulls on the waterline. Enemy Arab fleets were attacked in this manner outside Constantinople in 673 A.D. and also 717 A.D.

The innovations perhaps most resembling modern rheological knowledge are related to paper technology. In 1957 remnants of Western Han dynasty hemp paper (49 B.C.) were discovered in Baqiao in an eastern suburb of

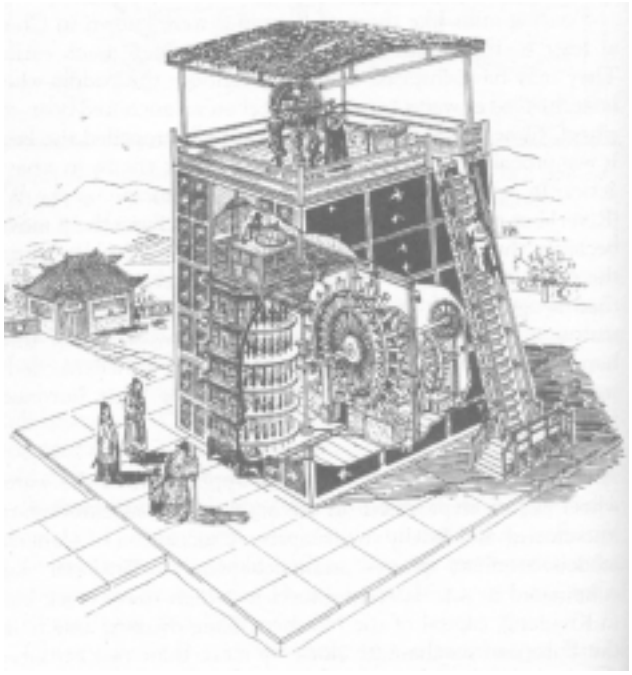

Figure B.4: Su Sung's water driven astronomical clock-tower, built in 1090. From [125]

Xi'an in Shaanxi Province (Northern Central China bordering Inner Mongolia). Microscopic study of these specimens indicated that a small amount of ramie (plant fibre) was combined with the base hemp pulp. These specimens represent the oldest known vegetable-fiber paper [124]. The ancient Chinese could in fact manufacture paper of specified tensile strength by altering the fibre content, much like modern fibre-filled composites. A similar technology using gums, pastes and starches was added in Baghdad during the migration of paper technology to Europe. By the 6th century A.D., there was available thicker paper for packaging and light structural use, through to various writing paper grades, and even soft, sometimes powdered and fragrant toilet paper for royalty (toilet paper is another invention of the Chinese). Starch-paste was widely used in the Tang Dynasty (618-907 A.D.) as filler and to keep fibers suspended in the vat during paper production. This was later replaced in the Song dynasty (960-1279 A.D.) with a sticky vegetable juice called *zhiyao* (*paper drug*), used to make a more even fibre distribution in the pulp (i.e. resistant to sedimentation). Similar approaches are used in modern food technology. The benefits of paper as a writing medium were exploited most in Europe. Part of the innovation of Gutenberg's printing press was the technology developed for ink. Johann Gutenberg invented the moveable text printing press in 1450 A.D., in the cathedral city of Mainz, on the Rhine River (see Fig. B.5). Paper technology in Europe was well developed by that stage, mostly by painters and artists in early rennaissance Italy. The other three printing technologies, the press, movable type and ink was made workable by Gutenberg. In relation to ink, printing required an ink with different characteristics from those of water-based writing ink which smudged, did not spread unformly, and leached through to the back-side of the paper. Italian painters in the previous century had invented the technique of mixing pigments (insoluble natural substances) in linseed oil. Gutenberg experimented successfully with a mixture of lampblack (chimney soot), turpentine, and linseed or walnut oil, reduced by heating. The new ink had the right consistency and wetting ability to adhere to slightly dampened

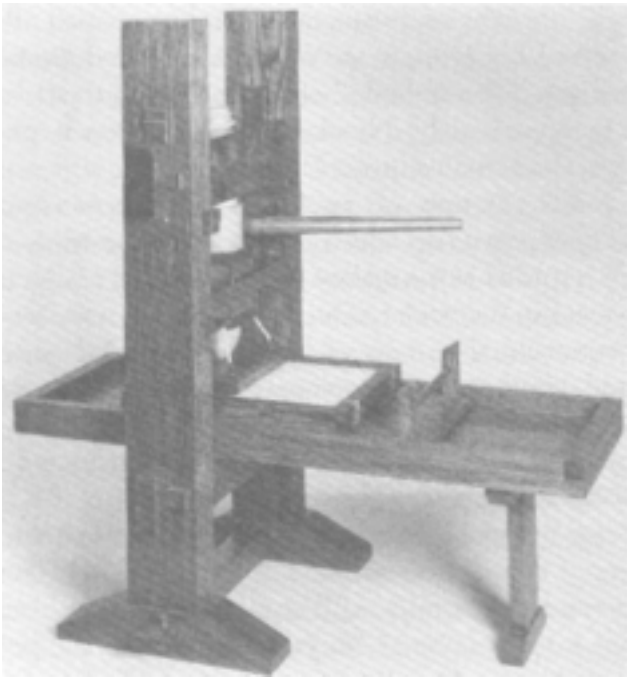

Figure B.5: The Gutenberg printing press. From [125]

paper without blurring, and was an attractive jet black. By the end of the Rennaissance, Europe and Asia clearly had the ability not just to harvest and use raw materials, but to modify and design man-made fluids and materials to suit a wide range of specific industrial requirements. These ranged from lubricants, to paints and inks, even to the idea of reinforcing structures using fibre composites.